Viral Mimicking Iron-Oxide Nanoplatforms for Highly Efficient Lymph Node Delivery and Lymphocyte Activation

By

Ryan Clauson

A dissertation submitted in partial fulfillment
of the requirements for the degree of
Doctor of Philosophy
(Pharmaceutical Sciences)
in The University of Michigan
2019

Doctoral Committee:

Assistant Professor Beata Chertok, Co-Chair
Professor Duxin Sun, Co-Chair
Assistant Professor Yu Lei
Assistant Professor James Moon
Professor David Smith

Ryan Clauson

rclauson@med.umich.edu

ORCID iD: 0000-0001-6044-8884

For my father –

Without your sacrifice and guidance, none of this could have been possible.

You have always been and will always be my hero.

Acknowledgements

Firstly, I would like to express my sincere gratitude to both of my advisors, Dr. Beata Chertok and Dr. Duxin Sun for their continuous support and guidance during my tenure at the University of Michigan. Dr. Chertok, thank you for developing me as a scientist, writer and problem solver. Dr. Sun, thank you for nurturing my skills as an independent researcher and for challenging me as a presenter. The advancements I have made as a scientist, leader and person are thanks in large part to both of your impacts in my life. I will be forever grateful for your investments in me.

Beyond my advisors, I would like to recognize the individual members of my thesis committee including Dr. David Smith, Dr. James Moon and Dr. Yu Leo Lei. Your astute insights and wealth of experience have been invaluable. Additionally, your challenges to my research ideas and methodologies have strengthened my capabilities as an independent critical thinker.

Next, I would like to acknowledge my lab mates for their incredible support academically, scientifically and emotionally over the last five years. From the Chertok Lab, I would like to thank Lindsay Scheetz, Dr. Mingsheng Chen and Brendan Berg. From the Sun Lab, I would like to specifically thank the members of the nano group including Dr. Hongwei Chen, Dr. Wei Gao and Hongxiang Hu.

Outside of the laboratory, I would be remiss if I did not recognize the friendships built during my time at the University of Michigan that were pivotal in maintaining my happiness and sanity. I will cherish the memories and your friendships for the rest of my life. I would specifically like to acknowledge, Nick Waltz, Phil Rzeczycki and Nate Truchan.

Last, but certainly not least, I would like to sincerely thank my family and future bride. To all of my family, your constant support throughout my entire academic career has given me the strength to complete this arduous journey. Without all of you, I would not be the man that I am today. To my loving fiancé Brenna, you are my rock and greatest source of inspiration. Thank you for your unwavering belief in me and the selflessness you exhibited for 800+ miles away as I pursued my dreams.

Table of Contents

List of Figures

List of Tables

List of Appendices

Abstract

Iron-oxide nanoparticles have been widely investigated as both diagnostic and therapeutic agents. Yet, as therapeutic agents, very limited research has been conducted to explore the potential of iron-oxide nanoparticles in vaccinology. Notably, there are no iron-oxide nanoparticle-based vaccines for cancer immunotherapy or infectious disease currently on the market. This reality is confounding because of the seemingly dynamic potential of iron-oxide nanoparticles in these applications. More specifically, iron-oxide nanoparticles possess numerous material characteristics that would make them highly attractive as carriers of vaccine components to immunologically relevant sites, such as the lymph nodes. These material characteristics include biodegradability, magnetic susceptibility, particle size control and surface composition diversity, among others. Accordingly, here we proposed to investigate the ability to leverage iron-oxide nanoparticles for lymph node targeting and lymphocyte activation toward design of efficacious vaccines.

In part one of this thesis, we explored how iron-oxide nanoparticles could be leveraged for the activation of humoral immunity. Activation of humoral immunity can be exploited to stimulate the production of antigen-specific antibodies with variable effector functionality that could be employed in both diagnostic and therapeutic applications (e.g. vaccines). Specifically, for engagement with the humoral immunity system, we developed an inorganic Au@Fe hybrid nanoparticle platform, coined inorganic virus-like nanoparticle (IVLN). As compared to traditional nanoparticle technologies, the IVLN mimics viral structure through the incorporation spherical geometry, topographical spiky antigenic clusters, optimal spatial distribution of antigenic clusters and extremely high local density of antigen with those clusters. We demonstrate that IVLNs dramatically improve B-cell activation, germinal center formation and production of antigen-specific antibodies with functional efficacy against HER2+ breast cancer in mice. Notably, as compared to traditional nanoparticle technologies, IVLNs increase the population of antigen-specific B-cells by 6-fold resulting in a 4 to 18-fold improvement in antigen-specific IgG production *in-vivo*.

In part two of this thesis, we investigated how iron-oxide nanoparticles could be leveraged for the activation of cellular immunity. Activation of cellular immunity facilitates the production of cytotoxic T lymphocytes with potential efficacy in the treatment of infectious diseases, as well as cancer. Specifically, for engagement with the cellular immunity branch, we developed a novel method to engineer lipid-coated iron-oxide nanoparticles (IONP-ML) using the phenomenon of lipid-stitching. This method allowed fabrication of IONP-ML with precise control of particle size, ultra high-density of biomolecule loading, and high MRI visibility. These characteristics translated to unprecedented *in-vivo* performance. Remarkably, the IONP-ML facilitated up to 200-fold increase in biomolecular loading and 9 to 40-fold increase in lymph node targeting efficiency as compared to previously reported technologies. As such, these materials could be broadly applicable in the efficient and tailored presentation of biomolecules in the lymph nodes toward induction of cellular immunity.

Overall, the work presented herein reaffirms the robust potential of iron-oxide based nanoplatforms as drug delivery vehicles, imaging modalities and immunomodulatory agents for both humoral and cellular immunity, thereby providing justification for the continued research, development and clinical translation of iron-oxide based nanoplatforms.

Preface

The content herein describes two unique approaches to the activation of lymphocytes utilizing iron-oxide nanoplatforms with virally inspired material design.

In Part 1 of this dissertation, iron-oxide nanoparticles are combined with gold nanoparticles to yield an inorganic virus-like nanoparticle (IVLN) system with a core-satellite morphology. The focus of this work was to develop virus mimicking nanoparticles for B lymphocyte activation. Traditional viral-like particles are the most efficacious vehicles in the activation of humoral immunity for antigen-specific antibody production. However, numerous manufacturing issues (e.g. scalability, post-translation modifications) and the potential for adverse immune events limit the robustness of their performance. To overcome these limitations, we sought to develop alternative virus-mimicking materials using inorganic nanoparticles. We hypothesized that the unique advantages in fabrication of inorganic materials could be leveraged to recapitulate the unique geometry and patterns of viral-like particles that are essential for efficacy, while minimizing potential complications. Herein, we explore the potential of the IVLN technology for antigen-specific antibody production against the human HER2/neu oncogenic protein.

In Part 2 of this dissertation, we report on the development of a novel method to fabricate iron-oxide nanoparticles coated with ultra-stable lipid shells. The focus of this work was to develop iron-oxide nanoparticles for image-monitored lymph node delivery and activation of CD8+ T lymphocytes. Although this application has been explored previously, to date, limited success has been achieved. The failures of established materials are most often attributed to poorly stable surface coatings that do not permit the high-density biomolecule loading and particle size control required for *in-vivo* applications. To address these limitations, we developed a novel method that utilizes the phenomenon of lipid stitching. We hypothesized that lipid stitching could be employed to produce stable iron-oxide nanoparticles well-defined lipid films on a particle's surface. Herein, we explore how to best leverage this method to control

nanoparticle size and support surface conjugation of biomolecules at ultra-high densities. In the context of cellular immunity, we propose that moving forward these materials would be ideally suited for the efficient delivery of subunit and conjugate vaccines, such as the model DNA-based covalent conjugate vaccine ovalbumin-CpG, to the lymph nodes.

Part 1:
Iron-Oxide Nanoplatforms for B-cell Activation

CHAPTER 1
Nanoparticles for Antigen-Specific Antibody Production: The Potential of Viral Mimicry

1.1 Introduction:

An antibody, or immunoglobulin, is a specialized glycoprotein produced by the immune system to neutralize pathogens, such as bacteria and viruses, in a highly specific manner[1]. The specificity of an antibody is not limited to these pathogens, however. In fact, antibodies have been developed against innumerable proteins, peptides, carbohydrates, nucleic acids and small molecules both synthetic and naturally occurring. Today, whether it be for protection against a wide-range of communicable diseases and cancer, or to provide valuable diagnostic and experimental research tools, antibodies are a critical part of both the healthcare and biotechnology fields[2, 3].

With the exception of recombinant antibodies that are solely produced using genetic manipulations of antibody coding genes *in-vitro*, antibodies are the result of animal immunizations to stimulate humoral immunity[4]. The B-cell, or B lymphocyte, is a type of immune cell that serves as both a lymphocyte and as an antigen-presenting cell in the humoral immunity branch of the adaptive immune response[1]. The major functional contribution of B-cells to the immune system is the production of antibodies. These antibodies are polyclonal in nature and will be the main focus of this review; the production of monoclonal antibodies following animal immunizations has been previously extensively reviewed elsewhere[5-7].

Antibody production is the result of B-cell activation and maturation in response to an antigen[1, 8]. For simplicity, in this review the term antigen will be used to describe any compound (small molecule), biomolecule (protein, peptide, carbohydrate) or pathogen (virus, bacteria, parasite) for which an antibody is being produced. B-cell activation most frequently occurs within the lymph nodes and happens in either a T-cell independent (TI) or T-cell dependent (TD) fashion[8-10]. T-cell independent B-cell activation is caused by two unique classes of antigens, known as TI-1 antigens and TI-2 antigens[11-13]. TI-1 antigens have intrinsic B-cell activating

properties regardless of B-cell receptor specificity (e.g. Lipopolysaccharide or CpG oligonucleotides)[12, 14]. TI-2 antigens are characterized by highly repetitive structures, most often associated with carbohydrates or synthetic polymers, which facilitate strong direct engagement and crosslinking of B-cell receptors[11, 13, 15]. Traditionally, T-cell independent B-cell activation results most significantly in the production of IgM antibodies with modest affinity and failure to stimulate an antigen-specific memory response. The only known exception to this rule is a viral infection, which has been shown to stimulate the production of high titer, antigen-specific IgM and IgG with memory in a T-cell independent manner[9, 16-18].

Those antigens that do not intrinsically stimulate B-cells or do not strongly crosslink B-cell receptors are considered T-cell dependent (TD) antigens[19]. TD antigens compromise the majority of antigens. As the name would suggest, T-cell dependent B-cell activation relies not only on the activation of B-cells through the B-cell receptor, but also necessitates CD4+ T-cell help. T-cell dependent B-cell activation can be described in a three-step process[19, 20]. First, B-cell receptors weakly associate with TD antigens promoting receptor-mediated endocytosis, degradation of the antigen and the subsequent presentation of the antigen on B-cell receptors in the context of Major Histocompatibility Complex II (MHC-II). Second, simultaneous to B-cell antigen presentation, CD4+ helper T-cells (commonly follicular T helper cells) are activated in an antigen-specific fashion by dendritic cells. Third, once active, these CD4+ T-cells cells interact with B-cells through two signals: T-cell receptor coupling to MHC-II on B-cell surfaces (signal 1) and CD40/CD40L co-stimulation (signal 2). Upon engagement of these two signals, B-cells are fully activated and B-cell proliferation is stimulated. Traditionally, it is this process that promotes germinal center formation and the maturation of antibody-secreting plasma cells that are responsible for the antibody class switching and somatic hypermutation necessary to produce high specificity and high avidity antibodies[21-23].

As a result of this complex mechanism however, the production of antibodies is not practical for many antigens, especially low molecular weight antigens, such as peptides or small molecules[24]. The failure to produce antibodies against these antigens is most of the result of inefficient delivery to the lymph nodes, as well as poor inherent immunogenicity. For this reason, particle-based delivery vehicles and adjuvants are most often a necessity for the production of high avidity, high specificity and high titer antibodies *in-vivo*[25, 26]. While the appropriate commercial adjuvant choices for efficacious B-cell activation and antibody production have been reviewed extensively elsewhere, the focus of this review is on the current status and future

prospective of nanoparticles as both adjuvants and delivery vehicles in vaccine development and antibody production research[25, 27-30].

1.2 Traditional Nanoparticles for B-cell Activation and Antibody Production:

The search for a universal scientific definition of the term nanoparticle is elusive, however, for most, nanoparticles are considered colloidal-based systems with particle sizes ranging from 1 to 1000 nanometers that have defined interfaces and behave in solution according to the principles of Brownian motion. Regardless of the definition, nanoparticles are classified based upon their physiochemical properties including composition, size, shape, surface properties, crystallinity, dispersion state and surface-to-volume ratio[31, 32]. The manipulation of these physiochemical properties across the variable nanoparticle types not only informs their uniqueness as materials, but also provides incredible opportunity for functional diversity. As a result, nanoparticles have been successively applied in far ranging applications including medicine, manufacturing and electronics[33, 34]. In the field of medicine, nanoparticles are widely researched and developed as drug delivery vehicles and immunostimulatory agents[35-37].

As drug delivery vehicles, nanoparticles are capable of achieving both active and passively mediated site-specific delivery in the body[38, 39]. For the specific application of antibody production, the most relevant delivery site is the lymph nodes[40]. The lymph nodes are secondary lymphoid organs, which serve as immunological filters for the body. More specifically, the lymph nodes are known to serve as critical sites for immune activation due to their high local density and spatial organization of antigen-presenting cells and lymphocytes[41, 42]. This proximity and organization facilitates efficient immune activation by dramatically improving the probability for coordinated cellular collisions.

The nanoparticle material properties for effective lymph node delivery including particle size, shape, surface charge, and stability have been studied extensively[43-46]. The most commonly cited material property for efficient lymph node delivery is particle size. According to the literature, nanoparticles with less than 200 nm diameter are capable of achieving passive lymph node delivery, while those nanoparticles with sizes in 200-500 nm range must be delivered to the lymph nodes actively[44]. This mechanistic difference is the result of lymphatic vessel physiology. While lymphatic vessel can range in diameter from 10-60 microns, the

lymphatic endothelial cell junctions that allow for entry of nanoparticles from the interstitial space are size-limiting[41, 47]. Due to the size of these junctions, nanoparticles greater than 200 nm in diameter do not efficiently enter lymphatic vessels. Conversely, nanoparticles or macromolecules with less than a 20 nm diameter more freely diffuse in and out of the lymphatic vessels and suffer from inefficient delivery as a result of leakage[45]. For these reasons, it has been demonstrated previously that nanoparticles with 10-100 nm particle sizes are delivered to lymph nodes with the greatest efficiency[48]. More narrowly, a particle size between 30-50 nm has been reported as being ideal for lymph node delivery[49-52].

Passive delivery indicates that nanoparticles are free and stable within the lymphatic fluid, while active delivery indicates that lymphatic transport is only possible in the context of migrating peripheral antigen-presenting cells that have up taken nanoparticles at the injection site[44]. These mechanistic differences in delivery would theoretically manifest in immunologically more efficacious outcomes for passive delivery as compared to active, especially in the context of B-cell activation and antibody production. This variance in efficacy is due to the fact that B-cells activation is significantly improved by direct presentation of antigen in its' native confirmation at high density on nanoparticle surfaces to facilitate B-cell receptor crosslinking for B-cell activation[53-55]. Based our current understanding of lymphatic transport of nanoparticles, this phenomenon would only be truly feasible in the context of passive delivery.

As immunostimulatory agents, nanoparticles have been shown on innumerable occasions to heighten the immune response acting both as adjuvants and as promoters of cellular uptake and antigen-presentation[37, 56-60]. Although the function of all nanoparticles as adjuvants is commonly debated in the literature, it is clear that some nanoparticles are composed of materials with inherently immunostimulatory components either synthetic or biologically derived. For example, inorganic nanoparticles such as carbon nanotubes, synthetic polymeric nanoparticles such as polyanhydride nanoparticles and biologically-derived polymeric nanoparticle such as chitosan nanoparticles have been shown previously to induce an inflammatory response that promotes the appropriate cytokine environment for immune stimulation based on their chemical composition[57, 61, 62]. On the other hand, materials such as liposomes and gold nanoparticles are most often considered chemically inert and do not contribute to the immune response based on chemical composition alone.

Taken together, it becomes evident that nanoparticles are capable as both delivery vehicles and as immunostimulatory agents for robust activation of the immune system, which

can be utilized to facilitate the production of high avidity, specificity and titer antibodies *in-vivo*. However, the choice of what nanoparticle to use for what application remains a critical decision.

1.2.1 Lipid Nanoparticles (Liposomes)

First described in the 1960's, liposomes are small artificial spherical vesicles that are composed of natural or synthetic phospholipids, which undergo self-assembly into one or more bilayers engulfing an aqueous core[63]. The popularity of liposomes is due to their simplicity in formulation, wide diversity and availability of the phospholipid components, as well as their profile as being highly biocompatible and highly biodegradable[64]. In fact, liposomes were the first nanoparticle-based drug delivery strategy to be successfully translated from research to clinical used, and represents the nanoparticle technology most widely approved as drug products by the FDA[65, 66].

Liposomes can be formulated as unilamellar or multilamellar vesicles with particle sizes ranging from 25-2500 nm having anionic or cationic surface character, depending upon their phospholipid composition and formulation scheme[63]. Liposomes are capable of carrying cargo in three separate compartments: the aqueous core, the hydrophobic acyl chain layer and the surface[67]. For the purposes of B-cell activation and antibody production, the most relevant loading mechanism is surface presentation due to direct contact with B-cells that promotes bivalent B-cell receptor engagement[46, 68]. Importantly, with the clinical acceptance of and commercialization of PEGylated phospholipids with diverse categories of functional moieties such as maleimide, azide, nitrilotriacetic acid and biotin, surface modification of liposomes with antigen has never been easier.

Based on literature review, liposomes have been previously utilized for antigen-specific antibody production in greater than twenty different publications (Table 1.1)[68-88]. The average serum antibody titer achieved across these publications is approximately 32,800. Despite this relatively modest average titer, liposomes have been used previously with great success. More specifically, two examples of the efficacious application of liposomes for antibody production in terms of antigen-specific IgG serum titers were reported by Moon et al and Yan et al[70, 86]. Moon et al was able to achieve a malaria antigen specific IgG titer of approximately 200,000 with a very low dose of 1 µg by incorporating the lipid adjuvant MPLA into the formulation[86]. Yan et al demonstrated serum titers between 10^5-10^6 for 1.5 µg HIV tat protein utilizing nickel-chelating methodology for liposomes surface modifications[70].

Despite the successful application of liposomes for antibody production in over thirty-five publications, several challenges for this technology remain. One such challenge is that liposomes are the subject of a significant anti-carrier response as the result of antibody production against the lipid and polymer components of the lipid formulation[67]. Due to this anti-carrier response, liposomes are exposed to rapid antibody-mediated blood clearance, which reduces their therapeutic efficacy during re-dosing. Another such challenge to the application of liposomes for antibody production is that, in the majority of cases, the use of high doses and adjuvants are still required to produce high titer antigen-specific antibodies[68, 74, 75, 81, 88].

1.2.2 Inorganic Nanoparticles

1.2.2.1 Gold Nanoparticles

The potentially most widely utilized inorganic nanoparticles in biotechnology today are gold nanoparticles[89-91]. As the name would imply, gold nanoparticles are gold metallic colloids that can be easily synthesized with controlled size, shape and surface properties[92, 93]. As such, gold nanoparticles can be engineered with a unique range of physiochemical properties, which make them valuable and adaptable in many fields including drug delivery, imaging, diagnostics and electronics.

As drug delivery vehicles, gold nanoparticles display ideal particle size, tunable surface properties and low toxicity[94]. Additionally, the intrinsic ability of gold nanoparticles to coordinate the commonly exploited gold-thiol (Au-S) bond facilitates surface functionalization with a wide-range of antigens containing naturally occurring or synthetically modified thiol moieties[95]. Gold nanoparticles have been previously employed as vehicles for antigen-specific antibody production in greater than twelve unique publications (Table 1.2)[60, 92, 96-102]. Notably, the average antigen-specific IgG serum titer observed in these publications was approximately 73,400. Notable applications of gold nanoparticles for antibody production in terms of titer and application diversity were published by Kumar et al and Dykman et al[60, 101]. Kumar et al demonstrated the ability to formulate gold nanoparticles as a vaccine against malaria using the Pfs230 protein, which resulted in the stimulation of antigen-specific IgG titers of approximately 640,000 using a 10 μg dose and the FDA-approved adjuvant alum[101]. This titer is significantly higher than the majority of literature published for gold nanoparticles by nearly an order of magnitude. In this vein, while Dykman et al produced modest titers of approximately 15,360

using bovine serum albumin as a model protein, the success of this group is in their incredible diversity of applications for gold nanoparticles including antibody production against influenza, foot-and-mouth disease virus, tuberculosis and small molecule drugs[60, 96, 97, 103, 104].

While gold nanoparticles have many advantages as nanoparticles for immune activation, several disadvantages of their use do exist. The most commonly considered disadvantages of using gold nanoparticles include lack of biodegradability, poor clearance, the potential for long-term toxicity associated with coatings and capping ligands, as well as the cost to manufacture gold nanoparticles at industrial scales[105, 106].

1.2.2.2 Silica Nanoparticles

Silica nanoparticles are nanoparticles composed of silicon dioxide that have demonstrated promise in a wide-range of biological application including drug delivery, imaging and tumor ablation[107, 108]. This promise is the result of the simplicity and precision of the synthetic process, which readily allows for manipulation of such material properties including particle size, shape, crystallinity, porosity and biodegradability[109, 110]. In this way, silica nanoparticles can be precisely engineered for specific applications without necessitating a one-size fits all philosophy. The most commonly utilized silica nanoparticle for drug delivery applications are known as mesoporous silica nanoparticles. Mesoporous silica nanoparticles have honeycomb-like structural features with high surface area and high reactivity, which facilitate high antigen payloads. In addition to their potential as delivery vehicles, silica nanoparticles are considered by many to be viable adjuvants for vaccines based on improved cellular uptake mechanisms[111-113].

Silica nanoparticles have been utilized previously for antigen-specific antibody production in at least seven applications (Table 1.2; three publications report titers)[114-120]. However, silica nanoparticles have been shown to only achieve modest antigen-specific IgG titers. Specifically, the highest antibody titer obtained with silica nanoparticles systems was 6,400 by Mahony et al against ovalbumin as a model protein antigen[114]. Beyond the modest stimulation antibody production, the main disadvantage associated with the use of silica nanoparticles is the potential for toxicity[121]. Toxicity of silica is most commonly linked to crystallinity and particle size. While it is now well established in healthcare and manufacturing that crystalline silica is toxic, traditionally amorphous silica is considered safe. However, recent

research utilizing silica nanoparticles suggests that the silanol groups that form on the nanoparticles surface interact with phospholipids in red blood cells leading to hemolysis[122, 123]. Additionally, there have been connections made between silica nanoparticles usage and the onset of melanoma[124].

1.2.2.3 Carbon Nanotubes

Carbon nanotubes are allotropes of carbon, which form highly stable hollow cylindrical nanostructures that can be synthesized as single, double or multi-walled structures[125]. The number of walls increases the surface area and tensile strength of the material. Due to their distinctive structure, carbon nanotubes are known to have unique mechanical, electrical, optical and thermal properties[125]. As such, carbon nanotubes have been utilized in applications ranging from scaffolds in tissue engineering to sensors for environmental toxins[126, 127].

As drug delivery vehicles, carbon nanotubes combine extraordinarily high surface to volume ratios and extensive diversity of potential biomolecule conjugation schemes[128, 129]. As immunostimulatory agents, carbon nanotubes have been shown to be able to stimulate a dramatic pro-inflammatory response, in addition to facilitating rapid and efficient cell entry[61, 130, 131]. Taken together, these characteristics make carbon nanotubes versatile delivery vehicles. Accordingly, carbon nanotubes have been evaluated as potential vehicles for antigen-specific antibody production in at least three previous applications (Table 1.2)[61, 131, 132]. The results of these applications demonstrate that while carbon nanotubes can be utilized for antibody production, the modest antigen-specific serum IgG titers between 1,000-10,000 achieved do not distinguish them as unique for this specific application.

Despite the continued application of carbon nanotubes as drug delivery vehicles and immunostimulatory agents, they suffer from several glaring drawbacks. Chief among these drawbacks includes a lack of biodegradability and high in-vivo toxicity[133, 134]. More specifically, carbon nanotubes have been connected in animal models to behave in an asbestos-like manner in the lungs leading to the spontaneous induction of lung cancer[135].

1.2.2.4 Iron-Oxide Nanoparticles

Iron-oxide nanoparticles (IONPs) are clinically accepted biomaterials with intrinsic physico-chemical properties including biocompatibility, biodegradation and magnetic susceptibility that make them versatile and safe nanoparticle candidates in biomedical applications[136-138]. Clinically, IONPs are utilized as FDA-approved biomaterials for diagnostic MRI imaging as T2-weighted contrast agents[139, 140]. IONPs can be synthesized by established techniq ues such as thermal decomposition with extreme precision of particle size and shape (spheres, rods, cubes)[137, 141]. Beyond the choice of size and shape, the most significant choice that must be made during IONP synthesis is surface coating material and formulation scheme. The potential surface coatings of IONPs for biomedical applications include synthetic polymers, sugars or lipids[142-144]. The choice of surface coating determines the capacity of an IONP to facilitate antigen surface conjugation while maintaining colloidal stability, and therefore governs the nanoparticles ultimate application scope both *in-vitro* and *in-vivo*.

Despite the extensive utilization of IONPs for biomedical research and medical diagnostics, few therapeutic applications have been successfully adapted. In fact, to date, only one publication reports the utilization of IONP nanoparticles for antigen-specific antibody production (Table 1.2). Interestingly, this publication by Pusic et al was able to stimulate the production of antigen-specific serum IgG titers between 10,000-100,000[145]. One potential explanation for the lack of translational therapeutics based on IONPs in literature could be that contradictory reports of the immunostimulatory potential of IONPs have been reported. For example, although Pusic et al reported on the successful application of IONPs for the treatment of malaria, other reports suggest that IONP administration can actually attenuate the production of antigen-specific IgG in animal models[146]. These conflicting reports may be linked to variability IONP surface coating materials and formulation methodologies. More specifically, although IONPs traditionally exhibit excellent biocompatibility and biodegradability, these features can be dramatically reduced by surface coatings that require harsh cross-linking procedures to facilitate antigen conjugation and high colloidal stability *in-vivo* (e.g. dextran)[147-149].

1.2.3 Polymeric Nanoparticles

1.2.3.1 PLGA Nanoparticles

Poly (lactic-co-glycolic) acid or PLGA is a biodegradable, controlled release block co-polymer. The biodegradation of PLGA is the result of the hydrolysis of ester linkages, the rate of which is determined by the relative hydrophobicity of the lactic and glycolic acid monomer units [150]. PLGA systems have received extensive attention in both research and clinical applications over the last three decades, and are considered to be the best-defined biomaterials for drug delivery [151]. Accordingly, PLGA has been widely explored in the fabrication of nanoparticles, microparticles, implants and injectables [151-154]. PLGA nanoparticles facilitate both antigen encapsulation and surface presentation via a myriad of chemistries. Inside, PLGA has been previously demonstrated to be able to encapsulate proteins, peptides, and small molecule drugs while sustaining controlled release integrity[155-157]. Outside, PLGA nanoparticles can either be formulated with specifically modified polymers to coordinate direct polymer modification or can be surface coated with functional PEGylated phospholipids to allow for conjugation based on thiols, click chemistry or biotin-avidin associations[158-162].

PLGA nanoparticles have been previously applied as drug delivery vehicles for antigen-specific antibody production in a number of applications including, but not limited to: ovalbumin, anthrax, malaria, bovine parainfluenza and clenbuterol (Table 1.3)[158, 163-167]. Interestingly, despite limited utilization of PLGA nanoparticles for antibody production to date, the average antigen specific serum IgG titer based on literature review is approximately 100,000. Of the applications listed above, the work by Manish et al stands out as being noteworthy[163]. With a single 100 µg dose of anthrax protective antigen domain protein, Manish et al were able to stimulate an antigen-specific IgG serum titer of approximately 310,000[163]. The implication of this data set is that, based on the depot-forming and controlled release nature of PLGA, it may be feasible to produce high titer, antigen-specific IgG with a single immunization. With alternative systems, this phenomenon would only be observed after multiple booster doses.

The drawback associated with the use of PLGA nanoparticles for antigen delivery is the potential to damage the antigen during both loading and release[168-170]. More specifically, many formulation methods for PLGA nanoparticles require exposure of sensitive antigens to organic solvents[170]. Additionally, as a result of the bulk-eroding nature of PLGA, the hydrolysis and reveal of oligomer units in the core produces a harsh acidic environment[168, 169]. Beyond these

potential complications, another drawback of PLGA is that the formulation of PLGA nanoparticles below 100 nanometers with high yield can be difficult and tedious in terms of size control and formulation stability[171]. Often, to achieve such particle size extensive and laborious filtration techniques are required. As a result, PLGA nanoparticles are not ideal vehicles for lymphatic transit.

1.2.3.2 Polyanhydride Nanoparticles

Polyanhydrides are a lesser-known class of biodegradable co-polymers with translation potential that can also be readily formulated into nanoparticles[172]. Clinically relevant polyanhydrides are based on the three diacids monomer units, sebacic acid or SA, 1,6-bis-(p-carboxyphenoxy)hexane or CPH, and 1,9-bis-(p-carboxyphenoxy)-3,6-dioxaoctane or CPTEG [173-175]. Polyanhydride nanoparticles have been shown previously to be non-inflammatory, non-toxic, and non-mutagenic [176]. Significantly as compared to PLGA nanoparticles, polyanhydride nanoparticles are more readily applicable to the stable encapsulation and delivery of protein based antigens due to their nature as surface eroding polymers and inclusion of amphiphilic units [177].

In addition to their delivery potential, polyanhydride nanoparticles have also been implicated to have inherent immunostimulatory or adjuvant-like properties based upon their composition[57, 178]. More specifically, polyanhydride polymer systems have been shown to stimulate a Th1 type immune response through TLR receptor pathways[57]. This immunostimulatory response has been demonstrated to be applicable to both the cellular and humoral branches of the adaptive immune response. As such, polyanhydride nanoparticles have been utilized for antigen-specific antibody production in at least eight publications with an average antigen-specific IgG titer of approximately 95,000 (Table 1.3)[164, 179-184]. Of these examples, the two most noteworthy applications were by Petersen et al and Ulery et al[181, 185]. Petersen et al produced titers between 10^5-10^6 using a 10 μg dose of anthrax protective antigen administered subcutaneously without additional adjuvant[181]. Ulery et al demonstrated that polyanhydride nanoparticles could be administered intranasally to produce titers between 10^4-10^5 against a 50 μg dose plague relevant surface antigens[185].

The potential drawbacks associated with the use of polyanhydride nanoparticles are complications in polymer reproducibility and toxicity associated with non-ideal organic solvent usage during formulation (e.g. chloroform, dichloromethane)[186-188]. As compared to PLGA that is

widely commercially available at highly characterized and defined compositions, polyanhydrides must be synthesized in house[186]. The requirement of in house synthesis can lead to dramatic batch-to-batch variability and lab-to-lab variability that can dramatically affect reproducibility and the transfer of information.

1.2.3.3 Chitosan Nanoparticles

Chitosan is a biologically derived, glucosamine-based, linear co-polymer that is produced by deacetylation of chitin[189, 190]. Chitin is a type of polysaccharide that is a primary component of the exoskeletons of crustaceans. The physiochemical properties of chitosan including degree of deacetylation and molecular weight alter the materials' solubility, encapsulation efficiency, degradation rate and formulation flexibility, and thereby determines chitosan's ultimate functionality[190]. Much like the synthetic polymers PLGA and polyanhydride, the biologically derived polmer chitosan behaves with controlled release character[191]. As a drug delivery vehicle, chitosan nanoparticles primarily deliver antigen via encapsulation, or more appropriately electrostatically mediated complexation[62, 192, 193]. Notably, chitosan is traditionally utilized in mucoadhesive applications due to its highly basic and cationic properties, including being FDA approved for wound dressing[194]. Thus, chitosan is more of a depot-forming material than a classical lymphatic trafficking agent. As an immunostimulatory agent, chitosan has been shown previously to stimulate the production of cytokines in a pro-inflammatory manner, to activate macrophages, dendritic cells and natural killer cells, as well as being connected to both anti-tumor immunity and anti-viral immunity[62, 195-198].

Chitosan nanoparticles have been utilized in a variety of applications for antigen specific antibody production including, but not limited to: ovalbumin, hepatitis B, H1N1 influenza, pneumococcal infection, E. coli, anthrax and snake venom (Table 1.4)[192, 193, 196-203]. Based on literature review, the average antigen-specific serum IgG titer produced while utilizing chitosan nanoparticles as the delivery vehicle and adjuvant was approximately 60,000. Two particular examples that stand out from this group are from Pawar et al and Malik et al[192, 196]. Utilizing glycol-chitosan nanoparticles for intranasal vaccination against Hepatitis B surface antigen, Pawar et al was able to stimulate antigen-specific IgG titers of approximately 100,000 using only a 10 μg dose and no additional adjuvant by changing the molecular weight of the chitosan polymer[196]. Alternatively, Malik et al demonstrated the potential to combine chitosan nanoparticles with additional adjuvant, such as CpG or poly I:C, to promote a more robust

immune response against anthrax[192]. More specifically, Malik et al showed a 2-fold enhancement of antigen-specific IgG titers from 100,000 (without CpG) to 200,000 (with CpG) by encapsulating the anthrax protective antigen into trimethyl chitosan nanoparticles and using CpG oligonucleotides as adjuvant[192].

Despite the promise of chitosan nanoparticle for both their delivery and immunostimulatory potential, several drawbacks of their use do exist. Chief among these drawbacks is that chitosan has poor solubility at physiological pH and is highly soluble at acidic pH, which dramatically effects degradation timing and informs antigen bioavailability[204]. In the specific context of B-cell activation and antibody production, chitosan nanoparticles rely on encapsulation for antigen loading and *in-vivo* depot formation for antigen delivery, which simultaneously limits lymph node delivery and B-cell receptor surface interactions with particulate antigens. Lastly, although chitosan is generally considered non-toxic and biocompatibility, recent studies have implicated chitosan in mutagenic genotoxicity[205].

1.2.4 Virus-Like Nanoparticles

Virus-like nanoparticles (VLPs) are self-assembled protein nanoparticles that are composed of viral-derived structural proteins[206-208]. VLPs do not contain the genetic material necessary to facilitate viral-induced host cell transformation and replication. As a result, VLPs are considered to be safe for human application. To date, VLP-based vaccines have been employed in at least 16 FDA approved and licensed products, including the FDA-approval of vaccines for Hepatitis B Virus (Recombivax) and Human Papillomavirus (Gardasil)[207]. Additionally, VLPs have been evaluated in more than 30 clinical trials for applications including Alzheimer's disease, breast cancer, nicotine addiction and rabies[207]. Based on the collective lessons learned from the development and clinical translation of virus-like nanoparticles it is clear that the unique functional efficacy of VLPs can be attributed to their unique structural features.

Structurally, VLPs are defined as having a rigid geometry with multivalent and high-density antigen display with particle sizes ranging between 30-500 nm[59, 207, 209, 210]. In other words, viruses are highly organized and repetitive structures by design that coalesce to display epitopes in high density with defined shape and patterns. Interestingly, this level of geometric patternization is unseen in any other biological system. As a result, it is now thought that the

immune system is capable of recognizing the structural features of viruses as pathogen associated molecular patterns, or PAMPs[210, 211]. Traditionally, PAMPs are molecules associated with groups of pathogens that are recognized by cells of the innate immune system via pathogen recognition receptors[212]. Examples of PAMPs would include materials such as lipopolysaccharide, flagellin or CpG oligonucleotides[212]. Nanoparticles would not traditionally be characterized as PAMPs, but virus-like particles are now considered by many to be. In this way, viral geometry in and of itself has been proven to be immunostimulatory in nature. More specifically, in the context of B-cell activation antibody production these unique structural features manifest in two different ways.

The first is highly efficient B-cell receptor engagement and cross-linking. Based upon experiments performed with synthetic polymers with antigens are defined spacing intervals, it is now better understood that B-cell activation is the result of B-cell receptor crosslinking or forced aggregation and that the optimal spatial resolution of antigens for this phenomenon to occur is 15-20 antigens within a 5-10 nm diameter[211, 213]. Viruses are known to frequently have surface antigens geometrically orientated with defined spacing and density that would satisfy these requirements[214, 215]. Notably, based on a biological recognition of this phenomenon, many viruses have evolved to reduce the extent of antigen surface density and controlled display to facilitate immune evasion (e.g. Human Immunodeficiency Virus)[216].

The second manner in which the structural features of VLPs are manifested is in the ability to stimulate the production of autoantibodies against self-antigens in addition to high titer antibody production against foreign antigens – an ability truly unique to VLPs[55]. Autoantibodies are antibodies formed against self-antigens and are most commonly associated with the onset of autoimmune diseases. As such, the immune system is regulated in such a way that autoantibody producing B-cells, which are frequently made by chance, should be weeded out and eliminated through a process known as tolerance[217]. Tolerance can either result in the clonal deletion of autoantibody producing B-cells, receptor editing to fix the recognition patterns or through the induction of B-cell anergy. However, in the case of viruses, B-cells are activated so strongly that they are influenced to escape tolerance regardless of the antigen's origin.

As a result of the intrinsic immunostimulatory nature of VLPs combined with the appropriate material properties for efficient lymphatic trafficking and retention, VLPs are ideal candidates as nanoparticles for antigen-specific antibody production against a wide-range of antigens. For example, VLPs have been utilized for antibody production in application including, but not limited to: influenza, human immunodeficiency virus, hepatitis B, respiratory syncytial

virus, middle eat respiratory syndrome, severe acute respiratory syndrome, hand foot and mouth disease virus, Alzheimer's disease, TNF-alpha, estriol, nicotine and tumor-associated carbohydrate antigen (Table 1.5)[55, 111, 215, 218-232]. Significantly, VLPs exhibit the highest average antigen-specific serum IgG titer at 120,000. Multiple examples of the successful application of VLPs for antibody production stand out in the literature. Skrastina et al confirmed the ability of VLPs to achieve dramatically high titers (titer = 300,000) against viral components when they employed the hepatitis B virus-like particle to stimulate an anti-hepatitis B surface antigen response[111]. Chackerian et al harnessed the autoantibody production capabilities of VLPs to produce high titer response against the self-antigen peptide TNF-alpha[224]. Lastly, Maurer et al demonstrate the dynamic range of VLPs by stimulating a strong humoral immune response against nicotine, a small molecule, which is a class of antigen that is traditionally difficult to stimulate a specific and high-titer antibody response against[220].

While the tremendously diverse and robust potential of VLPs is evident, this technology still has a number of disadvantages[233]. The first noteworthy drawback of VLPs is the unwanted level of non-specific immunogenicity toward the capsid structural components[234]. This immunogenicity often results in the off-target production of antibodies against the capsid itself, which leads to a high level anti-carrier response. This response can dramatically reduce therapeutic efficacy upon re-dosing. An additional disadvantage of VLP technology is if VLPs must be surface modified for antigen loading the protein can be denatured or the colloidal stability of the particle can be compromised[235]. Moreover, traditional bioconjugation schemes for antigen surface loading would dramatically reduce the pattern and density controls that are significant in VLP efficacy[214]. In terms of manufacturing, VLP formulations can be challenging[233]. More specifically, unlike other traditional nanoparticles that are chemically synthesized, VLPs must be genetically engineered, self-assembled and secondarily modified within a host cell. Different host cell types can include e. coli, yeast, insect cells, plant cells or other mammalian cells, each with its own unique advantages and disadvantages[236, 237]. Beyond the requirement of highly specialized technology to produce these materials, this formulation process lends itself to potentially poor reproducibility and can limit application scope. As a result of the potential formulation complications, alternative methodologies are currently being pursued to formulate viral-like nanoparticles in an attempt to capitalize on their class-leading efficacy while reducing technical difficulties. Accordingly, a new descriptor for nanoparticle regardless of class has been introduced in recent years – viral-mimicry.

1.3 The Potential of Virus-Mimicking Nanoparticles for Antibody Production

1.3.1 What is Viral Mimicry?

Viral mimicry is a derivative of molecular mimicry. Molecular mimicry is a biological phenomenon that can be evolutionarily developed or artificially engineered based on a fundamental understanding of the immune systems ability to recognize biomolecules or infectious agents with specific compositions, shapes, patterns, densities, topographies, etc[238, 239]. For example, researchers now believe that the human immunodeficiency virus employs molecular mimicry for immune evasion by limiting antigen surface density and patternization. As a result, HIV often fails to facilitate dual B-cell receptor engagement and crosslinking leading to B-cell anergy and failure to stimulate the humoral immune response[216]. Traditionally, molecular mimicry is discussed in the context of autoimmune diseases wherein self-antigen escapes immunological self-tolerance. However, in the context of viruses, molecular mimicry can be harnessed for beneficial immune stimulation.

As previously introduced, viruses have rigid geometries with multivalent and high-density antigen displays that are completely unique in biological systems. In response to these distinctive characteristics, the immune system has evolved to recognize geometric patternization and high-density antigen display as a sort of PAMP[210, 211]. Traditionally, PAMPs are recognized by the innate immune system through pathogen recognition receptors (PRR), such as toll-like receptors[212]. PRR engagement results in the induction of a pro-inflammatory cytokine response that adjuvants host immunity, both humoral and cellular[212]. In this way, viral structural properties could be considered self-adjuvanting and intrinsically immunostimulatory. Therefore, the ability to mimic these unique structural characteristics would be of the upmost interest to researchers attempting to develop the next generation of preventative and therapeutic nanoparticle-based vaccines.

1.3.2 Viral-Mimicking Nanoparticles for Antibody Production - Current Status

Viral-mimicking nanoparticles are those nanoparticles that are rationally designed and engineered based on the knowledge gained from studying how viral physiochemical properties either circumvent or foster the host immune response[240-242]. While protein-based virus-like

particles are most frequently discussed as viral-mimicking nanoparticles, recently research in this area has broadened to incorporate lipid, polymeric and inorganic nanoparticles[243-246]. While currently no comprehensive nanoparticle platform has been reported to replace true virus-like particles, significant advancements have been made in the imitation and application of the unique individual components of viruses. A few examples of the individual components that been adapted from viruses and engineered into viral-mimicking nanoparticles include: particle size, particle shape, surface topography, antigen display, antigen density and antigen organization (Table 1.6).

The role of nanoparticle size and shape was recently evaluated by Dykman et al and Niikura et al utilizing gold nanoparticles as a delivery platform with bovine serum albumin and West Nile Virus envelope protein as a model antigen system, respectively[60, 92]. Both Dykman and Niikura identified spherical nanoparticles between 40-50 nanometers as being the most effective at inducing antigen-specific antibody responses, and rod-shaped gold nanoparticles as being the least effective. Interestingly, both Dykman and Niikura also identified a particle-size dependent response in addition to the particle shape response. Larger nanoparticles (40-50 nm) were more approximately 2-fold more efficacious in stimulating antibody production as compared to their smaller counterparts (15-20 nm). Mechanistically, Niikura connected the variability in the immune response to different sized and shaped nanoparticles to the type and extent of the cytokine environment, and to a lesser extent cell uptake. More specifically, spherical nanoparticles of 40 nm diameter combined induction of a pro-inflammatory cytokine response with high cell uptake, while rod-shaped nanoparticles induced an inflammasome type response and cubes showed exceptionally low cellular uptake[92].

Beyond particle size and shape, one material property that has been connected to cellular uptake and could be used to influence the immune response is nanoparticle surface roughness, or topography. The significance of nanoparticle surface topography for cellular uptake was recently explored by Niu et al employing silica nanoparticles[247, 248]. Niu suggests that in addition to the receptor-mediated mechanisms for cellular uptake, the “nano-ecology” of viruses may contribute significantly and in part explain their unparalleled cellular delivery efficiencies and infectivity. While not specifically for the application of antibody production, Niu demonstrated in two separate publications that the surface roughness of nanoparticles could be manipulated to improve cellular uptake and delivery efficiency of genetic material or protein[247, 248]. Beyond the obvious improvement in biological relevance of the nanoparticle surfaces, this phenomenon could be applied for improved antigen-presenting cell activation that would be vital

in T-cell dependent B-cell activation. Additionally, surface roughness is known to contribute to improved antigen loading capacity on nanoparticle surfaces[247].

Nanoparticle surface loading of antigen is significant for the robust induction of the humoral immune response. While both surface presentation and encapsulation have been demonstrated to be viable strategies for the stimulation of antibody production, publications by researchers such as Kirby et al and Guan et al indicate the loading mechanism can be used to skew the balance of the immune response[68, 249]. More specifically, using a microparticle platform, Kirby et al determined that the immune response of surface presented antigen is skewed towards the humoral immune response, as compared to the cellular immune response for encapsulated antigen[249]. Similarly, using a liposomal system, Guan et al demonstrated that surface exposed peptide could stimulate an antigen-specific antibody response, while encapsulated peptide could not[68]. Despite the significance of the results reported by Kirby et al and Guan et al, no connection between antigen surface display and viral mimicry was ever addressed. Two publications that do make this connection and exploit this phenomenon for antigen-specific antibody production come from Riitho et al and Moon et al, who both produce viral-mimicking lipid-coated PLGA nanoparticles with surface antigen display as potential vaccine platforms for bovine virus diarrhea virus and malaria, respectively[158, 250]. But, surface antigen display alone is not sufficient to achieve true viral mimicry. The manner in which the antigen is displayed, in terms of density and organization, is of the upmost importance.

As previously introduced, antigen density and organization are known to influence the immunostimulatory potential of viral-like particles and therefore affect the dose response relationship, as well as the ability to stimulate autoantibodies[55, 211, 214, 215]. While the role of antigen density has been broadly explored and obtained design parameter in numerous publications, the ability to have any degree of control over antigen organization or patternization on nanoparticle surfaces has been elusive. One such publication that combines the significance of antigen density and organization is the work of Ingale et al, who developed a liposomal formulation using HIV envelope glycoprotein trimer[251]. Utilizing histidine tagged native HIV trimers and a liposomal formulation with nickel-NTA functionalized lipids at defined molar ratios, Ingale et al were able to produce 80 nm liposomes with native HIV envelope protein trimers with homogenous distribution and regular 13-15 nanometer spacing intervals[251]. These materials demonstrated the capacity to stimulate an effective antigen-specific antibody response, as well as the neutralizing antibody response required for protective vaccination.

1.3.3 Viral-Mimicking Nanoparticles for Antibody Production – Future Prospective

While many advances have been made in the design, engineering and application of viral-mimicking nanoparticles for antibody production, no single truly universal nanoparticle system has been developed that can compete with the combined delivery efficiency and immunostimulatory potential of viruses or viral-like particles. At present, many researchers are taking a selective view of material properties to be mimicked and have achieved a certain level of success in their intended application, but it may be time to take a more holistic approach to viral-mimicking nanoparticle design.

The ability to define an exact material design criterion for a holistic viral-mimicking nanoparticle platform is elusive. However, based on literature review, a suitable design for the next-generation of viral-mimicking nanoparticle for antigen-specific antibody production should include:

1. Spherical nanoparticle with particle size of approximately 40-50 nanometers.
2. Negatively charged surfaces with rough surface topography
3. Antigen surface presentation with defined spatial intervals and >10,000 molecules per μm^2.

At present, there is no one specific type of nanoparticle that stands out as being able to accomplish this feat. For this reason, the future of viral-mimicking nanoparticles for antibody production may be in hybrid systems. For example, the so-called core-satellite nanoparticles originally developed be Chen et al [252, 253]. This core-satellite nanoparticle is composed of a larger poly(siloxane) coated iron-oxide nanoparticle core complexed with numerous smaller gold nanoparticle satellites. This material has the ideal shape, size and surface charge. Moreover, the gold nanoparticle satellite density can be modified to simultaneous offer variable roughness as well as densely packed, thiol-reactive surfaces for biomolecule conjugation. While the potential of this system has yet to be explored for antibody production, this hybrid methodology in viral-mimicking nanoparticle material design is the way forward.

1.4 Conclusion

In modern scientific research and medicine, antibodies are critical research tools and therapeutic agents. In order to continue to advance their wide spread applicability, new technology must be developed to facilitate the production of high specificity and high avidity antibodies. Beyond advancing the *in-vitro* systems to improve the efficiency and accuracy of the monoclonal antibody production process, the best hope the industry has is to modernize *in-vivo* B-cell activation and antigen-specific antibody production. The old school methodology for antibody production relies on high doses, toxic adjuvants and the use of inefficient, poorly stable and weakly immunostimulatory carrier proteins. A modern approach to B-cell activation and antibody production is the utilization of nanoparticles. Nanoparticles can be engineered with ideal material properties to facilitate efficient delivery as well as immune activation. Numerous types of nanoparticles have been previously investigated to this end including: liposomes, inorganic nanoparticles, polymeric nanoparticles and viral-like nanoparticles. Of these systems, viral-like nanoparticles have been shown to be the most efficacious as a result of their unique structural properties. However, viral-like nanoparticles can be difficult to produce, while having poor reproducibility and have high anti-carrier responses that limit the effectiveness of future doses. As a result of these drawbacks, researchers have tried to find alternatives. The answer is viral-mimicry. To be considered a viral-mimicking system, the nanoparticles must be designed with some combination of viral inspired particle size, particle shape, surface properties, antigen density, antigen display, antigen organization, or surface topography. An ideal viral-mimicking nanoparticle would incorporate all of these things. However, while significant progress has been made in this research area, a nanoparticle with this holistic potential is not yet a reality. The development of a universal viral-mimicking nanoparticle platform remains elusive, but given the significance of antibodies in research and medicine, the pursuit is worthwhile.

1.5 Tables

Table 1.1: Lipid Nanoparticles for Antibody Production

Nanoparticle Type:	Application - Antigen	Immunization Scheme (Dose, Interval, Route)	Adjuvant	Isotype	Antibody Production: Absolute Amount, Titer, OD/D.F.	Author
Lipoplex	Ovalbumin (OVA)	Primary – 50 μg, IP Secondary (10 days) -50 μg, IP Tertiary (20 days) - 50 μg, IP	CpG	IgG	Anti-OVA IgG Titer – 10,000	Kim[69]
Liposome	Ovalbumin (OVA)	Primary – 100 μg, SC Secondary (14 days) – 100 μg, SC	α-galactosylceramide	IgG1 IgG2b	Anti-OVA IgG1 Titer – 100,000 Anti-OVA IgG2b Titer – 200	Okazaki[81]
Liposome	Conalbumin (ConA)	Primary – 20 μg, IV Secondary (21 days) – 20 μg, IV	n/a	IgG1 IgG2a	(IV) Anti-ConA IgG1 Titer - 131,072 (IV) Anti-ConA IgG2a Titer - 1024	Shahum[82]
Lipoplex	Hen Egg Lysozyme (HEL)	Primary – 50 μg, IP Secondary (10 days) - 50 μg, IP Tertiary (20 days) - 50 μg, IP	CpG	IgG	Anti-HEL IgG Titer – 20,000	Kim[69]
Liposome	Human Serum Albumin (HSA)	Primary – 240 ug, IV (Rabbits)	n/a	IgG	Anti-HSA IgG Titer ~ 65,536	Van Rooijen[83]
Merck Lipid Nanoparticles	Hepatitis B Surface Antigen (HBsAg)	Primary – 0.2 μg, IM Secondary (14 days) – 0.2 μg, IM	n/a	IgG	Anti-HBsAg IgG Titer ~ 200	Thoryk[84]
Multilamellar Vesicles	Hepatitis B Surface Antigen (HBsAg)	Primary – 0.25 μg, SC Secondary (10 days) - 0.25 μg, SC Tertiary (20 days) – 0.25 μg, SC	Incomplete Freund's Adjuvant	IgG	Anti-HBsAg IgG Titer - 10,000-100,000	Vangala[85]
Liposome	Recombinant *Plasmodium vivax* Circumsporozoite antigen	Primary – 1 μg, SC Secondary (21 days) - 1 μg, SC	MPLA	IgG	Anti-VMP IgG Titer – 200,000	Moon[86]
pH-sensitive Liposome	HIV gp120 V3 loop peptide (R15K) V3 loop peptide (T26K)	Primary – 10-50 μg, IM Secondary (7 days) – 5-25 μg, IM	n/a	IgG	Anti R15K IgG Titer – 800 Anti T26K IgG Titer – 6,400	Chang[87]
Liposome	HIV gp41 MPER peptides	Primary – 30 μg, ID Secondary (21 days) – 30 μg, ID Tertiary (42 days) – 30 μg, ID	MPLA	IgG	Anti-MPER-NH2 IgG Titer – 75,000 Anti-MPER-COOH IgG Titer – 20,000	Donius[88]
Liposome	*Leishmania mexicana* Surface Antigen (gp63) Lipophosphoglycan (LPG)	Primary – 5 μg, SC, IP Secondary (4 weeks) – 5 μg, SC, IP	Complete Freund's Adjuvant	IgG	(SC) Anti-Leishmania IgG Titer – 323 (IP) Anti-Leishmania IgG Titer – 1080	Russell[80]
Liposome	*Mycobacterium Tuberculosis* Mycobacterial fusion protein (Ag85B-ESAT-6)	Primary – 2 μg, SC Secondary (14 days) – 2 μg, SC Tertiary (28 days) – 2 μg, SC	Trehalose 6,6'-dibehenate (TBD)	IgG1 IgG2b	Anti-Ag85b-ESAT-6 IgG1 Titer – 15625 Anti-Ag85b-ESAT-6 IgG2b Titer –3125	Davidsen[79]
Liposome	Tetanus Toxoid (Ttd)	Primary – 2 μg, IP Secondary (4 weeks) – 2 μg, IP	n/a	IgG IgE	Anti-Ttd-IgG Titer - 4096 Anti-Ttd-IgE Titer - 64	Naito[78]
Outer Membrane Vesicles	Meningococcal B *Neisseria meningitides* Membrane Protein (PorA)	Primary – 1.5 μg, SC Secondary (14 days) – 1.5 μg, SC Tertiary (28 days) – 1.5 μg, SC	n/a	IgG IgG1 IgG2a IgG2b IgG3	Anti-PorA IgG Titer - 2512 Anti-PorA IgG1 Titer - 1445 Anti-PorA IgG2a Titer - 1622 Anti-PorA IgG2b Titer - 3311 Anti-PorA IgG3 Titer - 741	Arigita[77]

Liposome	Meningococcal B *Neisseria meningitides* Membrane Protein (P1)	Primary – 20 µg, SC Secondary (42 days) – 20 µg, SC	n/a	IgG + IgM	Anti-P1 IgG + IgM Titer – 100,000	Muttilainen[76]
Virus Mimetic Nanovesicles	Avian Influenza H1N1, Hemagglutinin	Primary – 100 µg, IM Secondary (14 days) – 100 µg, IM Tertiary (28 days) – 100 µg, IM	Alum	IgG	Anti-HA IgG Titer – 1,000	Zhang[75]
Virus Mimetic Nanovesicles	Human Papillomavirus L2 Capsid, peptide	Primary – 1.33 ug, IM Secondary (14 days) – 1.33 µg, IM Tertiary (28 days) – 1.33 µg, IM	Alum	IgG	Anti-L2 IgG Titer – 10,000	Zhang[254]
Liposome	Histone H3 C-terminal peptide	Primary – 60 µg, IP Secondary (21 days) – 60 µg, IP Tertiary (42 days) – 60 µg, IP	MPLA	IgG	Anti-H3 IgG Titer - 1600	Friede[74]
Liposome	Human Synthetic Mucin MUC1 Peptide (BP25)	Primary – 5 µg, FP Secondary (14 days) – 5 µg, IP	MPLA	IgG IgM	Anti-MUC1 IgG Titer - 6400 Anti-MUC1 IgM Titer - 1600	Guan[68]
Liposome	Dextran	Primary – 125 µg, SC Secondary (21 days) – 125 µg, SC	n/a	IgG	Anti-Dextran IgG Titer - 512	Sarkar[73]
Liposome	Lipopolysaccharide (LPS)	Primary – 50 µg, IP	n/a	IgG	Anti-LPS IgG Titer – 30,000-35,000	Nakhla[72]
Lipid Nickel Nanocapsule	HIV, Gag p41 protein	Primary – 1 µg, SC Secondary (14 days) – 1 µg, SC	n/a	IgG	Anti-Gag p41 IgG Titer – 5,000-10,000	Wadhwa[71]
Nickel-Lipid Nanoparticle	HIV, Tat protein	Primary – 1.5 µg, SC Secondary (14 days) – 1.5 µg, SC	n/a	IgG IgG1 IgG2a	Anti-Tat IgG Titer – 10^5-10^6 Anti-Tat IgG1 Titer – 10^5-10^6 Anti-Tat IgG2a Titer – 10^5	Yan[70]

Table 1.2: Inorganic Nanoparticles for Antibody Production

Nanoparticle Type:	Application - Antigen	Immunization Scheme (Dose, Interval, Route)	Adjuvant	Isotype	Antibody Production: Absolute Amount, Titer, OD/D.F.	Author
Gold	Bovine Serum Albumin (BSA)	Primary – 1.2 μg, IP Secondary (14 days) – 1.2 μg, IP Tertiary (28 days) – 1.2 μg, IP Quaternary (42 days) –1.2 μg, IP	CpG	IgG	Anti-BSA IgG Titer – 15,360	Dykman[60]
Gold	West Nile Virus Envelope Protein (WNVE)	Primary – 0.1 μg, IP Secondary (21 days) – 0.1 μg, IP Tertiary (42 days) – 0.1 μg, IP	n/a	IgG	Anti-WNVE IgG Titer – 1200	Niikura[92]
Gold	Foot and Mouth Disease Virus Peptide (FMD)	Primary – 6.25 μg, SC Secondary (10 days) – 6.25 μg, SC	Complete Freund's Adjuvant	IgG	Anti-FMD IgG Titer – 16,384	Dykman[96]
Gold	Foot and Mouth Disease Virus Peptide (FMD)	Dose: unknown Schedule: 7 injections over 9 weeks Route: IP or SC	Complete Freund's Adjuvant	IgG	Anti-FND IgG Titer – 60,000	Chen[255]
Gold	Malaria Plasmodium falciparum (Pfs230)	Primary – 10 μg, IM Secondary (21 days) – 10 μg, IM Tertiary (42 days) – 10 μg, IM	Alum	IgG	Anti-Pfs230 IgG Titer – 640,000	Kumar[101]
Gold	Streptococcus pneumonia type 14 capsular polysaccharide (Pn14PS)	Primary – 3 μg, SC Secondary (5 weeks) – 3 μg, SC Tertiary (10 weeks) – 3 μg, SC	MPLA Quil-a	IgG IgG1 IgG2a IgG2b IgG3	Anti-Pn14PS IgG Titer - 50 Anti-Pn14PS IgG1 Titer - 100 Anti-Pn14PS IgG2a Titer – 0 Anti-Pn14PS IgG2b Titer - 10 Anti-Pn14PS IgG3 Titer - 50	Dodi Safari[100]
Gold	Pseudomonas aeruginosa Flagellin	Primary – 10 μg, SC Secondary (14 days) – 10 μg, SC Tertiary (28 days) – 10 μg, SC	n/a	IgG	Anti-Flagellin IgG Titer - 1000	Dakterzada[99]
Gold	Diminazene (DMZ)	Primary – 100 μL, SC Secondary (14 days) – 100 μL, SC Tertiary (28 days) – 100 μL, SC Quaternary (42 days) –100 μL, SC	Complete Freund's Adjuvant	IgG	Anti-DMZ IgG Titer - 512	Staroverov[98]
Gold	Clenbuterol (CBL)	Primary – 12.5 μg, SC Secondary (14 days) – 12.5 μg, SC Tertiary (28 days) – 12.5 μg, SC Quaternary (42 days) –12.5 μg, SC	Complete Freund's Adjuvant	IgG	Anti-CBL IgG Titer – 256	Vasilenko[97]
Mesoporous Silica	Ovalbumin (OVA)	Primary – 10 μg, SC Secondary (14 days) – 10 μg, SC Tertiary (28 days) – 10 μg, SC	n/a	IgG	Anti-OVA IgG Titer - 6400	Mahony[114]
Silica	H1N1 Influenza Hemagglutinin Antigen (HAC1)	Primary – 10 μg, IT Secondary (21 days) – 10 μg, IT	c-di-GMP	IgG IgA	Anti-HAC1 IgG Titer – 100-1000 Anti-HAC1 IgA Titer – 100-1000	Neuhaus[119]
Mesoporous Silica	Micrurus ibiboboca Snake Venom	Primary – 10 μg, SC	n/a	IgG	Anti-Venom IgG Titer - 588	Mercuri[120]
Iron-Oxide	Malaria Merozoite Surface Protein (rMSP1)	Primary – 16 μg, IM, SC, IP Secondary (21 days) – 16 μg, IM, SC, IP Tertiary (42 days) – 16 μg, IM, SC, IP	n/a	IgG	(IM) Anti-rMSP1 IgG Titer – 10^4-10^5 (SC) Anti-rMSP1 IgG Titer – 10^2-10^3 (IP) Anti-rMSP1 IgG Titer – 10^3-10^4	Pusic[145]
Carbon Nanotubes	Foot and Mouth Disease Viral Peptide (FMDV)	Primary – 100 μg, IP Secondary (14 days) – 100 μg, IP	Complete Freund's Adjuvant	IgG	Anti-FMDV IgG Titer – 10,000	Pantarotto[132]
Carbon Nanotube	Azoxystrobin (AZc6)	Primary – 5 μg, SC Secondary (21 days) – 5 μg, SC Tertiary (42 days) – 5 μg, SC Quaternary (63 days) –5 μg, SC	Complete Freund's Adjuvant	IgG	Anti-AZc6 IgG Titer – 1000-10,000	Parra[61]
Multi-walled Carbon Nanotube	Ovalbumin (OVA)	Primary – 100 μg, IV Secondary (7 days) – 100 μg, IV	Complete Freund's Adjuvant	IgG IgG1	Anti-OVA IgG Titer - 2000 Anti-OVA IgG1 Titer - 2000	Grecco[131]

Table 1.3: Synthetic Polymeric Nanoparticles for Antibody Production

Nanoparticle Type:	Application - Antigen	Immunization Scheme (Dose, Interval, Route)	Adjuvant	Isotype	Antibody Production: Absolute Amount, Titer, OD/D.F.	Author
PLGA	Ovalbumin (OVA)	Primary – 25 μg, IM Secondary (14 days) – 25 μg, IM Tertiary (28 days) – 25 μg, IM	n/a	IgG	Anti-OVA IgG Titer – 50,000	Zhang[167]
PLGA	Ovalbumin (OVA)	Primary – 25 μg, IM Secondary – 25 μg, IM	MPLA + R837	IgG1 IgG2a IgG2b	Anti-OVA IgG1 Titer – 95,000 Anti-OVA IgG2a Titer – 110,000 Anti-OVA IgG2b Titer – 110,000	Kasturi[166]
PLGA	Anthrax Protective Antigen Domain (PAD4)	Primary – 100 μg, route not reported	n/a	IgG	Anti-PAD4 IgG Titer – 310,000	Manish[163]
Lipid-Coated PLGA	Malaria antigen (VMP001)	Primary – 2.5 μg, SC Secondary (21 days) – 2.5 μg, SC	MPLA	IgG	Anti-VMP IgG Titer – 10^5-10^6	Moon[158]
PLGA PMMA	Clenbuterol (CBL)	Primary – 25 μg, SC	n/a	IgG	(PLGA) Anti-CBL IgG Titer - 1414 (PMMA) Anti-CBL IgG Titer - 1682	Rodgers[165]
Polyanhydride	Ovalbumin (OVA)	Primary – 100 μg, SC, PO	Flagellin	IgG1 IgG2a	(SC) Anti-OVA IgG1 Titer – 512 (SC) Anti-OVA IgG2a Titer – 512 (PO) Anti-OVA IgG1 Titer – 128 (PO) Anti-OVA IgG2a Titer – 128	Salman[164]
Polyanhydride	Anthrax, Protective Antigen (PA)	Primary – 10 μg, SC Secondary (15 days) – 10 μg, SC	n/a	IgG	Anti-PA IgG Titer – 10^5-10^6	Petersen[181]
Polyanhydride	HIV, gp41 protein	Primary – 500 μg, SC Secondary (7 days) – 500 μg, SC Tertiary (14 days) – 500 μg, SC	n/a	IgG	Anti-gp41 IgG Titer – 100 - 1,000	Vela-Rameriz[182]
Polyanhydride	H5N1 Avian Influenza H5 Hemagglutinin trimer	Primary – 10 μg, SC Secondary (21 days) – 10 μg, SC Tertiary (42 days) – 10 μg, SC	Poly I:C	IgG	Anti-H5 IgG Titer - 100-1,000	Ross[183]
Polyanhydride	Yersinia pestis F1-V protein	Primary – 50 μg, IN	n/a	IgG	Anti-F1-V IgG Titer – 10^4-10^5	Ulery[185]
Polyanhydride	Pneumococcal Surface Protein A (PspA)	Primary – 25 μg, SC	n/a	IgG	Anti-PspA IgG Titer – 15,000-20,000	Haughney[256]
Polypropylene Sulfide	Ovalbumin (OVA)	Primary – 10 μg, IN Secondary (7 days) – 10 μg, IN Tertiary (21 days) – 10 μg, IN	Flagellin	IgG IgA	Anti-OVA IgG Titer – 10^5-10^7 Anti-OVA IgA Titer – 1000	Stano[257]
Guanidinylated Cationic Polymer	Ovalbumin (OVA)	Primary – 80 μg, ID Secondary (7 days) – 80 μg, ID Tertiary (14 days) – 80 μg, ID	n/a	IgG IgG1 IgG2a	Anti-OVA IgG Titer – 800,000 Anti-OVA IgG1 Titer – 3,750 Anti-OVA IgG2a Titer – 900,000	Li[258]
pH-responsive Block Co-Polymer	Ovalbumin (OVA)	Primary – 25 μg, ID Secondary (21 days) – 25 μg, ID	CpG	IgG1 IgG2c	Anti-OVA IgG1 Titer – 10^6-10^7 Anti-OVA IgG2c Titer – 10^4-10^5	Wilson[259]

Table 1.4: Biologically-Derived Polymeric Nanoparticles for Antibody Production

Nanoparticle Type:	Application - Antigen	Immunization Scheme (Dose, Interval, Route)	Adjuvant	Isotype	Antibody Production: Absolute Amount, Titer, OD/D.F.	Author
Chitosan-Polylysine	Ovalbumin (OVA)	Primary – 25 µg, SC Secondary (7 days) – 25 µg, SC Tertiary (14 days) – 25 µg, SC	CpG	IgG	Anti-OVA IgG Titer – 65,536	Han[199]
Chitosan	Ovalbumin (OVA)	Primary – 20 µg, IN Secondary (7 days) – 20 µg, IN Tertiary (14 days) – 20 µg, IN	CpG	IgG	Anti-OVA IgG Titer – 10,000	Slutter[193]
Alginate-coated Chitosan	Hepatitis B Surface Antigen (HBsAg)	Primary – 10 µg, SC Secondary (21 days) – 10 µg, SC	CpG	IgG IgG1 IgG2a	Anti-HBsAg IgG Titer – 3293 Anti-HBsAg IgG1 Titer – 2953 Anti-HBsAg IgG2a Titer - 1992	Borges[198]
Glycol Chitosan	Hepatitis B Surface Antigen (HBsAg)	Primary – 10 µg, IN Secondary (21 days) – 10 µg, IN	n/a	IgG IgA	Anti- HBsAg IgG Titer – 100,000 Anti- HBsAg IgA Titer – 10,000	Pawar[196]
Chitosan	H1NI Avian Influenza	Primary – 0.375 µg, SC Secondary (20 days) – 0.375 µg, SC	n/a	n/a	HI Titer – 4,000	Dzung[202]
Chitosan	Pneumococcal Type 12 Polysaccharide (Pn14PS)	Primary – dose unknown, ID Secondary (35 days) – dose unknown, ID	n/a	IgG IgG1 IgG2a IgG2b IgG3	Anti-Pn14PS IgG Titer - 100 Anti- Pn14PS IgG1 Titer – 500-5000 Anti- Pn14PS IgG2a Titer – 500-1000 Anti- Pn14PS Ig2b Titer – 100-1000 Anti- Pn14PS IgG3 Titer - 100	Haryono[197]
Chitosan	Escherichia coli Recombinant protein (EIT)	Primary – 20 µg, IN Secondary (28 days) – 20 µg, IN Tertiary (42 days) – 20 µg, IN	n/a	IgG IgA	Anti-EIT IgG Titer – 20,480 Anti-EIT IgA Titer – 20,480	Doavi[201]
Chitosan	Anthrax, Protective Antigen (PA)	Primary – 20 µg, SC, IM, IP Secondary (7 days) – 20 µg, SC, IM, IP Tertiary (15 days) – 20 µg, SC, IM, IP	CpG	IgG	(SC) Anti-PA IgG Titer – 200,000 (IM) Anti-PA IgG Titer – 175,000 (IP) Anti-PA IgG Titer – 150,000	Malik[192]
Chitosan	Borthops jaraca (BJV) Borthops erythromelas (BEV) Snake venom	Primary x 6 (1 per week) – 100 µL, SC	n/a	IgG	Anti-BJV IgG Titer – 102,400 Anti-BEV IgG Titer – 102,400	Rocha Soares[200, 260]

Table 1.5: Virus-Like Nanoparticles for Antibody Production

Nanoparticle Type:	Application - Antigen	Immunization Scheme (Dose, Interval, Route)	Adjuvant	Isotype	Antibody Production: Absolute Amount, Titer, OD/D.F.	Author
T7 Bacteriophage	Influenza A Virus M2 Protein (M2e)	Primary – 100 μg, SC Secondary (14 days) – 100 μg, SC Tertiary (28 days) – 100 μg, SC	Complete Freund's Adjuvant	IgG IgG1 IgG2a	Anti-M2e IgG Titer -100,000 Anti-M2e IgG1 Titer -100-1000 Anti-M2e IgG2a Titer -100,000	Hashemi[218]
Papaya Mosaic Virus	Influenza A Virus M2 Peptide (M2e)	Primary – 90 μg, IM Secondary (14 days) – 90 μg, IM	n/a	IgG IgG2a	Anti-M2e IgG Titer -51,200 Anti-M2e IgG2a Titer - 51,200	Therien[232]
Influenza Virus-Like Particle	Influenza Hemagglutinin (HA)	Primary – 1 μg, IM, IN Secondary (14 days) – 1 μg, IM, IN	IL-12	n/a	(IM) Anti-HA Titer - 3250 (IN) Anti-HA Titer - 6000	Galarza[231]
Influenza Virus-Like Particle	H9N2 Influenza Hemagglutinin (HA)	Primary – 15 μg, IM Secondary (21 days) – 15 μg, IM	Novasome	n/a	Anti-HA Titer - 1338	Pushko[230]
Influenza Virus-Like Particle	H7N9 Influenza Hemagglutinin (HA)	Primary – 2 μg, IM Secondary (14 days) – 2 μg, IM	Iscomatrix	n/a	Anti-HA Titer – 100-1000	Smith[261]
Plant Virus	HIV-1 gp41 peptide	Primary – 100 μg, SC Secondary (35 days) – 100 μg, SC	Alum	IgG	Anti-gp41 IgG Titer – 30,000-50,000	McLain[228]
Papaya Mosaic Virus	HIV-1 T20 peptide	Primary – 90 μg, IM Secondary (14 days) – 90 μg, IM	n/a	IgG IgG2a	Anti-T20 IgG Titer -25,600 Anti-T20 IgG2a Titer -25,600	Therien[232]
Hepatitis B Virus	Hepatitis B Surface Antigen (HBsAg) Peptide	Primary – 20 μg, IV	n/a	IgG IgM	Anti-HBsAg IgG Titer – 10,240 Anti-HBsAg IgM Titer - 160	Jegerlehner[215]
Hepatitis B Virus	Hepatitis B Virus Core Protein (HBc)	Primary – 25 μg, IP, SC Secondary (14 days) – 25 μg, IP, SC Tertiary (28 days) – 25 μg, IP, SC	Complete Freund's Adjuvant	IgG	(IP) Anti-HBc IgG Titer – 350,000 (SC) Anti-HBc IgG Titer – 350,000	Skrastina[111]
Glycoprotein Virus-Like Nanoparticles	Respiratory Syncytial Virus (RSV)	Primary – 10 μg, IM Secondary (28 days) – 10 μg, IM	n/a	IgG IgG1 IgG2a	Anti-RSV IgG Titer –25,600 Anti-RSV IgG1 Titer –6,400 Anti-RSV IgG2a Titer -25,600	Lee[227]
Coronavirus	Middle East Respiratory Syndrome (MERS)	Primary – 3 μg, IM Secondary (21 days) – 3 μg, IM	Matrix M1	n/a	Anti-MERS Titer - 1689	Coleman[226]
Coronavirus	Severe Acute Respiratory Syndrome (SARS)	Primary – 3 μg, IM Secondary (21 days) – 3 μg, IM	Matrix M1	n/a	Anti-SARS Titer - 3152	Coleman[226]
Enterovirus 71	Hand Foot and Mouth Disease Virus (HFMDV)	Primary – 10 μg, SC Secondary (14 days) – 10 μg, SC Tertiary (28 days) – 10 μg, SC	Alum	IgG	Anti-HFMDV IgG Titer – 32,768	Li[225]
Bacteriophage Qb	Alzheimer's Disease Human β-Amyloid Peptide (AB)	Primary – 11.2 μg, IM Secondary (14 days) – 11.2 μg, IM Tertiary (28 days) – 11.2 μg, IM	Complete Freund's Adjuvant	IgG	Anti-AB IgG Titer - 10^5-10^6	Chackerian[223]
Human Papillomavirus	TNF-alpha peptide	Primary – 15 μg, ID Secondary (14 days) – 15 μg, ID Tertiary (28 days) – 15 μg, ID	Complete Freund's Adjuvant	IgG	Anti-TNF-alpha IgG Titer – 5^4-10^5	Chackerian[224]
Tobacco Mosaic Virus	(Steroid) Estriol (E3)	Primary – 1 μg, SC Secondary (14 days) – 1 μg, SC Tertiary (28 days) – 1 μg, SC	Complete Freund's Adjuvant	IgG	Anti-E3 IgG Titer – 250,000-300,000	Zhao[222]
Tobacco Mosaic Virus	(Steroid) Estriol (E3)	Primary – 50 μg, SC Secondary (14 days) – 50 μg, SC Tertiary (28 days) – 50 μg, SC	Complete Freund's Adjuvant	IgG	Anti-E3 IgG Titer – 100,000-150,000	Wei[219]
Bacteriophage Qb	Nicotine	Primary – 60 μg, SC Secondary (14 days) – 60 μg, SC	Alum	IgG	Anti-Nicotine IgG Titer – 300,000-400,000	Maurer[220]
Bacteriophage Qb	Tumor-associated Carbohydrate Antigen (TACA)	Primary – 20 μg, SC Secondary (14 days) – 20 μg, SC Tertiary (28 days) – 20 μg, SC	n/a	IgG IgM	Anti-TACA IgG Titer – 5000 Anti-TACA IgM Titer - 1600	Yin[221]

Table 1.6: Viral Mimic Material Properties and Functional Role

Material Property	Parameter or Descriptor	Functional Role
Particle Size	20-300 nm	Lymph node delivery
Particle Shape (aspect ratio)	Spheres and rods	Biodistribution, cellular uptake
Surface Properties	Negative charge, hydrophilic	Lymph node delivery
Antigen Density	>150 molecules/μm^2	B-cell receptor crosslinking
Antigen Display	Surface presentation	B-cell receptor engagement
Antigen Organization	Geometric pattern with defined spacing intervals	PAMP
Surface Topography	Rough	Cellular uptake

1.6 Bibliography:

1 Hoffman, W., Lakkis, F. G. & Chalasani, G. B Cells, Antibodies, and More. *Clin J Am Soc Nephrol* 11, 137-154, doi:10.2215/CJN.09430915 (2016).

2 Chames, P., Van Regenmortel, M., Weiss, E. & Baty, D. Therapeutic antibodies: successes, limitations and hopes for the future. *Br J Pharmacol* 157, 220-233, doi:10.1111/j.1476-5381.2009.00190.x (2009).

3 Saeed, A. F., Wang, R., Ling, S. & Wang, S. Antibody Engineering for Pursuing a Healthier Future. *Front Microbiol* 8, 495, doi:10.3389/fmicb.2017.00495 (2017).

4 Frenzel, A., Hust, M. & Schirrmann, T. Expression of recombinant antibodies. *Front Immunol* 4, 217, doi:10.3389/fimmu.2013.00217 (2013).

5 Lipman, N. S., Jackson, L. R., Trudel, L. J. & Weis-Garcia, F. Monoclonal versus polyclonal antibodies: distinguishing characteristics, applications, and information resources. *ILAR J* 46, 258-268 (2005).

6 Liu, J. K. The history of monoclonal antibody development - Progress, remaining challenges and future innovations. *Ann Med Surg (Lond)* 3, 113-116, doi:10.1016/j.amsu.2014.09.001 (2014).

7 Kennedy, P. J., Oliveira, C., Granja, P. L. & Sarmento, B. Monoclonal antibodies: technologies for early discovery and engineering. *Crit Rev Biotechnol* 38, 394-408, doi:10.1080/07388551.2017.1357002 (2018).

8 LeBien, T. W. & Tedder, T. F. B lymphocytes: how they develop and function. *Blood* 112, 1570-1580, doi:10.1182/blood-2008-02-078071 (2008).

9 Liao, W. *et al.* Characterization of T-Dependent and T-Independent B Cell Responses to a Virus-like Particle. *J Immunol* 198, 3846-3856, doi:10.4049/jimmunol.1601852 (2017).

10 Phan, T. G., Gray, E. E. & Cyster, J. G. The microanatomy of B cell activation. *Curr Opin Immunol* 21, 258-265, doi:10.1016/j.coi.2009.05.006 (2009).

11 Mond, J. J., Lees, A. & Snapper, C. M. T cell-independent antigens type 2. *Annu Rev Immunol* 13, 655-692, doi:10.1146/annurev.iy.13.040195.003255 (1995).

12 Mond, J. J., Vos, Q., Lees, A. & Snapper, C. M. T cell independent antigens. *Curr Opin Immunol* 7, 349-354 (1995).

13 Obukhanych, T. V. & Nussenzweig, M. C. T-independent type II immune responses generate memory B cells. *J Exp Med* 203, 305-310, doi:10.1084/jem.20052036 (2006).

14 Hanihara-Tatsuzawa, F. *et al.* Control of Toll-like receptor-mediated T cell-independent type 1 antibody responses by the inducible nuclear protein IkappaB-zeta. *J Biol Chem* 289, 30925-30936, doi:10.1074/jbc.M114.553230 (2014).

15 Fehr, T. *et al.* Role of repetitive antigen patterns for induction of antibodies against antibodies. *Journal of Experimental Medicine* 185, 1785-1792, doi:DOI 10.1084/jem.185.10.1785 (1997).

16 Hebeis, B. J. *et al.* Activation of virus-specific memory B cells in the absence of T cell help. *J Exp Med* 199, 593-602, doi:10.1084/jem.20030091 (2004).

17 Szomolanyi-Tsuda, E., Le, Q. P., Garcea, R. L. & Welsh, R. M. T-Cell-independent immunoglobulin G responses in vivo are elicited by live-virus infection but not by immunization with viral proteins or virus-like particles. *J Virol* 72, 6665-6670 (1998).

18 Raval, F. M., Mishra, R., Garcea, R. L., Welsh, R. M. & Szomolanyi-Tsuda, E. Long-lasting T cell-independent IgG responses require MyD88-mediated pathways and are maintained by high levels of virus persistence. *MBio* 4, e00812-00813, doi:10.1128/mBio.00812-13 (2013).

19 Parker, D. C. T cell-dependent B cell activation. *Annu Rev Immunol* 11, 331-360, doi:10.1146/annurev.iy.11.040193.001555 (1993).

20 Janeway, C. *Immunobiology 5 : the immune system in health and disease*. 5th edn, (Garland Pub., 2001).

21 Sverremark, E. & Fernandez, C. Role of T cells and germinal center formation in the generation of immune responses to the thymus-independent carbohydrate dextran B512. *J Immunol* 161, 4646-4651 (1998).

22 Gatto, D. & Brink, R. The germinal center reaction. *J Allergy Clin Immunol* 126, 898-907; quiz 908-899, doi:10.1016/j.jaci.2010.09.007 (2010).

23 De Silva, N. S. & Klein, U. Dynamics of B cells in germinal centres. *Nat Rev Immunol* 15, 137-148, doi:10.1038/nri3804 (2015).

24 Leenaars, M. & Hendriksen, C. F. Critical steps in the production of polyclonal and monoclonal antibodies: evaluation and recommendations. *ILAR J* 46, 269-279 (2005).

25 Mohan, T., Verma, P. & Rao, D. N. Novel adjuvants & delivery vehicles for vaccines development: a road ahead. *Indian J Med Res* 138, 779-795 (2013).

26 Snapper, C. M. Distinct Immunologic Properties of Soluble Versus Particulate Antigens. *Front Immunol* 9, 598, doi:10.3389/fimmu.2018.00598 (2018).

27 Stills, H. F., Jr. Adjuvants and antibody production: dispelling the myths associated with Freund's complete and other adjuvants. *ILAR J* 46, 280-293 (2005).

28 Delahaut, P. Immunisation - Choice of host, adjuvants and boosting schedules with emphasis on polyclonal antibody production. *Methods* 116, 4-11, doi:10.1016/j.ymeth.2017.01.002 (2017).

29 Lore, K. & Karlsson Hedestam, G. B. Novel adjuvants for B cell immune responses. *Curr Opin HIV AIDS* 4, 441-446, doi:10.1097/COH.0b013e32832da082 (2009).

30 Matthews, K. *et al.* Clinical adjuvant combinations stimulate potent B-cell responses in vitro by activating dermal dendritic cells. *PLoS One* 8, e63785, doi:10.1371/journal.pone.0063785 (2013).

31 Khan, I. S., K.; Khan, I. Nanoparticles: Properties, applications and toxicities. *Arabian Journal of Chemistry* (2017).

32 Guo, D. X., G.; Luo, J. . Mechanical properties of nanoparticles: basics and applications. *Journal of Physics D: Applied Physics* 47, 1-25 (2013).

33 Salata, O. Applications of nanoparticles in biology and medicine. *J Nanobiotechnology* 2, 3, doi:10.1186/1477-3155-2-3 (2004).

34 Stark, W. J., Stoessel, P. R., Wohlleben, W. & Hafner, A. Industrial applications of nanoparticles. *Chem Soc Rev* 44, 5793-5805, doi:10.1039/c4cs00362d (2015).

35 Zhao, L. *et al.* Nanoparticle vaccines. *Vaccine* 32, 327-337, doi:10.1016/j.vaccine.2013.11.069 (2014).

36 Rizvi, S. A. A. & Saleh, A. M. Applications of nanoparticle systems in drug delivery technology. *Saudi Pharm J* 26, 64-70, doi:10.1016/j.jsps.2017.10.012 (2018).

37 Alshanqiti, F. M., Al-Masaudi, S. B., Al-Hejin, A. M., El-Baky, N. A. & Redwan, E. M. Development of nanoparticle adjuvants to potentiate the immune response against diphtheria toxoid. *Hum Antibodies* 26, 75-85, doi:10.3233/HAB-170324 (2018).

38 Sykes, E. A., Chen, J., Zheng, G. & Chan, W. C. Investigating the impact of nanoparticle size on active and passive tumor targeting efficiency. *ACS Nano* 8, 5696-5706, doi:10.1021/nn500299p (2014).

39 Sultana, S., Khan, M. R., Kumar, M., Kumar, S. & Ali, M. Nanoparticles-mediated drug delivery approaches for cancer targeting: a review. *J Drug Target* 21, 107-125, doi:10.3109/1061186X.2012.712130 (2013).

40 Pape, K. C., D.; Itano, A.; Jenkins, M. The Humoral Immune Response Is Initiated in Lymph Nodes by B Cells that Acquire Soluble Antigen Directly in the Follicles. *Immunity* 26, 491-502 (2007).

41 Thomas, S. N., Rohner, N. A. & Edwards, E. E. Implications of Lymphatic Transport to Lymph Nodes in Immunity and Immunotherapy. *Annu Rev Biomed Eng* 18, 207-233, doi:10.1146/annurev-bioeng-101515-014413 (2016).

42 Baldazzi, V., Paci, P., Bernaschi, M. & Castiglione, F. Modeling lymphocyte homing and encounters in lymph nodes. *BMC Bioinformatics* 10, 387, doi:10.1186/1471-2105-10-387 (2009).

43 Kang, S. *et al.* Effects of gold nanoparticle-based vaccine size on lymph node delivery and cytotoxic T-lymphocyte responses. *Journal of Controlled Release* 256, 56-67, doi:10.1016/j.jconrel.2017.04.024 (2017).

44 Manolova, V. *et al.* Nanoparticles target distinct dendritic cell populations according to their size. *Eur. J. Immunol.* 38, 1404-1413, doi:10.1002/eji.200737984 (2008).

45 Bachmann, M. F. & Jennings, G. T. Vaccine delivery: a matter of size, geometry, kinetics and molecular patterns. *Nat. Rev. Immunol.* 10, 787-796, doi:10.1038/nri2868 (2010).

46 Mueller, S. N., Tian, S. M. & DeSimone, J. M. Rapid and Persistent Delivery of Antigen by Lymph Node Targeting PRINT Nanoparticle Vaccine Carrier To Promote Humoral Immunity. *Mol. Pharmaceutics* 12, 1356-1365, doi:10.1021/mp500589c (2015).

47 Kesler, C. T., Liao, S., Munn, L. L. & Padera, T. P. Lymphatic vessels in health and disease. *Wiley Interdisciplinary Reviews-Systems Biology and Medicine* 5, 111-124, doi:10.1002/wsbm.1201 (2013).

48 Irvine, D. J., Hanson, M. C., Rakhra, K. & Tokatlian, T. Synthetic Nanoparticles for Vaccines and Immunotherapy. *Chem Rev* 115, 11109-11146, doi:10.1021/acs.chemrev.5b00109 (2015).

49 Rao, D. A., Forrest, M. L., Alani, A. W. G., Kwon, G. S. & Robinson, J. R. Biodegradable PLGA Based Nanoparticles for Sustained Regional Lymphatic Drug Delivery. *Journal of Pharmaceutical Sciences* 99, 2018-2031, doi:10.1002/jps.21970 (2010).

50 Reddy, S. T., Rehor, A., Schmoekel, H. G., Hubbell, J. A. & Swartz, M. A. In vivo targeting of dendritic cells in lymph nodes with poly(propylene sulfide) nanoparticles. *J. Control Release* 112, 26-34, doi:10.1016/j.jconrel.2006.01.006 (2006).

51 Reddy, S. T. *et al.* Exploiting lymphatic transport and complement activation in nanoparticle vaccines. *Nat. Biotechnol.* 25, 1159-1164, doi:10.1038/nbt1332 (2007).

52 Oussoren, C., Zuidema, J., Crommelin, D. J. A. & Storm, G. Lymphatic uptake and biodistribution of liposomes after subcutaneous injection .2. Influence of liposomal size, lipid composition and lipid dose. *Biochimica Et Biophysica Acta-Biomembranes* 1328, 261-272, doi:Doi 10.1016/S0005-2736(97)00122-3 (1997).

53 Harwood, N. E. & Batista, F. D. Antigen presentation to B cells. *F1000 Biol Rep* 2, 87, doi:10.3410/B2-87 (2010).

54 Ding, P. *et al.* Nanoparticle orientationally displayed antigen epitopes improve neutralizing antibody level in a model of porcine circovirus type 2. *Int J Nanomedicine* 12, 5239-5254, doi:10.2147/IJN.S140789 (2017).

55 Chackerian, B., Lenz, P., Lowy, D. R. & Schiller, J. T. Determinants of autoantibody induction by conjugated papillomavirus virus-like particles. *J Immunol* 169, 6120-6126 (2002).

56 Zhu, M. W., R.; Nie, G. . Applications of nanomaterials as vaccine adjuvants. *Human Vaccines and Immunotherapeutics* 10, 2761-2774 (2014).

57 Tamayo, I. *et al.* Poly(anhydride) nanoparticles act as active Th1 adjuvants through Toll-like receptor exploitation. *Clin Vaccine Immunol* 17, 1356-1362, doi:10.1128/CVI.00164-10 (2010).

58 Mody, K. P., A.; Mahony, D.; Cavallaro, A.; Yu, C.; Mitter, N. . Mesoporous silica nanoparticles as antigen carriers and adjuvants for vaccine delivery. *Nanoscale* 5, 5167-5179 (2013).

59 Buonaguro, F. M., Tornesello, M. L. & Buonaguro, L. Virus-like particle vaccines and adjuvants: the HPV paradigm. *Expert Rev Vaccines* 8, 1379-1398, doi:10.1586/erv.09.81 (2009).

60 Dykman, L. A. *et al.* Gold nanoparticles as an adjuvant: Influence of size, shape, and technique of combination with CpG on antibody production. *Int Immunopharmacol* 54, 163-168, doi:10.1016/j.intimp.2017.11.008 (2018).

61 Parra, J., Abad-Somovilla, A., Mercader, J. V., Taton, T. A. & Abad-Fuentes, A. Carbon nanotube-protein carriers enhance size-dependent self-adjuvant antibody response to haptens. *Journal of Controlled Release* 170, 242-251, doi:10.1016/j.jconrel.2013.05.019 (2013).

62 Koppolu, B. & Zaharoff, D. A. The effect of antigen encapsulation in chitosan particles on uptake, activation and presentation by antigen presenting cells. *Biomaterials* 34, 2359-2369, doi:10.1016/j.biomaterials.2012.11.066 (2013).

63 Akbarzadeh, A. *et al.* Liposome: classification, preparation, and applications. *Nanoscale Res Lett* 8, 102, doi:10.1186/1556-276X-8-102 (2013).

64 Kraft, J. C., Freeling, J. P., Wang, Z. Y. & Ho, R. J. Y. Emerging Research and Clinical Development Trends of Liposome and Lipid Nanoparticle Drug Delivery Systems. *Journal of Pharmaceutical Sciences* 103, 29-52, doi:10.1002/jps.23773 (2014).

65 Allen, T. M. & Cullis, P. R. Liposomal drug delivery systems: From concept to clinical applications. *Advanced Drug Delivery Reviews* 65, 36-48, doi:10.1016/j.addr.2012.09.037 (2013).

66 Zylberberg, C. M., S. . Pharmaceutical liposomal drug delivery: a review of new delivery systems and a look at the regulatory landscape. *Drug Delivery* 23, 3319-3329, doi:DOI: 10.1080/10717544.2016.1177136 (2016).

67 Sercombe, L. *et al.* Advances and Challenges of Liposome Assisted Drug Delivery. *Front Pharmacol* 6, 286, doi:10.3389/fphar.2015.00286 (2015).

68 Guan, H. H. *et al.* Liposomal formulations of synthetic MUC1 peptides: Effects of encapsulation versus surface display of peptides on immune responses. *Bioconjugate Chem* 9, 451-458, doi:DOI 10.1021/bc970183n (1998).

69 Kim, D. *et al.* Production of antibodies with peptide-CpG-DNA-liposome complex without carriers. *BMC Immunol* 12, 29, doi:10.1186/1471-2172-12-29 (2011).

70 Yan, W. *et al.* Lipid Nanoparticles with Accessible Nickel as a Vaccine Delivery System for Single and Multiple His-tagged HIV Antigens. *HIV AIDS (Auckl)* 2009, 1-11, doi:10.2147/HIV.S5729 (2009).

71 Wadhwa, S., Jain, A., Woodward, J. G. & Mumper, R. J. Lipid nanocapsule as vaccine carriers for his-tagged proteins: evaluation of antigen-specific immune responses to HIV I His-Gag p41 and systemic inflammatory responses. *Eur J Pharm Biopharm* 80, 315-322, doi:10.1016/j.ejpb.2011.10.016 (2012).

72 Nakhla, A. S., A.; Banoub, J.; Keough, K. Serum anti-LPS antibody production by rainbow trout (Oncorhynchus mykiss) in response to the administration of free and liposomally-incorporated LPS fromAeromonas salmonicida. *Fish and Shellfish Immunology* 7, 387-401 (1997).

73 Sarkar, A. K. & Das, M. K. Production of antibodies to dextran using liposome as adjuvant. *Immunol Invest* 20, 243-252 (1991).

74 Friede, M., Muller, S., Briand, J. P., Van Regenmortel, M. H. & Schuber, F. Induction of immune response against a short synthetic peptide antigen coupled to small neutral liposomes containing monophosphoryl lipid A. *Mol Immunol* 30, 539-547 (1993).

75 Zhang, P. *et al.* Virus-mimetic nanovesicles as a versatile antigen-delivery system. *Proc Natl Acad Sci U S A* 112, E6129-6138, doi:10.1073/pnas.1505799112 (2015).

76 Muttilainen, S. *et al.* The Neisseria meningitidis outer membrane protein P1 produced in Bacillus subtilis and reconstituted into phospholipid vesicles elicits antibodies to native P1 epitopes. *Microb Pathog* 18, 423-436 (1995).

77 Arigita, C. *et al.* Liposomal meningococcal B vaccination: role of dendritic cell targeting in the development of a protective immune response. *Infect Immun* 71, 5210-5218 (2003).

78 Naito, S. *et al.* Ovalbumin-liposome conjugate induces IgG but not IgE antibody production. *Int Arch Allergy Immunol* 109, 223-228, doi:10.1159/000237241 (1996).

79 Davidsen, J. *et al.* Characterization of cationic liposomes based on dimethyldioctadecylammonium and synthetic cord factor from M. tuberculosis (trehalose 6,6'-dibehenate)-a novel adjuvant inducing both strong CMI and antibody responses. *Biochim Biophys Acta* 1718, 22-31, doi:10.1016/j.bbamem.2005.10.011 (2005).

80 Russell, D. G. & Alexander, J. Effective immunization against cutaneous leishmaniasis with defined membrane antigens reconstituted into liposomes. *J Immunol* 140, 1274-1279 (1988).

81 Okazaki, S., Iwasaki, T., Yuba, E. & Watarai, S. Evaluation of pH-sensitive fusogenic polymer-modified liposomes co-loaded with antigen and alpha-galactosylceramide as an anti-tumor vaccine. *J Vet Med Sci* 80, 197-204, doi:10.1292/jvms.17-0491 (2018).

82 Shahum, E. T., HM. . Correlation between in vitro and in vivo behaviour of liposomal antigens. *Vaccine* 12, 1125-1131 (1994).

83 Van Rooijen, N. & Van Nieuwmegen, R. Association of an albumin antigen with phosphatidylcholine liposomes alters the nature of immunoglobulins produced during the immune response against the antigen. *Biochim Biophys Acta* 755, 434-438 (1983).

84 Thoryk, E. A. *et al.* Co-Administration of Lipid Nanoparticles and Sub-Unit Vaccine Antigens Is Required for Increase in Antigen-Specific Immune Responses in Mice. *Vaccines (Basel)* 4, doi:10.3390/vaccines4040047 (2016).

85 Vangala, A. *et al.* Comparison of vesicle based antigen delivery systems for delivery of hepatitis B surface antigen. *J Control Release* 119, 102-110, doi:10.1016/j.jconrel.2007.01.010 (2007).

86 Moon, J. J. *et al.* Enhancing humoral responses to a malaria antigen with nanoparticle vaccines that expand Tfh cells and promote germinal center induction. *Proc Natl Acad Sci U S A* 109, 1080-1085, doi:10.1073/pnas.1112648109 (2012).

87 Chang, J. S., Choi, M. J., Kim, T. Y., Cho, S. Y. & Cheong, H. S. Immunogenicity of synthetic HIV-1 V3 loop peptides by MPL adjuvanted pH-sensitive liposomes. *Vaccine* 17, 1540-1548 (1999).

88 Donius, L. R. *et al.* Generation of Long-Lived Bone Marrow Plasma Cells Secreting Antibodies Specific for the HIV-1 gp41 Membrane-Proximal External Region in the Absence of Polyreactivity. *J Virol* 90, 8875-8890, doi:10.1128/JVI.01089-16 (2016).

89 Dykman, L. A. & Khlebtsov, N. G. Immunological properties of gold nanoparticles. *Chem Sci* 8, 1719-1735, doi:10.1039/c6sc03631g (2017).

90 Saha, K., Agasti, S. S., Kim, C., Li, X. & Rotello, V. M. Gold nanoparticles in chemical and biological sensing. *Chem Rev* 112, 2739-2779, doi:10.1021/cr2001178 (2012).

91 Yeh, Y. C., Creran, B. & Rotello, V. M. Gold nanoparticles: preparation, properties, and applications in bionanotechnology. *Nanoscale* 4, 1871-1880, doi:10.1039/c1nr11188d (2012).

92 Niikura, K. *et al.* Gold Nanoparticles as a Vaccine Platform: Influence of Size and Shape on Immunological Responses in Vitro and in Vivo. *Acs Nano* 7, 3926-3938, doi:10.1021/nn3057005 (2013).

93 Grzelczak, M., Perez-Juste, J., Mulvaney, P. & Liz-Marzan, L. M. Shape control in gold nanoparticle synthesis. *Chem Soc Rev* 37, 1783-1791, doi:10.1039/b711490g (2008).

94 Ghosh, P., Han, G., De, M., Kim, C. K. & Rotello, V. M. Gold nanoparticles in delivery applications. *Adv Drug Deliv Rev* 60, 1307-1315, doi:10.1016/j.addr.2008.03.016 (2008).

95 Hakkinen, H. The gold-sulfur interface at the nanoscale. *Nat Chem* 4, 443-455, doi:10.1038/nchem.1352 (2012).

96 Dykman, L. S., S.; Mezhenny, P.; Fomin, A.; Kozlov, S.; Volkov, A.; Laskavy, V.; Shchyogolev, S. . Use of a synthetic foot-and-mouth disease virus peptide conjugated to gold nanoparticles for enhancing immunological response. *Gold Bulletin* 48, 93-101 (2015).

97 Vasilenko, O. A. *et al.* Obtainment of polyclonal antibodies to clenbuterol with the use of colloidal gold. *Immunopharmacol Immunotoxicol* 29, 563-568, doi:10.1080/08923970701691033 (2007).

98 Staroverov, S. A. *et al.* Preparation of polyclonal antibodies to diminazene and its detection in animal blood plasma. *Int Immunopharmacol* 8, 1418-1422, doi:10.1016/j.intimp.2008.05.014 (2008).

99 Dakterzada, F., Mohabati Mobarez, A., Habibi Roudkenar, M. & Mohsenifar, A. Induction of humoral immune response against Pseudomonas aeruginosa flagellin(1-161) using gold nanoparticles as an adjuvant. *Vaccine* 34, 1472-1479, doi:10.1016/j.vaccine.2016.01.041 (2016).

100 Safari, D. *et al.* Gold nanoparticles as carriers for a synthetic Streptococcus pneumoniae type 14 conjugate vaccine. *Nanomedicine (Lond)* 7, 651-662, doi:10.2217/nnm.11.151 (2012).

101 Kumar, R. *et al.* Nanovaccines for malaria using Plasmodium falciparum antigen Pfs25 attached gold nanoparticles. *Vaccine* 33, 5064-5071, doi:10.1016/j.vaccine.2015.08.025 (2015).

102 Chen, Y. S., Hung, Y. C., Lin, W. H. & Huang, G. S. Assessment of gold nanoparticles as a size-dependent vaccine carrier for enhancing the antibody response against

synthetic foot-and-mouth disease virus peptide. *Nanotechnology* 21, 195101, doi:10.1088/0957-4484/21/19/195101 (2010).

103 Staroverov, S. D., L. . Use of gold nanoparticles for the preparation of antibodies to tuberculin, the immunoassay of mycobacteria, and animal vaccination. *Nanotechnologies in Russia* 8, 816-822 (2013).

104 Dykman, L. S., S.; Mezhenny, P.; Fomin, A. . Effect of M2e peptide–gold nanoparticle conjugates on development of anti-influenza antibodies. *Gold Bulletin*, 1-7 (2018).

105 Yah, C. The toxicity of Gold Nanoparticles in relation to their physiochemical properties. *Biomedical Research India* 24, 400-413 (2013).

106 Alkilany, A. M. & Murphy, C. J. Toxicity and cellular uptake of gold nanoparticles: what we have learned so far? *J Nanopart Res* 12, 2313-2333, doi:10.1007/s11051-010-9911-8 (2010).

107 Narayan, R., Nayak, U. Y., Raichur, A. M. & Garg, S. Mesoporous Silica Nanoparticles: A Comprehensive Review on Synthesis and Recent Advances. *Pharmaceutics* 10, doi:10.3390/pharmaceutics10030118 (2018).

108 Zhou, Y. *et al.* Mesoporous silica nanoparticles for drug and gene delivery. *Acta Pharm Sin B* 8, 165-177, doi:10.1016/j.apsb.2018.01.007 (2018).

109 Wu, S. H., Mou, C. Y. & Lin, H. P. Synthesis of mesoporous silica nanoparticles. *Chem Soc Rev* 42, 3862-3875, doi:10.1039/c3cs35405a (2013).

110 Tang, F., Li, L. & Chen, D. Mesoporous silica nanoparticles: synthesis, biocompatibility and drug delivery. *Adv Mater* 24, 1504-1534, doi:10.1002/adma.201104763 (2012).

111 Skrastina, D. *et al.* Silica nanoparticles as the adjuvant for the immunisation of mice using hepatitis B core virus-like particles. *PLoS One* 9, e114006, doi:10.1371/journal.pone.0114006 (2014).

112 Mancino, D. & Ovary, Z. Adjuvant effects of amorphous silica and of aluminium hydroxide on IgE and IgG1 antibody production in different inbred mouse strains. *Int Arch Allergy Appl Immunol* 61, 253-258 (1980).

113 Carvalho, L. V. *et al.* Immunological parameters related to the adjuvant effect of the ordered mesoporous silica SBA-15. *Vaccine* 28, 7829-7836, doi:10.1016/j.vaccine.2010.09.087 (2010).

114 Mahony, D. *et al.* Mesoporous silica nanoparticles act as a self-adjuvant for ovalbumin model antigen in mice. *Small* 9, 3138-3146, doi:10.1002/smll.201300012 (2013).

115 Hirai, T. *et al.* Cutaneous exposure to agglomerates of silica nanoparticles and allergen results in IgE-biased immune response and increased sensitivity to anaphylaxis in mice. *Part Fibre Toxicol* 12, 16, doi:10.1186/s12989-015-0095-3 (2015).

116 Toda, T. & Yoshino, S. Enhancement of ovalbumin-specific Th1, Th2, and Th17 immune responses by amorphous silica nanoparticles. *Int J Immunopathol Pharmacol* 29, 408-420, doi:10.1177/0394632016656192 (2016).

117 Virginio, V. G. *et al.* Assessment of the adjuvant activity of mesoporous silica nanoparticles in recombinant Mycoplasma hyopneumoniae antigen vaccines. *Heliyon* 3, e00225, doi:10.1016/j.heliyon.2016.e00225 (2017).

118 Guo, H. C. *et al.* Immunization of mice by hollow mesoporous silica nanoparticles as carriers of porcine circovirus type 2 ORF2 protein. *Virol J* 9, 108, doi:10.1186/1743-422X-9-108 (2012).

119 Neuhaus, V. *et al.* A new adjuvanted nanoparticle-based H1N1 influenza vaccine induced antigen-specific local mucosal and systemic immune responses after administration into the lung. *Vaccine* 32, 3216-3222, doi:10.1016/j.vaccine.2014.04.011 (2014).

120 Mercuri, L. P. *et al.* Ordered mesoporous silica SBA-15: a new effective adjuvant to induce antibody response. *Small* 2, 254-256, doi:10.1002/smll.200500274 (2006).

121 Murugadoss, S. *et al.* Toxicology of silica nanoparticles: an update. *Arch Toxicol* 91, 2967-3010, doi:10.1007/s00204-017-1993-y (2017).

122 Lin, Y. S. & Haynes, C. L. Impacts of mesoporous silica nanoparticle size, pore ordering, and pore integrity on hemolytic activity. *J Am Chem Soc* 132, 4834-4842, doi:10.1021/ja910846q (2010).

123 Yu, T., Malugin, A. & Ghandehari, H. Impact of silica nanoparticle design on cellular toxicity and hemolytic activity. *ACS Nano* 5, 5717-5728, doi:10.1021/nn2013904 (2011).

124 Huang, X. *et al.* The promotion of human malignant melanoma growth by mesoporous silica nanoparticles through decreased reactive oxygen species. *Biomaterials* 31, 6142-6153, doi:10.1016/j.biomaterials.2010.04.055 (2010).

125 Saeed, K. K., I. . Carbon nanotubes-properties and applications: a review. *Carbon Letters* 14, 131-144 (2013).

126 Harrison, B. S. & Atala, A. Carbon nanotube applications for tissue engineering. *Biomaterials* 28, 344-353, doi:10.1016/j.biomaterials.2006.07.044 (2007).

127 Tilmaciu, C. M., M. . Carbon nanotube biosensors. *Frontiers in Chemistry* 3, 1-59 (2015).

128 Eatemadi, A. *et al.* Carbon nanotubes: properties, synthesis, purification, and medical applications. *Nanoscale Res Lett* 9, 393, doi:10.1186/1556-276X-9-393 (2014).

129 Bianco, A., Kostarelos, K. & Prato, M. Applications of carbon nanotubes in drug delivery. *Curr Opin Chem Biol* 9, 674-679, doi:10.1016/j.cbpa.2005.10.005 (2005).

130 Hassan, H. A. F. M. *et al.* Dual stimulation of antigen presenting cells using carbon nanotube-based vaccine delivery system for cancer immunotherapy. *Biomaterials* 104, 310-322, doi:10.1016/j.biomaterials.2016.07.005 (2016).

131 Grecco, A. C. *et al.* Up-regulation of T lymphocyte and antibody production by inflammatory cytokines released by macrophage exposure to multi-walled carbon nanotubes. *Nanotechnology* 22, 265103, doi:10.1088/0957-4484/22/26/265103 (2011).

132 Pantarotto, D. *et al.* Immunization with peptide-functionalized carbon nanotubes enhances virus-specific neutralizing antibody responses. *Chem Biol* 10, 961-966 (2003).

133 Yang, S. T., Luo, J. B., Zhou, Q. H. & Wang, H. F. Pharmacokinetics, Metabolism and Toxicity of Carbon Nanotubes for Biomedical Purposes. *Theranostics* 2, 271-282, doi:10.7150/thno.3618 (2012).

134 Liu, Y., Zhao, Y., Sun, B. & Chen, C. Understanding the toxicity of carbon nanotubes. *Acc Chem Res* 46, 702-713, doi:10.1021/ar300028m (2013).

135 Poland, C. A. *et al.* Carbon nanotubes introduced into the abdominal cavity of mice show asbestos-like pathogenicity in a pilot study. *Nature Nanotechnology* 3, 423-428, doi:10.1038/nnano.2008.111 (2008).

136 Ren, X. Q., Chen, H. W., Yang, V. & Sun, D. X. Iron oxide nanoparticle-based theranostics for cancer imaging and therapy. *Front. Chem. Sci. Eng.* 8, 253-264, doi:10.1007/s11705-014-1425-y (2014).

137 Wu, W., He, Q. G. & Jiang, C. Z. Magnetic Iron Oxide Nanoparticles: Synthesis and Surface Functionalization Strategies. *Nanoscale Res. Lett.* 3, 397-415, doi:10.1007/s11671-008-9174-9 (2008).

138 Wahajuddin & Arora, S. Superparamagnetic iron oxide nanoparticles: magnetic nanoplatforms as drug carriers. *International Journal of Nanomedicine* 7, 3445-3471, doi:10.2147/Ijn.S30320 (2012).

139 Qiao, R. R., Yang, C. H. & Gao, M. Y. Superparamagnetic iron oxide nanoparticles: from preparations to in vivo MRI applications. *Journal of Materials Chemistry* 19, 6274-6293, doi:10.1039/b902394a (2009).

140 Wang, Y. X. Current status of superparamagnetic iron oxide contrast agents for liver magnetic resonance imaging. *World J Gastroenterol* 21, 13400-13402, doi:10.3748/wjg.v21.i47.13400 (2015).

141 de Montferrand, C. *et al.* Iron oxide nanoparticles with sizes, shapes and compositions resulting in different magnetization signatures as potential labels for multiparametric detection. *Acta Biomater* 9, 6150-6157, doi:10.1016/j.actbio.2012.11.025 (2013).

142 Clauson, R. M., Chen, M., Scheetz, L. M., Berg, B. & Chertok, B. Size-Controlled Iron Oxide Nanoplatforms with Lipidoid-Stabilized Shells for Efficient Magnetic Resonance Imaging-Trackable Lymph Node Targeting and High-Capacity Biomolecule Display. *ACS Appl Mater Interfaces* 10, 20281-20295, doi:10.1021/acsami.8b02830 (2018).

143 Yang, K. M., Cho, H. I., Choi, H. J. & Piao, Y. Z. Synthesis of water well-dispersed PEGylated iron oxide nanoparticles for MR/optical lymph node imaging. *Journal of Materials Chemistry B* 2, 3355-3364, doi:10.1039/c4tb00084f (2014).

144 Tassa, C., Shaw, S. Y. & Weissleder, R. Dextran-Coated Iron Oxide Nanoparticles: A Versatile Platform for Targeted Molecular Imaging, Molecular Diagnostics, and Therapy. *Acc. Chem. Res.* 44, 842-852, doi:10.1021/ar200084x (2011).

145 Pusic, K. *et al.* Iron oxide nanoparticles as a clinically acceptable delivery platform for a recombinant blood-stage human malaria vaccine. *Faseb Journal* 27, 1153-1166, doi:10.1096/fj.12-218362 (2013).

146 Shen, C. C., Wang, C. C., Liao, M. H. & Jan, T. R. A single exposure to iron oxide nanoparticles attenuates antigen-specific antibody production and T-cell reactivity in

ovalbumin-sensitized BALB/c mice. *Int J Nanomedicine* 6, 1229-1235, doi:10.2147/IJN.S21019 (2011).

147 Arami, H., Khandhar, A., Liggitt, D. & Krishnan, K. M. In vivo delivery, pharmacokinetics, biodistribution and toxicity of iron oxide nanoparticles. *Chemical Society Reviews* 44, 8576-8607, doi:10.1039/c5cs00541h (2015).

148 Lee, H. *et al.* Thermally cross-linked superparamagnetic iron oxide nanoparticles: Synthesis and application as a dual Imaging probe for cancer in vivo. *J. Am. Chem. Soc.* 129, 12739-12745, doi:10.1021/ja072210i (2007).

149 Cole, A. J. *et al.* Polyethylene glycol modified, cross-linked starch-coated iron oxide nanoparticles for enhanced magnetic tumor targeting. *Biomaterials* 32, 2183-2193, doi:10.1016/j.biomaterials.2010.11.040 (2011).

150 Makadia, H. K. & Siegel, S. J. Poly Lactic-co-Glycolic Acid (PLGA) as Biodegradable Controlled Drug Delivery Carrier. *Polymers (Basel)* 3, 1377-1397, doi:10.3390/polym3031377 (2011).

151 Bala, I., Hariharan, S. & Kumar, M. N. PLGA nanoparticles in drug delivery: the state of the art. *Crit Rev Ther Drug Carrier Syst* 21, 387-422 (2004).

152 Cohen, S., Yoshioka, T., Lucarelli, M., Hwang, L. H. & Langer, R. Controlled delivery systems for proteins based on poly(lactic/glycolic acid) microspheres. *Pharm Res* 8, 713-720 (1991).

153 Grossman, S. A. *et al.* The intracerebral distribution of BCNU delivered by surgically implanted biodegradable polymers. *J Neurosurg* 76, 640-647, doi:10.3171/jns.1992.76.4.0640 (1992).

154 Eliaz, R. E. & Kost, J. Characterization of a polymeric PLGA-injectable implant delivery system for the controlled release of proteins. *J Biomed Mater Res* 50, 388-396 (2000).

155 Chan, J. M. *et al.* PLGA-lecithin-PEG core-shell nanoparticles for controlled drug delivery. *Biomaterials* 30, 1627-1634, doi:10.1016/j.biomaterials.2008.12.013 (2009).

156 Rescignano, N. *et al.* Protein encapsulation in biodegradable polymeric nanoparticles: morphology, fluorescence behaviour and stem cell uptake. *Macromol Biosci* 13, 1204-1212, doi:10.1002/mabi.201300140 (2013).

157 Silva, A. L. *et al.* Optimization of encapsulation of a synthetic long peptide in PLGA nanoparticles: low-burst release is crucial for efficient CD8(+) T cell activation. *Eur J Pharm Biopharm* 83, 338-345, doi:10.1016/j.ejpb.2012.11.006 (2013).

158 Moon, J. J. *et al.* Antigen-displaying lipid-enveloped PLGA nanoparticles as delivery agents for a Plasmodium vivax malaria vaccine. *PLoS One* 7, e31472, doi:10.1371/journal.pone.0031472 (2012).

159 Kokate, R. A. *et al.* Rationalizing the use of functionalized poly-lactic-co-glycolic acid nanoparticles for dendritic cell-based targeted anticancer therapy. *Nanomedicine* 11, 479-494, doi:10.2217/nnm.15.213 (2016).

160 Thamake, S. I., Raut, S. L., Ranjan, A. P., Gryczynski, Z. & Vishwanatha, J. K. Surface functionalization of PLGA nanoparticles by non-covalent insertion of a homo-bifunctional spacer for active targeting in cancer therapy. *Nanotechnology* 22, 035101, doi:10.1088/0957-4484/22/3/035101 (2011).

161 Bose, R. J., Lee, S. H. & Park, H. Lipid-based surface engineering of PLGA nanoparticles for drug and gene delivery applications. *Biomater Res* 20, 34, doi:10.1186/s40824-016-0081-3 (2016).

162 Song, X., You, J., Shao, H. & Yan, C. Effects of surface modification of As2O3-loaded PLGA nanoparticles on its anti-liver cancer ability: An in vitro and in vivo study. *Colloids Surf B Biointerfaces* 169, 289-297, doi:10.1016/j.colsurfb.2018.05.024 (2018).

163 Manish, M. B., R. . Antibody Response is Differentially Influenced by PLGA-PAD4 Particle Characteristics. *International Journal of Infection* 4, 1-9 (2017).

164 Salman, H. H., Irache, J. M. & Gamazo, C. Immunoadjuvant capacity of flagellin and mannosamine-coated poly(anhydride) nanoparticles in oral vaccination. *Vaccine* 27, 4784-4790, doi:10.1016/j.vaccine.2009.05.091 (2009).

165 Rodgers, E. E., C.; Po, L.; Mackie, D.; Scott, E.; Kreuter, J. . The potential of polymeric nanoparticles to increase the immunogenicity of the hapten clenbuterol. *Food and Agricultural Immunology* 9, 159-166 (1997).

166 Kasturi, S. P. *et al.* Programming the magnitude and persistence of antibody responses with innate immunity. *Nature* 470, 543-547, doi:10.1038/nature09737 (2011).

167 Zhang, W. *et al.* Immune responses to vaccines involving a combined antigen-nanoparticle mixture and nanoparticle-encapsulated antigen formulation. *Biomaterials* 35, 6086-6097, doi:10.1016/j.biomaterials.2014.04.022 (2014).

168 Estey, T., Kang, J., Schwendeman, S. P. & Carpenter, J. F. BSA degradation under acidic conditions: a model for protein instability during release from PLGA delivery systems. *J Pharm Sci* 95, 1626-1639, doi:10.1002/jps.20625 (2006).

169 Houchin, M. L. & Topp, E. M. Chemical degradation of peptides and proteins in PLGA: a review of reactions and mechanisms. *J Pharm Sci* 97, 2395-2404, doi:10.1002/jps.21176 (2008).

170 Patel, A., Cholkar, K. & Mitra, A. K. Recent developments in protein and peptide parenteral delivery approaches. *Ther Deliv* 5, 337-365, doi:10.4155/tde.14.5 (2014).

171 Astete, C. E. & Sabliov, C. M. Synthesis and characterization of PLGA nanoparticles. *J Biomater Sci Polym Ed* 17, 247-289 (2006).

172 Ulery, B. D. *et al.* Polymer chemistry influences monocytic uptake of polyanhydride nanospheres. *Pharm Res* 26, 683-690, doi:10.1007/s11095-008-9760-7 (2009).

173 Carrillo-Conde, B. R. *et al.* Sustained release and stabilization of therapeutic antibodies using amphiphilic polyanhydride nanoparticles. *Chemical Engineering Science* 125, 98-107, doi:DOI 10.1016/j.ces.2014.08.015 (2015).

174 Torres, M. P., Vogel, B. M., Narasimhan, B. & Mallapragada, S. K. Synthesis and characterization of novel polyanhydrides with tailored erosion mechanisms. *J Biomed Mater Res A* 76, 102-110, doi:10.1002/jbm.a.30510 (2006).

175 Dubey, P. K., Mishra, V., Jain, S., Mahor, S. & Vyas, S. P. Liposomes modified with cyclic RGD peptide for tumor targeting. *J Drug Target* 12, 257-264, doi:10.1080/10611860410001728040 (2004).

176 Katti, D. S., Lakshmi, S., Langer, R. & Laurencin, C. T. Toxicity, biodegradation and elimination of polyanhydrides. *Adv Drug Deliv Rev* 54, 933-961 (2002).

177 Jain, J. P., Modi, S., Domb, A. J. & Kumar, N. Role of polyanhydrides as localized drug carriers. *J Control Release* 103, 541-563, doi:10.1016/j.jconrel.2004.12.021 (2005).

178 Ulery, B. D. *et al.* Polymer Chemistry Influences Monocytic Uptake of Polyanhydride Nanospheres. *Pharmaceutical Research* 26, 683-690, doi:10.1007/s11095-008-9760-7 (2009).

179 Haughney, S. L. *et al.* Retention of structure, antigenicity, and biological function of pneumococcal surface protein A (PspA) released from polyanhydride nanoparticles. *Acta Biomater* 9, 8262-8271, doi:10.1016/j.actbio.2013.06.006 (2013).

180 De, S. R. J. *et al.* Immunogenicity of peanut proteins containing poly(anhydride) nanoparticles. *Clin Vaccine Immunol* 21, 1106-1112, doi:10.1128/CVI.00359-14 (2014).

181 Petersen, L. K., Phanse, Y., Ramer-Tait, A. E., Wannemuehler, M. J. & Narasimhan, B. Amphiphilic polyanhydride nanoparticles stabilize Bacillus anthracis protective antigen. *Mol Pharm* 9, 874-882, doi:10.1021/mp2004059 (2012).

182 Vela Ramirez, J. E. *et al.* Polyanhydride Nanovaccines Induce Germinal Center B Cell Formation and Sustained Serum Antibody Responses. *J Biomed Nanotechnol* 12, 1303-1311 (2016).

183 Ross, K. A. *et al.* Structural and antigenic stability of H5N1 hemagglutinin trimer upon release from polyanhydride nanoparticles. *J Biomed Mater Res A* 102, 4161-4168, doi:10.1002/jbm.a.35086 (2014).

184 Liu, C. S., Q.; Zheng, W.; Lv, Y.; Chen, X.; Li, X.; Zhu, Q.; Guo, X.; Ge, R.; Li, C. Poly(anhydride) nanoparticles act as effective adjuvants to elicit a persistent immune response. *RSC Advances* 7, 55459-55470, doi:DOI: 10.1039/c7ra11891k (2017).

185 Ulery, B. D. *et al.* Design of a protective single-dose intranasal nanoparticle-based vaccine platform for respiratory infectious diseases. *PLoS One* 6, e17642, doi:10.1371/journal.pone.0017642 (2011).

186 Siepmann, J. r., Siegel, R. A., Rathbone, M. J. & Controlled Release Society. *Fundamentals and applications of controlled release drug delivery*. (Springer : Controlled Release Society, 2012).

187 Reuber, M. D. Carcinogenicity of chloroform. *Environ Health Perspect* 31, 171-182, doi:10.1289/ehp.7931171 (1979).

188 Schlosser, P. M., Bale, A. S., Gibbons, C. F., Wilkins, A. & Cooper, G. S. Human health effects of dichloromethane: key findings and scientific issues. *Environ Health Perspect* 123, 114-119, doi:10.1289/ehp.1308030 (2015).

189 Mohammed, M. A., Syeda, J. T. M., Wasan, K. M. & Wasan, E. K. An Overview of Chitosan Nanoparticles and Its Application in Non-Parenteral Drug Delivery. *Pharmaceutics* 9, doi:10.3390/pharmaceutics9040053 (2017).

190 Aranaz, I. M., M.; Harris, R.; Panos, I.; Miralles, B.; Acosta, N.; Galed, G.; Heras, A. . Functional Characterization of Chitin and Chitosan. *Current Chemical Biology* 3, 203-230 (2009).

191 Yuan, Q., Shah, J., Hein, S. & Misra, R. D. Controlled and extended drug release behavior of chitosan-based nanoparticle carrier. *Acta Biomater* 6, 1140-1148, doi:10.1016/j.actbio.2009.08.027 (2010).

192 Malik, A., Gupta, M., Mani, R., Gogoi, H. & Bhatnagar, R. Trimethyl Chitosan Nanoparticles Encapsulated Protective Antigen Protects the Mice Against Anthrax. *Front Immunol* 9, 562, doi:10.3389/fimmu.2018.00562 (2018).

193 Slutter, B. & Jiskoot, W. Dual role of CpG as immune modulator and physical crosslinker in ovalbumin loaded N-trimethyl chitosan (TMC) nanoparticles for nasal vaccination. *J Control Release* 148, 117-121, doi:10.1016/j.jconrel.2010.06.009 (2010).

194 Croisier, F. J., C. . Chitosan-based biomaterials for tissue engineering. *European Polymer Journal* 49, 780-792 (2013).

195 Riteau, N. & Sher, A. Chitosan: An Adjuvant with an Unanticipated STING. *Immunity* 44, 522-524, doi:10.1016/j.immuni.2016.03.002 (2016).

196 Pawar, D. & Jaganathan, K. S. Mucoadhesive glycol chitosan nanoparticles for intranasal delivery of hepatitis B vaccine: enhancement of mucosal and systemic immune response. *Drug Deliv* 23, 185-194, doi:10.3109/10717544.2014.908427 (2016).

197 Haryono, A., Salsabila, K., Restu, W. K., Harmami, S. B. & Safari, D. Effect of Chitosan and Liposome Nanoparticles as Adjuvant Codelivery on the Immunoglobulin G Subclass Distribution in a Mouse Model. *J Immunol Res* 2017, 9125048, doi:10.1155/2017/9125048 (2017).

198 Borges, O. *et al.* Alginate coated chitosan nanoparticles are an effective subcutaneous adjuvant for hepatitis B surface antigen. *Int Immunopharmacol* 8, 1773-1780, doi:10.1016/j.intimp.2008.08.013 (2008).

199 Han, Y. D., Q.; Li, Y.; Tian, J. . In vitro and in vivo investigation of chitosan– polylysine polymeric nanoparticles for ovalbumin and CpG co-delivery. *RSC Advances* 7, 39962-39969 (2017).

200 Rocha Soares, K. S. *et al.* Serum production against Tityus serrulatus scorpion venom using cross-linked chitosan nanoparticles as immunoadjuvant. *Toxicon* 60, 1349-1354, doi:10.1016/j.toxicon.2012.09.010 (2012).

201 Doavi, T., Mousavi, S. L., Kamali, M., Amani, J. & Fasihi Ramandi, M. Chitosan-Based Intranasal Vaccine against Escherichia coli O157:H7. *Iran Biomed J* 20, 97-108 (2016).

202 Dzung, N. H., N.; Van, D.; Phuong, N.; Quynh, N.; Hiep, D.; Hiep, L. . Chitosan Nanoparticle as a Novel Delivery System for A/H1n1 Influenza Vaccine: Safe Property and Immunogenicity in Mice. *International Journal of Biotechnology and Bioengineering* 5, 915-922 (2011).

203 Slutter, B. *et al.* Conjugation of ovalbumin to trimethyl chitosan improves immunogenicity of the antigen. *J Control Release* 143, 207-214, doi:10.1016/j.jconrel.2010.01.007 (2010).

204 Bellich, B., D'Agostino, I., Semeraro, S., Gamini, A. & Cesaro, A. "The Good, the Bad and the Ugly" of Chitosans. *Mar Drugs* 14, doi:10.3390/md14050099 (2016).

205 Taner, G. Y., R.; Vardar, D.; Senyigit, T.; Ozer, O.; Degen, G.; Basaran, N. . Evaluation of the cytotoxic and genotoxic potential of lecithin/chitosan nanoparticles. *Journal of Nanoparticle Research* 16, 1-9, doi:DOI 10.1007/s11051-013-2220-2 (2014).

206 Zeltins, A. Construction and characterization of virus-like particles: a review. *Mol Biotechnol* 53, 92-107, doi:10.1007/s12033-012-9598-4 (2013).

207 Roldao, A. M., M.; Castilho, L.; Carrondo, M.; Alves, P. . Virus-like particles in vaccine development. *Expert Rev Vaccines* 9, 1149-1176, doi:DOI: 10.1586/erv.10.115 (2010).

208 Rohovie, M. J., Nagasawa, M. & Swartz, J. R. Virus-like particles: Next-generation nanoparticles for targeted therapeutic delivery. *Bioeng Transl Med* 2, 43-57, doi:10.1002/btm2.10049 (2017).

209 Ray, U. Virus-like Nanoparticles: Display Matters. *Proceedings of the Indian National Science Academy* 83, 81-84, doi:10.16943/ptinsa/2016/48580 (2017).

210 Mohsen, M. O., Gomes, A. C., Vogel, M. & Bachmann, M. F. Interaction of Viral Capsid-Derived Virus-Like Particles (VLPs) with the Innate Immune System. *Vaccines (Basel)* 6, doi:10.3390/vaccines6030037 (2018).

211 Hinton, H. J., Jegerlehner, A. & Bachmann, M. F. Pattern recognition by B cells: the role of antigen repetitiveness versus Toll-like receptors. *Curr Top Microbiol Immunol* 319, 1-15 (2008).

212 Mogensen, T. H. Pathogen recognition and inflammatory signaling in innate immune defenses. *Clin Microbiol Rev* 22, 240-273, Table of Contents, doi:10.1128/CMR.00046-08 (2009).

213 Bachmann, M. F. & Zinkernagel, R. M. The influence of virus structure on antibody responses and virus serotype formation. *Immunol Today* 17, 553-558 (1996).

214 Bachmann, M. F. *et al.* The Influence of Antigen Organization on B-Cell Responsiveness. *Science* 262, 1448-1451, doi:DOI 10.1126/science.8248784 (1993).

215 Jegerlehner, A. *et al.* Regulation of IgG antibody responses by epitope density and CD21-mediated costimulation. *Eur J Immunol* 32, 3305-3314, doi:10.1002/1521-4141(200211)32:11<3305::AID-IMMU3305>3.0.CO;2-J (2002).

216 Johnson, W. E. & Desrosiers, R. C. Viral persistence: HIV's strategies of immune system evasion. *Annu Rev Med* 53, 499-518, doi:10.1146/annurev.med.53.082901.104053 (2002).

217 Tsubata, T. B-cell tolerance and autoimmunity. *F1000Res* 6, 391, doi:10.12688/f1000research.10583.1 (2017).

218 Hashemi, H. *et al.* Immunization with M2e-Displaying T7 Bacteriophage Nanoparticles Protects against Influenza A Virus Challenge. *Plos One* 7, doi:ARTN e4576510.1371/journal.pone.0045765 (2012).

219 Wei, D. Z., X.; Chen, L.; Lan, X.; Li, Y.; Lin, Y.; Wang, Q. . Viral nanoparticles as antigen carriers: influence of shape on humoral immune responses in vivo. *RSC Advances* 4, 23017-23021 (2014).

220 Maurer, P. *et al.* A therapeutic vaccine for nicotine dependence: preclinical efficacy, and Phase I safety and immunogenicity. *Eur J Immunol* 35, 2031-2040, doi:10.1002/eji.200526285 (2005).

221 Yin, Z. *et al.* Boosting immunity to small tumor-associated carbohydrates with bacteriophage qbeta capsids. *ACS Chem Biol* 8, 1253-1262, doi:10.1021/cb400060x (2013).

222 Zhao, X. *et al.* Enhancing Antibody Response against Small Molecular Hapten with Tobacco Mosaic Virus as a Polyvalent Carrier. *Chembiochem* 16, 1279-1283, doi:10.1002/cbic.201500028 (2015).

223 Chackerian, B., Rangel, M., Hunter, Z. & Peabody, D. S. Virus and virus-like particle-based immunogens for Alzheimer's disease induce antibody responses against amyloid-beta without concomitant T cell responses. *Vaccine* 24, 6321-6331, doi:10.1016/j.vaccine.2006.05.059 (2006).

224 Chackerian, B., Lowy, D. R. & Schiller, J. T. Conjugation of a self-antigen to papillomavirus-like particles allows for efficient induction of protective autoantibodies. *J Clin Invest* 108, 415-423, doi:10.1172/JCI11849 (2001).

225 Li, H. Y., Han, J. F., Qin, C. F. & Chen, R. Virus-like particles for enterovirus 71 produced from Saccharomyces cerevisiae potently elicits protective immune responses in mice. *Vaccine* 31, 3281-3287, doi:10.1016/j.vaccine.2013.05.019 (2013).

226 Coleman, C. M. *et al.* Purified coronavirus spike protein nanoparticles induce coronavirus neutralizing antibodies in mice. *Vaccine* 32, 3169-3174, doi:10.1016/j.vaccine.2014.04.016 (2014).

227 Lee, Y. T. *et al.* Cellular Immune Correlates Preventing Disease Against Respiratory Syncytial Virus by Vaccination with Virus-Like Nanoparticles Carrying Fusion Proteins. *J Biomed Nanotechnol* 13, 84-98, doi:10.1166/jbn.2017.2341 (2017).

228 McLain, L., Porta, C., Lomonossoff, G. P., Durrani, Z. & Dimmock, N. J. Human immunodeficiency virus type 1-neutralizing antibodies raised to a glycoprotein 41 peptide expressed on the surface of a plant virus. *AIDS Res Hum Retroviruses* 11, 327-334, doi:10.1089/aid.1995.11.327 (1995).

229 Smith, G. E. *et al.* Development of influenza H7N9 virus like particle (VLP) vaccine: homologous A/Anhui/1/2013 (H7N9) protection and heterologous A/chicken/Jalisco/CPA1/2012 (H7N3) cross-protection in vaccinated mice challenged with H7N9 virus. *Vaccine* 31, 4305-4313, doi:10.1016/j.vaccine.2013.07.043 (2013).

230 Pushko, P. *et al.* Evaluation of influenza virus-like particles and Novasome adjuvant as candidate vaccine for avian influenza. *Vaccine* 25, 4283-4290, doi:10.1016/j.vaccine.2007.02.059 (2007).

231 Galarza, J. M., Latham, T. & Cupo, A. Virus-like particle (VLP) vaccine conferred complete protection against a lethal influenza virus challenge. *Viral Immunol* 18, 244-251, doi:10.1089/vim.2005.18.244 (2005).

232 Therien, A. *et al.* A versatile papaya mosaic virus (PapMV) vaccine platform based on sortase-mediated antigen coupling. *J Nanobiotechnology* 15, 54, doi:10.1186/s12951-017-0289-y (2017).

233 Donaldson, B., Lateef, Z., Walker, G. F., Young, S. L. & Ward, V. K. Virus-like particle vaccines: immunology and formulation for clinical translation. *Expert Rev Vaccines* 17, 833-849, doi:10.1080/14760584.2018.1516552 (2018).

234 McCluskie, M. J. *et al.* The effect of preexisting anti-carrier immunity on subsequent responses to CRM197 or Qb-VLP conjugate vaccines. *Immunopharmacol Immunotoxicol* 38, 184-196, doi:10.3109/08923973.2016.1165246 (2016).

235 Brune, K. D. *et al.* Plug-and-Display: decoration of Virus-Like Particles via isopeptide bonds for modular immunization. *Sci Rep* 6, 19234, doi:10.1038/srep19234 (2016).

236 Pattenden, L. K., Middelberg, A. P., Niebert, M. & Lipin, D. I. Towards the preparative and large-scale precision manufacture of virus-like particles. *Trends Biotechnol* 23, 523-529, doi:10.1016/j.tibtech.2005.07.011 (2005).

237 Masavuli, M. G., Wijesundara, D. K., Torresi, J., Gowans, E. J. & Grubor-Bauk, B. Preclinical Development and Production of Virus-Like Particles As Vaccine Candidates for Hepatitis C. *Front Microbiol* 8, 2413, doi:10.3389/fmicb.2017.02413 (2017).

238 Fujinami, R. S., von Herrath, M. G., Christen, U. & Whitton, J. L. Molecular mimicry, bystander activation, or viral persistence: infections and autoimmune disease. *Clin Microbiol Rev* 19, 80-94, doi:10.1128/CMR.19.1.80-94.2006 (2006).

239 Segal, Y. & Shoenfeld, Y. Vaccine-induced autoimmunity: the role of molecular mimicry and immune crossreaction. *Cell Mol Immunol* 15, 586-594, doi:10.1038/cmi.2017.151 (2018).

240 Somiya, M., Liu, Q. & Kuroda, S. Current Progress of Virus-mimicking Nanocarriers for Drug Delivery. *Nanotheranostics* 1, 415-429, doi:10.7150/ntno.21723 (2017).

241 Chattopadhyay, S., Chen, J. Y., Chen, H. W. & Hu, C. J. Nanoparticle Vaccines Adopting Virus-like Features for Enhanced Immune Potentiation. *Nanotheranostics* 1, 244-260, doi:10.7150/ntno.19796 (2017).

242 Parodi, A. *et al.* Bio-inspired engineering of cell- and virus-like nanoparticles for drug delivery. *Biomaterials* 147, 155-168, doi:10.1016/j.biomaterials.2017.09.020 (2017).

243 Wang, W. *et al.* Facile Synthesis of Uniform Virus-like Mesoporous Silica Nanoparticles for Enhanced Cellular Internalization. *ACS Cent Sci* 3, 839-846, doi:10.1021/acscentsci.7b00257 (2017).

244 Chen, S. & Chen, R. A Virus-Mimicking, Endosomolytic Liposomal System for Efficient, pH-Triggered Intracellular Drug Delivery. *ACS Appl Mater Interfaces* 8, 22457-22467, doi:10.1021/acsami.6b05041 (2016).

245 Ribeiro-Viana, R. *et al.* Virus-like glycodendrinanoparticles displaying quasi-equivalent nested polyvalency upon glycoprotein platforms potently block viral infection. *Nat Commun* 3, 1303, doi:10.1038/ncomms2302 (2012).

246 Lee, C. *et al.* Rabies Virus-Inspired Silica-Coated Gold Nanorods as a Photothermal Therapeutic Platform for Treating Brain Tumors. *Adv Mater* 29, doi:10.1002/adma.201605563 (2017).

247 Niu, Y. Y., M.; Meka, A.; Liu, Y.; Zhang, J.; Yang, Y.; Yu, C. . Understanding the contribution of surface roughness and hydrophobic modification of silica nanoparticles to enhanced therapeutic protein delivery. *Journal of Materials Chemistry B* 4, 212-219, doi:DOI: 10.1039/c5tb01911g (2016).

248 Niu, Y. T. *et al.* Nanoparticles Mimicking Viral Surface Topography for Enhanced Cellular Delivery. *Advanced Materials* 25, 6233-6237, doi:10.1002/adma.201302737 (2013).

249 Kirby, D. J. *et al.* Developing solid particulate vaccine adjuvants: surface bound antigen favours a humoural response, whereas entrapped antigen shows a tendency for cell mediated immunity. *Curr Drug Deliv* 10, 268-278 (2013).

250 Riitho, V. *et al.* Design and evaluation of the immunogenicity and efficacy of a biomimetic particulate formulation of viral antigens. *Sci Rep* 7, 13743, doi:10.1038/s41598-017-13915-x (2017).

251 Ingale, J. *et al.* High-Density Array of Well-Ordered HIV-1 Spikes on Synthetic Liposomal Nanoparticles Efficiently Activate B Cells. *Cell Rep* 15, 1986-1999, doi:10.1016/j.celrep.2016.04.078 (2016).

252 Chen, H. *et al.* Facile Fabrication of Near-Infrared-Resonant and Magnetic Resonance Imaging-Capable Nanomediators for Photothermal Therapy. *ACS Appl Mater Interfaces* 7, 12814-12823, doi:10.1021/acsami.5b01991 (2015).

253 Tan, Y. S. *et al.* Mitigating SOX2-potentiated Immune Escape of Head and Neck Squamous Cell Carcinoma with a STING-inducing Nanosatellite Vaccine. *Clin Cancer Res* 24, 4242-4255, doi:10.1158/1078-0432.CCR-17-2807 (2018).

254 Zhang, L. *et al.* Zwitterionic hydrogels implanted in mice resist the foreign-body reaction. *Nat Biotechnol* 31, 553-556, doi:10.1038/nbt.2580 (2013).

255 Chen, Y. S., Hung, Y. C., Lin, W. H. & Huang, G. S. Assessment of gold nanoparticles as a size-dependent vaccine carrier for enhancing the antibody response against synthetic foot-and-mouth disease virus peptide. *Nanotechnology* 21, doi:Artn 19510110.1088/0957-4484/21/19/195101 (2010).

256 Haughney, S. L. *et al.* Retention of structure, antigenicity, and biological function of pneumococcal surface protein A (PspA) released from polyanhydride nanoparticles. *Acta Biomaterialia* 9, 8262-8271, doi:10.1016/j.actbio.2013.06.006 (2013).

257 Stano, A. v. d. V., A.; Martino, M.; Swartz, M.; Hubbell, J.; Simeoni, E. . PPS nanoparticles as versatile delivery system to induce systemic and broad mucosal immunity after intranasal administration. *Vaccine* 29, 804-812 (2011).

258 Li, P. S., G.; Zhang, X.; Song, H.; Zhang, C.; Wang, W.; Li, C.; Song, B.; Wang, C.; Kong, D. . Guanidinylated cationic nanoparticles as robust protein antigen delivery systems and adjuvants for promoting antigen-specific immune responses in vivo. *Journal of Materials Chemistry B* 4, 5608-5620 (2016).

259 Wilson, J. T. *et al.* pH-Responsive Nanoparticle Vaccines for Dual-Delivery of Antigens and Immunostimulatory Oligonucleotides. *Acs Nano* 7, 3912-3925, doi:10.1021/nn305466z (2013).

260 Soares, K. S. R. *et al.* Antivenom Production against Bothrops jararaca and Bothrops erythromelas Snake Venoms Using Cross-Linked Chitosan Nanoparticles as an Immunoadjuvant. *Toxins (Basel)* 10, doi:10.3390/toxins10040158 (2018).

261 Smith, E. M. *et al.* Risk factors and survival by HPV-16 E6 and E7 antibody status in human papillomavirus positive head and neck cancer. *International Journal of Cancer* 127, 111-117, doi:10.1002/ijc.25015 (2010).

CHAPTER 2

Engineering Inorganic Virus-Like Nanoparticles with Viral Structural and Functional Mimicry for Lymph Node Homing, B-cell Activation and Enhanced Antigen-Specific Antibody Production

2.1 Abstract:

Virus-like nanoparticles (VLN) are an alternative to viruses as a delivery strategy. However, engineering of VLNs is limited by the difficulty of incorporating viral mimicry. Here, we generated inorganic VLNs (IVLN), which mimic viral structure and function for lymph node homing, B-cell activation, and antigen-specific antibody production. The IVLNs were synthesized with viral-like spiky topography using Au@Fe hybrid nanoparticle technology. Hubs of antigen were controlled at viral-like densities of 20,000-25,000 molecules/um^2 with display organization in a 3D patch pattern at ~6 nm intervals critical for B cell receptor crosslinking. IVLNs have unique viral-like functions to improve lymph node homing and distribution into subcapsular sinus macrophages and B-cells by 3-fold, facilitate 6-fold enhanced of B cell activation, and 4 to 18-fold antigen specific IgG production with prophylactic anti-cancer efficacy against HER2+ breast cancer in mice. The IVLN with viral-like structure and function may have broad applications to modulate immune responses.

2.2 Introduction:

Viruses are known to be the most efficient delivery vehicles to generate efficacious immunological responses[1,2]. Therefore, it has become desirable to utilize viruses in a wide variety of application such as vaccines, antibody production and gene delivery[3-5]. However, the use of traditional live attenuated or heat-killed viruses as a delivery tool is challenging due to their safety profiles, difficulty in manufacturing and associated non-specific immune responses[6-8]. Accordingly, alternative approaches have been developed to exploit the structural feature of viruses while minimizing these concerns.

To replace traditional viruses, virus-like particles (VLP) have emerged as delivery vehicles for many applications[9]. VLPs are protein-based nanoparticles that are composed of viral capsid proteins that self-assemble into geometrically rigid three-dimensional nanospheres that directly resemble viral structure and confirmation without the viral genome[10,11]. Thus, VLPs are considered a viable and safe alternative to traditional viruses[12]. VLPs are especially advantageous as B-cell vaccine for viral vaccines[13,14]. For instance, clinically human papillomavirus (HPV) VLP vaccines using HPV L1 capsid proteins widely used to prevent HPV infection[15-17]. Several other VLP vaccines have been made to prevent infections including an FDA-approved vaccine for hepatitis B virus, as well as vaccines for influenza, norovirus and chikungunya virus currently undergoing clinical trials[18-21]. However, numerous obvious disadvantages of VLPs formulation and usage remain. First, it is very difficult to reproducibly and controllably synthesize and manufacture VLPs due to a reliance on viral capsid protein self-assembly within an expression host for particle formation[22,23]. Second, VLPs are known to strongly activate B-cells to generate antibodies against capsid proteins, which is the very purpose VLPs as vaccines to prevent viral infections, However, if the immunity is intended to be directed against other proteins or peptides conjugated to the VLP carrier, this anti-carrier response dramatically limits the specificity and strength of the intended immune response[24,25].

As a result of the challenges associated with the use of VLPs, there has been increasing interest in the development of novel nanoparticle systems that mimic viral-like structure and function[1,26-28]. To date, the most traditional approaches in the development of viral mimicry nanoparticles for the delivery of antigens include the use of liposomes, polymeric nanoparticles and inorganic nanoparticles[29-32]. Indeed, these nanoparticles have been extensively evaluated in both the context of drug delivery and vaccine development and have been found to more

efficaciously stimulate B-cell and T-cell immunity as compared to soluble antigens. However, these traditional nanoparticle systems do not ideally represent viral-like structure and material properties, nor do they exhibit any viral-like function to stimulate the immune response.

To engineer an authentic viral mimicking nanoparticle system, which is not only representative of viral-like structure, but also function, a more holistic design approach needs to be considered. This viral mimicking nanoparticle system needs to have viral-like surface topography, antigen density and antigen display organization, which is very difficult to achieve with traditional nanoparticle technologies. In addition to complex design elements, the viral mimicking nanoparticle system must also have appropriate particle size, surface charge and antigen immunogenicity which is rather easy to achieve with any nanoparticle system.

In this study, we surmised a holistic approach to viral mimicking nanoparticle design through the development of an inorganic virus-like nanoparticle (IVLN) technology that mimics viral structure and function. This technology is based on a hybrid Fe@Au core/satellite nanoparticle technology, which is composed of ultra-small gold nanosatellites (AuNP, 2-3 nm) anchored to an iron-oxide nanoparticle core (IONP, 15-20 nm). These nanosatellites provide viral-like spiky and rough surface topography. The overall size of the IVLN is 20-30 nm under transmission electron microscopy (TEM) with a hydrodynamic size of 60-70 nm by dynamic light scattering (DLS). The antigen display density was controlled to be greater than 10,000 molecules per micron squared (2,000 peptides per IVLN). Antigen display organization and surface topography were controlled in a patch pattern with ~6 nm distance between clusters, which may be critical for B-cell receptor crosslinking and robust activation[33]. Based on these material design parameters, our IVLN incorporates unique structural features including spiky surface topography, high antigen density and patterned antigen display that are more virally relevant and significantly distinctive from any other current inorganic nanoparticle technology[34-38]. Additionally, we tested IVLN viral-like function in terms of lymph node homing, lymph node immune cell uptake and specific distribution[39], as well as the ability to facilitate robust stimulation of B-cell immunity in an antigen-specific fashion. As compared to a traditional nanoparticle system, our IVLN proved to have the viral-like functional to improve lymph node homing (3-fold), increase B-cell specific interactions (3-fold), to promote antigen-specific B-cell proliferation (6-fold) and germinal center formation (3-fold), and to enhance antigen-specific IgG antibody production (4 to 18-fold) that function to prevent cancer growth in a mouse model of HER2+ breast cancer. Taken together, these data suggest that the IVLN both effectively mimics

viral-like structure and exhibits viral-like function, which may have broad applications as a delivery technology to boost antigen-specific immunity.

2.3 Experimental Section:

Materials. All reagents were used as obtained from commercial sources without further purification, except for γ-Methacryl oxypropyltrimethoxysilane (98%) that was purified by distillation under reduced pressure and 2,2-Azobis(isobutyronitrile) (98%) that was purified by recrystallization in ethanol. Iron oxide (III) (FeO(OH), hydrated, catalyst grade, 30−50 mesh), oleic acid (technical grade, 90%), ammonium iron (II) sulfate hexahydrate (ACS reagent, 99%), 1-octadecene (technical grade, 90%), anhydrous tetrahydrofuran (THF, 99.8%), carbon disulfide (99.9%), magnesium turnings (>99.5%), 2-chloro-2-phenylacetyl chloride (CPAC, 90%), poly(ethylene oxide) monomethyl ether (PEO), anhydrous dioxane (99.8%), dimethylformamide (DMF, 99.9%), dimethyl sulfoxide (DMSO, 99.9%), o-phenanthroline monohydrate (ACS reagent, 99%), hydroquinone (ACS reagent, 99%, sodium sulfide, chloroauric acid, nitric acid (ACS reagent, 70%), and hydrochloric acid (ACS reagent, 37%) were purchased from Sigma-Aldrich. Mouse uncoated IgG and IgM Total ELISA Ready-SET-Go! Kits, 1-Step Ultra TMB-ELISA substrate solution, HRP-conjugated goat anti-mouse IgG1 secondary antibody, HRP-conjugated goat anti-mouse IgG2a secondary antibody, Nunc Immobilizer Amino 96-well ELISA plates, BupH carbonate bicarbonate buffer packs (coating buffer), Pierce protein free PBS tween blocking buffer, 20x PBS-tween wash buffer, Geneticin (G418) selective antibiotic, Invitrogen eBioscience fixable viability dye eFluor 780, and Molecular Probes streptavidin Alexa Fluor 647 conjugate were obtained from Thermo Fisher Scientific. HRP conjugated goat anti-mouse IgG secondary antibody, Zombie UV fixable viability kit, FITC anti-mouse CD19, PE/Dazzle 594 anti-mouse IgD, Alexa Fluor 647 anti-mouse/house GL7 antigen, Brilliant Violet 421 and PE/Dazzle 594 anti-mouse/human CD45R/B220, FITC anti-mouse CD95, Brilliant Violet 421 anti-mouse/human CD11b, FITC anti-mouse CD169 and PE goat anti-mouse IgG secondary antibody were purchased from BioLegend. HER2 peptides (CDDDPESFDGDPASNTAPLQPEQLQ, Biotin-PESFDGDPASNTAPLQPEQLQ, CDDDPESFDGDPASNTAPLQPEQLQGGGK) were custom synthesized by LifeTein. 30 nm iron-oxide nanoparticles cores stabilized by oleic acid in chloroform were purchased from Ocean Nanotech. DSPE-PEG(2000) and DSPE-PEG(2000)maleimide were obtained from Avanti Polar

Lipids. 2'3'-cGAMP was acquired from InvivoGen. Fluorescamine was purchased from MP Biomedicals. Sulfo-Cy5.5 NHS ester was acquired from Lumiprobe. Microvette 500 Z-Gel serum collection vials with clotting factor were obtained from Sarstedt. Matrigel Basement Membrane Matrix was purchased from Corning. Gold and iron ICP standards were purchased from Fluka Analytical.

Mice. All animal experiments were conducted according to the protocols approved by the University of Michigan Committee on Use and Care of Animals (UCUCA). BALB/c mice ages 5-7 weeks were purchased from Charles River Labs.

Cells. All cells were maintained at 37C, 5% CO_2/95% air atmosphere and approximately 85% relative humidity. D2F2/E2 cells (provided by Dr. Wei-Zen Wei[40]) were cultured in complete DMEM high glucose supplemented with 10% NCTC 109 media, 1% L-glutamine, 1% MEMs non-essential amino acids, 0.5% sodium pyruvate, 2.5% sodium bicarbonate, 1% pen/strep, 5% cosmic calf serum, 5% fetal bovine serum, 500 µg/mL Geneticin and 50 µM 2-mercaptoethanol. RAW264.7 macrophages were cultured in complete RPMI-1640 media supplemented with 10% fetal bovine serum, 1% L-glutamine, 1% MEMs non-essential amino acids, 1% sodium pyruvate and 1% pen/strep. Primary B-cells were cultured in RPMI-1640 media supplemented with 10% heat-inactivated fetal bovine serum.

Formulation and Characterization of Inorganic Virus-Like Nanoparticles (IVLN). The IVLN was formulated based on previously reported protocols by our group with minor modifications[41]. The final Au to Fe ratio of the formulated IVLN was quantified by inductively coupled plasma mass spectrometry (ICP-MS) using a Perkin-Elmer Nexion 2000 based on previously reported protocols modified from analysis by ICP-OES[42]. IVLN formulations were imaged by transmission electron microscopy (TEM) using the JEOL 3011 High Resolution Electron Microscope. The true particle size of AuNPs, IONPs and IVLNs was quantified using ImageJ software. The volume-weighted hydrodynamic particle size, polydispersity index and zeta-potential of all formulations in milliQ water at 25°C was evaluated with the Malvern Zetasizer Nano-ZS using dynamic light scattering and phase analysis light scattering, respectively.

Lipid-Coated Iron-Oxide Nanoparticle Formulations (IONP). Lipid-coated iron-oxide nanoparticles were prepared based on previously reported methods for thin-film hydration with minor modifications[43,44]. 10 mg of DSPE-PEG(2000)-maleimide was added to 1 mg of 30-nm iron-oxide nanoparticle cores stabilized by oleic acid in chloroform as gently mixed. The resulting solution was subjected to solvent rotary evaporation to remove all chloroform and form

a thin film. Simultaneously, this film and 100 mM PBS, pH 7.4 were heated to 75°C in an oven. Upon reaching temperature, hot PBS was rapidly added to the film and mixed immediately and vigorously to facilitate thin film hydration. The resulting nanoparticle solution was stored at 4°C to promote lipid self-assembly. Free phospholipid was removed by magnetic separation overnight at 4°C using the EasySep magnetic separator device (StemCell).

IONP-HER2 and IVLN-HER2 Formulations. HER2 peptides were conjugated to both IONP and IVLN through thiol-mediated chemistries. Specifically, IONP-HER2 was formulated via maleimide chemistry and IVLN-HER2 was formulated via the gold-thiol linkage. HER2 peptide was added to IONP at 1.5x weight ratio excess in milliQ and incubated overnight at 4°C. HER2 peptide was added to IVLN-HER2 at 5x weight ratio excess in milliQ and incubated overnight at 4°C. Both materials were purified either by magnetic separation overnight at 4°C using magnetic separation, or by centrifugal separation at 10,000 x g for 30 minutes at 4°C. Peptide loading was determined using fluorescent quantification using a modified fluorescamine peptide quantification assay in the presence of nanoparticles (Ex/Em: 390/465 nm, Biotek Cytation 5)[45]. Quantification was performed using a standard curve with increasing peptide concentration with standardized concentration of nanoparticles (IONP or IVLN) to account for quenching effects.

Immunizations and Serum Collection. At day 0, mice were immunized with the equivalent of 50 μg or 5 μg of HER2 peptide plus 10 μg of cGAMP regardless of formulation type. Subsequently, at day 14, mice were boosted twice at two-week intervals with 50% of the original dosage for both antigen and adjuvant (day 14 and 28). To evaluate serum antibody titers, blood was collected by submandibular puncture 10 days after each immunization (day 10, 24 and 38). Serum was separated from whole blood by centrifugal separation at 10,000 x g for 5 minutes at 25°C using the Microvette 500 Ser-Gel collection vessels with clotting activator.

Enzyme-Linked Immunosorbent Assay (ELISA). Absolution quantification of total IgG and total IgM antibody analysis was performed using the mouse uncoated total IgG and total IgM ELISA kits based on manufacturer recommended protocols (Thermo Fisher). Antigen-specific IgG, IgG1 and IgG2a antibody titers were quantified based on previously established protocols for indirect ELISA with minor modifications[46]. Specifically, HER2 peptides (200 μL, 100 ug/mL in 100 mM carbonate buffer, pH 9.4) were chemically conjugated to ELISA plates through the terminal amine group utilizing Nunc Immobilizer Amino immunoassay plates by overnight incubation with exposure to light at room temperature. Following overnight incubation, ELISA plates were washed three times with 100 mM PBS, pH 7.4 with 2% Tween-20. Subsequently,

ELISA plates were blocked overnight at 4°C with 300 µL of ELISA blocker (Pierce Protein-Free PBS Blocking Buffer). Following blocking, the ELISA plates were washed 3x. Serum samples containing primary antibodies were serially diluted (10^1-10^8 fold) using 100 mM PBS, pH 7.4 containing 10% ELISA blocker reagent and added to each well at 200 µL total for 2 hour incubation at room temperature. Following sample addition, the ELISA plates were washed 3x. 500-fold diluted A\anti-IgG-HRP, anti-IgG1-HRP, or anti-IgG2a-HRP was added at 100 µL to each well and incubated for 1 hour at room temperature. After 1 hour, the ELISA plates were washed 5x. Next, 100 µL of 1-Step Ultra TMB Substrate Solution was added to each well and allowed to incubate and develop color for 15-20 minutes at room temperature with gentle agitation. After 15-20 minutes, color development was stopped by the addition of 100 µL of 100 mM sulfuric acid. Colorimetric development was quantified by absorbance spectroscopy at 450 nm using the BioTek Cytation 5 plate reader. Antibody titers were determined by any absorbance signal at a given dilution factor that was greater than the PBS control absorbance signal plus three standard deviations[47].

Quantification of Nanoparticle Delivery to Lymph Nodes *in-vivo*. Mice were injected subcutaneously in the left hock with either IONP or IVLN at 200 µg total Fe per mouse. At the designated time intervals, mice were sacrificed and lymph nodes of interest were dissected for *ex-vivo* analysis. The extent of nanoparticle delivery to the lymph nodes was quantified using ICP-MS based on previously reported protocols modified from analysis by ICP-OES[48].

Quantification of Peptide Delivery to Lymph Nodes *in-vivo*. To facilitate quantification of peptide delivery to lymph nodes, lysine terminally modified HER2 peptides were chemically conjugated to sulfo-Cy5.5 NHS Ester. This conjugation was carried out at a 5-fold molar excess of sulfo-Cy5.5 NHS Ester to HER2 peptide. IONP-HER2-Cy5.5 and IVLN-HER2-Cy5.5 were subjected to Cy5.5 functionalization after initial peptide conjugation was completed in order to enable facile purification of excess fluorescent dye by magnetic separation. Subsequent to Cy5.5 functionalization, mice were injected as previously stated. After 3 hours, mice were sacrificed and lymph nodes of interest were dissected for *ex-vivo* analysis by IVIS imaging. IVIS imaging was utilized for semi-quantification of peptide delivery in terms of radiant efficiency.

In-vitro Cell Uptake. IVLN-HER2 and IONP-HER2 cellular uptakes was evaluated in RAW264.7 macrophages and primary B-cells isolated from murine spleens using an EasySep Mouse B-cell isolation kit. Nanoparticle samples were incubated at 50 µg/mL Fe with cells for 18 hours in blank RPMI media at 37C, 5% CO_2/95% air atmosphere and approximately 85%

relative humidity. After 18 hours, cells were lifted by cell scraping and washed thrice with phosphate-buffered saline (PBS). Following the wash steps, resulting cell pellets were re-suspended in 1 mL of PBS, cell counted and then digested in 1 mL aqua regia (1:3 molar ratio nitric acid: hydrochloric acid) for analysis by ICP-MS.

In-vivo Cell Uptake. IVLN-HER-Cy5.5 and IONP-HER2-Cy5.5 were injected subcutaneously in the left hock with either Lipid-IONP or IVLN at 200 μg total Fe per mouse. At 3 hours and 24 hours, mice were sacrificed and lymph nodes of interest were dissected for *ex-vivo* analysis by flow cytometry. Lymph nodes were dissociated by mechanical methods to prepare single cell suspensions. Single cell suspensions of lymph node cells were stained for analysis by flow cytometry using the MoFlo Astrios flow cytometer. Viable cells (Zombie UV) were identified as either B-cells ($B220^+$) or subcapsular sinus macrophages ($CD169^{high}CD11b^+$) and evaluated for positive nanoparticle interactions (Cy5.5). Flow cytometry data was analyzed by FCS express.

Antigen-Specific B-cell and Germinal Center Flow Cytometry. Mice were immunized as previously introduced. At day 10, mice were sacrificed and lymph nodes were dissected for *ex-vivo* analysis by flow cytometry. Antigen-specific B-cell analysis was accomplished using tetramer staining based on previously established protocols with minor modifications[49]. HER2/neu peptide tetramers were prepared by mixture of biotin-labeled HER2 peptide with Alexa Fluor 647 labeled streptavidin at a 4:1 molar ratio at room temperature for 1 hour without further purification. Antigen-specific B-cell population were identified using CD19, and the HER2-peptide tetramer using flow cytometry. Germinal center B-cell populations were identified using the following markers B220, IgD, GL7 and CD95 ($B220^+IgD_{low}GL7^+CD95^+$).

Tumor Studies. Forty-nine days after the primary immunization, mice were inoculated with 250,000 D2F2/E2 cells subcutaneously in the right flank. D2F2/E2 cells were prepared at 2.5e6 cells/mL in 100 μL and mixed at equal volume with Matrigel matrix. Tumor size was quantified by caliper measurements every 7 days. Tumor volumes were calculated using the following equation:

$$Tumor\ Volume = {xy^2}/{2}$$

End points were determined by using the End-Stage Illness Scoring System; mice receiving an End-Stage Illness Score greater than 6 were euthanized by CO_2 asphyxiation.

Statistics.

Data are expressed as mean ± standard deviation (SD), unless otherwise specified. Comparisons between two groups were made using the unpaired Student's *t*-test. Means of multiple groups were compared with the one-way analysis of variance (ANOVA), followed by post hoc Tukey's pairwise comparisons. All probability values are two-sided, and values of $p < 0.05$ were considered statistically significant. Statistical analyses were carried out using the GraphPad Prism 7 software package.

2.4 Results:

Generation of Inorganic Virus-Like Nanoparticles (IVLN) that Mimic Viral-like Properties

To achieve viral-like spiky and rough surface topography, we attached ultra-small gold nanoparticles (AuNP, 2-3 nm), termed satellites, onto the surface of an iron-oxide nanoparticle core (IONP, 15 nm) to produce the Au@Fe hybrid nanoparticle platform coined inorganic virus-like nanoparticle (IVLN) (Figure 2.1A). AuNP attachment to IONP is achieved by the interaction between reactive AuNP surfaces and free siloxane moieties present in the polymer used to coat the IONP. The IONP of the IVLN was synthesized by thermal decomposition to produce a 15-nm spherical core stabilized by oleic acid in chloroform based on established techniques (Figure S1A). To achieve aqueous stabilization, the IONP was coated with a poly(siloxane) and poly(ethylene glycol) containing di-block co-polymer based on procedures previously reported by our group[41]. Separately, ultra-small gold nanoparticles or satellites (AuNP) with ~3 nm sizes were prepared using a modified precipitation method by reduction of chloroauric acid in aged sodium sulfide[50] (Figure S1B). The resulting AuNP solution is added to an IONP solution at defined weight ratios and incubated overnight at 4°C to allow for self-assembly.

To control the density of viral-like spiky structures and therefore the extent of biologically relevant roughness on IVLN surfaces, we adjusted the ratios of AuNPs to IONPs within the initial formulation. The number of AuNPs on the surface of IONPs was initially quantified by the amount of gold (Au) and iron (Fe) present after magnetic purification (Figure 2.2A) and was subsequently validated by TEM (Figure 2.2B). To quantify the amount of Au loading per Fe, inductively coupled plasma mass spectrometry (ICP-MS) was performed. With ICP-MS, it was determined that the average loading efficiency on a per weight basis was 73 ±

7% with linear dependence (R^2 = 0.997) (Figure 2.2A). Notably, above an initial loading ratio of 60% weight Au to Fe, destabilization of nanoparticles in solution was observed (data not shown) and was therefore not the focus of further research. Based on known crystalline structure and quantified particle size and weight of Au and Fe respectively[51,52], it was possible to quantify the number of AuNP satellites per IONP as theoretically ranging from 1 to 14 (Figure 2.2A).

To provide visual confirmation of AuNP and IONP-polymer self-assembly to form the IVLN, transmission electron microscopy (TEM) was performed (Figure 2.2B). TEM imaging confirmed that by controlling the initial loading ratio of Au to Fe on a per weight basis it is possible to yield IVLNs with variable AuNP surface density and qualitatively intriguing viral-like character (Figure 2.2B-insert). From the TEM images in Figure 2.2B, IONP-polymer core and AuNP diameters were quantified to be 15.9 ± 1.3 nm and 2.3 ± 0.4 nm, respectively. TEM visualization of AuNPs per IONP revealed that the 10%, 20% and 30% Au to Fe weight loading conditions yielded IVLNs with 4 ± 2, 9 ± 3 and 13 ± 5 AuNPs per IONP-polymer core, respectively. These report values agree with the theoretically calculated number of AuNP on the IVLN surfaces discussed previously.

To control the distance between viral-like spiky structures with optimal distance of 5-10 nm, which is an ideal distance for B-cell receptor activation[33], we adjusted the number of AuNP on the IVLN surfaces. Under optimal formulation conditions, IVLNs can be produced with a minimum average distance between 5.1-6.3 nm between AuNPs, based on rudimentary models (Figure 2.2C, Supporting Information). In addition to average inter-particle distance, the number of AuNPs per unit area was determined to be approximately 20,000-25,000 AuNPs per square micron, which is a value that compares favorably to the antigen density reported for viral-like particles[53] (e.g. Hepatitis B Virus, ~ 20,000 antigens per μ^2) (Figure 2.2D).

To further evaluate the viral mimicking nature of the IVLN, we next evaluated the capacity for and mechanism of peptide loading in this system. We choose a non-viral and non-capsid oncogenic human HER2/neu-specific peptide. Based on previously published works, this HER2 peptide contains a B-cell epitope with an overlapping CD4 helper T-cell epitope[54-56]. In order to effectively control antigen density, display and organization, we developed the IVLN to facilitate peptide conjugations specifically to the viral-like spiky structures (AuNPs) and not to the surrounding polymeric surfaces (IONP). Therefore, a cysteine containing terminal flank was added to the HER2 peptide antigen to facilitate facile loading to the IVLN via the Au-S linkage (CDDD-PESFDGDPASNTAPLQPEQLQ). During conjugation trials, polymer-coated IONP alone

without attached AuNPs was used as control. From the data in Figure 2.2E, it is evident that high levels of peptide conjugation are observed for IVLNs with AuNP present, but not on the IONP core alone (black symbols). Additionally, the correlation analysis revealed a positive correlation between peptide loading and AuNP number (R = 0.95) (Figure S2). Taken together, these results suggest that, although there is low-level non-specific physical association to the core (~12% under saturated loading conditions), peptide loading is AuNP dependent. Thus, peptide conjugation to IVLN surfaces is AuNP localized, which implies that the IVLN is characterized by patchy peptide distribution. In this way, the IVLN facilitates patterned antigen display in patchy clusters confined to spiky structural elements with defined 5-10 nm spatial intervals. This patterned antigen display is viral-like in nature and cannot be reproduced by traditional nanoparticle systems that employ homogeneous antigen distribution on their surfaces.

The density and capacity of peptide loading on IVLN surfaces was evaluated under three separate formulation conditions: 0%, 10% and 30% Au to Fe final weight loading ratio (wt/wt), which corresponds to 0 AuNPs, 4 AuNPs and 13 AuNPs per IONP-polymer core, respectively (Figure 2.2A). Peptide quantification revealed that, at saturated peptide loading conditions, the 0%, 10% and 30% wt/wt formulations were loaded with 232 ± 73, 888 ± 42 and 1954 ± 157 peptides per IVLN, respectively (Figure 2.2E). When these same values were standardized by total number of AuNPs per IVLN it was determined that maximum peptide loading per AuNP was 227 ± 5 (Figure S2).

The optimal size and surface charge are also critical for viral mimicry[1,28]. Accordingly, we next assessed the IVLN's material properties to determine if the material was suitable for *in-vivo* applications, as well as being appropriately aligned with virally relevant physiochemical properties. Before incubation with peptide, IVLNs prepared at a 30% Au to Fe final weight loading ratio (IVLN-Blank) were shown to have a 55 ± 3 nm particle size, 0.19 ± 0.04 PDI and a -16 ± 4 mV zeta-potential (Figure 2.2G, Table S1). After peptide loading of IVLNs under saturating conditions (IVLN-Peptide), the IVLN-Peptide was shown to have a 60 ± 2 nm particle size, 0.20 ± 0.03 PDI and a -17 ± 1 mV zeta-potential. Significantly, under *in-vivo* relevant serum conditions, IVLN-peptide samples were shown to be stable between 12 and 24 hours (Figure S3). Taken together, IVLN-Peptide was determined to have optimal material properties for *in-vivo* applications.

Inorganic Virus-Like Nanoparticles Enhanced Antigen-Specific Antibody Production in Mice

As previously introduced, viral mimicking nanoparticles have been utilized in a wide-range of *in-vitro* and *in-vivo* applications, but the most significant application of viral-like structure and function is to activate B-cells for antigen-specific antibody production[9,13,17,55,57-59]. Accordingly, based on the established viral-like material properties of IVLNs, we first set out to test if the IVLN can utilized to induced antigen-specific antigen production *in-vivo* against a non-capsid oncogenic human HER2/neu-specific peptide (HER2). For these experiments, IVLNs were prepared at a final Au to Fe weight loading ratio of 30% wt/wt (~14 AuNP per IONP core) with high density peptide conjugation (~2000 peptide per IVLN). To effectively evaluate the significance of viral-like properties for the application of antigen-specific antibody production, we directly compared our IVLN to a traditional nanoparticle system, lipid-coated iron-oxide nanoparticle (IONP-HER2), formulated with an identical number of HER2 peptides per nanoparticle. IONP-HER2 has a 30-nm iron-oxide nanoparticle core and a functionalized DSPE-PEG(2000)-maleimide shell that facilitates facile peptide conjugation (Figure 2.1B). Notably, IONP-HER2 has similar material properties in terms of volume-weighted hydrodynamic particle size (68 ± 5 nm), PDI (0.22 ± 0.02) (Figure 2.2H, Table S2). and maximum peptide number per particle (2323 ± 394 peptides per IONP) as compared to IVLN-HER2 (Figure 2.2F). However, as a traditional nanoparticle system, IONP-HER2 have smooth PEGylated surfaces with homogeneous peptide distribution. Therefore, the side-by-side comparison of IVLN-HER2 and IONP-HER2 would offer valuable insights into the role of viral mimicry for *in-vivo* function.

To begin these studies, BALB/c mice were immunized with IVLN-HER2, IONP-HER2 or soluble HER2 peptide (50 μg peptide, 10 μg cGAMP) at day 0 and boosted twice at 14-day intervals (Figure 2.3A). The dose of HER2 peptide was matched across all treatment groups. Complete serum analysis was performed after two booster immunizations (day 38) because this time point was determined to be most responsive and therefore most relevant (Figure S4). At day 38, 10 days after the second booster immunization, serum was analyzed for total IgM, total IgG, antigen-specific IgG and the antigen-specific IgG isotypes, IgG1 and IgG2a. From this serum analysis, IVLN-HER2 was determined to have a 4-fold higher antigen-specific IgG titer (35840 ± 14022 vs. 9600 ± 9051; $p < 0.01$) a 3-fold higher antigen-specific IgG1 titer (11200 ± 9600 vs. 3840 ± 2427; $p = 0.15$) and a 5-fold higher antigen-specific IgG2a titer (15680 ± 10144 vs. 3200 ± 1960; $p < 0.05$) as compared to IONP-HER2; Moreover, VLN-HER2 yielded a 12-fold

higher antigen-specific IgG titer (35840 ± 14022 vs. 2880 ± 2086; $p < 0.001$), an 8-fold higher antigen-specific IgG1 titer (11200 ± 9600 vs. 1360 ± 1117; $p < 0.05$) and a 14-fold higher antigen-specific IgG2a titer (15680 ± 10144 vs. 1140 ± 1288; $p < 0.01$) as compared to soluble HER2 peptide. Interestingly, this analysis revealed that IVLN-HER2 generated significantly higher HER2 antigen-specific IgG antibody titers (3 to 12-fold) as compared to both IONP-HER2 and soluble HER2 peptide, despite the fact that both IVLN-HER2 and IONP-HER2 were both shown to significantly increase the quantity of total IgG (non-specific) as compared to soluble HER2 peptide treated (IVLN: $p < 0.001$; IONP: $p < 0.001$) and PBS control mice (IVLN: $p < 0.001$; IONP: $p < 0.001$) (Figure 2.3B). No statistically significant difference in total IgM antibody production was observed between any treatment groups (Figure S5, $p = 0.22$). Overall, these data are revealing and significantly suggest that the viral-like properties of IVLNs are beneficial for antigen-specific antibody production.

After establishing the potential of viral-like properties for antigen-specific antibody production, we next asked if these observations were applicable at low dose. Accordingly, to test if a low dose of IVLN-HER2 was also effective for the induction of HER2-specific antibody production, we lowered the dose from 50 μg to 5 μg while maintaining the adjuvant dose and repeated the study above (Figure 2.3C). Despite a 10-times lower dose, IVLN-HER2 enhanced HER2-specific IgG antibody production by 7 to 18-fold in comparison with IONP-HER2. Specifically, IVLN-HER2 generated an 8-fold higher HER2-specific IgG titer (23040 ± 16689 vs. 2880 ± 716; $p < 0.05$) am 18-fold higher HER2-specific IgG1 titer (6400 ± 4525 vs. 350 ± 100; $p = 0.15$) and a 13-fold higher HER2-specific IgG2a titer (12800 ± 9050 vs. 1000 ± 400; $p < 0.05$) as compared to IONP-HER2. Moreover, IVLN-HER2 yielded a 14-fold higher antigen-specific IgG titer (23040 ± 16689 vs. 1200 ± 566; $p < 0.05$), a 7-fold higher antigen-specific IgG1 titer (6400 ± 4525 vs. 450 ± 252; $p < 0.05$) and a 14-fold higher antigen-specific IgG2a titer (12800 ± 9051 vs. 1800 ± 1617; $p < 0.05$) as compared to soluble HER2 peptide. Thus, IVLNs have not only demonstrated to maintain functional efficacy across the range of peptide doses typically employed for antibody production in commercial application, but they have also displayed the dose sparing potential that would be critical to potential therapeutic applications and clinical translations.

Based on an understanding of the requirement of B-cell receptor crosslinking for B-cell activation[33,36,53] and subsequent germinal center formation, we also tested how different antigen density and spatial distributions on IVLN surfaces effected anti-HER2 antibody production. Control over antigen density and spatial distribution was achieved either by attaching variable

quantities of AuNPs per IVLN surface with identical peptide number per AuNP (variable - AuNP #), or by conjugating different peptide amounts to AuNPs on IVLN surfaces with identical numbers of AuNP (variable – peptide #). In this study, BALB/c mice were immunized with HER2 peptide (50 μg HER2 peptide, 10 μg cGAMP) as adjuvant at day 0 and boosted once at day 14. Serum was collected for analysis 10-days following administration.

We first evaluated the role of AuNP number and inter-particle distances on IVLN surfaces on HER2-specific IgG antibodies production using three different Au to Fe final weight loading ratios: 10%, 20% and 30% wt/wt. These IVLNs have AuNP to IONP ratios between 4:1 to 14:1 and distances between AuNPs ranging from ~12 to ~5 nm. The HER2-specific IgG tilters were 10540 ± 5298, 23820 ± 10717 and 64500 ± 30765 for 10%, 20% and 30% wt/wt LLN, respectively (Figure S6). This initial result suggested that minimizing antigen spatial distributions on IVLN surfaces improved antibody production.

Subsequently, we evaluated the effect of antigen density on HER2-specific antigen production for IVLNs with a fixed number of AuNPs per IONP core. For the IVLN with 30% wt/wt ratio (AuNP to IONP ratio is 14:1, distance between AuNP is ~5 nm), low density peptide on IVLN surfaces yielded a mean antigen-specific IgG antibody titer of 16340 ± 6107, while high density peptide on IVLN surface yielded a median titer of 64500 ± 30765 (Figure S6). This trend was also observed in IVLN with 20% wt/wt ratio (AuNP to IONP 9 to 1, distance between AuNPs is ~8 nm), where low peptide density produced median titers of 2100 ± 1067 and high peptide density generated antibody titer of 23820 ± 10717, respectively. However, for IVLN with the 10% wt/wt Au/Fe ratio (AuNP to IONP ratio is 4 to 1, distance between peptide patch is ~12 nm). Peptide density did not correlate with antibody production. Presumably, this is due to a greater than 10 nm distance between AuNPs on IVLN surfaces. These data suggest that higher peptide density (2000 peptides/IVLN) and higher number of AuNPs per IVLN surface (14:1, distance between AuNP less than 10 nm) are the optimal viral-like properties for antigen-specific antibody production, which was used in Figure 2.3.

Inorganic Virus-Like Nanoparticles Enhance HER2-specific Antibody Production with Preventative Efficacy to Inhibit HER2+ Breast Cancer Growth in Mice

Next, we asked whether the antigen-specific antibodies induced by IVLN-HER2 immunization were functionally active as intended. As previously introduced, the peptide of interest in this study is an oncogenic human HER2/neu-specific peptide. Based on previously reported literature, this epitope is contained with the original whole protein immunogen used to produce pertuzumab (Perjeta®)[54]. Pertuzumab has known anti-cancer efficacy against HER2+ breast cancer, and thus is an ideal model for the functional evaluation of antibodies produced by IVLN-HER2[60,61]. Therefore, we employed IVLN-HER2 as a vaccine to test if the induced HER2-specific antibodies had *in-vivo* prophylactic efficacy to inhibit tumor growth using breast cancer xenograft model using a murine breast cancer cells (D2F2/E2) with high HER2 expression The D2F2/E2 cell line is a BALB/c derived murine breast cancer cell line with a human HER2/neu transfection and cell surface expression[40].

The prophylactic tumor inhibition study was initiated by subcutaneous flank inoculation with $2.5x10^5$ cells per mouse at day 49 following a primary immunization plus three additional booster administrations at 14-day intervals (Figure 2.4A). The results of this prophylactic anti-tumor study revealed that, as compared to the PBS control, IVLN-HER2 displayed a marked statistically significant reduction in tumor volume over 6-weeks at a dose of 50 μg (125 ± 239 mm^2 vs. 1843 ± 661 mm^2, $p < 0.001$) (Figure 2.4B) and 5 μg (583 ± 392 mm^2 vs. 1843 ± 661 mm^2, $p < 0.001$) (Figure 2.4C). In addition, the prophylactic anti-cancer efficacy appears to be directly correlated not only to the specificity of these endogenous antibodies to the D2F2/E2 cell line (Figure S7), but also to the titer of antigen-specific antibody. These results highlight the therapeutic potential of and provides functional validation for endogenous HER2-specific antibodies induced by IVLN-HER2 administration.

Inorganic Virus-Like Nanoparticles Promote Lymph Node Homing and Viral-Like Distribution and Uptake by Immune Cells in Lymph Nodes.

Upon validating that IVLNs can be utilized to facilitate enhanced antigen-specific antibody production as to compared traditional nanoparticle systems and soluble peptides, we next set out to test if our IVLNs have viral-like functions as compared to traditional nanoparticles (Figure 2.5). In order to test if IVLNs has viral mimicking functionality, we first evaluated its propensity for lymph node homing in terms of delivery extent and retention[62,63]. Second, within the lymph node, we need to determine if IVLNs can be specifically targeted to B-cell zones since the lymph nodes are primary sites for B-cell activation and the formation of germinal centers that are ultimately responsible for initiating antigen-specific IgG antibody production[64-66]. Third, we also tested if IVLNs had viral-like cellular distribution patterns within lymph nodes. As sites with dense populations of antigen-presenting cells and lymphocytes, the lymph nodes are known to be critically important in viral sequestration and directed immune activation[39,67]. This functionality is the result of unique physiological features that have been developed for viral recognition and viral-specific immune activation. For example, subcapsular sinus macrophages are a highly specialized phenotype of macrophage that is responsible for viral uptake and direct presentation to B-cells to promote directed viral clearance via antigen-specific antibody production[39,68].

Lymph node homing was quantified for IVLN-HER2, IONP-HER2 and soluble HER2 peptide following administration by subcutaneous hock immunization, which was determined to be the most efficient delivery pathway[69] (Figure S8). IVLN-HER2 and IONP-HER2 delivery kinetics to the lymph nodes (popliteal and inguinal) was determined using ICP-MS quantification of Fe in excised lymph nodes based on previously reported techniques with minor modifications[42,48]. It was determined that while the t_{max} of both IVLN-HER2 and IONP-HER2 was 3 hours post-administration, the percent of initial nanoparticle dose delivered was 5.1 ± 1.6% and 1.9 ± 0.8% ($p < 0.05$) for IVLN-HER2 and IONP-HER2, respectively (Figure 2.6A). Over 48 hours, IVLN-HER2 was shown to have a 3.5-fold higher ($p < 0.05$) in overall exposure compared to IONP-HER2 based on area under the curve (AUC) measurements. Moreover, the retention of nanoparticles within the lymph node over 48 hours was higher for IVLN-HER2 (68 ± 11%) as compared to IONP-HER2 (43 ± 18%) ($p = 0.12$). In addition to the direct quantification of nanoparticle delivery by ICP-MS, fluorescently labeled peptides were also used to monitor the

lymph node delivery for IVLN-HER2, IONP-HER2 and soluble HER2 peptides at 3 hours using IVIS imaging of excised popliteal and inguinal lymph nodes (Figure 2.6B). IVIS imaging revealed that IVLN-HER2 led to a 4.3-fold improvement in lymph node homing as compared to both the IONP-HER2 and soluble HER2 peptide ($p < 0.001$; $p < 0.001$), where IONP-HER2 and HER2 have no statistically significant difference in delivery ($p > 0.99$).

Subsequently, we tested if IVLN-HER2 had viral-like distributions within the lymph node, especially in subcapsular sinus macrophage and B-cell populations, as compared to IONP-HER2[65,66,68]. To answer this question, fluorescently labeled IVLN-HER2 were injected by subcutaneous hock immunization and flow cytometry was applied 3 hours post-administration to identify IVLN-HER2 or IONP-HER2 positive cells of different phenotypes. More specifically subcapsular sinus macrophages where identified as CD11b+CD169^{high} double-positive and B-cells were identified as B220+[68,70]. This analysis revealed that after 3-hours and relative to the IONP-HER2, IVLN-HER2 improved subcapsular sinus macrophage uptake by 1.7-fold (86.7 ± 2.4% vs. 52.2 ± 2.8%, $p < 0.001$) and B-cell uptake by 3.4-fold (63.9 ± 1.1% vs. 19.7 ± 2.2%, $p < 0.001$) (Figure 2.6C).

Cellular uptake of IVLN-HER2 and IONP-HER2 was confirmed *in-vitro* in RAW 264.7 macrophages and primary B-cells isolated from murine spleens. Compared to the IONP-HER2 control group, IVLN-HER2 improved cellular uptake by 3-fold in macrophages (30.3 ± 1.1 pg Fe/cell vs. 11.8 ± 1.3 pg Fe/cell, $p < 0.001$) and 2-fold in B-cells (2.0 ± 0.4 pg Fe/cell vs. 0.8 ± 0.4 pg Fe/cell, $p < 0.01$) (Figure 2.6D). The mechanism for IVLN uptake was further evaluated *in-vitro* by comparison of cellular uptake with increasing AuNP number and density of IVLN surfaces. Notably, without peptide loading and as directly compared to the blank IONP core without AuNP association, IVLN improved cellular uptake by 6-fold in macrophages (30.3 ± 1.1 pg Fe/cell vs. 4.7 ± 0.9 pg Fe/cell, $p < 0.001$), and 4-fold in primary B-cells (2.0 ± 0.4 pg Fe/cell vs. 0.5 ± 0.2 pg Fe/cell, $p < 0.001$) (Figure S9). Notably, the viral-like spiky structures and rough surface topography provided by AuNP complexation to IVLN surfaces led to increased cellular uptake with increasing number of AuNP loading on IVLN surfaces and matched an exponential function for both cell types (RAW264.7, $R^2 = 0.902$; B-cells, $R^2 = 0.918$) (Figure S9).

Inorganic Virus-Like Nanoparticles Increase Germinal Center Formation and Immune Cell Activation in the Lymph Node

To further mechanistically evaluate the inductive capacity of IVLNs for antigen-specific antibody production, we next examined both the extent of germinal center formation and activation of antigen-specific B-cells *in-vivo*. Firstly, the extent of germinal center formation was evaluated 10 days after the primary immunization of BALB/c mice with IVLN-HER2, IONP-HER2 and soluble HER2 peptide at a dose of 50 μg. Germinal centers were identified as class-switched B-cells ($B220^{+}IgD_{low}$) that are double-positive for CD95 and GL-7 markers[71,72] (Figure 2.7A). Quantification of by flow cytometry revealed that immunization with IVLN-HER2 resulted in a 2.6-fold and an 8-fold increase in the proportion of germinal center type B-cells ($B220^{+}IgD_{low}CD95^{+}GL7^{+}$) as compared to IONP-HER2 (18.1 ± 2.4% vs. 7.0 ± 2.1%, $p < 0.001$) and soluble HER2 peptide (18.1 ± 2.4% vs. 2.2 ± 0.9%, $p < 0.001$), respectively (Figure 2.7B). Additionally, IONP-HER2 administration yielded an approximately 3-fold increase in germinal centers as compared to soluble HER2 peptide (7.0 ± 2.1% vs. 2.2 ± 0.9%, $p < 0.05$). These results correlate nicely to the observed increase of antigen-specific IgG antibodies described previously.

Secondly, the proliferation of antigen-specific B-cells was measured utilizing fluorescently-labeled streptavidin HER2 peptide tetramer staining based on previously reported protocols[49] (Figure 2.7C). Antigen-specific B-cells were identified as viable lymph node cells that were double positive for CD19 and the HER2 peptide tetramer. The results of this analysis demonstrate that IVLN-HER2 treatment produced an approximately 6-fold proliferation in the p antigen-specific B-cell population as compared to both IONP-HER2 (3.0 ± 2.0 % vs. 0.5 ± 0.2%, $p < 0.05$) and soluble HER2 peptide (3.0 ± 2.0 % vs. 0.5 ± 0.1%, $p < 0.05$) (Figure 2.7D). No statistical differences in the antigen-specific B-cell population were detected for IONP-HER2 vs. soluble HER2 peptide ($p = 0.72$). Taken together, these data suggest that the viral mimicking features of IVLN-HER2 have the unique ability to activate antigen-specific B cells, which is associated with increased antigen-specific antibody production.

2.5 Discussion:

Viral-like characteristics are ideal material properties for the rational design and engineering of nanomaterials critical to the advancement of nanotechnology for immunomodulatory applications[1,26,28]. These nanomaterials have robust potential to stimulate both humoral and cellular immunity. As such, nanoparticles with viral-like structural and function could be used for the induction of antigen-specific immunity leading to the production of high quantity and affinity antibodies. These antibodies could be deployed in as invaluable research tools or as therapeutic agents in the treatment of infection disease and cancer.

To date, only 4-5 different virus-like particles (VLPs) are FDA-approved and clinically available, all of which are designed to prevent viral infection based on viral capsid composition[73]. For example, prophylactic VLP vaccines for HPV (such as Gardasil®) have been generated using the self-assembly of HPV L1 capsid proteins to provide durable long-term efficacy against HPV infection[74]. Indeed, these VLP-based vaccines are more effective than monomer capsid proteins alone for the activation of B cell-mediated humoral immunity and production of neutralizing antibodies as a result of multivalent interactions with B cell receptors[14,53,75,76]. However, these VLP-based vaccines are ineffective in the treatment of established HPV tumors because the HPV VLP only contains capsid proteins, not the oncogenic E6/E7 antigens that are responsible for HPV associated cancer[14,77,78]. Most recently, a VLP with HER2 peptides was generated using acinetobacter phage coat protein AP205, which showed excellent efficacy against HER2+ breast cancer in animal model[79]. Despite the success of this application however, traditionally it is extremely challenging to generate VLP using oncogenic proteins since the oncogenic proteins do not have necessary properties to facilitate VLP-self-assembly VLP[80,81]. The simplest solution to this problem is to chemical conjugate oncogenic proteins and peptides to VLP surfaces. However, the strong B-cell response and antibody production against the capsid proteins of VLP itself yields a high-level non-specific (anti-carrier) immunological response with regard to the intended application of the nanomaterial to generate an immunological response for the specific cargo of interest (i.e. HER2 peptide)[24,25].

Although many alternative nanoparticle technologies claiming viral influence have been developed for antigen delivery and immunomodulation, these more traditional nanoparticle systems are not truly effective viral mimics and are therefore potentially limited in application scope. Here, we report the development of true inorganic virus-like nanoparticle (IVLN), which employs a more holistic approach to viral mimicry material design. This IVLN not only mimics

viral-like structure and material properties[1,27,33,37,38,53] (spiky and rough surface topography, variable antigen density, patterned antigen distribution and sub-100 nm particle size), but also demonstrates viral-like functional capabilities[39,62,65,67] (lymph node homing and cellular distributions, immune cell activation and antigen-specific antibody production). IVLNs are composed of a hybrid Au@Fe core-satellite type nanoparticle, which utilizes a 16-nm polysiloxane and polyethylene glycol containing diblock polymer coated iron-oxide nanoparticle core (IONP) with 2.5-nm gold nanoparticle satellites (AuNP). IVLNs can be produced with variable surface topography, antigen density and antigen spatial resolution. Moreover, the IVLN has optimal particle size, shape and surface charge for efficient lymph node delivery and retention. Further, these IVLNs can be easily manufactured with large scale for future applications.

To evaluate the viral-like functions of our IVLN, we purposely utilized, as antigen, a HER2 peptide containing both B-cell and CD4 T-cell epitopes such that we could evaluate the IVLN for B-cell activation and antigen-specific antibody production in mice[54-56]. In this study, we compared IVLNs to a traditional nanoparticle system, lipid-coated iron-oxide nanoparticles (IONP-HER2) with the same antigen at identical peptide loading per nanoparticle. By conventional thought, lipid-coated iron-oxide nanoparticles would be considered a viral-mimicking nanoparticle technology based on its' particle size and antigen density. However, we demonstrate our IVLN-HER2 is uniquely different from IONP-HER2 in both structure and function.

Our results showed that the IVLN-HER2 is truly significant for B-cell activation and antigen-specific antibody production. Specifically, by manipulating the spatial distribution of AuNPs on IVLN surfaces and the peptide density confined to those AuNPs, antigen-specific IgG antibody titers were increased by 3 to 18-fold as compared to IONP-HER2. Significantly, as compared to IONP-HER2 at high dose, IVLN-HER2 was determined to have 4-fold, 3-fold and 5-fold higher antigen-specific IgG, IgG1 and IgG2a titers, respectively; at low dose, IVLN-HER2 was shown to improve antigen-specific IgG, IgG1 and IgG2a titers 8-fold, 18-fold and 15-fold, respectively. Since both IVLN-HER2 and IONP-HER2 have highly comparable hydrodynamic particle size, surface charge, core shape and peptide loading per unit nanoparticle, any quantifiable differences in antibody production by these two structures could be attributed to increasingly viral-like structure and function. Mechanistically, IVLN-HER2 immunization led to enhanced antigen-specific antibody production as a result of greater homing capacity to the lymph nodes, unique viral-like distribution in lymph nodes and higher intracellular uptake, which

together promoted a significant increase in overall antigen-specific B-cell proliferation and germinal center formation. Finally, IVLN-HER2 induced HER2/neu-specific antibody production in mice, which were functional in the prophylactic inhibition of HER2+ breast cancer growth, as intended based on the known HER2+ anti-tumor efficacy of pertuzumab[60,61]. It is noteworthy, that while IVLN-HER2 may have the potential to serve as a B-cell based cancer vaccine for HER2+ breast cancer in the future, this was not the main emphasis of this current work. Current evidence suggests that research in this direction is warranted, but no major conclusions can be surmised at this time.

In summation, we generated an inorganic virus-like nanoparticle (IVLN) platform using a holistic philosophy for viral mimicking material design and engineering. The IVLN has unique viral-like spiky topographical structures, spherical geometry, optimal size and negatively charged surfaces. The high-density antigen display and organization on IVLN surfaces is controlled by the surface density of and peptide binding specificity to AuNPs, which facilitate the patchy patterned distribution of antigen at 5-10 nm spatial intervals optimal for B-cell activation. In addition to these viral-like structural elements, the IVLN also exhibits viral mimicking functionality in terms of lymph node homing, lymph node cellular distributions, immune cell activation and enhanced functionally active antigen-specific antibody production. These data suggest that our unique IVLN technology, which redefines conventional knowledge of viral mimicking nanoparticle design, may have broad applications for efficient delivery and efficacious immunomodulation *in-vivo*.

2.6 Acknowledgements:

The authors would like to thank Dr. Wei-Zen Wei of Wayne State University for the generous donation of the D2F2/E2 cell line.

2.7 Authorships:

Ryan M. Clauson[†], Hongwei Chen[*,†], Brett Hill[‡], Syed Monem Rizvi[‡], Kai Sun[¥], Fei Wen[‡] and Duxin Sun[*,†]

[†]Department of Pharmaceutical Sciences, College of Pharmacy;
University of Michigan, Ann Arbor, Michigan 48109, United States

[‡] Department of Chemical Engineering, College of Engineering;
University of Michigan, Ann Arbor, Michigan 48109, United States

[¥] Michigan Center for Materials Characterization;
University of Michigan, Ann Arbor, Michigan 48109, United States

2.8 Figures:

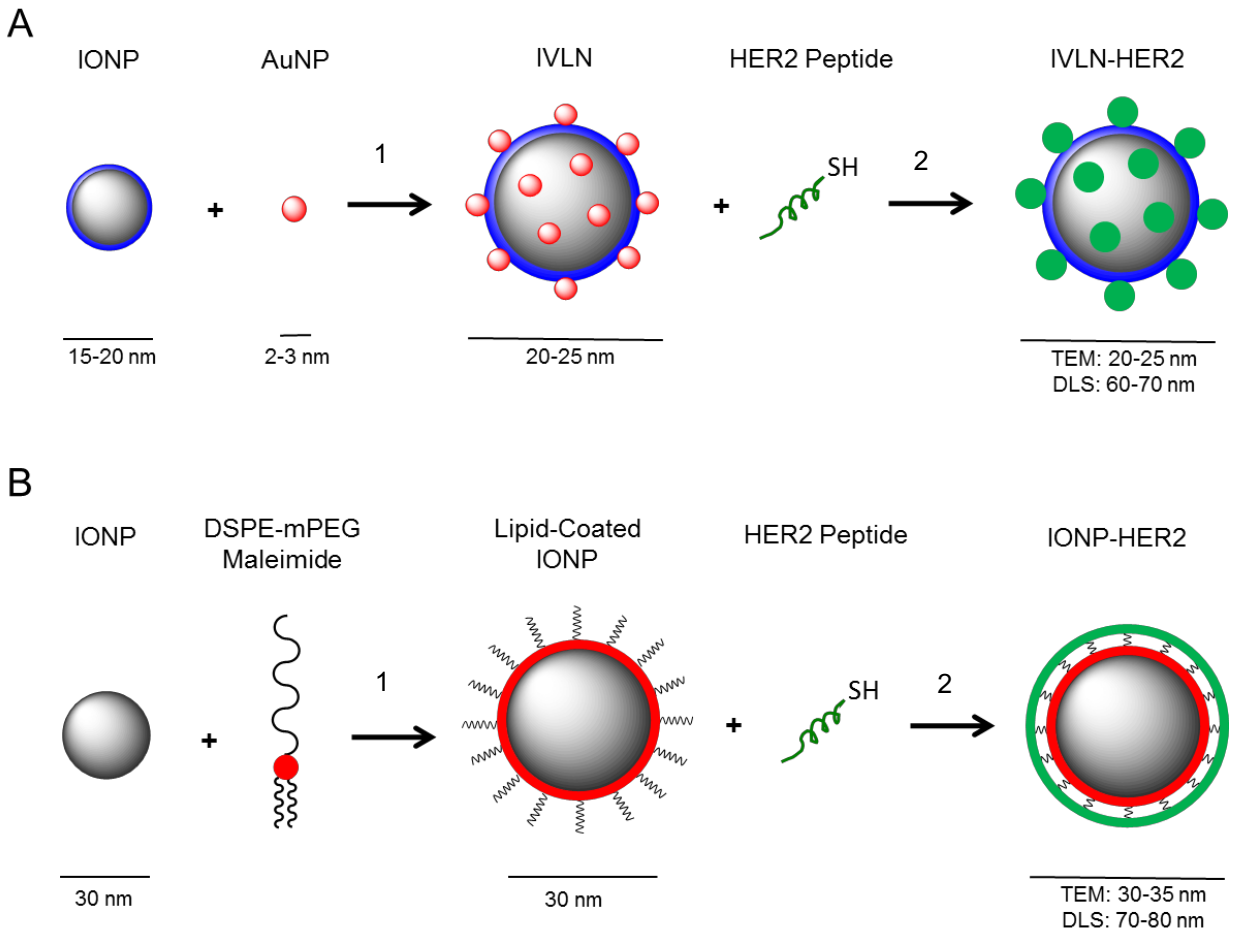

Figure 2.1. Nanoparticle Formulation and Viral-Like Structure Schematic. (A) Schematic representation of the step-wise production of peptide functionalized inorganic virus-like nanoparticles (IVLN-HER2) by the (1) self-assembly of AuNPs to polymer-coated IONP surfaces via the gold-siloxane interaction (IVLN) followed by the (2) conjugation of terminal cysteine-modified HER2 peptide to IVLN via gold-thiol bonding. (B) Schematic representation of step-wise formulation of peptide functionalized lipid-coated iron-oxide nanoparticles (IONP-HER2) by the (1) coating of iron-oxide nanoparticles with maleimide activated DSPE-mPEG phospholipids followed by the (2) conjugation of terminal cysteine-modified HER2 peptide to IONP via non-reducing thiol-directed chemistry.

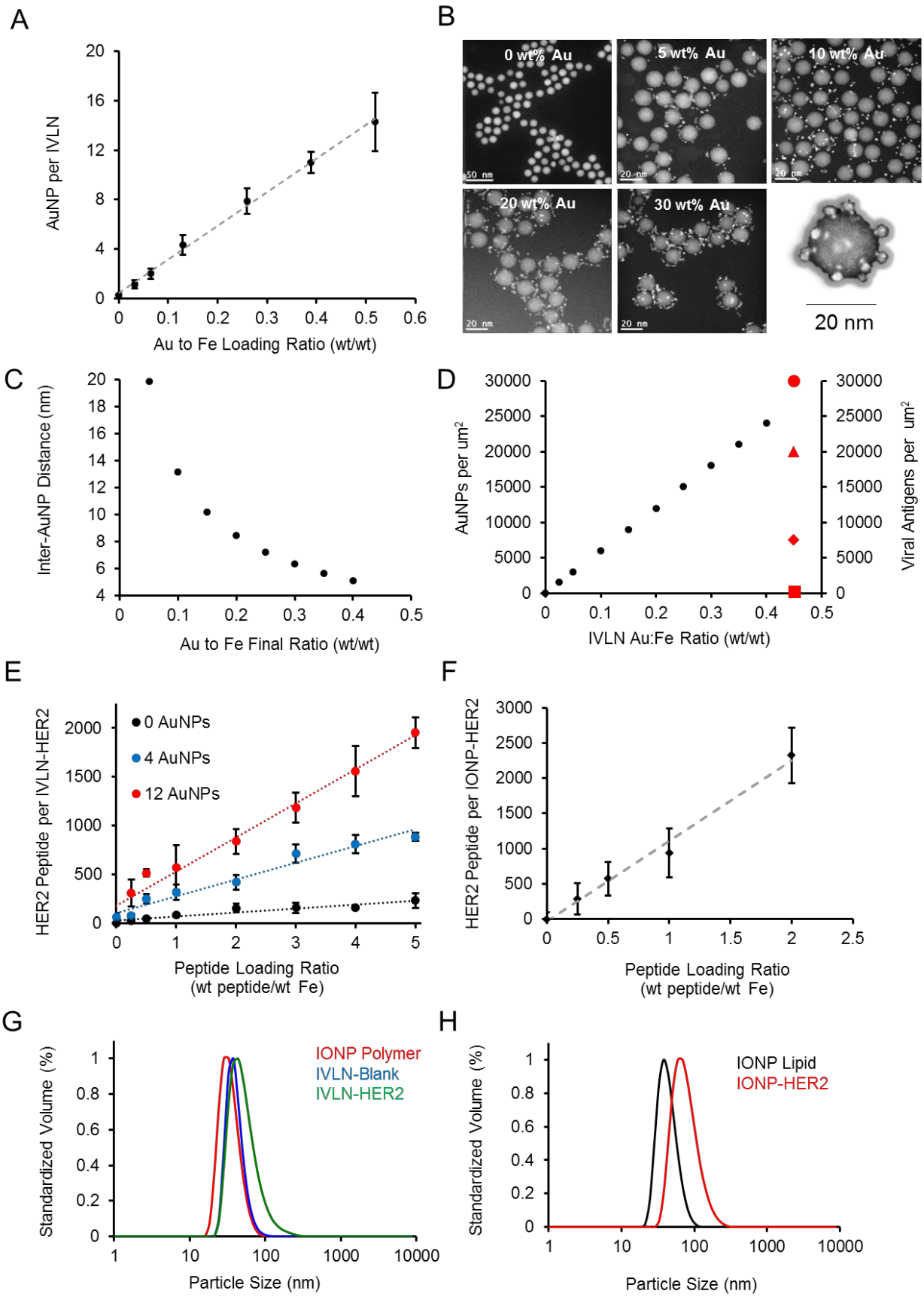
A
AuNP per IVLN
Au to Fe Loading Ratio (wt/wt)
B
0 wt% Au
5 wt% Au
10 wt% Au
20 wt% Au
30 wt% Au
20 nm
C
Inter-AuNP Distance (nm)
Au to Fe Final Ratio (wt/wt)
D
AuNPs per um2
Viral Antigens per um2
IVLN Au:Fe Ratio (wt/wt)
E
HER2 Peptide per IVLN-HER2
0 AuNPs
4 AuNPs
12 AuNPs
Peptide Loading Ratio
(wt peptide/wt Fe)
F
HER2 Peptide per IONP-HER2
Peptide Loading Ratio
(wt peptide/wt Fe)
G
Standardized Volume (%)
IONP Polymer
IVLN-Blank
IVLN-HER2
Particle Size (nm)
H
Standardized Volume (%)
IONP Lipid
IONP-HER2
Particle Size (nm)

Figure 2.2. Inorganic Virus-Like Nanoparticle (IVLN) Formulation and Viral Mimicry. (A) Quantitative analysis of ultra-small gold nanoparticle (AuNP) loading per polymer-coated iron-oxide nanoparticles core (IONP-polymer) by inductively coupled plasma mass spectrometry (ICP-MS); data represent mean ± SD, n ≥ 6; curve is fit using linear regression model, R^2 = 0.998, $p < 0.001$. (B) Representative transmission electron microscopy (TEM) images of IVLN formulations at increasing gold (Au) to iron (Fe) final weight loading ratios from 0-30% wt/wt; scale-bar: 0% wt condition (50 nm); scale-bar: 5-30% wt conditions (20 nm). (B-insert) High resolution TEM image of single nanoparticle from 30% wt condition with background subtraction image processing. (C) Mathematical modeling of theoretical distances between AuNPs on IVLN surfaces. (D) Mathematical modeling of theoretical density (nanoparticles per unit area) of AuNPs on IVLN surfaces and as compared to the known antigen density on viral capsids (symbol legend: square = HIV; diamond = rotavirus; triangle = hepatitis B virus; circle = human papillomavirus). (E) Quantification of peptide loading capacity and mechanism on IVLNs with variable AuNP surface loading (0 AuNPs – black; 4 AuNPs – blue; 12 AuNPs – red) determined by a modified fluorescamine fluorescent detection assay; data represent mean ± SD, n = 3; curve is fit using linear regression model, (0 AuNPs: R^2 = 0.904, $p < 0.01$; 4 AuNPs: R^2 = 0.962, $p < 0.01$; 12 AuNPs: R^2 = 0.977, $p < 0.001$). (F) Quantification of peptide loading capacity on lipid-coated iron-oxide nanoparticles (IONP-HER2); data represent mean ± SD, n = 3; curve is fit using linear regression model (R^2 = 0.989, $p < 0.001$). (G) Representative volume-weighted particle size distributions for IONP-polymer core (red), IVLN-blank (blue) and IVLN-HER2 (green) by dynamic light scattering (DLS). (H) Representative volume-weighted particle size distributions for blank lipid-coated iron-oxide nanoparticles (IONP Lipid, black) and peptide coated IONP Lipid (IONP-HER2, red). SD, standard deviation; DLS, dynamic light scattering.

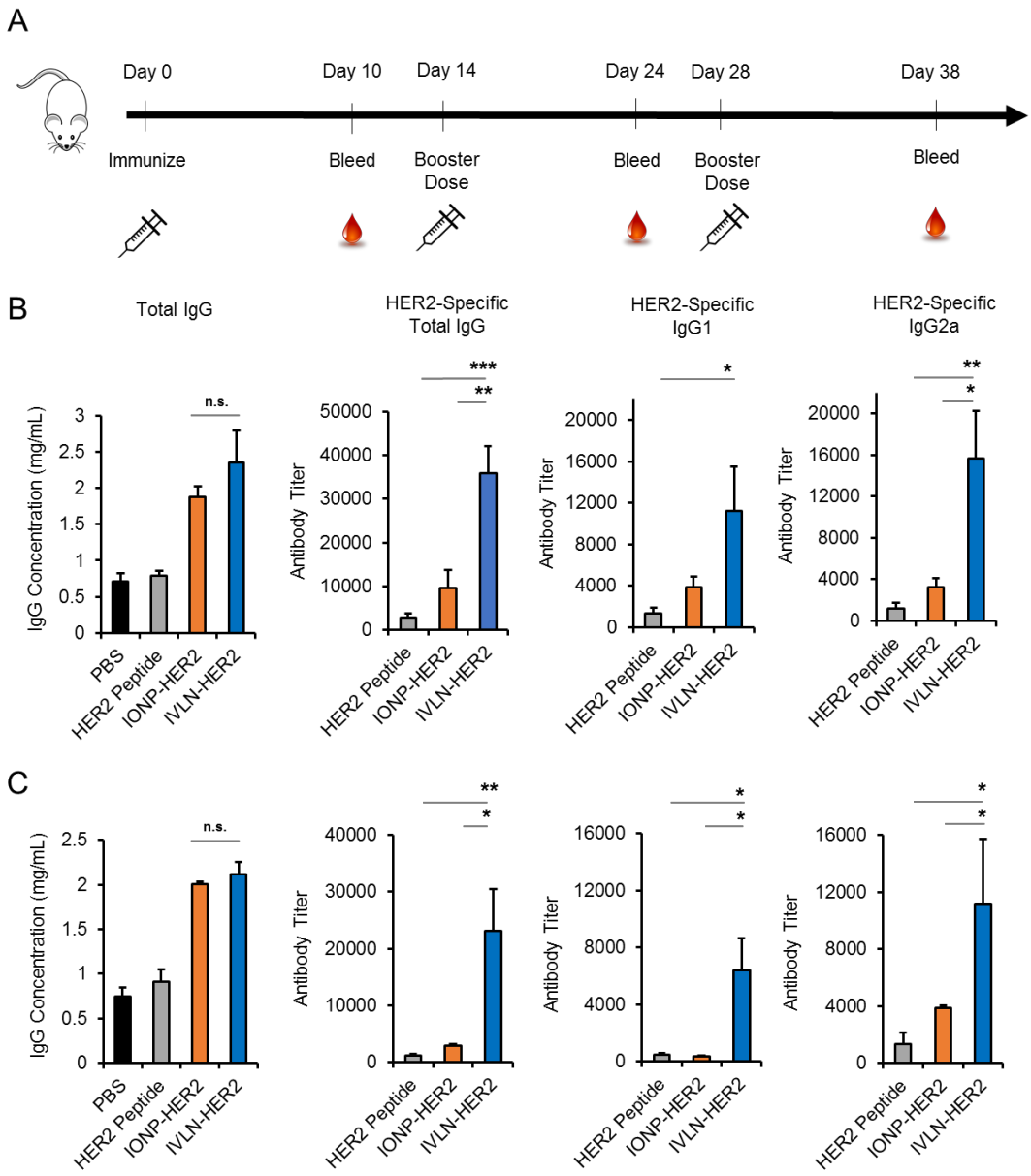

Figure 2.3. Inorganic Virus-Like Nanoparticle (IVLN) Enhanced Antigen-Specific Antibody Production in Mice. (A) Animal study immunization and analytical sampling timeline. (B) Quantification of non-specific total IgG and antigen-specific antibody titers (IgG, IgG1 and IgG2a) from the serum of BALB/c mice at day 38 and at 50 μg HER2 peptide + 10 μg cGAMP as adjuvant; data represent mean ± SE, n = 5. (C) Quantification of non-specific total IgG and antigen-specific antibody titers (IgG, IgG1 and IgG2a) from the serum of BALB/c mice at day 38 and at 5 μg HER2 peptide + 10 μg cGAMP as adjuvant; data represent mean ± SE, n = 5. Statistical comparisons are based on one-way ANOVA, followed by post hoc Tukey's pairwise comparisons. The asterisks denote statistical significance at the level of * $p < 0.05$, ** $p < 0.01$, *** $p < 0.001$. ANOVA, analysis of variance; SE, standard error; n.s., no statistical significance.

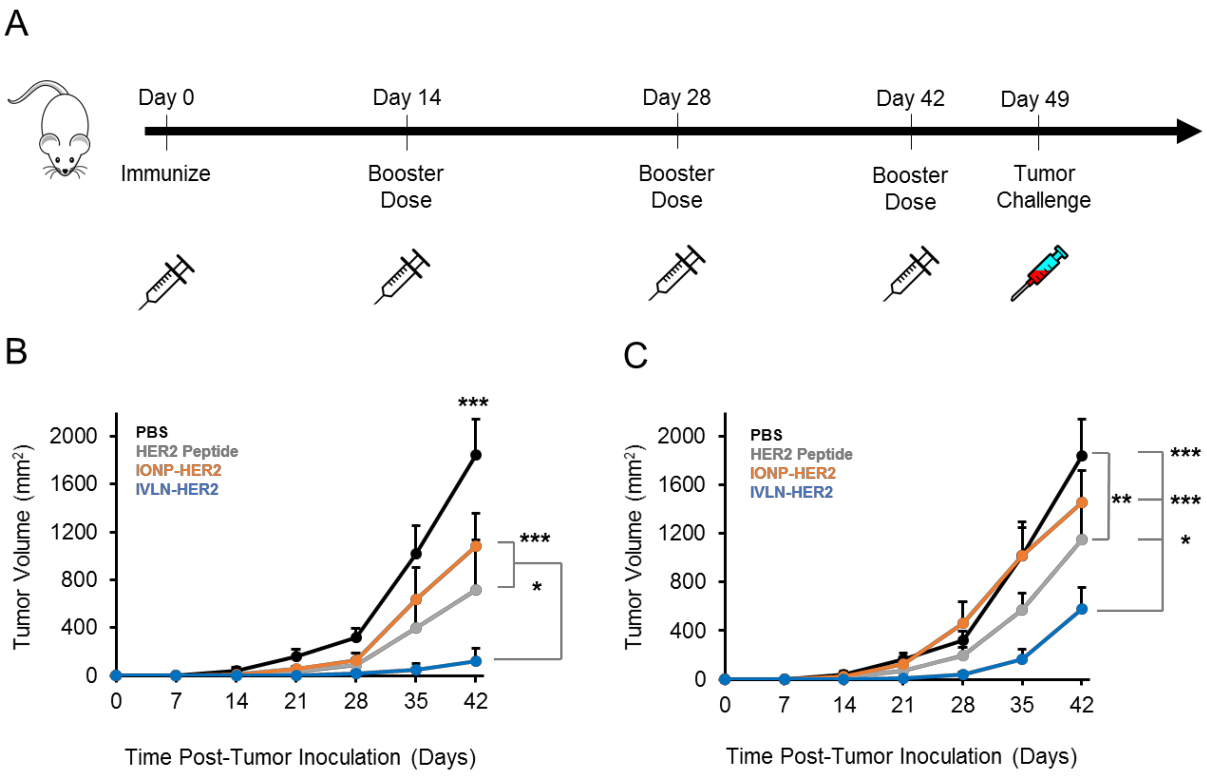

Figure 2.4. Prophylactic HER2+ Breast Cancer Anti-Tumor Efficacy. (A) Animal study immunization and HER2+ breast cancer (D2F2/E2) tumor inoculation timeline. (B) Tumor volume growth curves for D2F2/E2 tumors subcutaneously implanted into the flank of BALB/c mice at 250,000 cells per mouse treated with 50 μg HER2 peptide dose + 10 μg cGAMP and (C) 5 μg HER2 peptide dose + 10 μg cGAMP; data represent mean ± SE, n = 5. Statistical comparisons are based on one-way ANOVA, followed by post hoc Tukey's pairwise comparisons. The asterisks denote statistical significance at the level of * $p < 0.05$, ** $p < 0.01$, *** $p < 0.001$. ANOVA, analysis of variance; SE, standard error.

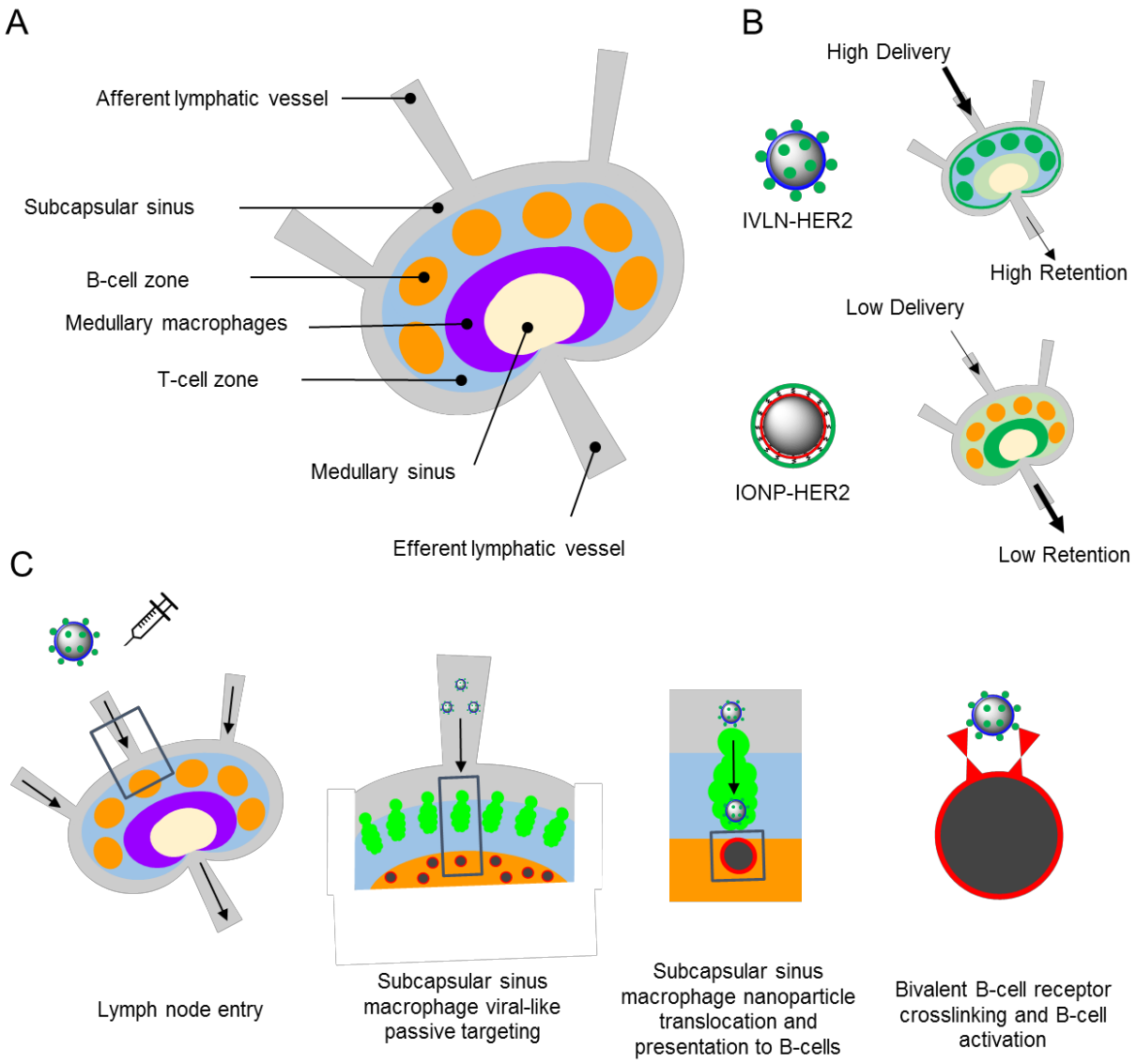

Figure 2.5. Lymph Node Distribution and Viral-Like Function Schematic. (A) Schematic representation of lymph node architecture and physiological features. (B) Schematic representation of the viral-like function of lymph node homing. IVLN-HER2 displays highly efficient delivery to and retention within the lymph node by viral-like passive targeting to subcapsular sinus macrophages and B-cells. IONP-HER2 displays less efficient delivery to and poor retention within the lymph node by failing to achieve viral-like passive targeting to subcapsular sinus macrophages and B-cells. (C) IVLN-HER2 nanoparticle step-wise journey to the lymph node through afferent vesicles, viral-like interactions with subcapsular sinus macrophages, translocation across the subcapsular sinus and direct presentation to B-cells with bivalent B-cell receptor crosslinking in the lymph node follicle.

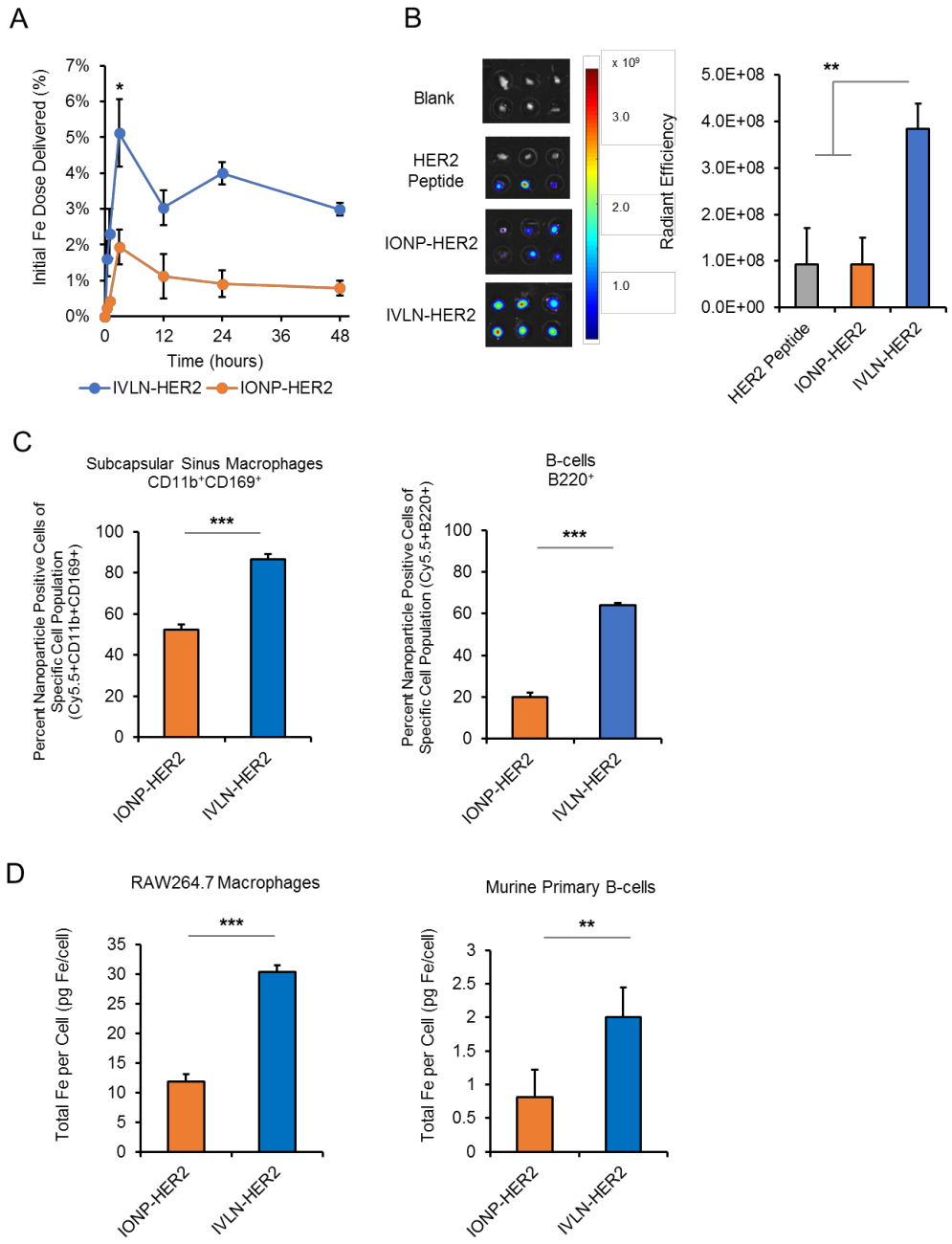

Figure 2.6. Viral-like Functionality Assessment: Lymph Node Homing, Distribution and Immune Cell Uptake. (A) Quantification of nanoparticle delivery to lymph nodes (popliteal + inguinal) ipsilateral to the administration site at designated time intervals represented as the percentage of initial iron-oxide delivered using ICP-MS; data represent mean ± SE, n = 3. (B) Representative ex-vivo IVIS fluorescence images and semi-quantitative analysis (popliteal (top) + inguinal (bottom)) of peptide delivery to lymph nodes acquired 3 hours after administration of Cy5.5-labeled soluble HER2 peptide, IONP-HER2-Cy5.5 and IVLN-HER2-Cy5.5 (Ex/Em = 675/720 nm, exposure = 0.5 s). The color bar represents mean radiant efficiency

(p/s/cm2/sr)/(μW/cm2); data represent mean ± SD, n = 3. (C) Quantification of in-vivo nanoparticle distribution to specific immune cell populations in the lymph nodes as identified by flow cytometry (Cy5.5-labeled nanoparticles); Subcapsular sinus macrophages are identified as CD11b+CD169^{high}; B-cells are identified as B220+; data represent mean ± SD, n = 3. (D) Quantification of in-vitro cell uptake of nanoparticles in RAW264.7 macrophages and murine primary B-cells by ICP-MS quantification of total Fe standardized by cell count (pg Fe per cell); data represent mean ± SD, n = 3. Statistical comparisons are based on one-way ANOVA, followed by post hoc Tukey's pairwise comparisons or by Student's unpaired T-test. The asterisks denote statistical significance at the level of ** $p < 0.01$, *** $p < 0.001$. ANOVA, analysis of variance; SD, standard deviation; SE, standard error.

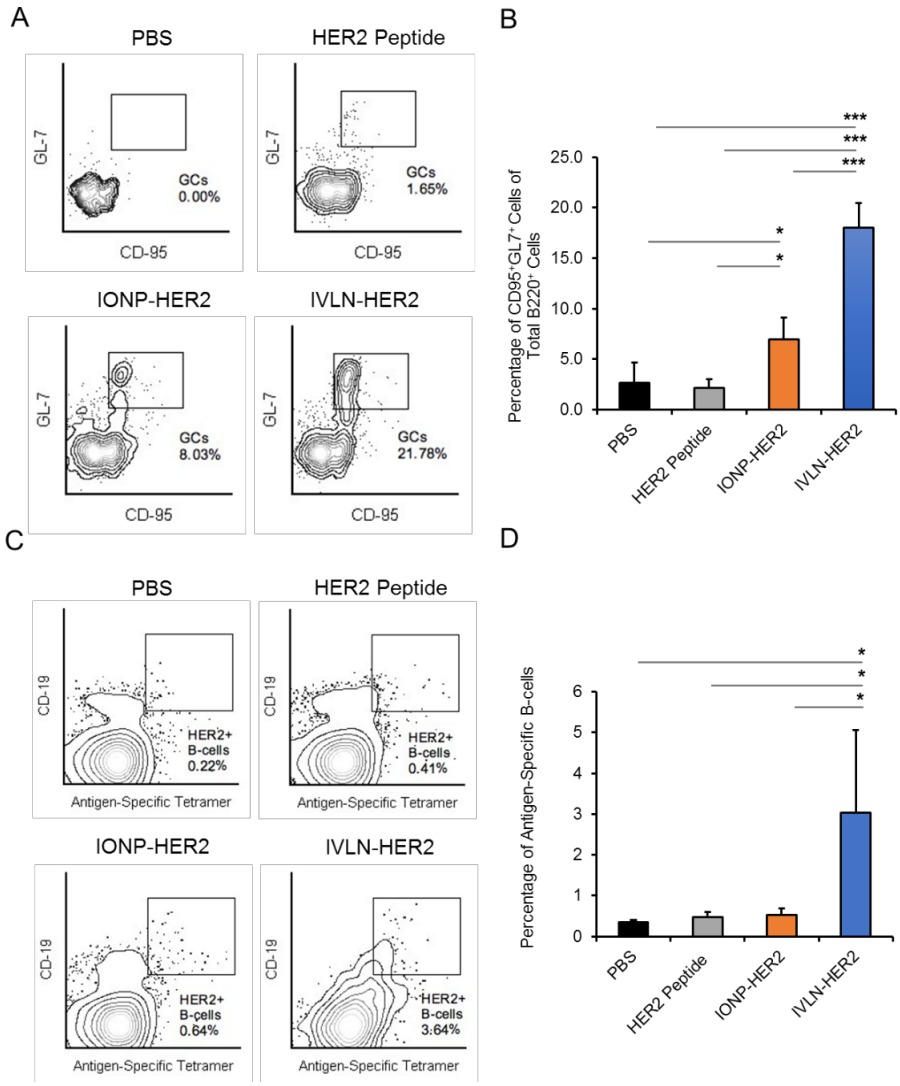

Figure 2.7. In-vivo Germinal Center Formation and Antigen-Specific B-cells. (A) Representative FACS plots for the gating strategy of germinal center cells. Germinal center cells were identified as the $B220^{+}IgD_{low}$ population that was double-positive for mature germinal center cell marker CD95 and GL-7. (B) Quantification of percentage of germinal center type cells of the total B220+ B-cell population induced 10 days after the primary immunization at 50 µg HER2 peptide dose + 10 µg cGAMP as adjuvant; data represent mean ± SE, n ≥ 3. (C) Representative FACS plots for the gating strategy of HER2-specific B-cells using B-cell receptor tetramer staining, identified as the CD19+Tetramer+ population. (D) Quantification of the percentage of HER2-specific B-cells of total viable cells induced 10 days after the primary immunization at 50 µg HER2 peptide dose + 10 µg cGAMP as adjuvant; data represent mean ± SE, n ≥ 3. Statistical comparisons are based on one-way ANOVA, followed by post hoc Tukey's pairwise comparisons. The asterisks denote statistical significance at the level of * $p < 0.05$, *** $p < 0.001$. ANOVA, analysis of variance; SE, standard error.

2.9 Supporting Information

The supporting information, figures and tables from Chapter 2 are available in Appendix A.

2.10 Bibliography

1 Bachmann, M. F. & Jennings, G. T. Vaccine delivery: a matter of size, geometry, kinetics and molecular patterns. *Nat Rev Immunol* 10, 787-796, doi:10.1038/nri2868 (2010).

2 Jennings, G. T. & Bachmann, M. F. Designing recombinant vaccines with viral properties: a rational approach to more effective vaccines. *Curr Mol Med* 7, 143-155 (2007).

3 Minor, P. D. Live attenuated vaccines: Historical successes and current challenges. *Virology* 479-480, 379-392, doi:10.1016/j.virol.2015.03.032 (2015).

4 VanBlargan, L. A., Goo, L. & Pierson, T. C. Deconstructing the Antiviral Neutralizing-Antibody Response: Implications for Vaccine Development and Immunity. *Microbiol Mol Biol Rev* 80, 989-1010, doi:10.1128/MMBR.00024-15 (2016).

5 Nayerossadat, N., Maedeh, T. & Ali, P. A. Viral and nonviral delivery systems for gene delivery. *Adv Biomed Res* 1, 27, doi:10.4103/2277-9175.98152 (2012).

6 Thomas, C. E., Ehrhardt, A. & Kay, M. A. Progress and problems with the use of viral vectors for gene therapy. *Nat Rev Genet* 4, 346-358, doi:10.1038/nrg1066 (2003).

7 Kumru, O. S. *et al.* Vaccine instability in the cold chain: mechanisms, analysis and formulation strategies. *Biologicals* 42, 237-259, doi:10.1016/j.biologicals.2014.05.007 (2014).

8 Kling, S. Viral Vaccination and Allergy. *Curr Allergy Clin Im* 22, 173-177 (2009).

9 Plummer, E. M. & Manchester, M. Viral nanoparticles and virus-like particles: platforms for contemporary vaccine design. *Wiley Interdiscip Rev Nanomed Nanobiotechnol* 3, 174-196, doi:10.1002/wnan.119 (2011).

10 Pokorski, J. K. & Steinmetz, N. F. The art of engineering viral nanoparticles. *Mol Pharm* 8, 29-43, doi:10.1021/mp100225y (2011).

11 Zeltins, A. Construction and characterization of virus-like particles: a review. *Mol Biotechnol* 53, 92-107, doi:10.1007/s12033-012-9598-4 (2013).

12 Roy, P. & Noad, R. Virus-like particles as a vaccine delivery system: myths and facts. *Hum Vaccin* 4, 5-12 (2008).

13 Masavuli, M. G., Wijesundara, D. K., Torresi, J., Gowans, E. J. & Grubor-Bauk, B. Preclinical Development and Production of Virus-Like Particles As Vaccine Candidates for Hepatitis C. *Front Microbiol* 8, doi:ARTN 241310.3389/fmicb.2017.02413 (2017).

14 Wang, J. W. & Roden, R. B. S. Virus-like particles for the prevention of human papillomavirus-associated malignancies. *Expert Review of Vaccines* 12, 129-141, doi:10.1586/Erv.12.151 (2013).

15 Olsson, S. E. *et al.* Induction of immune memory following administration of a prophylactic quadrivalent human papillomavirus (HPV) types 6/11/16/18 L1 virus-like particle (VLP) vaccine. *Vaccine* 25, 4931-4939, doi:10.1016/j.vaccine.2007.03.049 (2007).

16 Shi, L. *et al.* GARDASIL: prophylactic human papillomavirus vaccine development--from bench top to bed-side. *Clin Pharmacol Ther* 81, 259-264, doi:10.1038/sj.clpt.6100055 (2007).

17 Schiller, J. T. & Lowy, D. R. Understanding and learning from the success of prophylactic human papillomavirus vaccines. *Nat Rev Microbiol* 10, 681-692, doi:10.1038/nrmicro2872 (2012).

18 Roldao, A., Mellado, M. C., Castilho, L. R., Carrondo, M. J. & Alves, P. M. Virus-like particles in vaccine development. *Expert Rev Vaccines* 9, 1149-1176, doi:10.1586/erv.10.115 (2010).

19 Chang, L. J. *et al.* Safety and tolerability of chikungunya virus-like particle vaccine in healthy adults: a phase 1 dose-escalation trial. *Lancet* 384, 2046-2052, doi:10.1016/S0140-6736(14)61185-5 (2014).

20 Treanor, J. J. *et al.* A novel intramuscular bivalent norovirus virus-like particle vaccine candidate--reactogenicity, safety, and immunogenicity in a phase 1 trial in healthy adults. *J Infect Dis* 210, 1763-1771, doi:10.1093/infdis/jiu337 (2014).

21 Landry, N. *et al.* Preclinical and clinical development of plant-made virus-like particle vaccine against avian H5N1 influenza. *PLoS One* 5, e15559, doi:10.1371/journal.pone.0015559 (2010).

22 Fuenmayor, J., Godia, F. & Cervera, L. Production of virus-like particles for vaccines. *New Biotechnol* 39, 174-180, doi:10.1016/j.nbt.2017.07.010 (2017).

23 Palomares, L. A. & Ramirez, O. T. Challenges for the production of virus-like particles in insect cells: The case of rotavirus-like particles. *Biochem Eng J* 45, 158-167, doi:10.1016/j.bej.2009.02.006 (2009).

24 McCluskie, M. J. *et al.* The effect of preexisting anti-carrier immunity on subsequent responses to CRM197 or Qb-VLP conjugate vaccines. *Immunopharmacol Immunotoxicol* 38, 184-196, doi:10.3109/08923973.2016.1165246 (2016).

25 Jegerlehner, A. *et al.* Carrier induced epitopic suppression of antibody responses induced by virus-like particles is a dynamic phenomenon caused by carrier-specific antibodies. *Vaccine* 28, 5503-5512, doi:10.1016/j.vaccine.2010.02.103 (2010).

26 Chattopadhyay, S., Chen, J. Y., Chen, H. W. & Hu, C. J. Nanoparticle Vaccines Adopting Virus-like Features for Enhanced Immune Potentiation. *Nanotheranostics* 1, 244-260, doi:10.7150/ntno.19796 (2017).

27 Spohn, G. & Bachmann, M. F. Exploiting viral properties for the rational design of modern vaccines. *Expert Rev Vaccines* 7, 43-54, doi:10.1586/14760584.7.1.43 (2008).

28 Somiya, M., Liu, Q. & Kuroda, S. Current Progress of Virus-mimicking Nanocarriers for Drug Delivery. *Nanotheranostics* 1, 415-429, doi:10.7150/ntno.21723 (2017).

29 Lee, C. *et al.* Rabies Virus-Inspired Silica-Coated Gold Nanorods as a Photothermal Therapeutic Platform for Treating Brain Tumors. *Adv Mater* 29, doi:10.1002/adma.201605563 (2017).

30 Lee, C. *et al.* Virus-mimetic polymer nanoparticles displaying hemagglutinin as an adjuvant-free influenza vaccine. *Biomaterials* 183, 234-242, doi:10.1016/j.biomaterials.2018.08.036 (2018).

31 Ingale, J. *et al.* High-Density Array of Well-Ordered HIV-1 Spikes on Synthetic Liposomal Nanoparticles Efficiently Activate B Cells. *Cell Rep* 15, 1986-1999, doi:10.1016/j.celrep.2016.04.078 (2016).

32 Riitho, V. *et al.* Design and evaluation of the immunogenicity and efficacy of a biomimetic particulate formulation of viral antigens. *Sci Rep* 7, 13743, doi:10.1038/s41598-017-13915-x (2017).

33 Hinton, H. J., Jegerlehner, A. & Bachmann, M. F. Pattern recognition by B cells: the role of antigen repetitiveness versus Toll-like receptors. *Curr Top Microbiol Immunol* 319, 1-15 (2008).

34 Jegerlehner, A. *et al.* Regulation of IgG antibody responses by epitope density and CD21-mediated costimulation. *Eur J Immunol* 32, 3305-3314, doi:Doi 10.1002/1521-4141(200211)32:11<3305::Aid-Immu3305>3.0.Co;2-J (2002).

35 Liu, W. L. & Chen, Y. H. High epitope density in a single protein molecule significantly enhances antigenicity as well as immunogenicity: a novel strategy for modern vaccine development and a preliminary investigation about B cell discrimination of monomeric proteins. *Eur J Immunol* 35, 505-514, doi:10.1002/eji.200425749 (2005).

36 Bachmann, M. F. *et al.* The influence of antigen organization on B cell responsiveness. *Science* 262, 1448-1451 (1993).

37 Niu, Y. *et al.* Nanoparticles mimicking viral surface topography for enhanced cellular delivery. *Adv Mater* 25, 6233-6237, doi:10.1002/adma.201302737 (2013).

38 Wang, W. *et al.* Facile Synthesis of Uniform Virus-like Mesoporous Silica Nanoparticles for Enhanced Cellular Internalization. *ACS Cent Sci* 3, 839-846, doi:10.1021/acscentsci.7b00257 (2017).

39 Junt, T. *et al.* Subcapsular sinus macrophages in lymph nodes clear lymph-borne viruses and present them to antiviral B cells. *Nature* 450, 110-114, doi:10.1038/nature06287 (2007).

40 Whittington, P. J. *et al.* Her-2 DNA versus cell vaccine: immunogenicity and anti-tumor activity. *Cancer Immunol Immunother* 58, 759-767, doi:10.1007/s00262-008-0599-x (2009).

41 Chen, H. W. *et al.* Facile Fabrication of Near-Infrared-Resonant and Magnetic Resonance Imaging-Capable Nanomediators for Photothermal Therapy. *Acs Appl Mater Inter* 7, 12814-12823, doi:10.1021/acsami.5b01991 (2015).

42 Clauson, R. M., Chen, M., Scheetz, L. M., Berg, B. & Chertok, B. Size-Controlled Iron Oxide Nanoplatforms with Lipidoid-Stabilized Shells for Efficient Magnetic Resonance

Imaging-Trackable Lymph Node Targeting and High-Capacity Biomolecule Display. *ACS Appl Mater Interfaces* 10, 20281-20295, doi:10.1021/acsami.8b02830 (2018).

43 Tong, S., Hou, S., Ren, B., Zheng, Z. & Bao, G. Self-assembly of phospholipid-PEG coating on nanoparticles through dual solvent exchange. *Nano Lett* 11, 3720-3726, doi:10.1021/nl201978c (2011).

44 Shtykova, E. V. *et al.* Structure and properties of iron oxide nanoparticles encapsulated by phospholipids with poly(ethylene glycol) tails. *J Phys Chem C* 111, 18078-18086, doi:10.1021/jp075235c (2007).

45 Udenfriend, S. *et al.* Fluorescamine: a reagent for assay of amino acids, peptides, proteins, and primary amines in the picomole range. *Science* 178, 871-872 (1972).

46 Sanchez, A. B. *et al.* A general process for the development of peptide-based immunoassays for monoclonal antibodies. *Cancer Chemother Pharmacol* 66, 919-925, doi:10.1007/s00280-009-1240-1 (2010).

47 van Loon, A. M. & van der Veen, J. Enzyme-linked immunosorbent assay for quantitation of toxoplasma antibodies in human sera. *J Clin Pathol* 33, 635-639 (1980).

48 Chertok, B., Cole, A. J., David, A. E. & Yang, V. C. Comparison of electron spin resonance spectroscopy and inductively-coupled plasma optical emission spectroscopy for biodistribution analysis of iron-oxide nanoparticles. *Mol Pharm* 7, 375-385, doi:10.1021/mp900161h (2010).

49 Franz, B., May, K. F., Jr., Dranoff, G. & Wucherpfennig, K. Ex vivo characterization and isolation of rare memory B cells with antigen tetramers. *Blood* 118, 348-357, doi:10.1182/blood-2011-03-341917 (2011).

50 Gobin, A. M., Watkins, E. M., Quevedo, E., Colvin, V. L. & West, J. L. Near-infrared-resonant gold/gold sulfide nanoparticles as a photothermal cancer therapeutic agent. *Small* 6, 745-752, doi:10.1002/smll.200901557 (2010).

51 Lu, Y., Wang, L., Chen, D. & Wang, G. Determination of the concentration and the average number of gold atoms in a gold nanoparticle by osmotic pressure. *Langmuir* 28, 9282-9287, doi:10.1021/la300893e (2012).

52 Kokate, M., Garadkar, K. & Gole, A. One pot synthesis of magnetite-silica nanocomposites: applications as tags, entrapment matrix and in water purification. *J Mater Chem A* 1, 2022-2029, doi:10.1039/c2ta00951j (2013).

53 Cheng, W. The Density Code for the Development of a Vaccine? *J Pharm Sci* 105, 3223-3232, doi:10.1016/j.xphs.2016.07.020 (2016).

54 Rockberg, J., Schwenk, J. M. & Uhlen, M. Discovery of epitopes for targeting the human epidermal growth factor receptor 2 (HER2) with antibodies. *Mol Oncol* 3, 238-247, doi:10.1016/j.molonc.2009.01.003 (2009).

55 Shukla, S., Wen, A. M., Commandeur, U. & Steinmetz, N. F. Presentation of HER2 epitopes using a filamentous plant virus-based vaccination platform. *J Mater Chem B* 2, 6249-6258, doi:10.1039/c4tb00749b (2014).

56 Jasinska, J. *et al.* Inhibition of tumor cell growth by antibodies induced after vaccination with peptides derived from the extracellular domain of Her-2/neu. *Int J Cancer* 107, 976-983, doi:10.1002/ijc.11485 (2003).

57 Balmelli, C. *et al.* Nasal immunization of mice with human papillomavirus type 16 virus-like particles elicits neutralizing antibodies in mucosal secretions. *J Virol* 72, 8220-8229 (1998).

58 Elsayed, H. *et al.* Intrastructural Help: Harnessing T Helper Cells Induced by Licensed Vaccines for Improvement of HIV Env Antibody Responses to Virus-Like Particle Vaccines. *J Virol* 92, doi:10.1128/JVI.00141-18 (2018).

59 Lee, Y. T. *et al.* Intranasal vaccination with M2e5x virus-like particles induces humoral and cellular immune responses conferring cross-protection against heterosubtypic influenza viruses. *PLoS One* 13, e0190868, doi:10.1371/journal.pone.0190868 (2018).

60 Ocana, A., Amir, E. & Pandiella, A. Dual targeting of HER2-positive breast cancer with trastuzumab emtansine and pertuzumab: understanding clinical trial results. *Oncotarget* 9, 31915-31919, doi:10.18632/oncotarget.25739 (2018).

61 Swain, S. M. *et al.* Pertuzumab, trastuzumab, and docetaxel in HER2-positive metastatic breast cancer. *N Engl J Med* 372, 724-734, doi:10.1056/NEJMoa1413513 (2015).

62 Tam, H. H. *et al.* Sustained antigen availability during germinal center initiation enhances antibody responses to vaccination. *Proc Natl Acad Sci U S A* 113, E6639-E6648, doi:10.1073/pnas.1606050113 (2016).

63 Cubas, R. *et al.* Virus-like particle (VLP) lymphatic trafficking and immune response generation after immunization by different routes. *J Immunother* 32, 118-128, doi:10.1097/CJI.0b013e31818f13c4 (2009).

64 De Silva, N. S. & Klein, U. Dynamics of B cells in germinal centres. *Nat Rev Immunol* 15, 137-148, doi:10.1038/nri3804 (2015).

65 Carrasco, Y. R. & Batista, F. D. B cells acquire particulate antigen in a macrophage-rich area at the boundary between the follicle and the subcapsular sinus of the lymph node. *Immunity* 27, 160-171, doi:10.1016/j.immuni.2007.06.007 (2007).

66 Mohsen, M. O., Gomes, A. C., Vogel, M. & Bachmann, M. F. Interaction of Viral Capsid-Derived Virus-Like Particles (VLPs) with the Innate Immune System. *Vaccines (Basel)* 6, doi:10.3390/vaccines6030037 (2018).

67 Loo, C. P. *et al.* Lymphatic Vessels Balance Viral Dissemination and Immune Activation following Cutaneous Viral Infection. *Cell Rep* 20, 3176-3187, doi:10.1016/j.celrep.2017.09.006 (2017).

68 Kuka, M. & Iannacone, M. The role of lymph node sinus macrophages in host defense. *Ann N Y Acad Sci* 1319, 38-46, doi:10.1111/nyas.12387 (2014).

69 Kamala, T. Hock immunization: a humane alternative to mouse footpad injections. *J Immunol Methods* 328, 204-214, doi:10.1016/j.jim.2007.08.004 (2007).

70 Gray, E. E. & Cyster, J. G. Lymph node macrophages. *J Innate Immun* 4, 424-436, doi:10.1159/000337007 (2012).

71 Forsell, M. N. E., Kvastad, L., Sedimbi, S. K., Andersson, J. & Karlsson, M. C. I. Regulation of Subunit-Specific Germinal Center B Cell Responses to the HIV-1 Envelope Glycoproteins by Antibody-Mediated Feedback. *Front Immunol* 8, 738, doi:10.3389/fimmu.2017.00738 (2017).

72 Chen, C. *et al.* Uhrf1 regulates germinal center B cell expansion and affinity maturation to control viral infection. *J Exp Med* 215, 1437-1448, doi:10.1084/jem.20171815 (2018).

73 Mohsen, M. O., Zha, L., Cabral-Miranda, G. & Bachmann, M. F. Major findings and recent advances in virus-like particle (VLP)-based vaccines. *Semin Immunol* 34, 123-132, doi:10.1016/j.smim.2017.08.014 (2017).

74 Chackerian, B., Lowy, D. R. & Schiller, J. T. Conjugation of a self-antigen to papillomavirus-like particles allows for efficient induction of protective autoantibodies. *J. Clin. Invest.* 108, 415-423, doi:10.1172/jci11849 (2001).

75 Rodriguez-Limas, W. A., Sekar, K. & Tyo, K. E. J. Virus-like particles: the future of microbial factories and cell-free systems as platforms for vaccine development. *Curr. Opin. Biotechnol.* 24, 1089-1093, doi:10.1016/j.copbio.2013.02.008 (2013).

76 Pierce, S. K. & Liu, W. The tipping points in the initiation of B cell signalling: how small changes make big differences. *Nat Rev Immunol* 10, 767-777, doi:10.1038/nri2853 (2010).

77 Melief, C. J. M., van Hall, T., Arens, R., Ossendorp, F. & van der Burg, S. H. Therapeutic cancer vaccines. *J. Clin. Invest.* 125, 3401-3412, doi:10.1172/jci80009 (2015).

78 Melero, I. *et al.* Therapeutic vaccines for cancer: an overview of clinical trials. *Nat. Rev. Clin. Oncol.* 11, 509-524, doi:10.1038/nrclinonc.2014.111 (2014).

79 Palladini, A. *et al.* Virus-like particle display of HER2 induces potent anti-cancer responses. *Oncoimmunology* 7, e1408749, doi:10.1080/2162402X.2017.1408749 (2018).

80 van der Burg, S. H., Arens, R., Ossendorp, F., van Hall, T. & Melief, A. J. M. Vaccines for established cancer: overcoming the challenges posed by immune evasion. *Nat. Rev. Cancer* 16, 219-233, doi:10.1038/nrc.2016.16 (2016).

81 Goldberg, M. S. Immunoengineering: how nanotechnology can enhance cancer immunotherapy. *Cell* 161, 201-204, doi:10.1016/j.cell.2015.03.037 (2015).

Part 2:
Iron-Oxide Nanoplatforms for T-cell Activation

CHAPTER 3

Size-Controlled Iron Oxide Nanoplatforms with Lipidoid-Stabilized Shells for Efficient MRI-Trackable Lymph Node Targeting and High Capacity Biomolecule Display

3.1 Abstract

Nanoplatforms for biomolecule delivery to the lymph nodes have attracted considerable interest as vectors for immunotherapy. Core-shell iron oxide nanoparticles are particularly appealing because of their potential as theranostic MRI-trackable vehicles for biomolecule delivery. The key challenge to utilizing iron oxide nanoparticles in this capacity is control of their coating shells to produce particles with predictable size. Size determines both the carrier capacity for biomolecule display and the carrier ability to target the lymph nodes. In this study, we develop a novel coating method to produce core-shell iron oxide nanoparticles with controlled size. We utilize lipid-like molecules to stabilize self-assembled lipid shells on the surface of iron oxide nanocrystals, allowing formation of consistent coatings on nanocrystals of varying size (10-40 nm). We further demonstrate the feasibility of leveraging the ensuing control of nanocarrier size for optimizing the carrier functionalities. Coated nanoparticles with 10 nm and 30 nm cores supported biomolecule display at 10-fold and 200-fold higher capacities than previously reported iron oxide nanoparticles, while preserving monodisperse sub-100 nm size populations. In addition, accumulation of the coated nanoparticles in the lymph nodes could be tracked by MRI and, at 1-hour post injection, demonstrated significantly enhanced lymph node targeting. Notably, lymph node targeting was 9-40 folds higher than for previously reported nanocarriers, likely due to the ability of these nanoparticles to robustly maintain their sub-100nm size *in vivo*. This approach can be broadly applicable for rational design of theranostic nanoplatforms for image-monitored immunotherapy.

3.2 Introduction

The presentation of immunoactive biomolecules to the lymph nodes has the potential to treat a number of intractable human diseases including infectious diseases and cancer. The lymph nodes are the central sites for immune activation, and thus, present an important target for therapeutic immunomodulation[1]. Because soluble immunoactive biomolecules are typically inefficient in accessing lymph nodes and stimulating immunity, nanoparticles have attracted considerable interest as platforms for biomolecule delivery and presentation[2]. The nanoparticles' performance as lymph node carriers is largely determined by their material properties, such as size and capacity for biomolecule surface display[3]. Although a variety of nanoparticle systems have been investigated, development of biomolecule-displaying nanocarriers with well-defined material characteristics still represents a considerable challenge[4].

One key criterion in developing nanoparticles as lymph node carriers is the ability to control nanocarrier size[5]. Size is critical to several aspects of nanocarriers' biological performance. For example, size largely determines the multivalency of biomolecule display on the nanoparticle surface[5, 6]. High multivalency can mimic the natural presentation of antigens and adjuvants by pathogens and can play a significant role in directing immune responses[7]. Larger nanoparticles possess larger surface area per particle, and thus, can achieve higher multivalency compared to their smaller counterparts[3]. In addition, the size of nanocarriers also determines their efficiency in reaching the lymph nodes from their intradermal injection site[8]. Nanocarriers with small sub-100 nm size are efficient in accessing lymph nodes because they can leverage the size-restrictive mechanism of lymphatic drainage[9]. Thus, to control delivery and presentation of immunoactive biomolecules, there is a need in development of nanocarriers with controlled size[5].

Among nanoparticles investigated for lymph node targeting, nanoparticles based on FDA-approved biodegradable and biocompatible iron oxide are particularly appealing[10, 11]. Iron oxide nanocrystals can be synthesized as controlled monodisperse populations over a range of particle size (10-40 nm)[12, 13]. These well-defined cores provide a scaffold for engineering controlled core-shell nanocarriers. Furthermore, iron oxide also exhibits magnetic properties and high r2 relaxivities for MRI detection, and can be tracked by MRI imaging *in vivo*[14, 15]. Imaging is being widely explored as a companion technology for drug delivery because it can be leveraged to validate delivery, optimize dosage regiments, or monitor therapeutic response[16]. The unique combination of properties of the iron oxides makes them attractive candidates for development of theranostic nanoplatforms with well-defined material characteristics[17, 18].

One key aspect in developing core-shell iron oxide nanoparticles is the engineering of their coating shells. Engineering surface coatings with controlled size and high capacity to display biomolecules, while optimally leveraging the nanocrystal's magnetic properties for MRI detection, represents a considerable challenge[12]. As-synthesized, iron oxide nanocrystals are stabilized by surface-grafted hydrophobic ligands, such as oleic acid, and require coating with hydrophilic shells[19]. Although myriad coating strategies exist, most methods render nanoparticles non-biodegradable or attenuate magnetic properties[12, 20]. For example, biopolymer coatings typically require covalent cross-linking, which can compromise biodegradability[21]. Alternatively, coatings by surface-anchoring ligands, such as catechols, involves replacement of the original ligands, which can perturb the nanocrystal and compromise magnetic properties[20].

One alternative approach utilizes amphiphilic lipids[22]. Amphiphilic lipids can form protective lipid gels on the nanocrystal's surface by assembling with the surface-grafted ligands[23]. Coating by self-assembly is advantageous because it circumvents the need for covalent cross-linking or chemical alterations to the nanocrystal, thus preserving biodegradability and magnetic properties. A number of formulations have been developed to coat nanocrystals with amphiphilic lipids, such as phospholipid-PEG[23, 24]. However, controlling the coating shell across a range of iron oxide sizes is still a difficult challenge. Spherical nanocrystals with different diameters exhibit different surface curvatures, which significantly impact lipid self-assembly[25, 26]. Packing of amphiphilic lipids on surfaces of larger nanocrystals resembles packing on planar surfaces, which generates structural gaps on the surface[27]. This leads to lower packing densities for larger nanocrystals, non-homogenous coatings, and difficulty in controlling size[28]. Although coating of small nanocrystals (<20 nm) has been widely explored, few examples of coating larger nanocrystals (>20 nm) have been reported to date[29]. Larger nanocrystals offer higher relaxivities for MRI detection[29, 30] and larger surface area per particle for increasing multivalency of biomolecule display[3]. Thus, to rationally design theranostic iron oxide nanocarriers, there is a need to engineer controllable coatings over a range of nanocrystal sizes.

Here, we develop a method to generate self-assembled lipid coatings on iron oxide surfaces that provide robust control of nanoparticle size. Our approach is inspired by a biophysical phenomenon of "lipid stitching". It has been demonstrated that non-covalent stitching of lipid bilayers by agents that can link opposing monolayers of lipid membranes can significantly improve the coherency of lipid gels on planar surfaces[27]. Previous strategies to form

self-assembled coatings on nanocrystal surfaces relied on micelle-like self-assembly mediated solely by hydrophobic interactions[23, 24]. In contrast, the activity of the “stitching” agents is likely due to a combination of hydrophobic and electrostatic interactions. We hypothesized that if lipid-stitching could be applied to the iron oxide nanocrystals, consistent stabilization of both small and large nanocrystals could be achieved, thus allowing control of nanoparticle size. To test this hypothesis, we coated oleic acid stabilized nanocrystals with phospholipid-PEG and lipidoids (Figure 3.1A). We considered that lipidoids, cationic agents with hydrophobic tails, could act as “stitching” agents to stitch hydrophobic and anionic regions of surface bilayers. Our results reveal the feasibility of this approach. Our method produced consistent coatings on nanocrystals of varying size (10-40 nm), allowing robust control of particle size. We demonstrate that the ability to control the nanocarriers’ size could be leveraged to optimize their functionality. Significantly, compared to previously reported spherical particles of sub-100 nm size, our coated nanoparticles were 9- to 40-fold more efficient in reaching the lymph nodes, likely due to robust size preservation *in vivo*. Furthermore, larger nanoparticles (30 nm core) displayed 3-fold higher r2 relaxivity and 20-fold higher capacity for biomolecule display compared to their smaller counterparts (10 nm core), while reaching the lymph nodes with similar efficiency. Notably, larger nanoparticles could carry thousands of model antigen and adjuvant biomolecules per particle, exhibiting 200-fold higher multivalency than previously reported iron oxides, while preserving the advantageous sub-100nm size to efficiently access the lymph nodes, deliver biomolecules and allow tracking of delivery by MRI. To our knowledge, our method to coat nanocrystals is the first to provide robust size control across a range of available iron oxide nanocrystal sizes (10-40 nm), which can be leveraged to optimize the nanocarrier performance. Our approach is broadly applicable for engineering rationally designed nanoplatforms for image-guided biomolecule delivery to the lymph nodes.

3.3 Experimental Section

Materials. All reagents were used as obtained from commercial sources without further purification. Lipids including DSPE-mPEG [1,2-distearoyl-sn-glycero-3-phosphoethanolamine-N-[methoxy(polyethylene glycol)-2000] and DSPE-PEG-PDP [1,2-distearoyl-sn-glycero-3-phosphoethanolamine-N-[PDP(polyethylene glycol)-2000] were acquired from Avanti Polar Lipids. Oleic acid stabilized iron oxide nanoparticles in chloroform were obtained from Ocean Nanotech. CpG oligonucleotides with a 3'-terminal disulfide bridge modification were purchased from IDT DNA Technologies. These sequences included CpG-S-S-CH_3 [CpG (5') TTGCAGTTCTTGCAGTACCT-$(CH_2)_3$-S-S-CH_3 (3')] and CpG_{comp}-Cy5.5 [CpG-Cy5.5 (5') AGGTACTGCAAGGACTGCAA-$(CH_2)_3$-Cy5.5 (3')]. The model peptide with a terminal free thiol (peptide-SH) [GLSQNRDVRENQRAREC] was obtained from GenScript custom peptide synthesis. TCEP [Tris(2-carboxyethyl) phosphine hydrochloride], chloroform, absolute ethanol, phenol, sulfuric acid, dichloromethane and methanol were procured from Sigma-Aldrich. SYBR Gold Nucleic Acid Gel Stain (10,000X) was obtained from Thermo Fisher.

Mice. All animal experiments were conducted according to the protocols approved by the University of Michigan Committee on Use and Care of Animals (UCUCA). C57BL/6 mice and C57BL/6 albino mice were purchased from Charles River Labs.

Formulation of Multi-Lipid-Coated Iron-Oxide Nanoparticles (IONP-ML). Prior to formulation, the concentration of IONP-OA was determined by inductively coupled plasma optical emission spectroscopy (ICP-OES, Perkin-Elmer Optima 2000 DV) as previously described[31]. Multi-lipid-coated iron-oxide nanoparticles (IONP-ML) were formulated by a three-step ethanol thin film hydration and solvent exchange method. In step one, IONPs stabilized by oleic acid (IONP-OA), lipidoid and DSPE-mPEG were dispersed in chloroform and dried by nitrogen evaporation to produce a lipid film. This lipid film contained 3.32 mg of total lipid/lipidoid per mg Fe with a lipid composition of lipidoid:DSPE-mPEG at a mol % ratio of 77:23, unless otherwise specified. In step two, the IONP lipid film (an equivalent of 1mg Fe) is rehydrated in absolute ethanol (500 µL) at 65°C for 2 hours. In step three, the samples are cooled to room temperature and then dialyzed against phosphate-buffered saline (PBS, 100 mM PBS, pH 7.4; MWCO = 20,000).

Analysis of IONP-ML Recovery in Aqueous Solution. To evaluate the recovery of stabilized IONP-ML in aqueous solution, the stabilized fraction of nanoparticles was separated from unstable and agglomerated IONPs by gravity filtration and magnetic separation. The stabilized

fraction was analyzed for total iron (Fe) with ICP-OES and compared to the initial quantity of iron oxide added per formulation. Iron oxide recovery was calculated as follows:

$$\text{Iron Oxide Recovery in Aqueous Solution (\%)} = \frac{\text{Resuspended Iron Oxide in aqueous solution (mg Fe)}}{\text{Initial Iron Oxide in chloroform (mg Fe)}} \text{x100\%}$$

Characterization of IONP-ML. The composition of IONP-ML lipid coatings was analyzed by thin layer chromatography (TLC) according to a previously reported protocol with minor modifications[32]. Briefly, prior to analysis, lipid-coated nanoparticles were purified by magnetic separation using MidiMACS MS magnetic columns (Miltenyi Biotec), frozen with liquid nitrogen and lyophilized. To extract lipids, dried samples were dispersed in chloroform (15 mg/mL). The lipid-containing soluble fraction was separated from the iron oxide precipitate using magnetic separation. This fraction was spotted on TLC plates (silica gel matrix, Sigma-Aldrich), run with dichloromethane/methanol (DCM:MeOH) mobile phase (80:20 v/v) and stained with iodine. FT-IR spectra were collected using a Perkin-Elmer Spectrum BX FT-IR spectrophotometer. The morphological characterization of nanoparticle samples was performed using transmission electron microscopy operating at 300 kV (TEM, JEOL USA, Inc.). Quantitative analysis of TEM images to evaluate particle size and shell layer thickness was conducted using Image J software. Background subtraction was employed to better visualize IONP-OA and IONP-ML shells according to the method of Hartig[33]. The hydrodynamic diameters (volume-weighted) and zeta potentials of all materials were analyzed using dynamic light scattering (DLS) and phase analysis light scattering, respectively at 25°C, 100 mM PBS, pH 7.4 (Malvern Zetasizer Nano-ZS). The magnetization of IONP-OA and IONP-ML were performed at 293K using the MPMS-XL Superconducting Quantum Interference Device (SQUID) magnetometer (Quantum Design Inc. San Diego, CA). The r_2 relaxivity of ML-IONP was determined by T_2-weighted MRI. MRI was performed using a 33 cm horizontal-bore, 7 T Agilent MR imaging system (Agilent, Palo Alto, CA). A quadrature 59 mm volume radiofrequency coil was used to scan a 396-well polystyrene plate containing nanoparticle solutions. MRI scans were acquired using fast spin echo multi-slice sequence (fsems) with the following parameters: TR = 4000 s, TE = 30 ms and 60 ms, FOV: 20 x 20 mm over 256 x 128 matrix; slice thickness = 1 mm). Image analysis to estimate transverse (r_2) relaxivity was conducted as previously described[14].

Synthesis of IONP-ML-CpG. PDP-activated lipid-coated iron-oxide nanoparticles (IONP-ML-PDP) were prepared as described above for IONP-ML, with a modified lipid composition of C12-98(5):DSPE-mPEG:DSPE-PEG-PDP at a mol % ratio of 77:11.5:11.5 (denoted as 50% PDP).

IONP-ML-PDP, were functionalized with CpG oligonucleotides in a two-step process (IONP-ML-CpG). In the first step, the 3'-terminal disulfide bridge of CpG-S-S-CH3 was reduced with TCEP overnight to produce a free terminal sulfhydryl group (CpG-SH). CpG-SH was then purified with anion exchange chromatography (HiTrap Q FF column, GE Healthcare), desalted and concentrated by ultrafiltration (1,000 Da MWCO). Subsequently, the oligonucleotide content was determined by spectrophotometric analysis (260nm, Nanoquant Plate, Tecan Infinite M1000 PRO). In the second step, IONP-ML-PDP was incubated with CpG-SH (at 3:1 molar ratio of CpG:PDP) at room temperature overnight. The product (IONP-ML-CpG) was separated from unreacted CpG using magnetic chromatography.

Synthesis of IONP-ML-Peptide. IONP-ML-PDP was prepared as described above. To conjugate thiolated peptide (Peptide-SH) to IONP-ML-PDP, the reactants were incubated at a molar ratio of 3:1 (Peptide-SH:PDP) in PBS (100 mM, pH 7.4) at room temperature overnight. The product (IONP-ML-Peptide) was separated from unreacted peptide using magnetic chromatography.

Characterization of IONP-ML-CpG. To validate conjugation of CpG, IONP-ML-CpG was evaluated by anion exchange chromatography and agarose gel electrophoresis. Anion exchange chromatography was performed using columns with quaternary ammonium matrix (HiTrap Q FF column, GE Healthcare). Samples were loaded onto anion exchange columns. The columns were washed with 10 column volumes of PBS (100 mM, pH 7.4) and then with 10 column volumes of NaCl (2M) to elute matrix-retained nanoparticles. Wash and elution fractions (2 mL) were analyzed for IONP-ML content by spectrophotometric analysis (600 nm, Tecan M1000 PRO). Elution profiles of IONP-ML-CpG were compared to an IONP-ML-PDP control. Electrophoretic migration of IONP-ML-CpG was assessed using agarose gel electrophoresis 0.8% agarose, TAE, 75V, 30 minutes. Gels were imaged with the UVP ChemiDoc-It^2 Imager and migration distances were quantified using Image J software. CpG content in the functionalized IONP-ML-CpG was analyzed by densitometry based on previously described procedures with minor modifications[34]. Briefly, the IONP-ML-CpG samples were first digested for 2 hours with TCEP (100 mM aqueous solution), and then subjected to electrophoresis to visualize CpG by SYBR gold staining (4% agarose, TAE, 75 V, 30 minutes). Gels were imaged using UVP ChemiDoc-It^2 Imager. Concentrations of CpG were quantified by densitometry using known concentrations of free CpG for calibration. To estimate CpG content of the nanoparticles per unit nanoparticle, CpG concentrations in IONP-ML-CpG samples were normalized by nanoparticles' concentrations. Nanoparticle concentrations were determined by ICP-OES.

Characterization of IONP-ML-Peptide. To validate conjugation of a model peptide, IONP-ML-Peptide was evaluated by a Ninhydrin colorimetric assay[35]. Briefly, IONP-ML-Peptide (100 µg total Fe) was mixed with 6M HCl (0.4 mL) at 125°C for 30 minutes. After acid digestion, 6M NaOH (0.4 mL) was added to neutralize the pH. Subsequently, the resulting solution (500 uL) was mixed with an equal volume of Ninhydrin reagent (2 g Ninhydrin, 75 mL DMSO, 25 mL 3M Sodium Acetate, pH 5.5) and heated in a boiling water bath for 20 minutes. Samples volumes were adjusted by addition of PBS to offset solvent losses due to evaporation, and then samples were analyzed by spectrophotometry (570 nm, Tecan M1000 PRO). Calibration curves were constructed using standard peptide solutions also containing IONP-ML-PDP. The iron concentration of IONP-ML-PDP in the standard solutions was equivalent to the iron concentration of the analyte to offset the absorbance of iron at 570 nm.

***In-vivo* MRI-tracked Delivery to the Lymph Nodes.** To examine delivery of IONP-ML (10 nm and 30 nm cores) and IONP-ML-CpG (30 nm cores) to the lymph nodes *in-vivo*, mice (C57BL/6 mice, n = 3) were injected with the nanoparticles (12 mg Fe/kg[36]) intradermally into the forepaw. Delivery to the lymph nodes was evaluated by MRI imaging *in-vivo* and by analysis of excised lymph nodes *ex-vivo*. MRI was performed using a 33 cm horizontal-bore, 7 Tesla Agilent MR imaging system (Agilent, Palo Alto, CA). Animals were anesthetized with 2% isoflurane/air mixture and maintained at 37°C with forced heated air inside the magnet. The thoracic region of the animals was placed in the center of a 35 mm diameter quadrature RF volume coil. Images were acquired before and 1 hour post-administration of nanoparticles. IONP-ML delivery to lymph node was monitored utilizing gradient echo (TR = 300 ms, TE = 5 ms, slice thickness, FOV of 25 x 25 mm over 128 x 128 matrix) and T_2-weighted fast spin-echo multi-slice (TR = 4000 ms, TE = 60 ms, slice thickness = 1 mm, FOV of 25 x 25 mm over 256 x 128 matrix) MRI sequences. During image acquisition, a spatial saturation band was placed over the region of the lungs in order to reduce respiratory noise interference.

Following MRI post-scans, the animals were euthanized, brachial and axillary lymph nodes ipsilateral and contralateral to the injection site were excised for *ex-vivo* analysis and stored at -80°C until analysis.

To evaluate delivery of biomolecules using the IONP-ML nanoplatforms, the IONP-ML-CpG was complexed with a fluorescently tagged complementary sequence (CpG_{comp}-Cy5.5). Mice were treated with IONP-ML-CpG/CpG_{comp}-Cy5.5 (n=4) or free CpG_{comp}-Cy5.5 (n = 4) via an intradermal injection into the forepaw (12 mg Fe/kg). One hour post-administration animals were

imaged by whole body fluorescence imaging (675/720 nm ex/em, exposure = 0.25 seconds) using IVIS imaging system. Subsequently, the animals were euthanized and brachial and axillary lymph nodes were excised for *ex-vivo* analysis.

***Ex-vivo* Analysis of Lymph Node Delivery.** Excised lymph nodes were analyzed for the content of iron oxide nanoparticles and the content of the model biomolecule CpG_{comp}-Cy5.5, by electron spin resonance (ESR) spectroscopy and fluorescence imaging, respectively. ESR spectroscopy was performed using an EMX ESR spectrometer (Bruker Instruments Inc., Billerica, MA) according to the method of Chertok et al[14]. The acquisition parameters were: resonant frequency: ~9.3 GHz, microwave power: 200 mW, temperature: 145K, modulation amplitude: 5G and receiver gain: 5×10^4. Fluorescence imaging of the excised lymph nodes (640/675 nm ex/em, exposure = 0.25 seconds) was carried out using IVIS Spectrum. Image analysis was conducted with the Living Image software.

Statistical Analysis. Data are expressed as mean ± S.D., unless otherwise specified. Comparisons between two groups were made using the unpaired Student's t test. Means of multiple groups were compared with the one-way ANOVA, followed by *post hoc* Tukey's pairwise comparisons. All probability values are two-sided, and values of $p < 0.05$ were considered statistically significant. Curve fitting and statistical analyses were carried out using OriginPro8 (OriginLab) and GraphPad Prism 7 software packages.

3.4 Results and Discussion

Formation of lipid-PEG/lipidoid coated iron oxide nanoparticles

To coat oleic acid stabilized nanocrystals with phospholipid-PEG and lipidoids, we used a variation of a thin film hydration method[24]. Thin film hydration method typically involves dispersion of the nanocrystals and the lipids in a thin film, followed by hydration of the film with an aqueous buffer to produce coated nanoparticles. Although this method is simple and commonly utilized to coat iron oxide nanocrystals, it suffers from several drawbacks. The abrupt introduction of solid lipid/nanocrystal dispersions to a non-solvent, water, induces phase separation and often results in irreversible aggregation of nanocrystals and low yields. Instead of directly hydrating the film with water, we pursued a gradual solvent exchange. We first hydrated the film with ethanol (EtOH) and then dialyzed the resulting nanoparticle suspension into water. We considered that replacing the abrupt introduction of solid lipid/nanocrystal dispersions to a non-solvent, water, with a gradual solvent exchange could allow the lipids to phase transition gradually minimizing phase separation and aggregation[37]. Thin film hydration in EtOH yielded higher recoveries of lipidoid-stabilized nanoparticles than the direct hydration with aqueous PBS (Supporting Information, Figure S11). Therefore, we adopted this modified method for our subsequent studies.

Using this method, we tested a series of lipidoids and traditional cationic lipids for their ability to facilitate stabilization of 20-nm iron oxide nanocrystals (Supporting Information, Figure S12 and Figure S13). As a measure of nanoparticle stabilization, we calculated the recovery of water dispersible iron oxide relative to the initial amount of iron oxide in formulations. While negligible recoveries were observed without lipidoids, addition of 25% lipidoids (w/w) into lipid compositions resulted in aqueous recovery of a significant fraction (14-27%) of initial iron. This finding indicated that lipidoids were a critical component for nanoparticle stabilization in our system. Interestingly, lipidoids with high numbers of alkyl chains (4-5) yielded significantly higher stabilization than traditional cationic phospholipids with two alkyl chains (e.g. C12-98(5) vs DOTAP: 27 ± 6% vs 3 ± 2%, $p < 0.001$). It is possible that in contrast to cationic phospholipids that are oriented to expose their headgroups on the surface, lipidoids can fully intercalate the hydrophobic interior and “stitch” the opposing monolayers together. Lipidoid C12-98(5) exhibited the highest level of stabilization (27 ± 6%) and was selected for further studies.

We next asked whether lipidoid C12-98(5) could stabilize nanocrystals of different sizes (Figure 3.1B). Indeed, addition of 22% w/w lipidoid to coating compositions resulted in significantly higher nanoparticle recoveries compared to coatings without lipidoids for nanocrystals of all tested sizes (10 nm: 0.6 ± 0.4% vs. 9 ± 2%, p <0.01; 20 nm: 1.0 ± 0.8% vs. 18 ± 4%, p <0.001; 30 nm: 0.8 ± 0.8% vs. 35 ± 5%, p < 0.001; 40 nm: 2 ± 1% vs. 62± 8%, p <0.001). Further increases in the stabilization efficiency could be achieved by increasing C12-98(5) concentration in lipid compositions. The stabilization efficiency increased sigmoidally (Boltzmann sigmoidal model, R^2 = 0.99; p < 0.001 (40 nm) or three parameter non-linear logistic model, R^2 = 0.99; p < 0.001 (30 nm), R^2 = 0.99; p < 0.001 (20 nm), R^2 = 0.99; p < 0.001 (10 nm)), reaching saturation at threshold C12-98(5) concentrations of approximately 45% (%w/w). Significantly, at saturation, about 85% recovery could be obtained for nanocrystals of all particle sizes (10 nm-40 nm, Figure 3.1B).

To examine the nature of the nanoparticle coatings, we assessed the coatings by TLC, FT-IR, and zeta potential. For TLC analysis, we lyophilized magnetically-separated nanoparticles and extracted the coating from the surface by re-dispersing the nanoparticles in chloroform. TLC chromatograms confirmed presence of the lipidoid C12-98(5) and phospholipid-PEG on the nanoparticles' surfaces (Supporting Information, Figure S14). FT-IR provided further evidence of the coating composition (Figure 3.1C). The spectrum of coated nanoparticles IONP-ML displayed additional peaks (1100 cm^{-1}, 1560 cm^{-1} and 1650 cm^{-1}) not observed for oleic acid stabilized nanocrystals IONP-OA. The peaks at 1100 cm^{-1} corresponded to the ether bond (C-O-C stretching) of the PEG chains, while the peaks at 1560 cm^{-1} and 1650 cm^{-1} corresponded to the amide bond (N-H bending and C=O stretching, respectively) of the acrylamide chains. These peaks confirmed the addition of the PEG-containing DSPE-mPEG(2000) and acrylamide-containing C12-98(5), respectively, to the nanocrystal's surface.

Interestingly, coated nanoparticles of all sizes displayed nearly electroneutral zeta potential (~4 mV, Table 3.1). Our measurements of PEG packing densities indicated that IONP-ML with a 30 nm nanocrystal's diameter contain 11,740 phospholipid-PEG molecules per particle (Supporting Information, Section 5). Given the negative charge of the phosphate groups, this density of the anionic phospholipids on the nanoparticle's surface should have translated to a strongly negative zeta potential. Indeed, previous studies reported highly electronegative zeta potentials (-29 mV) for iron oxide coatings that contained DSPE-mPEG2000 as a single component[26, 38]. Thus, the electroneutral zeta potential of our IONP-ML provides additional evidence for surface integration of cationic lipidoids and reveals charge

neutralization. It is likely that the charge neutralization is a manifestation of the electrostatic interactions between the cationic amine groups of the lipidoids and anionic phosphate groups of the DSPE-mPEG, which stabilize the coating shell.

Lipidoid stitched coatings mediate formation of iron oxide nanoparticles with robust size control across a range of nanocrystal sizes

We next examined the morphology and size of coated nanoparticles by TEM and DLS. Lipid-PEG/lipidoid stabilized nanocrystals IONP-ML were individually coated and exhibited monocrystalline core-shell morphology (Figures 3.2A and 3.2B). Notably, this IONP-ML morphology in aqueous solution was reproducible across a range of nanocrystal sizes, similar to the original IONP-OA dispersed in chloroform (Figure 3.2A).

Distinct homogenous shells could be observed by TEM for IONP-ML nanoparticles of all sizes (Figure 3.2C). The shells of the IONP-ML nanoparticles measured about 5 nm and were significantly thicker than the shells of the IONP-OA nanocrystals for each examined nanocrystal size ($p < 0.001$, Figure 3.2D). The observed shell on the IONP-ML surface likely represents the tightly packed hydrophobic portion of the coating. The reported length estimates for the oleic acid and the DSPE are 1.7 nm and 3.2 nm, respectively[25]. Given these estimates, the hydrophobic part of the phospholipid-PEG is unlikely to directly interdigitate with the surface-anchored oleic acid. Rather, both the oleic acid and the DSPE-mPEG shell components likely interdigitate with the alkyl chains of the lipidoid, which "stitches" the oppositely oriented tails of the two hydrophobic monolayers together. Notably, quantitative analysis of the coating thicknesses revealed that the shell thicknesses did not differ significantly for the nanoparticles of different size ($p = 0.18$, Figure 3.2D). This finding indicated that the coating could be formed reproducibly across a range of nanocrystal sizes.

We next examined the hydrodynamic diameters of IONP-ML (Figure 3.3 and Table 3.1). The IONP-ML of all particle sizes exhibited monodisperse populations, as evident by their polydispersity indices of less than 0.2 (Table 3.1)[39]. Notably, for nanocrystals of a given core size, the mean hydrodynamic diameter of coated IONP-ML was highly reproducible between formulations (Figure 3.3A). Most significantly, the mean hydrodynamic diameters of the IONP-ML displayed a very strong positive correlation with the nanocrystals' core diameters (Pearson

R^2 coefficient of 0.98, $p < 0.001$, Figure 3.3B). This finding indicated that our coating method provided a way to achieve control of nanoparticle's hydrodynamic size using nanocrystals of defined size as a starting material.

Interestingly, our experimentally measured values of the hydrodynamic diameter for nanoparticles of different sizes were in a close agreement with the theoretical estimates calculated using a scaling model (Figure 3.3B and Supporting Information, Section 6)[40-42]. The hydrodynamic diameter of the PEGylated nanoparticles in aqueous solution is known to depend on the extent of coiling or stretching of PEG chains on the nanoparticle's surface (Figure 3.3C)[40, 42]. Surface-grafted PEG chains extend out from the particle's surface, forming a layer of thickness L. The scaling model provides an estimate of this layer while accounting for the three major factors: 1) the radius (Rc) of the nanoparticle's sphere to which the PEG chains are attached, the so-called "hard sphere", 2) the packing density of PEG, and 3) the characteristics of the PEG chains. For a system with given characteristics of the PEG polymer, PEG2000, direct dependence of the PEG layer thickness on the radius of the nanocrystal's core implies consistent structure of the coating shell. Thus, the close agreement between the calculated and the measured values of the hydrodynamic diameters in our system supports consistent structure of the shell across nanoparticles of different core sizes.

Notably, our coating shells displayed very high PEG packing densities (Supporting Information, Section 5 and 6). Among previously reported DSPE-mPEG coatings for iron oxide, the highest PEG packing densities were ~0.5 PEG/nm^2 per unit area of the "hard sphere"[40]. In previous studies, because the coatings with DSPE-mPEG have typically been formed by a micelle-like self-assembly, these densities are similar to the packing densities for DSPE-mPEG micelles[42]. In contrast, our shells displayed packing densities of ~2.5 PEG/nm^2 per unit area of the "hard sphere", which is 5-fold higher than the values reported previously. The high packing density is likely due to the lipidoids' ability to "stitch" the components of lipid shells on the iron oxide surfaces. This stitched high-density packing likely is the factor that governs size control by allowing formation of consistent shell structures for nanocrystals of different sizes.

IONP-ML retain magnetic properties of the original iron oxide nanocrystals and display high r2 relaxivities

One challenge in developing core-shell iron oxide nanocarriers as theranostics is maintaining magnetic properties during formation of the coating shells[12]. Magnetic properties, which determine the ability of iron oxides to function as MRI-trackable theranostics, can be significantly attenuated by the coating process[20]. The attenuation is typically related to perturbation of the nanocrystal's surface during processes such as ligand exchange. Coating by amphiphilic self-assemblies is typically advantageous in maintaining magnetic properties because it does not rely on direct interactions of the coating material with the inorganic surface of the nanocrystal. To confirm the ability of our coating procedure to maintain magnetic properties, we assessed the saturation magnetization (Ms) of the IONP-ML (Figure 3.4A). The Ms values for IONP-ML with 10 nm (44 ± 7 emu/g Fe) and 30 nm core sizes (83 ± 5 emu/g Fe) were in close agreement with the previously reported Ms values for oleic acid-stabilized nanocrystals of the same sizes (10 nm:45 emu/g Fe ; 30 nm:87 emu/g Fe)[43]. Furthermore, IONP-ML and IONP-OA with 10 nm crystals exhibited no significant differences in saturation magnetization (44 ± 7 emu/g Fe vs 48 ± 7 emu/g Fe, $p = 0.43$, Figure 3.4A-insert). These findings validated that our coating method can robustly preserve the original magnetic properties of the iron oxide nanocrystals.

We further assessed the superparamagnetic property of the stabilized IONP-MLs (Figure 3.4B). Superparamagnetic behavior signifies that while the IONPs can be magnetized by an applied magnetic field, they regain zero net magnetic moment in the absence of magnetic field[44]. This property is essential for preventing magnetically induced agglomeration of IONPs *in vivo*[30, 44]. Superparamagnetic behavior is typically determined by nanocrystal size and can be exhibited by nanocrystals with up to 35 nm diameters[45]. Indeed, following initial attainment of induced magnetization of 39 ± 6 emu/g Fe (10 nm core) and 78 ± 4 emu/g Fe (30 nm core) in the applied fields of 4000 Ga, IONP-ML were found to completely demagnetize (10 nm core: 0 ± 2 emu/g Fe; 30 nm core: 0 ± 3 emu/g Fe) in the applied field of 0 Ga, confirming their desirable superparamagnetic behavior. The superparamagnetic behavior of the IONP-ML suggested that they are unlikely to magnetically agglomerate *in vivo*.

Finally, we also assessed the transverse r2 relaxivities of the IONP-ML (Figures 3.4C and 3.4D). The transverse r2 relaxivity is an inherent property of iron oxides, which determines

their ability to function as MRI contrast agents[46]. The relaxivity of the IONP-ML with 10 nm cores (66 ± 4 $mM^{-1}s^{-1}$) was similar to that of clinically utilized MRI contrast agents (e.g. Combidex, 65 $mM^{-1}s^{-1}$; Ferumoxytol 83 $mM^{-1}s^{-1}$)[47, 48]. Notably, larger IONP-ML with 30nm cores exhibited a 3-fold enhancement in r2 relative to their smaller counterparts (30 nm: 205 ± 10 $mM^{-1}s^{-1}$ vs 10 nm: 66 ± 4 $mM^{-1}s^{-1}$, $p<0.001$). This enhancement is likely due to the larger nanocrystal size and stronger saturation magnetization. High transverse relaxivities of the IONP-ML suggested that these particles would be detectable by MRI *in vivo*.

IONP-ML can rapidly and efficiently access lymph nodes and allow tracking of delivery by MRI

The advantageous combination of properties of the IONP-ML, including sub-100 nm size, high r2 relaxivity and superparamagnetic behavior, prompted us to examine their potential as theranostic vehicles for MRI-trackable lymph node delivery. To assess this potential, we injected the IONP-ML intradermally into the forepaw of C57BL/6 mice and examined delivery to the draining lymph nodes by MRI (Figure 3.5).

Baseline T2-weighted (T2W) axial images through the thoracic region allowed clear delineation of the brachial lymph nodes. We therefore chose these lymph nodes for qualitative assessment of the IONP-ML delivery by MRI. We examined both the 10 nm core (Figure 3.5A) and the 30 nm core (Figure 3.5B) IONP-ML. At one-hour post-administration, Gradient Echo (GE) and T2W images for both nanocarriers displayed a region of pronounced hypointensity relative to their respective GE and T2W pre-scans. This hypointensity was co-localized with the brachial lymph nodes ipsilateral to the injection site. The observed hypointensity reflects the presence of iron oxide within the tissue and, thus, the delivery of the IONP-ML to the draining brachial lymph nodes. In contrast, no GE/T2W signal reduction could be discerned in the lymph nodes contralateral to the injection site, consistent with draining-node selective delivery. To validate the MRI results, we quantified the iron oxide content in excised ipsilateral and contralateral lymph nodes (brachial + axillary) of test mice injected with either the 10 nm or 30 nm core nanoparticles (Figure 3.5C). The lymph nodes of the “blank” mice that received no nanoparticles were used as controls. Consistent with the MRI observations, no increase in the iron oxide content relative to controls was observed for the contralateral lymph nodes, from either the 10 nm (10 nm: 0.15 ± 0.04 μg Fe (baseline) vs. 0.20 ± 0.04 μg Fe (contralateral), $p >$

0.99) or the 30 nm (30 nm: 0.13 ± 0.01 μg Fe (baseline) vs. 0.18 ± 0.06 μg Fe (contralateral), $p > 0.99$) test groups. In contrast, the ipsilateral lymph nodes of each test group displayed more than 100-fold higher iron oxide content relative to controls (10 nm: 0.15 ± 0.04 μg Fe (baseline) vs. 21 ± 11 μg Fe (ipsilateral), $p < 0.001$; 30 nm: 0.13 ± 0.01 μg Fe (baseline) vs. 21 ± 5 μg Fe (ipsilateral), $p < 0.001$). These findings validated the MRI results and firmly corroborated that IONP-ML with both 10 nm and 30 nm cores could be delivered to the draining lymph nodes and tracked by MRI.

Significantly, both the 10 nm core and the 30 nm core IONP-ML could access the draining lymph nodes rapidly and efficiently. To reach the lymph nodes from the intradermal injection site, nanocarriers can either be actively shuttled to the lymph node by migratory dendritic cells or passively drain to the lymph nodes through the lymphatics[5, 9]. The latter mechanism is much more rapid and efficient than the former. Following administration, nanocarriers that leverage the lymphatic drainage typically reach the lymph nodes within 1-2 hours while the delivery based on the migratory cells typically displays an 8-24 hour lag time[5, 9]. In addition, delivery of 0.2%-1% of the initial dose (ID) within 2 hours of administration has been previously reported for nanocarriers that drain through the lymphatics, while the delivery by migratory cells is typically at least 10-fold less efficient[8, 9, 49]. Notably, we achieved accumulations of 9 ± 4 and 8 ± 2 % ID within 1 hour of administration for the IONP-ML with 10 nm and 30 nm cores, respectively. In addition, nanoparticles could be observed in the draining lymph nodes as early as 15 minutes post injection (Figure 3.5D). This rapid and efficient delivery is consistent with the lymphatic drainage path. Interestingly, 1-hour GE post-scans displayed a hypointense trail from the site of administration to the ipsilateral brachial lymph node (Figure 3.5D). This trail likely reflects the lymphatic vessels enhanced by the nanocarriers as they drain to the lymph nodes, directly mapping delivery of the IONP-MLs by the lymphatic drainage.

To drain to the lymph nodes following intradermal or subcutaneous administration, the nanoparticles must be convectively transported through the interstitial matrix and enter the afferent lymphatic vessels[50]. For spherical nanoparticles, this pathway is typically restricted to carriers of sub-100 nm size, likely due to the network geometry of the interstitial extracellular matrix and the sieving action of the valve-like cell-cell junctions in the lymphatic vessels[51]. Thus, the ability of the IONP-ML to leverage the lymphatic drainage reflects that these particles can robustly maintain their small sub-100 nm size *in vivo*. Interestingly, despite their larger size, the 30 nm core IONP-ML (~53 nm hydrodynamic diameter) could access the lymph nodes as

efficiently (p= 0.96) as their smaller 10 nm core counterparts (~34 nm hydrodynamic diameter). These findings are consistent with previous reports, demonstrating little difference in lymphatic trafficking between carriers within the 30-70 nm size range[52, 53]. Most significantly, the extent of the lymph node delivery for the IONP-ML of both the 10 nm and the 30 nm core sizes was 9- to 40-fold more efficient compared to the previously reported spherical particles of sub-100 nm size within similar time frames (0.2%-1% ID within 2 hr)[52]. This enhanced efficiency is likely due to the high density of surface PEGylation of the IONP-ML (~2.5 molecules/nm^2) enabled by their lipidoid-stitched coatings. Previous work demonstrated that PEGylation could significantly enhance lymph node drainage of nanocarriers by blocking interactions with the extracellular matrix at the injection site[49, 54]. It is likely that dense PEG layers on the surfaces of the IONP-ML exerted a similar effect.

IONP-ML allow surface conjugation of biomolecules at high grafting capacity and density, while maintaining sub-100 nm particle size

Delivery vectors that can rapidly and efficiently traffic to the lymph nodes while displaying biomolecules on their surfaces are highly advantageous in the context of therapeutic immunomodulation because they can mimic the presentation of antigens and adjuvants by pathogens[5, 55]. Given the highly efficient trafficking of the IONP-ML to the lymph nodes, we next sought to examine whether IONP-ML could facilitate surface display of biomolecules. To test biomolecule conjugation to the IONP-ML surface, we chose a peptide and a CpG oligonucleotide as model biomolecules. These biomolecules have demonstrated considerable potential as immunomodulatory antigens and adjuvants, respectively[56, 57].

To conjugate these model biomolecules to the nanoparticle's surface, we replaced 50% of DSPE-mPEG in the coating formulations with the functionalized lipid DSPE-PEG-PDP. Integration of functionalized phospholipids had no significant effect on either the recovery (10 nm: p = 0.99; 30 nm: p = 0.98) or the particle size (10 nm: p = 0.84; 30 nm: p = 0.99) of the resulting formulations (Supporting Information, Figure S15). Using disulfide exchange chemistry, we coupled either the CpG oligonucleotide or the peptide, each functionalized with a free thiol, to the surface of IONP-ML-PDP and then purified the nanoparticles by magnetic separation to remove unreacted biomolecules (Figure 3.6A). Quantitative analysis confirmed successful

conjugation (Figures 3.6B and 3.6C). Comparison to control (0% PDP) formulations further revealed that the majority of the nanoparticle-associated biomolecules (~95% and ~90% for the CpG and the peptide, respectively) were covalently conjugated rather than non-specifically adsorbed to the nanoparticle's surface. Under equivalent experimental conditions, higher extent of coupling was observed for the peptide compared to the CpG (10 nm: $p<0.001$, 30 nm: $p=0.02$). This is likely due to lower thiol reactivity and higher level of electrostatic repulsions associated with the higher thiol pKa and higher charge density of the oligonucleotides[58-60]. To further corroborate accessibility of the conjugated biomolecules on the nanoparticle surface, we analyzed CpG-loaded nanoparticles (IONP-ML-CpG) by anion exchange chromatography (Figure 3.6E). Control IONP-ML nanoparticles could be eluted from the quaternary ammonium column matrix with the flow-through, consistent with their nearly electroneutral surface potential (30 nm: -5 ± 2 mV, Table 3.2). In contrast, electronegative (30 nm: -20 ± 4 mV, Table 3.2) CpG-modified nanoparticles were retained by the cationic matrix and required solutions of high ionic strength (2M NaCl) for elution. Because interaction of the nanoparticle-loaded biomolecules with the column matrix requires display of the biomolecule on the particle's surface, this finding corroborated accessibility of anionic CpG on the surface of IONP-ML-CpG.

Most significantly, conjugation yielded strikingly high multivalencies and densities of biomolecule display. IONP-ML with 10 nm cores could be loaded with 102 ± 9 and 240 ± 36 molecules of CpG and peptide per particle, respectively (Figure 3.6B). These loadings are 10-fold higher than the loadings previously reported (10 molecules of CpG per particle and 23 molecules of peptide per particle) for lipid-coated iron oxide nanoparticle of similar sizes (~40 nm)[61, 62]. Furthermore, increasing the particle sizes from 10 nm to 30 nm cores allowed further increase of the loading by 27-fold (30 nm vs 10 nm: 2771 ± 205 molecules/particle vs 102 ± 9 molecules/particle, $p<0.001$) and 22-fold (30 nm vs 10 nm: 5452 ± 1654 molecules/particle vs 240 ± 36 molecules/particle) for CpG and peptide, respectively (Figure 3.6C). These loading multivalencies are comparable to the highest loadings reported so far for nanoparticles of similar sizes (2.5×10^{-11} µg peptide per particle for gold nanoparticles vs 1.8×10^{-11} µg peptide per particle for IONP-ML-peptide, 30 nm core)[63]. Likewise, the high multivalencies also translated to high densities of biomolecule display per unit surface area. Peptide loading could be achieved at densities of ~0.06 molecules/nm^2 and ~0.6 molecules/nm^2 for the 10 nm and 30 nm core IONP-MLs, respectively (Supporting Information, Table S9). These densities are more than 10-fold and 100-fold higher, respectively, than the estimated density (~0.005 molecules/nm^2) for previously reported lipid-coated iron oxide nanoparticle of similar sizes (~40 nm)[62].

Accumulating evidence reveals that the multivalency and the density of biomolecule display can significantly impact immune response because these features are pivotal to pathogen-induced immune activation[7]. In this context, several studies have explored how pathogen-associated biophysical attributes such as antigen/adjuvant surface densities affect immunity and have begun formulating the rules for design of nanoparticle-based immunomodulating technologies[64]. One elegant meta-analysis of existing viral vaccines suggested that high densities (0.01-0.05 molecules/nm^2) display of protein antigens on a nanocarrier's surface is likely to be the key for stimulating strong immune responses[7]. Each immunogenic protein further contains about 10 epitopes, yielding the density requirement of about 0.1-0.5 epitopes/nm^2 [65]. Notably, our 30 nm core IONP-ML nanoparticles can robustly fulfill this requirement, suggesting that they embody the potential for design of efficient vaccines.

Until now, high surface loadings of biomolecules could only be achieved with nanoparticles that allow direct covalent conjugation of PEG tethers to the nanoparticle's surface, such as gold nanoparticles[63]. In contrast, achieving high-capacity loading of biomolecules on nanoparticles coated by lipid self-assemblies appears to be difficult. Reported loadings have been limited to only few tens of molecules per particle[61, 62]. Previous methods to coat nanocrystals by phospholipid coatings have been based on micelle-like self-assembly[23]. Although such assemblies can facilitate biomolecule attachment, they may not be sufficiently stable to withstand biomolecule loadings at high capacity. Indeed, previous reports demonstrated significant enhancement in biomolecule loading onto the phospholipid-coated iron oxide with covalently cross-linked phospholipids[66]. In our system, the stability of the self-assembled lipid shell is likely enhanced by lipidoid-mediated stitching. This stabilization allows the shell to withstand surface loading of biomolecules at high capacity, while circumventing the need for covalent cross-linking. Examination of the nanoparticle morphology by TEM supports this notion, as high density CpG conjugation to the IONP-ML's surface did not appear to substantially perturb the nanoparticle's shell (Figure 3.6D).

Importantly, despite high-capacity conjugation of biomolecules, IONP-MLs were still able to maintain small sub-100 nm hydrodynamic diameters (Table 3.2). The biomolecule-loaded IONP-ML preserved their monodispersity as reflected by their polydispersity index of less than 0.2 (Table 3.2)[39]. In addition, both 10 nm core and 30 nm core IONP-ML-CpG (hydrodynamic diameters: 43 ± 2 nm and 81 ± 2 nm) migrated on the agarose gel (0.8%) as single bands with a narrow band spread (10 nm: ± 0.65 mm, 30 nm: ± 0.83 mm) and no evident trailing (Figure 3.6F). These migration patterns further corroborated lack of aggregation and monodispersity of

nanoparticle populations following conjugation of biomolecules[67, 68]. In addition, the content of biomolecules attached to the nanoparticle's surface was not significantly affected by incubation with serum (Supporting Information, Figure S16), suggesting that the biomolecule-loaded nanoparticles could be leveraged for delivery *in vivo*.

IONP-ML with 30 nm core size can facilitate biomolecule delivery to the lymph nodes

Intrigued by the fact that the 30 nm core IONP-ML exhibited remarkable capacity for biomolecule display while preserving small sub-100 nm size, we asked whether these particles could traffic to the lymph nodes and facilitate biomolecule delivery. To address this question, we examined lymph node delivery of the IONP-ML-CpG with 30 nm cores. To visualize the delivery of the nanocarrier-attached CpG, we complexed the CpG with the complementary fluorophore-tagged oligonucleotide strand, CpG_{comp}-Cy5.5 (Figure 3.7A). Thus, both components of our system, the nanocarrier and the biomolecule cargo, could be tracked by imaging: MRI and fluorescence imaging, respectively.

Indeed, similar to the biomolecule-free IONP-ML, biomolecule-loaded IONP-ML-CpG could efficiently access the lymph nodes as evidenced by MRI (Figure 3.7B). One hour after injection, pronounced hypointensity in the ipsilateral brachial lymph nodes was observed on both the GE and T2W images compared to respective pre-scans. This signal reduction reflected successful delivery of the biomolecule-displaying nanocarriers to the draining lymph nodes. Notably, IONP-ML-CpG showed no significant decrease in iron oxide uptake in the ipsilateral lymph nodes relative to the IONP-ML (IONP-ML: 8 ± 2% ID vs. IONP-ML-CpG: 6 ± 2% ID, $p = 0.22$, Figure 3.7C). This finding indicated that the display of CpG on the nanocarrier's surface did not significantly interfere with lymphatic trafficking. Furthermore, fluorescence imaging *in vivo* revealed a strong fluorescence signal in the axillary area ipsilateral to the injection site (Figure 3.7B). Imaging of intact excised ipsilateral and contralateral lymph nodes further confirmed that the fluorescence signal was localized to the draining brachial and axillary lymph nodes (Figure 3.7D). Moreover, comparison to a soluble antiCpG-Cy5.5 control revealed a 3.5-fold higher fluorescence for biomolecule delivery via IONP-ML-CpG relative to the control ($p < 0.001$, Figure 3.7E). These findings corroborated that the IONP-ML-CpG nanocarrier could effectively mediate the delivery of its biomolecule cargo to the draining lymph nodes. Thus,

IONP-ML can serve as a MRI-trackable platform for delivery of biomolecules to the lymph nodes.

3.5 Conclusions

Taken together, our results demonstrate that core-shell iron oxide nanoparticles IONP-ML display the desired material characteristics for MRI-trackable biomolecule delivery to the lymph nodes and surface display of biomolecules at high capacity. These functionalities of the IONP-ML are largely determined by their controlled particle sizes. To engineer IONP-ML with controlled size, we developed a novel method to coat iron oxide nanocrystals with lipid-stitched shells. This method relies on integration of lipidoids, cationic agents with hydrophobic tails, into lipid coatings to "stitch" together the opposing lipid monolayers on the iron oxide surface, likely by a combination of hydrophobic and electrostatic interactions. Formation of consistent nanocrystal coatings allowed engineering of core-shell nanoparticles with controlled particle sizes. Unlike previous methods to coat iron oxide with amphiphilic lipids, our method is not limited to coating nanocrystals with small size (< 20 nm) but can provide robust stabilization of nanocrystals with both small (< 20 nm) and large (> 20 nm) sizes.

In the context of immunomodulation, size is one of the key parameters in determining the nanocarrier's biological performance. The range of nanoparticle sizes that can achieve direct access to the lymph nodes through lymphatic drainage has an upper limit of approximately 100 nm. Thus, it is important to develop biomolecule-displaying nanocarriers with sizes below this threshold. Indeed, the IONP-ML with both 10 nm and 30 nm core sizes, translating to ~34 nm and ~53 nm hydrodynamic diameters, could rapidly and efficiently access the lymph nodes. Within the sub-100nm size range, larger nanocarriers offer an additional advantage of larger surface area and thus larger capacity for biomolecule display while still preserving the capability to leverage lymphatic drainage. Indeed, the 30 nm core (~53 nm hydrodynamic diameter) IONP-ML displayed biomolecule loading capacities among the highest reported to date while also accessing the lymph nodes rapidly and efficiently. Carriers that can mimic the biophysical attributes of pathogens, including small size and high multivalency/density of biomolecule display, possess a significant potential for design of effective pathogen-mimetic vaccines. Thus, by allowing stabilization of nanocrystals of both small and large sizes, our method offers a versatile nanoplatform design that could potentially be leveraged to direct immune responses for specific therapeutic applications.

Finally, our coating method also allowed preservation of the iron oxide's magnetic properties. Consequently, high r2 relaxivities of the IONP-ML could be harnessed for *in vivo* tracking of these nanoparticles by MRI. The ability to visualize the nanocarriers by non-invasive imaging offers attractive benefits of tracking delivery and personalizing dosage regimens to augment therapeutic benefit.

Overall, the combination of properties displayed by IONP-ML including controlled sub-100 nm size, high r2 relaxivities and high capacities for biomolecule display makes these particles attractive platforms for MRI-trackable delivery of biomolecules to the lymph nodes. The versatility and multifunctionality of these platforms could potentially be leveraged for rational design of a wide variety of image-guided immunomotherapy applications.

3.6 Acknowledgements

This work was supported in part by the St. Baldrick's Foundation Career Award (B.C.) and the UM College of Pharmacy faculty start-up fund (B.C.). We thank Martin Maier and Muthusamy Jayaraman from Alnylam Pharmaceuticals for the generous gift of C12-98(5) to support our animal work.

3.7 Authorship

Ryan M. Clauson,[†] Mingsheng Chen,[†] Lindsay M. Scheetz,[†] Brendan Berg,[‡] and Beata Chertok*,[†,‡]

[†]Department of Pharmaceutical Sciences, College of Pharmacy, and [‡]Department of Biomedical Engineering, College of Engineering, University of Michigan, Ann Arbor, Michigan 48109, United States

* Corresponding Author

3.8 Figures

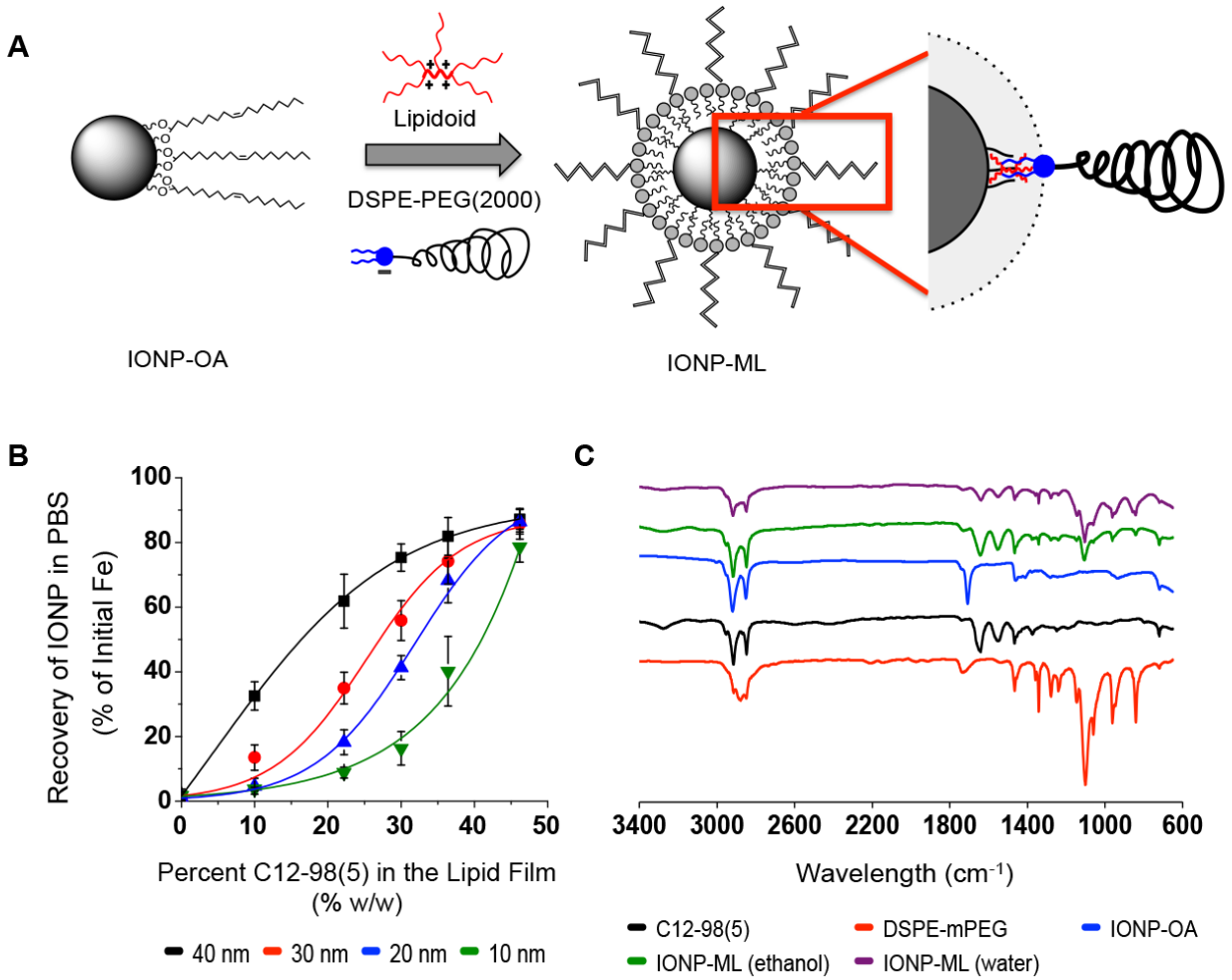

Figure 3.1 - Formulation of multi-lipid-coated iron-oxide nanoparticles (IONP-ML). (A) Schematic depiction of IONP-ML formulation method. (B) Dependence of the nanocrystal stabilization efficiency on the content of C12-98(5) lipidoid in lipid formulations; Data represents mean ± S.D., n ≥ 3; the curves depict fits using Boltzmann sigmoidal model, R^2 = 0.99; p < 0.001 (40 nm) or three parameter non-linear logistic model, R^2 = 0.99; p < 0.001 (30 nm), R^2 = 0.99; p < 0.001 (20 nm), R^2 = 0.99; p < 0.001 (10 nm); (C) Representative FT-IR spectra of IONP-ML and formulation components. S.D., standard deviation.

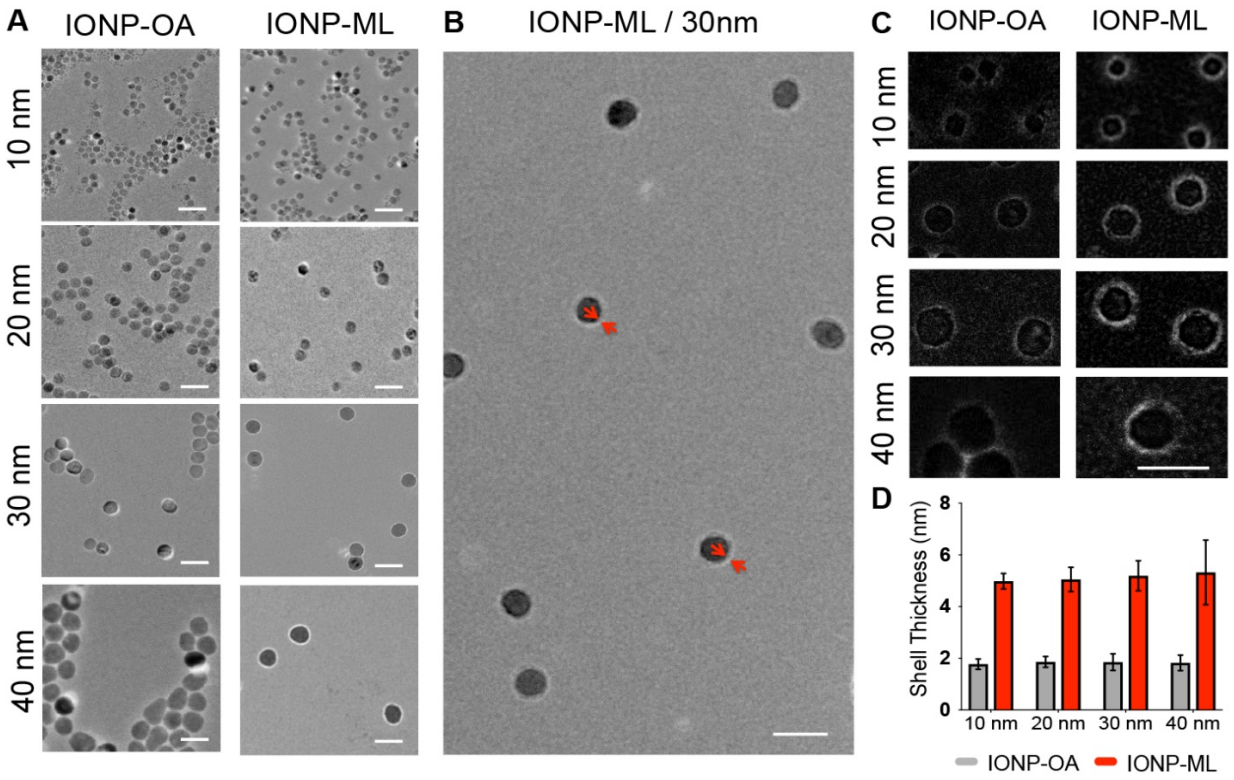

Figure 3.2 - Characterization of IONP-ML by TEM. (A) Representative TEM micrographs of the original oleic acid stabilized nanocrystals (IONP-OA) dispersed in chloroform (left column) and the multi-lipid stabilized IONPs (IONP-ML) dispersed in water (right column). (B) Representative TEM micrograph of 30 nm IONP-ML dispersed in water, arrows identify lipid shell layer. (C) Representative IONP-OA and IONP-ML TEM micrographs; background subtraction was carried out according to the method of Hartig to better visualize shell morphology.[59] (D) Quantitative analysis of the lipid shell thickness, quantified from TEM micrographs; Data represents mean ± S.D, n ≥ 50. TEM, transmission electron microscopy; S.D., standard deviation. Scale bars: 50 nm.

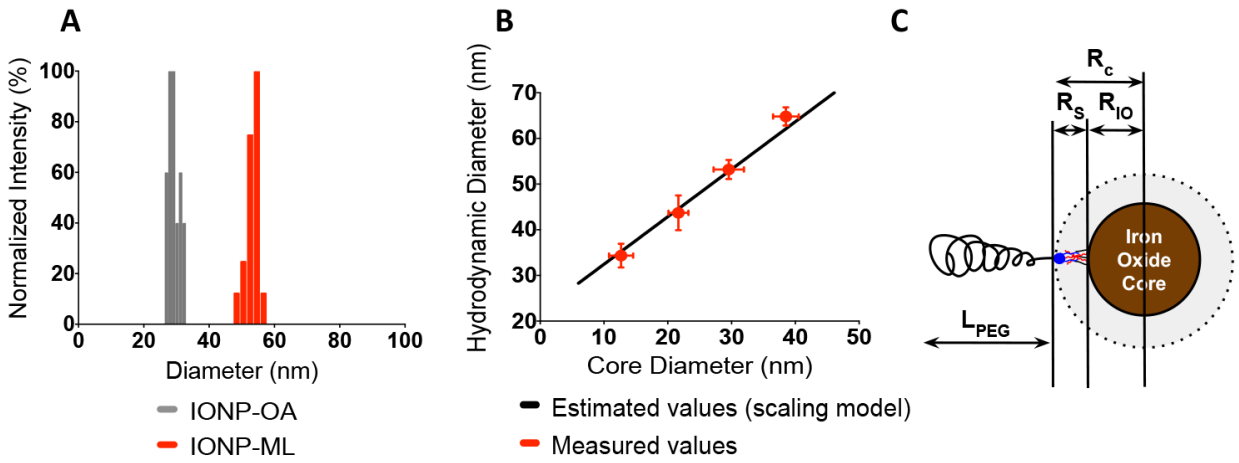

Figure 3.3 - Size control of the IONP-ML. (A) Reproducibility of particle size across formulations: histograms represent distributions of mean particle size for repeated IONP-ML formulations and respective original nanocrystal samples IONP-OA with 30 nm cores (n = 18, formulation replicates). (B) Correlation between the hydrodynamic diameter of the coated particles IONP-ML (DLS, 10 nm - 30 nm: n = 7, 40 nm: n = 3) and the core diameters of respective nanocrystals IONP-OA (TEM, 10 nm – 40 nm: n ≥ 75); Data represents mean ± S.D; Pearson R^2 coefficient 0.98, $p < 0.001$; Theoretical values were calculated using a scaling model; model is described in Supporting Information, Section 5 and 6. (C) Schematic depiction of the scaling model; L= thickness of the PEG layer, R_s = radius of the interdigitated lipid shell, R_{IO} =radius of the iron-oxide nanocrystal's core, R_c = radius of the "hard sphere"; description of the model is provided in Supporting Information, Section 5 and 6. TEM, transmission electron microscopy; DLS, dynamic light scattering; S.D., standard deviation.

Nanoparticle	Core Diameter[1] (nm)	Hydrodynamic Diameter[2] (nm)	Polydispersity Index[2] (PDI)	Zeta-Potential[2] (mV)
IONP- ML	13 ± 2	35 ± 3	0.17 ± 0.05	-4 ± 1
	22 ± 2	44 ± 4	0.19 ± 0.02	-4 ± 1
	30 ± 2	53 ± 2	0.15 ± 0.06	-5 ± 2
	39 ± 2	65 ± 2	0.16 ± 0.03	-4 ± 2

Table 3.1. Characterization of the IONP-ML nanoparticles

[1]Core diameters measured by TEM; Data represents mean ± S.D., n = 75.
[2]Samples were dispersed in phosphate-buffered saline (PBS), pH 7.4; Data represents mean ± S.D.,
n ≥ 5.

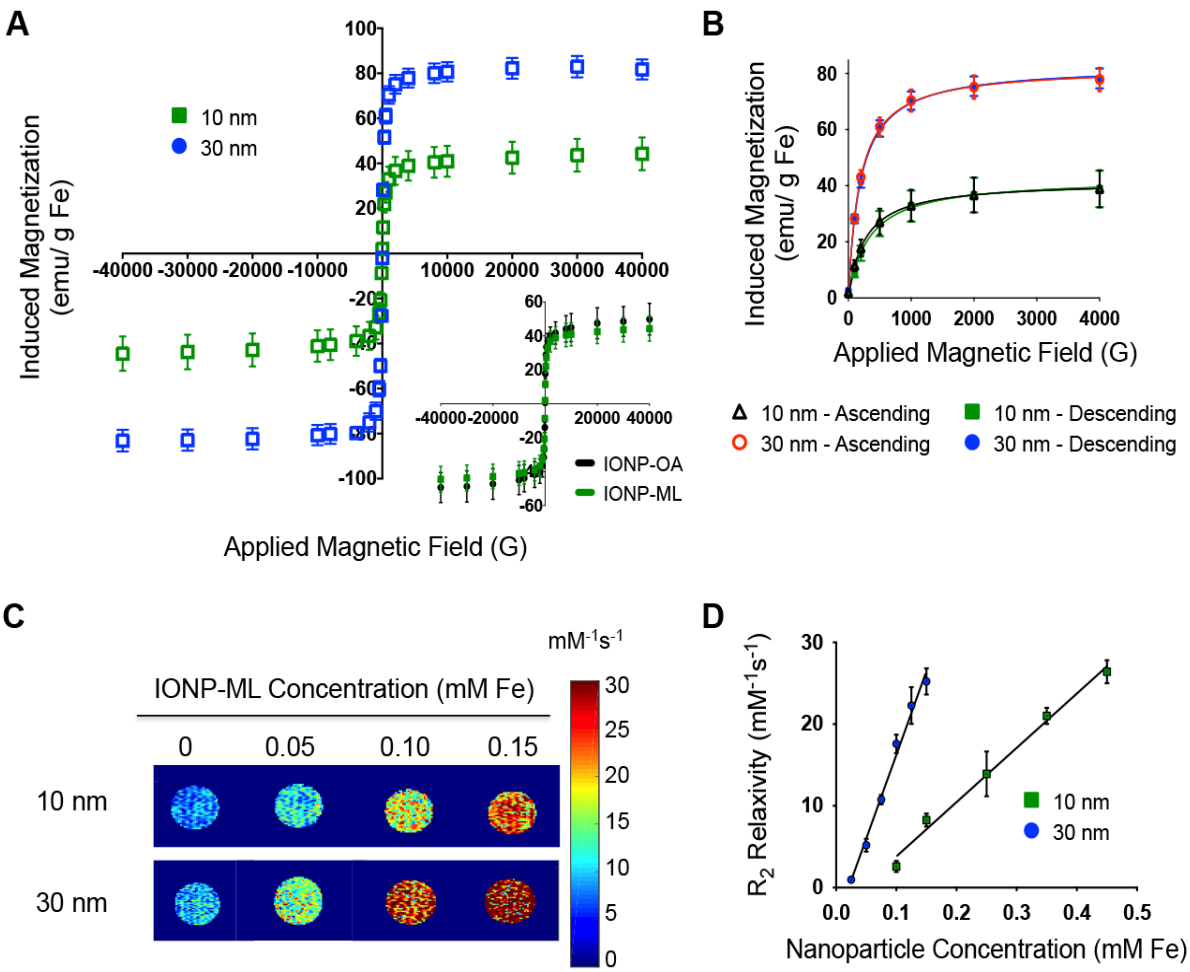

Figure 3.4 - Evaluation of IONP-ML's magnetic properties. (A) Induced magnetization of the IONP-ML in an applied magnetic field, measured by SQUID magnetometry; Data represents mean ± S.D., n = 3. (A-Insert) Comparison of the induced magnetization for original IONP-OA and IONP-ML (10 nm core); Data represents mean ± S.D., n = 3. (B) Analysis of superparamagnetic behavior: induced magnetization with increasing and subsequently decreasing applied magnetic fields; Data represents mean ± S.D, n = 3; the curves depict fits using hyperbolic model, R^2 = 0.92; p < 0.001 (10 nm ascending), R^2 = 0.93; p < 0.001 (10 nm descending), R^2 = 0.99; p < 0.001 (30 nm ascending), R^2 = 0.99; *p* < 0.001 (30 nm descending); Data represents mean ± S.D., n = 3. (C) Representative R_2 relaxivity maps for aqueous solutions of IONP-MLs *in-vitro*; Color bar represents R_2 relaxivity values ($mM^{-1}s^{-1}$). (D) R_2 relaxivity of IONP-MLs dispersed in 100 mM PBS, pH 7.4; Data represents mean ± S.D, n = 3; Curves are fitted using linear regression model R^2 = 0.97; p < 0.001 (10 nm), R^2 = 0.99; p < 0.001 (30 nm). SQUID, superconducting quantum interference device; S.D., standard deviation.

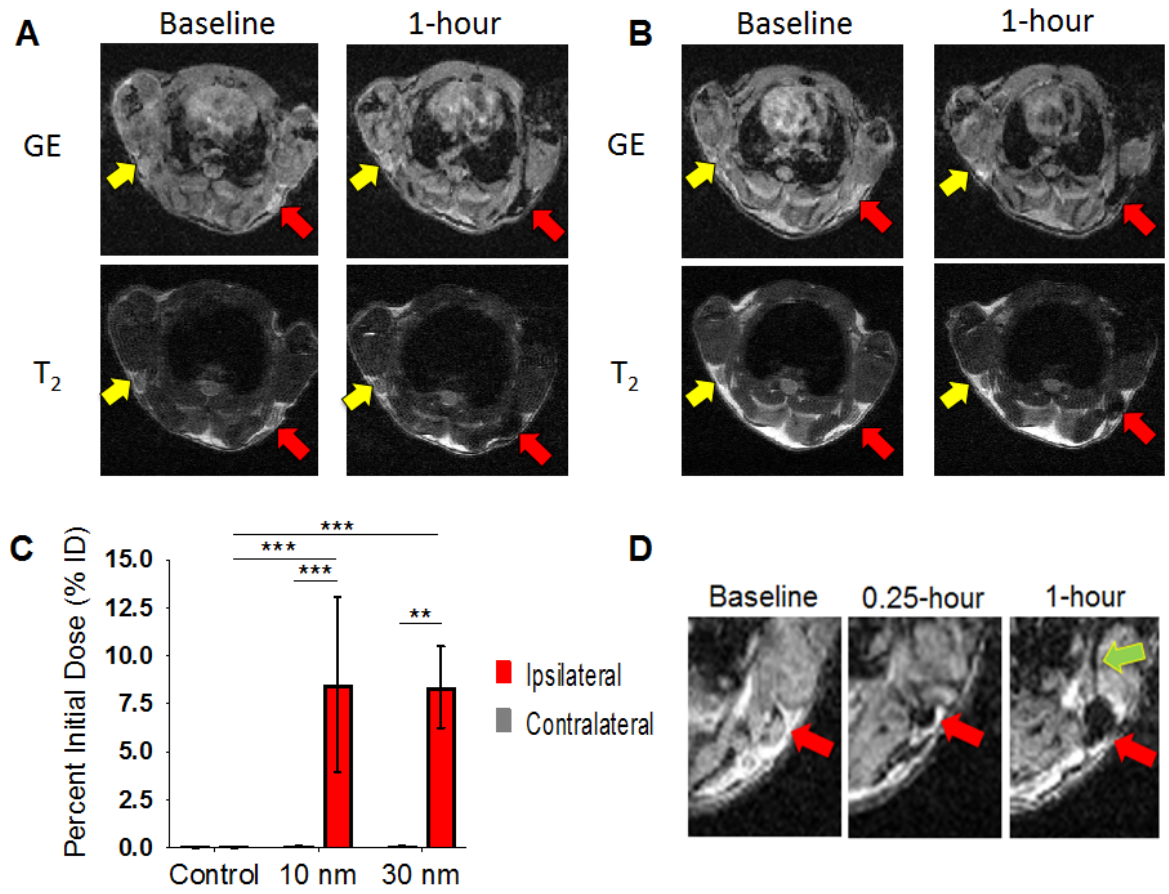

Figure 3.5 - *In-vivo* MRI-tracked lymph node delivery of the IONP-ML following intradermal administration. (A) Representative gradient-echo (GE) and T2-weighted (T_2) MRI images acquired before (baseline) and after (1-hour) administration of 10 nm core IONP-ML. Arrows depict contralateral (yellow), and ipsilateral (red) brachial lymph nodes. (B) Representative gradient-echo (GE) and T2-weighted (T_2) MRI images acquired before (baseline) and after (1-hour) administration of 30 nm core IONP-ML. Arrows depict contralateral (yellow), and ipsilateral (red) brachial lymph nodes. (C) Quantitative analysis of iron oxide concentrations in intact excised lymph nodes by ESR spectroscopy; Data (mean ± S.D, n ≥ 3) represent percent of injected dose delivered to either ipsilateral or contralateral lymph nodes (axillary and brachial lymph nodes combined). (D) Representative GE images depicting ipsilateral brachial lymph nodes before and sequentially after injection of IONP-ML with 30 nm cores. Statistical comparisons are based on one-way ANOVA, followed by *post hoc* Tukey's pairwise comparisons. Asterisks denote statistical significance at the level of **p < 0.01, ***p < 0.001. ANOVA, analysis of variance; S.D., standard deviation. MRI, magnetic resonance imaging; ESR spectroscopy, electron spin resonance spectroscopy; S.D., standard deviation.

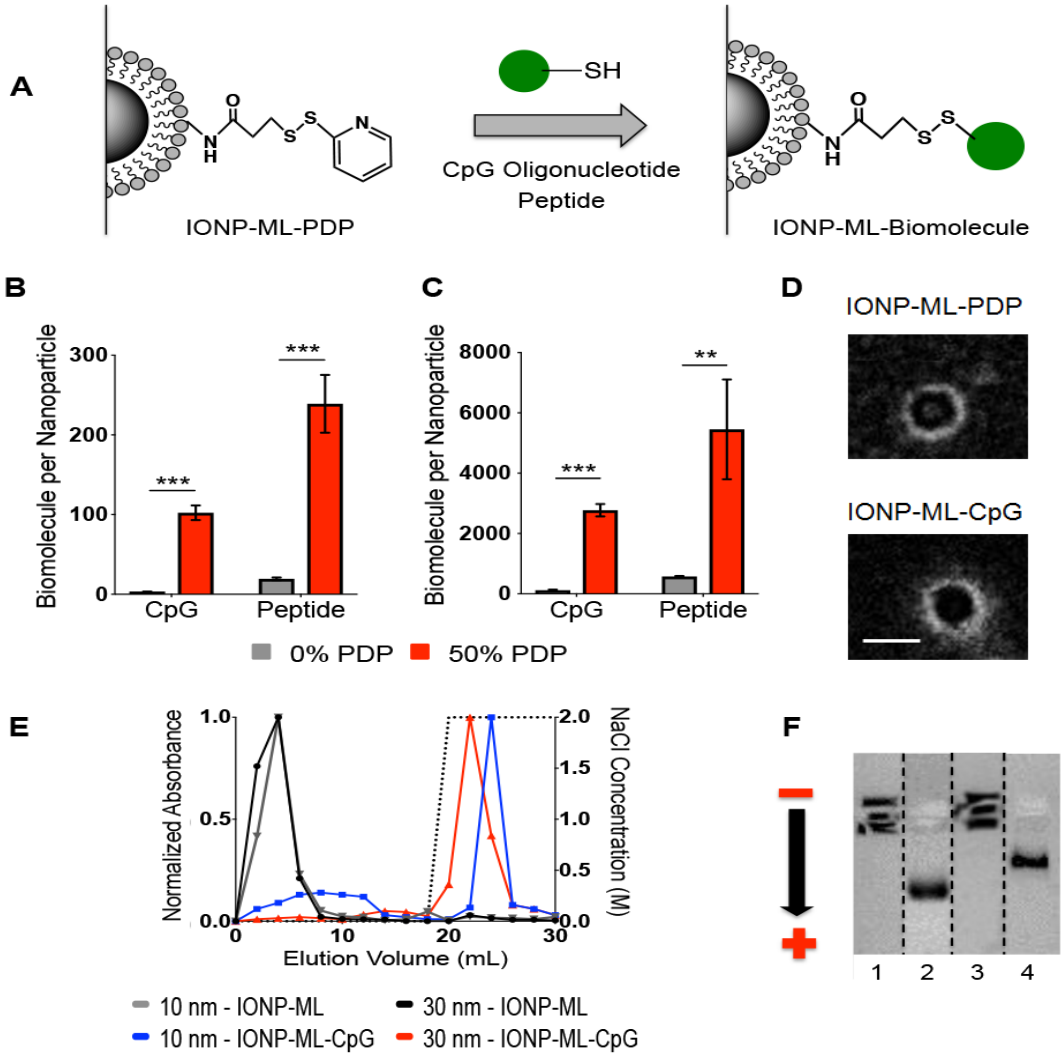

Figure 3.6 - Conjugation of model biomolecules (CpG oligonucleotide and peptide) to the surface of IONP-ML. (A) Schematic depiction of the chemical conjugation route to load model biomolecules to the surface of IONP-ML. (B) Quantitative analysis of functionalization with CpG oligonucleotide and peptide for IONP-ML-PDP with 10 nm core size; Data represents mean ± S.D, n = 3;. (C) Quantitative analysis of functionalization with CpG oligonucleotide and peptide for IONP-ML-PDP with 30 nm core size; Data represents mean ± S.D, n = 3;.(D) Representative TEM micrographs of IONP-ML-PDP before and after surface modification with CpG (IONP-ML-CpG); scale bar: 10 nm. (E) Evaluation of IONP-ML-CpG by anion exchange chromatography (2M NaCl eluent). (F) Evaluation of IONP-ML-CpG by agarose gel electrophoresis (0.8% agarose, TAE, 75 V, 15 minutes; Lanes: (1) 10 nm core IONP-ML-PDP control, (2) 10 nm core IONP-ML-CpG, (3) 30 nm core IONP-ML-PDP control, (4) 30 nm core IONP-ML-CpG; Statistical comparisons are based on two-tailed unpaired Student's t-test. Asterisks denote statistical significance at the level of **p < 0.01, ***p < 0.001. TEM, transmission electron microscopy; S.D., standard deviation.

Nanoparticle	Core Diameter (nm)	Hydrodynamic Diameter (nm)	Polydispersity Index (PDI)	Zeta-Potential (mV)
IONP-ML-PDP	~10	35 ± 3	0.17 ± 0.05	-4 ± 1
	~30	53 ± 2	0.15 ± 0.06	-5 ± 2
IONP-ML-CpG	~10	43 ± 2	0.20 ± 0.01	-22 ± 2
	~30	81 ± 2	0.12 ± 0.02	-20 ± 4
IONP-ML-Peptide	~10	49 ± 2	0.18 ± 0.08	-3 ± 1
	~30	86 ± 4	0.16 ± 0.02	-1 ± 2

Table 3.2 - Characterization of IONP-ML-CpG and IONP-ML-Peptide nanoparticles.

Samples were dispersed in phosphate-buffered saline (PBS), pH 7.4;
Data represents mean ± S.D., n ≥ 5.

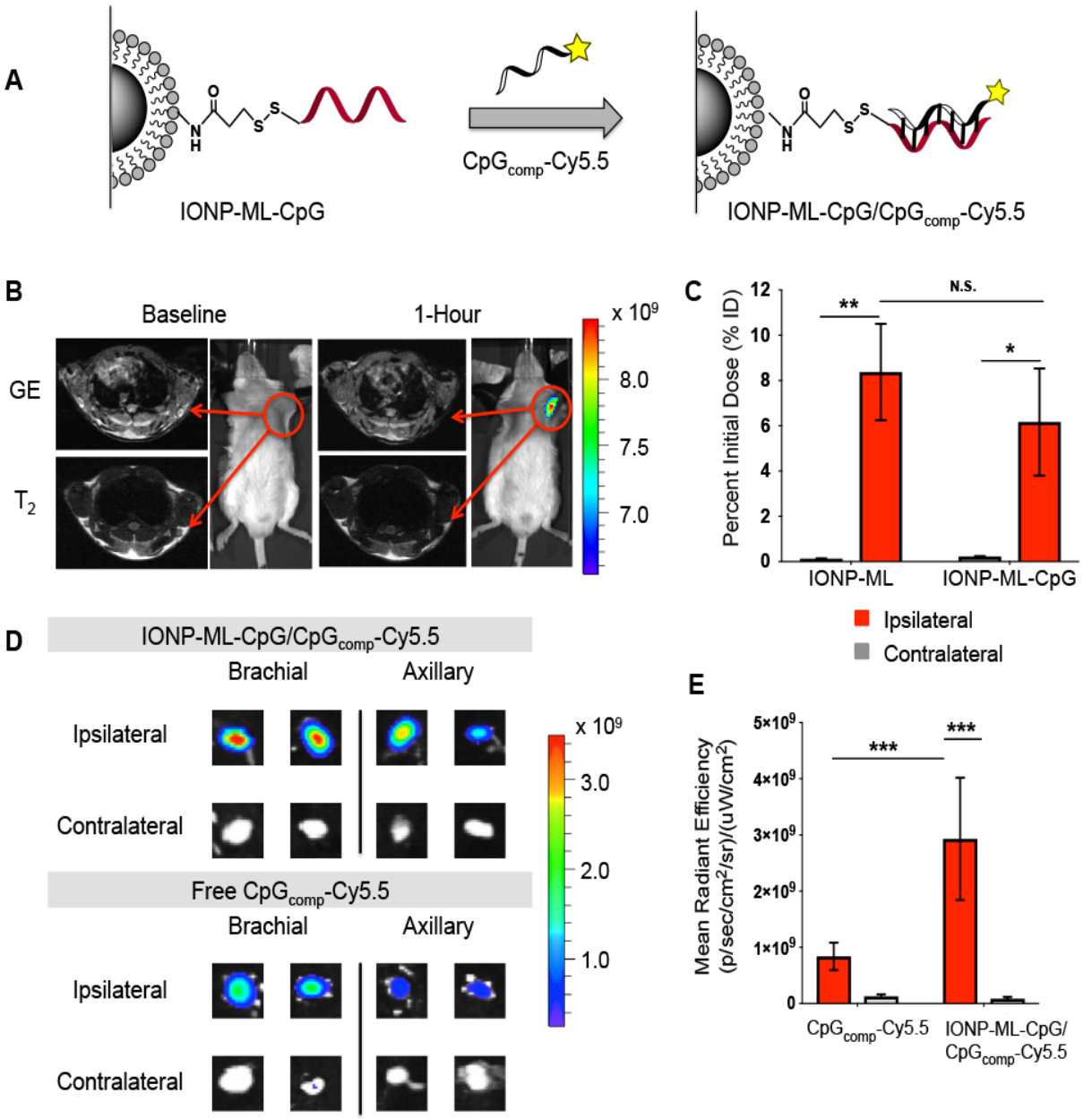

Figure 3.7 - *In vivo* lymph node delivery of biomolecule-displaying IONP-ML-CpG following intradermal injection. (A) Labeling of IONP-ML-CpG with a fluorescently-tagged CpG$_{comp}$-Cy5.5 via complementary base pairing (IONP-ML-CpG/CpG$_{comp}$-Cy5.5. (B) Representative GE and T_2 weighted MRI images and IVIS fluorescence images (Ex/Em = 675/720 nm, exposure = 0.25 s) acquired before (baseline) and after (1 hour) administration of fluorescently labeled IONP-ML-CpG/CpG$_{comp}$-Cy5.5 (30 nm core); Arrows identify brachial lymph node on GE and T_2-weighted MRI images. Color bar represents mean radiant efficiency expressed as photon flux per second per square centimeter per steradian divided by microwatt per square centimeter (p/sec/cm^2/sr)/(μW/cm^2). (C) *Ex vivo* quantitative analysis of nanoparticle delivery to the ipsilateral and contralateral lymph nodes (axillary and brachial lymph nodes combined) following

intradermal injection of 30 nm core IONP-ML and IONP-ML-CpG, (measured by ESR spectroscopy); Data represents mean ± S.D, n ≥ 3. (D) Representative fluorescence images of ipsilateral and contralateral lymph nodes *ex vivo*, acquired 1 hour after intradermal injection of IONP-ML-CpG/CpG_{comp}-Cy5.5 and free CpG_{comp}-Cy5.5 (Ex/Em = 640/675 nm, exposure = 0.25 s). Color bar represents mean radiant efficiency (p/sec/cm^2/sr)/(μW/cm^2). (E) Quantitative analysis of CpG_{comp}-Cy5.5 delivery to ipsilateral and contralateral lymph nodes (axillary and brachial lymph nodes combined) following intradermal injection of free CpG-Cy5.5 and IONP-ML-CpG/CpG_{comp}-Cy5.5; Data represents mean ± S.D, n = 4; Statistical comparisons are based on one-way ANOVA, followed by *post hoc* Tukey's pairwise comparisons. Asterisks denote statistical significance at the level of *$p < 0.05$, **$p < 0.01$, ***$p < 0.001$. N.S. denotes no statistical significance. MRI, magnetic resonance imaging; ESR spectroscopy, electron spin resonance spectroscopy; ANOVA, analysis of variance; S.D., standard deviation.

3.8 Supporting Information

This material is published in *ACS Applied Materials and* Interfaces. The following supporting information and figures are available in Appendix B. Coating of iron oxide nanocrystals by modified thin film hydration, lipidoid synthesis, screening of lipidoids and cationic phospholipids for iron oxide stabilization, analysis of lipid coating composition by TLC, determination of PEG packing density, theoretical size estimation of PEGylated core-shell iron oxide nanoparticles, characterization of PDP-functionalized nanoparticles, estimation of biomolecule loading: mutivalency and surface density.

3.9 Bibliography

1 Trevaskis, N. L., Kaminskas, L. M. & Porter, C. J. H. From sewer to saviour - targeting the lymphatic system to promote drug exposure and activity. *Nat. Rev. Drug Discovery* 14, 781-803, doi:10.1038/nrd4608 (2015).

2 Toy, R. & Roy, K. Engineering nanoparticles to overcome barriers to immunotherapy. *Bioeng. Transl. Med.* 1, 47-62, doi:10.1002/btm2.10005 (2016).

3 Zhao, L. *et al.* Nanoparticle vaccines. *Vaccine* 32, 327-337, doi:10.1016/j.vaccine.2013.11.069 (2014).

4 Desai, N. Challenges in Development of Nanoparticle-Based Therapeutics. *Aaps J* 14, 282-295, doi:10.1208/s12248-012-9339-4 (2012).

5 Bachmann, M. F. & Jennings, G. T. Vaccine delivery: a matter of size, geometry, kinetics and molecular patterns. *Nat. Rev. Immunol.* 10, 787-796, doi:10.1038/nri2868 (2010).

6 Mora-Solano, C. & Collier, J. H. Engaging adaptive immunity with biomaterials. *J. Mater. Chem. B* 2, 2409-2421, doi:10.1039/c3tb21549k (2014).

7 Cheng, W. The Density Code for the Development of a Vaccine? *J. Pharm. Sci.* 105, 3223-3232, doi:10.1016/j.xphs.2016.07.020 (2016).

8 Reddy, S. T., Rehor, A., Schmoekel, H. G., Hubbell, J. A. & Swartz, M. A. In vivo targeting of dendritic cells in lymph nodes with poly(propylene sulfide) nanoparticles. *J. Control Release* 112, 26-34, doi:10.1016/j.jconrel.2006.01.006 (2006).

9 Manolova, V. *et al.* Nanoparticles target distinct dendritic cell populations according to their size. *Eur. J. Immunol.* 38, 1404-1413, doi:10.1002/eji.200737984 (2008).

10 Ren, X. Q., Chen, H. W., Yang, V. & Sun, D. X. Iron oxide nanoparticle-based theranostics for cancer imaging and therapy. *Front. Chem. Sci. Eng.* 8, 253-264, doi:10.1007/s11705-014-1425-y (2014).

11 Pusic, K. *et al.* Iron oxide nanoparticles as a clinically acceptable delivery platform for a recombinant blood-stage human malaria vaccine. *Faseb J* 27, 1153-1166, doi:10.1096/fj.12-218362 (2013).

12 Wu, W., He, Q. G. & Jiang, C. Z. Magnetic Iron Oxide Nanoparticles: Synthesis and Surface Functionalization Strategies. *Nanoscale Res. Lett.* 3, 397-415, doi:10.1007/s11671-008-9174-9 (2008).

13 Li, W. L., Lee, S. S., Wu, J. W., Hinton, C. H. & Fortner, J. D. Shape and size controlled synthesis of uniform iron oxide nanocrystals through new non-hydrolytic routes. *Nanotechnology* 27, 1-7, doi:Artn 32400210.1088/0957-4484/27/32/324002 (2016).

14 Chertok, B. *et al.* Iron oxide nanoparticles as a drug delivery vehicle for MRI monitored magnetic targeting of brain tumors. *Biomaterials* 29, 487-496, doi:10.1016/j.biomaterials.2007.08.050 (2008).

15 Na, H. B., Song, I. C. & Hyeon, T. Inorganic Nanoparticles for MRI Contrast Agents. *Adv Mater* 21, 2133-2148, doi:10.1002/adma.200802366 (2009).

16 Lammers, T., Kiessling, F., Hennink, W. E. & Storm, G. Nanotheranostics and Image-Guided Drug Delivery: Current Concepts and Future Directions. *Mol. Pharmaceutics* 7, 1899-1912, doi:10.1021/mp100228v (2010).

17 Shen, Z. Y. *et al.* Multifunctional Theranostic Nanoparticles Based on Exceedingly Small Magnetic Iron Oxide Nanoparticles for T-1-Weighted Magnetic Resonance Imaging and Chemotherapy. *Acs Nano* 11, 10992-11004, doi:10.1021/acsnano.7b04924 (2017).

18 Yen, S. K., Padmanabhan, P. & Selvan, S. T. Multifunctional Iron Oxide Nanoparticles for Diagnostics, Therapy and Macromolecule Delivery. *Theranostics* 3, 975-992, doi:10.7150/thno.4827 (2013).

19 Hyeon, T., Lee, S. S., Park, J., Chung, Y. & Na, H. B. Synthesis of highly crystalline and monodisperse maghemite nanocrystallites without a size-selection process. *Journal of the American Chemical Society* 123, 12798-12801 (2001).

20 Smolensky, E. D., Park, H. Y. E., Berquo, T. S. & Pierre, V. C. Surface functionalization of magnetic iron oxide nanoparticles for MRI applications - effect of anchoring group and

ligand exchange protocol. *Contrast Media Mol. Imaging* 6, 189-199, doi:10.1002/cmmi.417 (2011).

21 Lee, H. *et al.* Thermally cross-linked superparamagnetic iron oxide nanoparticles: Synthesis and application as a dual Imaging probe for cancer in vivo. *J. Am. Chem. Soc.* 129, 12739-12745, doi:10.1021/ja072210i (2007).

22 Soenen, S. J. H., Hodenius, M. & De Cuyper, M. Magnetoliposomes: versatile innovative nanocolloids for use in biotechnology and biomedicine. *Nanomedicine* 4, 177-191, doi:10.2217/17435889.4.2.177 (2009).

23 Tong, S., Hou, S., Ren, B., Zheng, Z. & Bao, G. Self-assembly of phospholipid-PEG coating on nanoparticles through dual solvent exchange. *Nano Lett.* 11, 3720-3726, doi:10.1021/nl201978c (2011).

24 Chen, Y. J. *et al.* Synthesis, self-assembly, and characterization of PEG-coated iron oxide nanoparticles as potential MRI contrast agent. *Drug Dev. Ind. Pharm.* 36, 1235-1244, doi:10.3109/03639041003710151 (2010).

25 Shtykova, E. V. *et al.* Structure and properties of iron oxide nanoparticles encapsulated by phospholipids with poly(ethylene glycol) tails. *J. Phys. Chem. C* 111, 18078-18086, doi:10.1021/jp075235c (2007).

26 Huang, X. L. *et al.* Self-assembled virus-like particles with magnetic cores. *Nano Lett.* 7, 2407-2416, doi:10.1021/nl071083l (2007).

27 Zhang, L., Spurlin, T. A., Gewirth, A. A. & Granick, S. Electrostatic stitching in gel-phase supported phospholipid bilayers. *J. Phys. Chem. B* 110, 33-35, doi:10.1021/jp055995s (2006).

28 Meyer, T. A., Quinto, C. A. & Bao, G. Control of Iron Oxide Nanoparticle Clustering Using Dual Solvent Exchange. *Ieee Magn Lett* 7, doi:Artn 170090410.1109/Lmag.2015.2508006 (2016).

29 Poselt, E. *et al.* Relaxivity Optimization of a PEGylated Iron-Oxide-Based Negative Magnetic Resonance Contrast Agent for T-2-Weighted Spin-Echo Imaging. *Acs Nano* 6, 1619-1624, doi:10.1021/nn204591r (2012).

30 Lee, N. & Hyeon, T. Designed synthesis of uniformly sized iron oxide nanoparticles for efficient magnetic resonance imaging contrast agents. *Chem. Soc. Rev.* 41, 2575-2589, doi:10.1039/c1cs15248c (2012).

31 Chertok, B., Cole, A. J., David, A. E. & Yang, V. C. Comparison of electron spin resonance spectroscopy and inductively-coupled plasma optical emission spectroscopy for biodistribution analysis of iron-oxide nanoparticles. *Mol. Pharmaceutics* 7, 375-385, doi:10.1021/mp900161h (2010).

32 Akinc, A. *et al.* A combinatorial library of lipid-like materials for delivery of RNAi therapeutics. *Nat Biotechnol* 26, 561-569, doi:10.1038/nbt1402 (2008).

33 Hartig, S. M. Basic image analysis and manipulation in ImageJ. *Curr. Protoc. Mol. Biol.* Chapter 14, 14.15.11-14.15.13, doi:10.1002/0471142727.mb1415s102 (2013).

34 Suenaga, E. & Nakamura, H. Prestaining method as a useful tool for the agarose gel electrophoretic detection of polymerase chain reaction products with a fluorescent dye SYBR (R) gold nucleic acid gel stain. *Anal. Sci.* 21, 619-623, doi:DOI 10.2116/analsci.21.619 (2005).

35 Chertok, B., David, A. E. & Yang, V. C. Polyethyleneimine-modified iron oxide nanoparticles for brain tumor drug delivery using magnetic targeting and intra-carotid administration. *Biomaterials* 31, 6317-6324, doi:10.1016/j.biomaterials.2010.04.043 (2010).

36 Thorek, D. L. J. *et al.* Non-invasive mapping of deep-tissue lymph nodes in live animals using a multimodal PET/MRI nanoparticle. *Nat Commun* 5, 1-9, doi:ARTN 309710.1038/ncomms4097 (2014).

37 Saegusa, K. & Ishii, F. Triangular phase diagrams in the phospholipid-water-alcohol system for the preparation of lipid vesicles (liposomes) using the coacervation technique. *Langmuir* 18, 5984-5988, doi:UNSP LA011841210.1021/la0118412 (2002).

38 Radu, M. *et al.* Exposure to Iron Oxide Nanoparticles Coated with Phospholipid-Based Polymeric Micelles Induces Biochemical and Histopathological Pulmonary Changes in Mice. *Int. J. Mol. Sci.* 16, 29417-29435, doi:10.3390/ijms161226173 (2015).

39 Araujo-Neto, R. P. *et al.* Monodisperse sodium oleate coated magnetite high susceptibility nanoparticles for hyperthermia applications. *J. Magn. Magn. Mater.* 364, 72-79, doi:10.1010/j.jmmm.2014.04.001 (2014).

40 Tong, S., Hou, S., Zheng, Z., Zhou, J. & Bao, G. Coating optimization of superparamagnetic iron oxide nanoparticles for high T2 relaxivity. *Nano Lett.* 10, 4607-4613, doi:10.1021/nl102623x (2010).

41 Needham, D. & Dewhirst, M. W. Materials Science and Engineering of the Low Temperature Sensitive Liposome (LTSL): Composition-Structure-Property Relationships That Underlie its Design and Performance. *Rsc Smart Mater*, 33-79, doi:10.1039/9781849736800-00033 (2013).

42 Johnsson, M., Hansson, P. & Edwards, K. Spherical micelles and other self-assembled structures in dilute aqueous mixtures of poly(ethylene glycol) lipids. *J. Phys. Chem. B* 105, 8420-8430, doi:10.1021/jp0110881 (2001).

43 Kalidasan, V., Liu, X. L., Herng, T. S., Yang, Y. & Ding, J. Bovine Serum Albumin-Conjugated Ferrimagnetic Iron Oxide Nanoparticles to Enhance the Biocompatibility and Magnetic Hyperthermia Performance. *Nano-Micro Lett.* 8, 80-93, doi:10.1007/s40820-015-0065-1 (2016).

44 Wang, Y. X. J., Hussain, S. M. & Krestin, G. P. Superparamagnetic iron oxide contrast agents: physicochemical characteristics and applications in MR imaging. *Eur Radiol* 11, 2319-2331, doi:DOI 10.1007/s003300100908 (2001).

45 Bietenbeck, M., Florian, A., Faber, C., Sechtem, U. & Yilmaz, A. Remote magnetic targeting of iron oxide nanoparticles for cardiovascular diagnosis and therapeutic drug delivery: where are we now? *Int. J. Nanomed.* 11, 3191-3203, doi:10.2147/Ijn.S110542 (2016).

46 Yoo, D., Lee, J. H., Shin, T. H. & Cheon, J. Theranostic Magnetic Nanoparticles. *Accounts Chem Res* 44, 863-874, doi:10.1021/ar200085c (2011).

47 Corot, C., Robert, P., Idee, J. M. & Port, M. Recent advances in iron oxide nanocrystal technology for medical imaging. *Adv Drug Deliver Rev* 58, 1471-1504, doi:10.1016/j.addr.2006.09.013 (2006).

48 Daldrup-Link, H. E. *et al.* MRI of Tumor-Associated Macrophages with Clinically Applicable Iron Oxide Nanoparticles. *Clin Cancer Res* 17, 5695-5704, doi:10.1158/1078-0432.Ccr-10-3420 (2011).

49 Mueller, S. N., Tian, S. M. & DeSimone, J. M. Rapid and Persistent Delivery of Antigen by Lymph Node Targeting PRINT Nanoparticle Vaccine Carrier To Promote Humoral Immunity. *Mol. Pharmaceutics* 12, 1356-1365, doi:10.1021/mp500589c (2015).

50 Swartz, M. A. The physiology of the lymphatic system. *Adv. Drug Delivery Rev.* 50, 3-20, doi:Doi 10.1016/S0169-409x(01)00150-8 (2001).

51 Leak, L. V. Studies on the permeability of lymphatic capillaries. *J. Cell Biol.* 50, 300-323 (1971).

52 Kjellman, P., Fredriksson, S., Kjellman, C., Strand, S. E. & Zandt, R. I. Size-dependent lymphatic uptake of nanoscale-tailored particles as tumor mass increases. *Future Sci. OA* 1, doi:10.4155/fso.15.60 (2015).

53 Hawley, A. E., Davis, S. S. & Illum, L. Targeting of Colloids to Lymph-Nodes - Influence of Lymphatic Physiology and Colloidal Characteristics. *Adv. Drug Delivery Rev.* 17, 129-148, doi:Doi 10.1016/0169-409x(95)00045-9 (1995).

54 De Koker, S. *et al.* Engineering Polymer Hydrogel Nanoparticles for Lymph Node-Targeted Delivery. *Angew. Chem. Int. Edit.* 55, 1334-1339, doi:10.1002/anie.201508626 (2016).

55 Irvine, D. J., Hanson, M. C., Rakhra, K. & Tokatlian, T. Synthetic Nanoparticles for Vaccines and Immunotherapy. *Chem. Rev.*, 11109–11146, doi:10.1021/acs.chemrev.5b00109 (2015).

56 Li, W., Joshi, M. D., Singhania, S., Ramsey, K. H. & Murthy, A. K. Peptide Vaccine: Progress and Challenges. *Vaccines* 2, 515-536, doi:10.3390/vaccines2030515 (2014).

57 Shirota, H., Tross, D. & Klinman, D. M. CpG Oligonucleotides as Cancer Vaccine Adjuvants. *Vaccines* 3, 390-407, doi:10.3390/vaccines3020390 (2015).

58 Wall, S. B., Oh, J. Y., Diers, A. R. & Landar, A. Oxidative modification of proteins: an emerging mechanism of cell signaling. *Front Physiol* 3, 1-9, doi:UNSP 36910.3389/fphys.2012.00369 (2012).

59 Thapa, B. & Schlegel, H. B. Density Functional Theory Calculation of pK(a)'s of Thiols in Aqueous Solution Using Explicit Water Molecules and the Polarizable Continuum Model. *J Phys Chem A* 120, 5726-5735, doi:10.1021/acs.jpca.6b05040 (2016).

60 Sedighi, A. & Krull, U. J. Rapid Immobilization of Oligonucleotides at High Density on Semiconductor Quantum Dots and Gold Nanoparticles. *Langmuir* 32, 13500-13509, doi:10.1021/acs.langmuir.6b03840 (2016).

61 Ruiz-de-Angulo, A., Zabaleta, A., Gomez-Vallejo, V., Llop, J. & Mareque-Rivas, J. C. Microdosed Lipid-Coated Ga-67-Magnetite Enhances Antigen-Specific Immunity by Image Tracked Delivery of Antigen and CpG to Lymph Nodes. *Acs Nano* 10, 1602-1618, doi:10.1021/acsnano.5b07253 (2016).

62 Sungsuwan, S., Yin, Z. J. & Huang, X. F. Lipopeptide-Coated Iron Oxide Nanoparticles as Potential Glycoconjugate-Based Synthetic Anticancer Vaccines. *ACS Appl. Mater. Inter.* 7, 17535-17544, doi:10.1021/acsami.5b05497 (2015).

63 Lin, A. Y. *et al.* High-density sub-100-nm peptide-gold nanoparticle complexes improve vaccine presentation by dendritic cells in vitro. *Nanoscale Res. Lett.* 8, 1-11, doi:10.1186/1556-276X-8-72 (2013).

64 Leleux, J. A., Pradhan, P. & Roy, K. Biophysical Attributes of CpG Presentation Control TLR9 Signaling to Differentially Polarize Systemic Immune Responses. *Cell Rep.* 18, 700-710, doi:10.1016/j.celrep.2016.12.073 (2017).

65 Plotkin, S. A., Orenstein, W. A. & Offit, P. A. *Vaccines*. Sixth edition. edn, (Elsevier Saunders, 2013).

66 Kang, B. & Choi, S. J. Preparation of stabilized magnetic nanoparticles with polymerizable lipid and anchor compounds. *Anal. Biochem.* 446, 87-89, doi:10.1016/j.ab.2013.10.036 (2014).

67 Zhu, X. & Mason, T. G. Passivated gel electrophoresis of charged nanospheres by light-scattering video tracking. *J. Colloid Interface Sci.* 428, 199-207, doi:10.1016/j.jcis.2014.04.024 (2014).

68 Hanauer, M., Pierrat, S., Zins, I., Lotz, A. & Sonnichsen, C. Separation of nanoparticles by gel electrophoresis according to size-and shape. *Nano Lett.* 7, 2881-2885, doi:10.1021/nl071615y (2007).

CHAPTER 4

The Content of CpG-DNA in Antigen-CpG Conjugate Vaccines Determines Their Cross-Presentation Activity

4.1 Abstract

Cross-presentation, the process that facilitates display of exogenous antigens on MHC-I molecules, is a crucial step in the cascade of CD8 T cell activation. Potentiation of cross-presentation therefore represents an essential design criterion for development of subunit vaccines that target the induction of CD8 T cell immunity. Covalent conjugation of CpG-DNA to antigenic proteins has shown the potential to promote cross-presentation and has attracted great interest as a promising approach for vaccine development. However, heterogeneous product mixtures that result from typical conjugation schemes precluded identification of active conjugate species and impeded optimization of cross-presentation activity. In this report, we explore the effect of molecular composition of antigen-CpG conjugates on their cross-presentation activity using model Ovalbumin (OVA)-CpG conjugates. We developed a method to generate antigen-CpG conjugates with defined molecular compositions and leveraged this method to produce a series of OVA-CpG conjugates with one, two and three CpG molecules linked to OVA. We observed that conjugates containing one CpG per OVA enhanced cross-presentation by 4-fold compared to native OVA, while conjugates with higher contents of CpG provided no cross-presentation enhancement. These differences are likely due to enhanced aggregation propensity observed for conjugates that carry more than one CpG per OVA. Our findings suggest that tuning molecular composition of antigen-CpG conjugates to maintain physical stability may be essential for achieving potent cross-presentation activity. Our method to generate defined conjugates could facilitate such molecular tuning and may be useful for continued development of antigen-CpG vaccines.

4.2 Introduction

Synthetic subunit vaccines that can elicit CD8 T cell immunity are highly desirable as a potential therapeutic strategy for combating intracellular pathogens and cancer[1, 2]. Subunit vaccines are often based on purified or recombinant protein antigens[3]. Activation of antigen-specific CD8 T cell immunity requires display of antigenic epitopes on the surface of antigen-presenting cells (APCs) in the context of MHC class I molecules[4, 5]. Routing of exogenous proteins in APCs for display on MHC class I molecules relies on a process known as cross-presentation[4, 5]. Because cross-presentation is a pivotal step in the CD8 T cell activation cascade, potentiation of cross-presentation is an essential design criterion for development of subunit vaccines that target the induction of CD8 T cell immunity[6]. To overcome the poor performance of exogenous proteins as substrates for the cross-presentation pathway, vaccine formulations typically integrate adjuvants to promote cross-presentation[7]. One potent class of adjuvants that can enhance cross-presentation is unmethylated cytosine-phosphate-guanine (CpG) oligodeoxynucleotides[8, 9]. The enhancement of the cross-presentation activity by CpG adjuvants largely depends on a vaccine formulation[10, 11]. Although a wide range of subunit vaccine formulations utilizing CpG has been explored, tuning vaccine compositions for enhanced cross-presentation still represents a considerable challenge[6, 12].

One extensively studied approach to develop CpG-containing vaccine formulations relies on covalent conjugation of CpG with protein antigens[11, 13-17]. While physical addition of CpG to vaccine formulations can enhance immunity, close proximity of antigenic proteins and CpG in antigen-presenting cells was found to be crucial for stimulating robust cross-presentation[10, 18]. Covalent conjugation of CpG to antigenic proteins can co-localize both the antigen and the adjuvant components in the same antigen-presenting cell[11]. Because this co-localization activity was found to promote cross-presentation, antigen-CpG conjugates have attracted considerable interest as potential vaccines[10, 19-21]. Nevertheless, the translational potential of antigen-CpG conjugates has not been realized to date[22, 23]. Although antigen-CpG conjugates have been widely studied, discrepancies in their ability to induce cross-presentation exist. While some studies have shown dramatic, many-fold potentiation of cross presentation[11, 24] compared to corresponding antigen/CpG mixtures, other studies investigating conjugates with the same CpG and antigen components reported modest enhancement of cross-presentation activity[10, 16]. Elucidation of factors that underlie this variability is pivotal for further translational development of antigen-CpG conjugate vaccines.

One factor that has recently come into focus in the context of cross-presentation is the physical stability of protein antigens[25-28]. Accumulating evidence suggests that antigenic proteins need to preserve their physical stability for effective routing into the cross-presentation pathway in APCs[26, 28]. While chemical conjugation of CpG with antigens offers an attractive advantage of antigen/adjuvant co-delivery into the same antigen-presenting cell, conjugation may also provoke protein destabilization and aggregation[29-31]. It has been demonstrated that protein destabilization induced by functionalization chemistries depends on the degree of functionalization[30, 32, 33]. Antigen-CpG conjugates have been previously synthesized as highly heterogeneous mixtures containing a wide range of molecular species with different contents of CpG[11, 14, 16, 34]. Different extents of CpG functionalization may differentially affect conjugate stability, and thus the conjugate intracellular routing and activity. Surprisingly, despite significant interest in antigen-CpG vaccines, the effect of the extent of conjugation on conjugate activity has not been evaluated to date.

Herein, we explore the effect of molecular composition of the antigen-CpG conjugates on their cross-presentation activity. We developed a method to produce antigen-CpG conjugates with defined molecular compositions. Using this method, we generated a series of model Ovalbumin (OVA)-CpG conjugates with different contents of CpG. We observed that OVA-CpG conjugates with higher CpG contents exhibited higher propensity to aggregation compared to their counterparts with lower contents of CpG. Most significantly, we found that only conjugates containing one mol CpG per mol Ovalbumin, but not the conjugates with higher contents of CpG, promoted cross-presentation activity, likely due to increased aggregation propensity of the conjugates with higher CpG contents. To our knowledge, this study is the first to evaluate the effect of molecular composition of CpG-based conjugate vaccines on their stability and cross-presentation activity. Our findings suggest that tuning molecular composition of antigen-CpG conjugates to maintain physical stability may be essential for their continued development as vaccines with potent cross-presentation activity.

4.3 Results and Discussion

Previous synthetic methods to produce protein-CpG conjugates included coupling of protein and CpG *via* maleimide-sulfur thioether linkages and di-sulfide linkages[14, 19, 35]. We selected di-sulfide chemistry based on recent reports demonstrating the enhanced vaccination potential of di-sulfide linked conjugates compared to thioether conjugates *in vivo*[19]. Ovalbumin (OVA) was selected as a model antigenic protein, because of its wide previous use in this capacity, and the availability of well-characterized model systems to evaluate the cross-presentation of OVA[11, 14, 36, 37]. To synthesize model di-sulfide-linked OVA-CpG conjugates we utilized di-sulfide exchange chemistry using a heterobifunctional cross-linker SPDP[38]. This chemistry involves functionalization of lysines' side chains with SPDP to introduce PDP functional groups onto the protein surface, and subsequent reaction of functionalized proteins with free-thiol carrying CpG oligonucleotide to produce di-sulfide linked conjugates (Scheme 1A).

Previous methods to produce protein-CpG conjugates resulted in highly heterogeneous product mixtures. For example, up to 5 different conjugate species were previously identified in a single OVA-CpG product[11, 14, 16]. Such heterogeneity precludes identification of the active conjugate species. To generate conjugates with better defined molecular compositions, we developed a method that integrates two levels of compositional control (Scheme 1B). First, we employed functionalization of OVA with controlled contents of PDP functional groups. Previous studies demonstrated that the extent of PDP functionalization can be controlled by varying the feed ratio of the SPDP to protein[32]. Consistent with previous reports, we found that in the range of 5-15 mol SPDP per mol OVA, the PDP content in the resulting OVA-PDP products increased linearly (R^2=0.99) with the increasing ratios of SPDP to OVA, allowing tunable functionalization (Figure S17). Using this method, we produced a series of differentially functionalized OVA-PDP species with average PDP contents of 1.4 ± 0.1, 2.1 ± 0.3 and 3.3 ± 0.3 mol PDP per mol OVA. We termed these species OVA-1-PDP, OVA-2-PDP and OVA-3-PDP, respectively.

Subsequently, we reacted the functionalized OVA-PDP with thiolated CpG (CpG-SH) at a 1:1 molar ratio to produce OVA-CpG conjugates. The crude conjugates exhibited a multi-band pattern on SDS-PAGE electrograms (Figure S18). Within the molecular weight range of expected conjugates (34-77 kDa), a combination of a dominant high-density band and several auxiliary low-density bands was observed. This pattern suggested enrichment in formation of a predominant conjugate species, but it also revealed that separation is required to isolate the

major product. We therefore sought to develop a separation procedure as a second level of compositional control. Based on previous reports, separation of protein-CpG conjugates with different molecular compositions appears to be difficult[11, 14, 16]. Previous attempts to achieve separation relied on size exclusion chromatography[11, 14, 16, 19, 37]. However, conjugates could not be resolved likely due to small size differences (~6.5kDa) between conjugates with different CpG contents. Because CpG possesses high density of negative charge, we considered that the conjugates could be separated based on differences in CpG-imparted charge. We developed a separation method that utilizes anion exchange chromatography with a stair-step sodium chloride elution gradient (Supporting Information, Figure S19). This method allowed us to resolve the crude products into fractions eluting at different ionic strengths. Consistent with the SDS-PAGE electrograms, anion exchange chromatograms of the crude products revealed presence of one predominant and several auxiliary species. For example, reaction products of the OVA-3-PDP with equimolar CpG-SH resulted in a predominant peak eluting at 0.75 M NaCl, and three smaller auxiliary peaks eluting at 0.5 M, 0.4 M and 0.3 M of NaCl, respectively (Figure S19).

Using this method, we isolated the major product from each of the three crude conjugate mixtures obtained by reacting CpG-SH with the OVA-1-PDP, OVA-2-PDP and OVA-3-PDP, respectively. Isolated desalted species displayed a single peak on anion exchange chromatograms, corroborating successful separations (Figure 4.1A). To identify the composition of the recovered species, we performed analysis by SDS-PAGE electrophoresis and quantified the oligonucleotide content per unit protein for each species. Within the molecular weight range of 34-77 kDa, all species displayed a single band on SDS-PAGE electrograms, suggesting formation of homogenous conjugate products (Figure 4.1B). Successive species requiring increasing ionic strengths for elution from the quaternary ammonium matrix exhibited corresponding progressive increase in molecular weight, suggesting that they carried increasing content of anionic CpG. Estimated molecular masses of ~51.6 kDa, ~59.9 kDa and ~67.7 kDa for different conjugate species were in a reasonably good agreement with the expected molecular masses for conjugates containing 1 mol CpG/mol OVA (51.3kDa), 2 mol CpG/mol OVA (57.6kDa) and 3 mol CpG/mol OVA (63.9 kDa), respectively. Consistent with this observation, quantitative analysis revealed molecular compositions of 0.8±0.1, 2.2±0.2 and 3.3±0.2 mol CpG per mol OVA for respective conjugates (Figure 4.1C). Taken together, these results corroborated generation of conjugates with defined molecular compositions and different

contents of CpG. We termed the resulting conjugates OVA-1-CpG, OVA-2-CpG and OVA-3-CpG and used them for further analysis.

Having generated a series of OVA-CpG conjugates with different CpG contents, we asked whether the CpG content in these conjugates affects their cross-presentation activity. To assess cross-presentation, we quantified activation of B3Z hybridoma CD8 T cells[36]. These cells produce β-galactosidase upon recognition of the OVA-derived epitope SIINFEKL in the context of MHC class I molecules on antigen-presenting cells and, therefore, provide a measure of vaccine's ability to facilitate cross-presentation (Figure 4.2A). To assess the effect of conjugation on the cross-presentation activity, we compared performance of the covalently conjugated OVA-CpG species (OVA-1-CpG, OVA-2-CpG and OVA-3-CpG) with the respective physical mixtures of the conjugate's molecular components (OVA-1-PDP+1 CPG, OVA-2-PDP+2 CPG, OVA-3-PDP+3 CPG, respectively; Figure 4.2B). Interestingly, the OVA-2-CpG and OVA-3-CpG conjugates failed to enhance the cross-presentation activity beyond the basal levels observed with the physical mixtures (OVA-2-CpG: 6 ± 1 mU vs. OVA-2-PDP+2CpG: 4.3 ± 0.3 mU, p= 0.85; OVA-3-CpG: 4 ± 2 mU vs. OVA-3-PDP+3 CpG: 5 ± 2 mU, p= 0.95). In contrast, the monomeric OVA-1-CpG conjugate induced a 4-fold enhancement of the cross-presentation activity compared to the physically mixed controls (OVA-1-CpG: 19 ± 1 mU vs. OVA-1-PDP+1 CpG: 5 ± 1 mU, p <0.0001).

Recent studies demonstrated that denaturation and aggregation of antigenic proteins may skew their routing in antigen-presenting cells and diminish their cross-presentation activity[25-28]. We therefore asked whether the observed differences in the activities of OVA-CpG conjugates could be related to their physical stability. Previous studies demonstrated that the tendency of misfolded and destabilized proteins to form early multimeric intermediates on their path to aggregation, or the aggregation propensity, can be used as a measure of protein destabilization[39]. To assess aggregation propensity, we carried out SDS-PAGE analysis of the conjugates followed by densitometry analysis of SDS-PAGE electrograms[40]. The conjugates displayed two distinct density peaks; a peak of lower molecular weight (<77kDa) corresponding to the soluble conjugate and a peak of higher molecular weight corresponding to early aggregation intermediates (>77kDa). We observed that the fraction of the monomeric conjugate decreased and the fraction of multimeric aggregation intermediates increased with the increasing CpG content in the conjugates (Figure 4.3A). Quantitative analysis further revealed that the aggregation propensities of both the OVA-2-CpG and OVA-3-CpG conjugates were significantly higher than that of the native OVA (OVA-2-CpG: 24 ± 8 % vs OVA: 7 ± 5 %, p=

0.035; OVA-3-CpG: 57 ± 9 % vs OVA: 7 ± 5 %, p <0.001). In contrast, the aggregation propensity of the OVA-1-Cpg conjugate did not differ significantly from that of the native OVA (OVA-1-CpG: 8 ± 6 % vs OVA: 7 ± 5 %, p= 0.99; Figure 4.3B). These findings demonstrate that the monomeric OVA-1-CpG conjugate is superior to conjugates with higher CpG contents in preserving physical stability, similar to the native OVA.

Interestingly, the aggregation propensity of the OVA-CpG conjugates was in a reasonably good agreement with their ability to facilitate cross-presentation. While minimally aggregated monomeric OVA-1-CpG conjugate induced pronounced enhancement in cross-presentation compared to native OVA (OVA-1-CpG: 19 ± 1 mU vs. OVA: 5 ± 1 mU, p < 0.001), the OVA-2-CpG and OVA-3-CpG conjugates with increased propensity to aggregation failed to provide cross-presentation enhancement (OVA-2-CpG: 6 ± 1 mU vs. OVA: 5 ± 1 mU, p = 0.99; OVA-3-CpG: 4 ± 2 mU vs. OVA: 5 ± 1 mU, p = 0.99). Previous studies demonstrated that cross-presentation efficiency of exogenous proteins could be pronouncedly reduced by protein destabilization and aggregation. For example, Palliser et al. found that aggregated forms of heat shock proteins displayed a 4-10-fold reduction in cross-presentation compared to the monomeric forms of these proteins[26]. Similarly, the misfolded aggregation-prone variant of OVA was found to exhibit a significantly lower cross-presentation efficiency compared to its stable soluble counterparts[28]. In the context of these findings, the increased propensity of the OVA-2-CpG and OVA-3-CpG conjugates to aggregation has likely played an important role in reducing their cross-presentation activity compared to the stable OVA-1-CpG conjugates.

The differences in cross-presentation efficiency for monomeric and aggregated proteins were previously ascribed to differences in the mechanism of cell internalization, which in turn determines the efficiency of intracellular routing into the cross-presentation machinery[26]. For example, the monomeric heat shock proteins were shown to internalize via receptor-mediated endocytosis, leading to efficient routing into the cross-presentation pathway[26]. In contrast, aggregated proteins were found to be uptaken by phagocytosis, leading to less efficient cross-presentation[26]. Previous analysis of protein-CpG conjugates demonstrated that enhancement in cross-presentation efficiency by covalent conjugation could be largely attributed to the CpG-guided internalization of the conjugates via DNA receptor-mediated endocytosis[11, 24]. It is possible that aggregation of the destabilized conjugates with high content of CpG (OVA-2-CpG and OVA-3-CpG) redirects their uptake toward phagocytosis, thereby skewing the intracellular processing toward less efficient cross-presentation, but further work is needed to discern the mechanism

4.4 Conclusions

In summary, we developed a novel method to produce defined protein-CpG conjugate species and leveraged this method to assess the effect of CpG content in protein-CpG conjugates on cross-presentation activity. Although numerous studies examined protein-CpG conjugates as potential vaccines, the effect of conjugate composition on activity has been largely overlooked likely due to the difficulty in generating protein-CpG conjugates with defined molecular compositions. Our results reveal that only the conjugate functionalized with one mol CpG per mol protein, but not the conjugates with higher degree of CpG functionalization, enhance cross-presentation activity. These differences are likely due to enhanced aggregation propensity observed for conjugates that carry more than one CpG per OVA. Our results suggest that tuning molecular composition of protein-CpG conjugates to preserve physical stability may be essential for potentiation of cross-presentation activity. Our method to generate defined protein-CpG conjugates may be useful for tuning conjugate compositions and stability and, therefore, warrants further investigation for development of conjugate vaccines with potent cross-presentation activity.

4.5 Acknowledgements

This work was supported by the University of Michigan College of Pharmacy faculty start-up fund (to B.C.) and the William and Sally Seale Fund for Cancer Research (to B.C.).

4.6 Authorship

Ryan M. Clauson,[†] Brendan Berg,[‡] and Beata Chertok*,[†,‡]

[†]Department of Pharmaceutical Sciences, College of Pharmacy, and [‡]Department of Biomedical Engineering, College of Engineering, University of Michigan, Ann Arbor, Michigan 48109, United States

* Corresponding Author

4.7 Figures

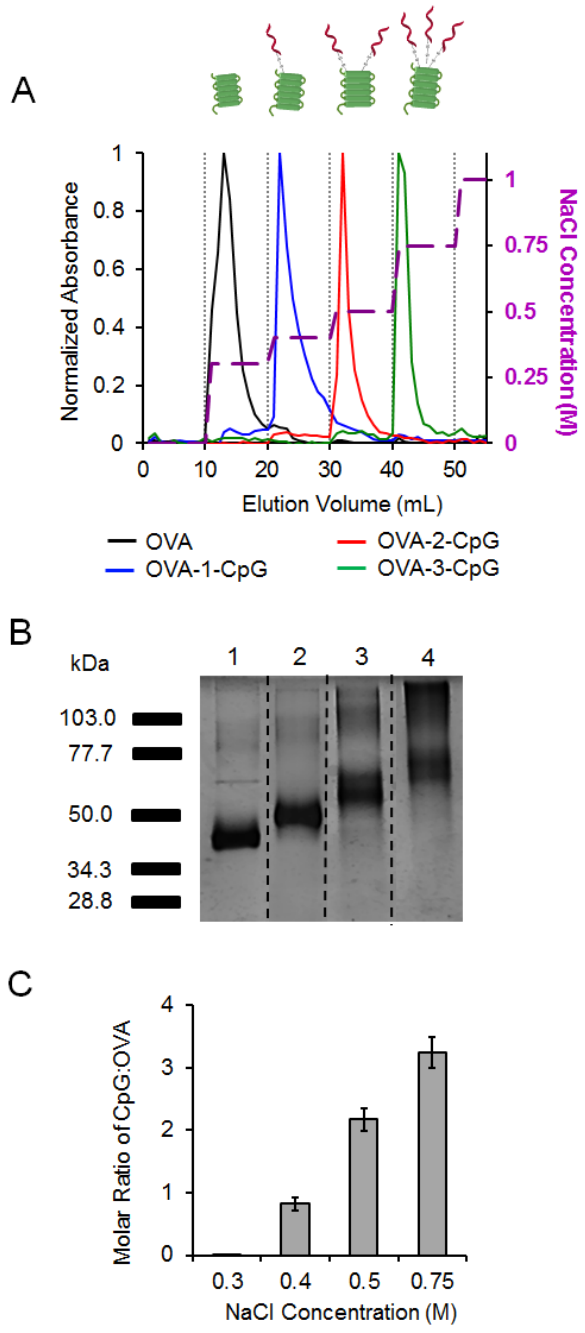

Figure 4.1 - Analysis of OVA-CpG conjugates. (A) Representative anion exchange chromatograms for isolated and purified conjugate species OVA-1-CpG (blue), OVA-2-CpG (red) and OVA-3-CpG (green). Anion exchange chromatography was carried out using quaternary ammonium solid phase with a stair-step sodium chloride (NaCl) elution gradient (purple dashed line). Native Ovalbumin (OVA, black) was used as a control. (B) Representative image of SDS polyacrylamide gel electrophoresis (SDS-PAGE) (10%, 75V, 90 minutes) for OVA (lane 1), OVA-1-CpG (lane 2), OVA-2-CpG (lane 3) and OVA-3-CpG (lane 4), visualized using silver staining. Molecular weights were analyzed using the ladder of protein standards. (C) Quantification of molecular compositions of the OVA-CpG conjugates. Molar ratios of CpG to OVA were quantified by BCA and SYBR Gold assays to determine the contents of protein and single-stranded DNA, respectively. Data represents mean ± S.D., n = 3.

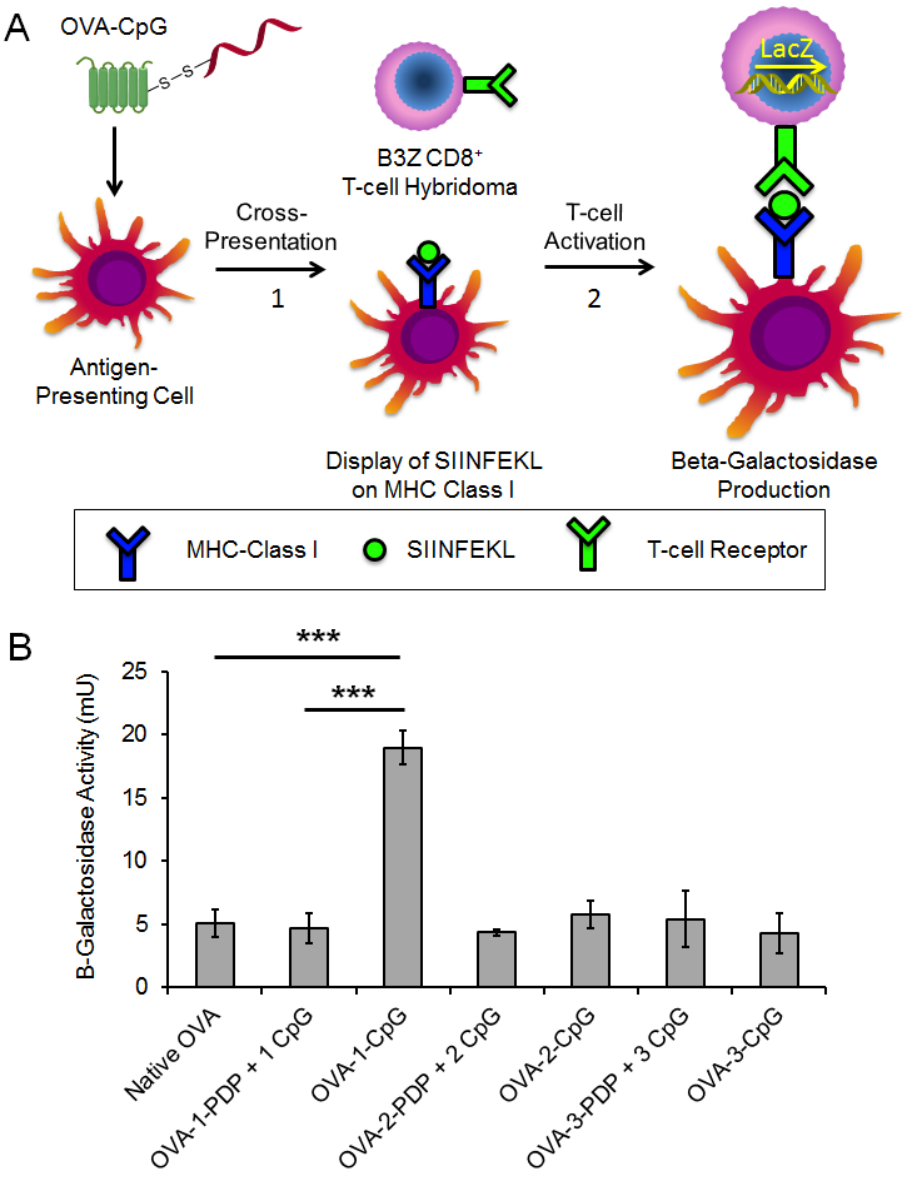

Figure 4.2 - *In vitro* cross-presentation assay using B3Z CD8 T-cell hybridoma. (A) Schematic depiction of the assay: Step I - OVA-CpG conjugates are routed into the cross-presentation pathway in Antigen-Presenting Cells (APCs). As a result, the Ovalbumin's predominant immunogenic epitope SIINFKEL is displayed in the context of MHC class I molecules on the APCs surface. Step II- In response to recognition of the SIINFKEL-MHC class I complexes on APCs, B3Z T cells are activated to produce β-galactosidase enzyme (β-Gal) providing a quantitative measure of the cross-presentation. (B) Quantitative analysis of the cross-presentation for OVA-CpG conjugates and the physical mixtures of the respective conjugate's molecular components. The activity of β-Gal is expressed in milliUnits (mU), based on calibration with the purified β-Gal enzyme of known enzymatic activity. Data represent mean ± SD, n = 3. Statistical analysis is based on a one-way ANOVA, followed by post hoc Tukey's pairwise comparisons. Asterisks denote statistically significant differences at the level of ***$p < 0.001$.

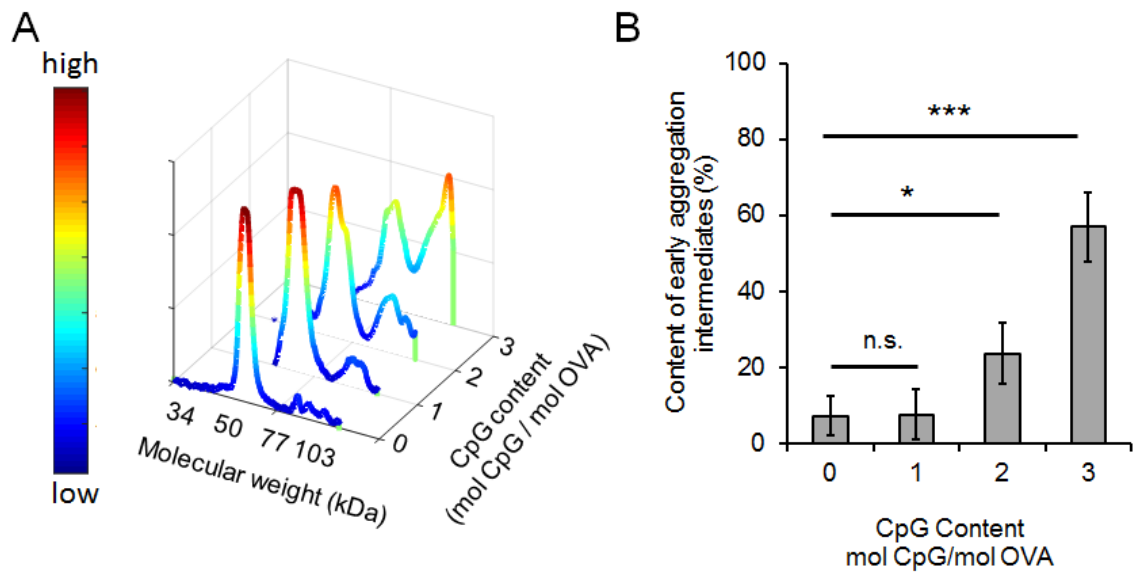

Figure 4.3 - Analysis of the aggregation propensity in OVA-CpG conjugates. (A) Representative SDS-PAGE densitograms for OVA-CpG conjugates. Molecular weights were calibrated using the ladder of protein standards. (B) Quantitative analysis of aggregation propensity for OVA-CpG conjugates with difference contents of CpG relative to native OVA. Data represent mean ± SD, n = 3. Statistical analysis is based on a one-way ANOVA, followed by post hoc Tukey's pairwise comparisons. Asterisks denote statistically significant differences: *p < 0.05, **p < 0.01, ***p < 0.001, n.s.: p>0.05.

4.8 Supporting Information

A final version of this chapter is published in *Bioconjugate Chemistry*. The following supporting information and figures are available in Appendix C. Synthesis, purification and characterization procedures for Ovalbumin-CpG conjugates, description of the *in vitro* cross-presentation assay, supplementary figures: OVA functionalization with controlled extent of PDP, SDS-PAGE and anion exchange chromatography characterization of crude OVA-CpG conjugates.

4.9 Bibliography

1 Appay, V., Douek, D. C. & Price, D. A. CD8(+) T cell efficacy in vaccination and disease. *Nature Medicine* 14, 623-628, doi:10.1038/nm.f.1774 (2008).

2 Pennock, N. D., Kedl, J. D. & Kedl, R. M. T Cell Vaccinology: Beyond the Reflection of Infectious Responses. *Trends Immunol* 37, 170-180, doi:10.1016/j.it.2016.01.001 (2016).

3 Moyle, P. M. & Toth, I. Modern Subunit Vaccines: Development, Components, and Research Opportunities. *Chemmedchem* 8, 360-376, doi:10.1002/cmdc.201200487 (2013).

4 Kurts, C., Robinson, B. W. S. & Knolle, P. A. Cross-priming in health and disease. *Nature Reviews Immunology* 10, 403-414, doi:10.1038/nri2780 (2010).

5 Joffre, O. P., Segura, E., Savina, A. & Amigorena, S. Cross-presentation by dendritic cells. *Nature Reviews Immunology* 12, 557-569, doi:10.1038/nri3254 (2012).

6 Liu, H. P. & Irvine, D. J. Guiding Principles in the Design of Molecular Bioconjugates for Vaccine Applications. *Bioconjugate Chemistry* 26, 791-801, doi:10.1021/acs.bioconjchem.5b00103 (2015).

7 Fehres, C. M., Unger, W. W. J., Garcia-Vallejo, J. J. & van Kooyk, Y. Understanding the biology of antigen cross-presentation for the design of vaccines against cancer. *Frontiers in Immunology* 5, doi:UNSP 14910.3389/fimmu.2014.00149 (2014).

8 Bode, C., Zhao, G., Steinhagen, F., Kinjo, T. & Klinman, D. M. CpG DNA as a vaccine adjuvant. *Expert Rev Vaccines* 10, 499-511, doi:10.1586/erv.10.174 (2011).

9 Kuchtey, J., Chefalo, P. J., Gray, R. C., Ramachandra, L. & Harding, C. V. Enhancement of dendritic cell antigen cross-presentation by CpG DNA involves type I IFN and stabilization of class I MHC mRNA. *J Immunol* 175, 2244-2251 (2005).

10 Datta, S. K., Cho, H. J., Takabayashi, K., Horner, A. A. & Raz, E. Antigen-immunostimulatory oligonucleotide conjugates: mechanisms and applications. *Immunol Rev* 199, 217-226, doi:10.1111/j.0105-2896.2004.00149.x (2004).

11 Maurer, T. *et al.* CpG-DNA aided cross-presentation of soluble antigens by dendritic cells. *European Journal of Immunology* 32, 2356-2364, doi:Doi 10.1002/1521-4141(200208)32:8<2356::Aid-Immu2356>3.0.Co;2-Z (2002).

12 Moyer, T. J., Zmolek, A. C. & Irvine, D. J. Beyond antigens and adjuvants: formulating future vaccines. *J Clin Invest* 126, 799-808, doi:10.1172/Jci81083 (2016).

13 Heit, A. *et al.* Protective CD8 T cell immunity triggered by CpG-protein conjugates competes with the efficacy of live vaccines. *J Immunol* 174, 4373-4380 (2005).

14 Cho, H. J. *et al.* Immunostimulatory DNA-based vaccines induce cytotoxic lymphocyte activity by a T-helper cell-independent mechanism. *Nature Biotechnology* 18, 509-514 (2000).

15 Tighe, H. *et al.* Conjugation of protein to immunostimulatory DNA results in a rapid, long-lasting and potent induction of cell-mediated and humoral immunity. *European Journal of Immunology* 30, 1939-1947, doi:Doi 10.1002/1521-4141(200007)30:7<1939::Aid-Immu1939>3.0.Co;2-# (2000).

16 Hassan, H. A. F. M. *et al.* Dual stimulation of antigen presenting cells using carbon nanotube-based vaccine delivery system for cancer immunotherapy. *Biomaterials* 104, 310-322, doi:10.1016/j.biomaterials.2016.07.005 (2016).

17 Ignacio, B. J., Albin, T. J., Esser-Kahn, A. P. & Verdoes, M. Toll-like Receptor Agonist Conjugation: A Chemical Perspective. *Bioconjugate Chemistry* 29, 587-603, doi:10.1021/acs.bioconjchem.7b00808 (2018).

18 Nierkens, S. *et al.* In vivo colocalization of antigen and CpG within dendritic cells is associated with the efficacy of cancer immunotherapy. *Cancer Res* 68, 5390-5396, doi:10.1158/0008-5472.CAN-07-6023 (2008).

19 Kramer, K., Shields, N. J., Poppe, V., Young, S. L. & Walker, G. F. Intracellular Cleavable CpG Oligodeoxynucleotide-Antigen Conjugate Enhances Anti-tumor Immunity. *Molecular Therapy* 25, 62-70, doi:10.1016/j.ymthe.2016.10.001 (2017).

20 Shirota, H., Sano, K., Kikuchi, T., Tamura, G. & Shirato, K. Regulation of murine airway eosinophilia and Th2 cells by antigen-conjugated CpG oligodeoxynucleotides as a novel antigen-specific immunomodulator. *Journal of Immunology* 164, 5575-5582, doi:DOI 10.4049/jimmunol.164.11.5575 (2000).

21 Alignani, D. *et al.* Orally administered OVA/CpG-ODN induces specific mucosal and systemic immune response in young and aged mice. *Journal of Leukocyte Biology* 77, 898-905, doi:DOI 10.1189/jlb.0604330 (2005).

22 Scheiermann, J. & Klinman, D. M. Clinical evaluation of CpG oligonucleotides as adjuvants for vaccines targeting infectious diseases and cancer. *Vaccine* 32, 6377-6389, doi:10.1016/j.vaccine.2014.06.065 (2014).

23 Hanagata, N. CpG oligodeoxynucleotide nanomedicines for the prophylaxis or treatment of cancers, infectious diseases, and allergies. *Int J Nanomedicine* 12, 515-531, doi:10.2147/IJN.S114477 (2017).

24 Heit, A. *et al.* Cutting edge: Toll-like receptor 9 expression is not required for CpG DNA-aided cross-presentation of DNA-conjugated antigens but essential for cross-priming of CD8 T cells. *J Immunol* 170, 2802-2805 (2003).

25 Thai, R. *et al.* Antigen stability controls antigen presentation. *Journal of Biological Chemistry* 279, 50257-50266, doi:10.1074/jbc.M405738200 (2004).

26 Palliser, D., Guillen, E., Ju, M. & Eisen, H. N. Multiple intracellular routes in the cross-presentation of a soluble protein by murine dendritic cells. *J Immunol* 174, 1879-1887 (2005).

27 Scheiblhofer, S., Laimer, J., Machado, Y., Weiss, R. & Thalhamer, J. Influence of protein fold stability on immunogenicity and its implications for vaccine design. *Expert Review of Vaccines* 16, 479-489, doi:10.1080/14760584.2017.1306441 (2017).

28 Schnorrer, P. *et al.* The dominant role of CD8(+) dendritic cells in cross-presentation is not dictated by antigen capture. *Proceedings of the National Academy of Sciences of the United States of America* 103, 10729-10734, doi:10.1073/pnas.0601956103 (2006).

29 Manning, M. C., Chou, D. K., Murphy, B. M., Payne, R. W. & Katayama, D. S. Stability of protein pharmaceuticals: an update. *Pharm Res* 27, 544-575, doi:10.1007/s11095-009-0045-6 (2010).

30 Castellanos, I. J., Al-Azzam, W. & Griebenow, K. Effect of the covalent modification with poly(ethylene glycol) on alpha-chymotrypsin stability upon encapsulation in poly(lactic-co-glycolic) microspheres. *Journal of Pharmaceutical Sciences* 94, 327-340, doi:10.1002/jps.20243 (2005).

31 Reid, R. E. *Peptide and protein drug analysis*. (M. Dekker, 2000).

32 Slutter, B. *et al.* Conjugation of ovalbumin to trimethyl chitosan improves immunogenicity of the antigen. *J Control Release* 143, 207-214, doi:10.1016/j.jconrel.2010.01.007 (2010).

33 Peeters, J. M., Hazendonk, T. G., Beuvery, E. C. & Tesser, G. I. Comparison of four bifunctional reagents for coupling peptides to proteins and the effect of the three moieties on the immunogenicity of the conjugates. *J Immunol Methods* 120, 133-143 (1989).

34 Tao, Y., Ju, E. G., Li, Z. H., Ren, J. S. & Qu, X. G. Engineered CpG- Antigen Conjugates Protected Gold Nanoclusters as Smart Self- Vaccines for Enhanced Immune Response and Cell Imaging. *Advanced Functional Materials* 24, 1004-1010, doi:10.1002/adfm.201302347 (2014).

35 Shirota, H. *et al.* Novel roles of CpG oligodeoxynucleotides as a leader for the sampling and presentation of CpG-tagged antigen by dendritic cells. *Journal of Immunology* 167, 66-74 (2001).

36 Karttunen, J., Sanderson, S. & Shastri, N. Detection of rare antigen-presenting cells by the lacZ T-cell activation assay suggests an expression cloning strategy for T-cell antigens. *Proc Natl Acad Sci U S A* 89, 6020-6024 (1992).

37 Kramer, K., Young, S. L. & Walker, G. F. Comparative Study of 5 '- and 3 '-Linked CpG-Antigen Conjugates for the Induction of Cellular Immune Responses. *Acs Omega* 2, 227-235, doi:10.1021/acsomega.6b00368 (2017).

38 Carlsson, J., Drevin, H. & Axen, R. Protein thiolation and reversible protein-protein conjugation. N-Succinimidyl 3-(2-pyridyldithio)propionate, a new heterobifunctional reagent. *Biochem. J.* 173, 723-737 (1978).

39 Betts, S., Speed, M. & King, J. Detection of early aggregation intermediates by native gel electrophoresis and native western blotting. *Amyloid, Prions, and Other Protein Aggregates* 309, 333-350 (1999).

40 Pathak, M., Dutta, D. & Rathore, A. Analytical QbD: Development of a native gel electrophoresis method for measurement of monoclonal antibody aggregates. *Electrophoresis* 35, 2163-2171, doi:10.1002/elps.201400055 (2014).

CHAPTER 5

Conclusions and Future Directions

5.1 Iron-Oxide Nanoplatforms for B-cell Activation Conclusions

For longer than a decade now, scientists have been attempting to translate their fundamental knowledge of viruses and viral-like material properties to the rational design and engineering of novel nanomaterials[1-5]. The earliest iterations of these nanomaterials were the so-called virus-like particles (VLPs)[6-10]. VLPs are protein-based nanoparticles that are the product of viral capsid protein self-assembly[6]. To date, VLPs have been successfully developed as five different FDA-approved and clinically available products (e.g. Gardasil®)[11,12]. Yet, despite the success of this product and other similar products, the wide-spread application of VLPs as universal carriers has not yet been realized. This failure is most likely the result of manufacturing difficulties due to the reliance on protein self-assembly for formulation, as well as a high-level anti-carrier immunological response that both reduces re-dosing efficacy and limits the extent and specificity of the intended immune response against loaded cargo[6,13-15].

As a result of these challenges, there has been increasing interest in the development of alternative nanoparticle systems that are viral inspired[1,2,4,5]. These so-called, viral mimicking nanoparticles are rationally designed and engineered based on a fundamental understanding of viral physical and chemical material properties. The viral material properties most commonly utilized to inform the design of viral mimicking nanoparticles include: particle size, particle shape, charge, hydrophobicity, antigen display, antigen organization, antigen density and surface topography[1,2,4,5]. While many advances have been made in the design, engineering and application of viral-mimicking nanoparticles, no one truly universal nanoparticle system has emerged. We believe that this failure is because, at present, researchers appear to be taking

too selective of a view of the material properties to be mimicked[16-19]. Based upon the limitations of current viral-mimicking nanoparticle systems, we surmised that it may be time to take a more holistic approach to viral-mimicking nanoparticle design. More specifically, we wanted to incorporate a level of antigen display organization that could not be achieved with established technologies.

To accomplish this, we developed an inorganic virus-like nanoparticle (IVLN). The IVLN has unique viral-like spiky topographical structures, high-density antigen display, spherical geometry, optimal size and negatively charged surfaces. The IVLN was produced using a hybrid Au@Fe core-satellite nanoparticle technology based on previously established technique by our group. More specifically, the IVLN is composed of a single 15 nm poly(siloxane) and poly(ethylene glycol) diblock copolymer coated iron-oxide nanoparticles with a defined quantity of 3 nm gold nanoparticles (AuNPs), or satellites, attached to the surface via gold-siloxane binding. The extent of AuNP attachment to IVLN surfaces was determined by initial weight ratio incubations of Au to Fe in solution. Depending on the formulation conditions, the IVLN could be produced with between 2 to 14 AuNPs per IVLN. In other words, the IVLN can be produced with inter-satellite distance between ~20 to 5 nm and satellite density between 1500 to 25,000 satellites per micron square. For the specific application of B-cell activation, antigen density between 5-10 nm is ideal for B-cell receptor crosslinking; while for viral mimicry, antigen density between ~200 to 30,000 (HIV to HPV) antigens per micron square is most relevant[3,20,21].

In this way, the extent of AuNPs attachment is absolutely critical to the viral-like character of the IVLN. Depending on the extent of AuNPs attachment, IVLNs can be produced with variable surface topography, antigen density and antigen spatial resolution because antigen loading is specific to AuNPs and not to the polymer-coated core. Specifically, under saturating conditions with 12 AuNPs per IVLN, ~2000 peptides can be conjugated to IVLN surfaces with ~12% non-specific binding to the core and ~200 peptides per individual AuNP. In this way, the IVLN have more biologically relevant surfaces with patchy patterned distribution of antigen at 5-10 nm spatial intervals. This patterned antigen display is viral-like in nature and cannot be reproduced by traditional nanoparticle systems that have smooth surface with homogeneous antigen distribution.

Beyond viral-like structural properties, the IVLN is additionally capable of performing viral-like function. The most significant of these functions is B-cell activation and antigen-specific antibody production[8,22-27]. As compared to a traditional viral mimicking nanoparticle with similar

particle size, peptide loading and serum stability, the IVLN resulted in between 4 to 18-fold higher antigen-specific antibody titers. Notably, this functionality was directly connected to the viral-like structural properties of the IVLN. Specifically, by decreasing inter-nanoparticle distance (~12 nm to ~5 nm distance) to a range ideal for B-cell receptor crosslinking while maintain antigen loading per gold nanoparticle (200 peptides per IVLN) it was possible to improve antigen-specific IgG antibody titers by 6-fold. Additionally, by increasing the antigen loading per gold nanoparticle (50 to 200 peptides per IVLN) for a given inter-nanoparticle distance (~5 nm) the antigen-specific IgG antibody titers was increased by 4-fold. Taken together, these data points indicate that inter-nanoparticle (antigen cluster) distance and antigen density (within the cluster) are both critical for B-cell activation. Significantly, this is a deviation from conventional knowledge that only consider the antigen density for homogeneously distributed systems.

Mechanistically, the improved functional efficacy of the IVLN formulated under optimal conditions was correlated to significant improvements in viral-like functional elements in terms of lymph node homing, cellular distributions and immune cell activation[7,28-31]. More specifically, as compared to a traditional viral mimicking nanoparticle control, the IVLN facilitated 3.5-fold higher lymph node exposure over 48 hours, 3-fold higher relevant immune cell uptake (B-cells and subcapsular sinus macrophages), 2.5-fold higher germinal center formation and 6-fold higher stimulation of antigen-specific B-cells.

Overall, we believe that the IVLN is not only capable of viral-like structural mimicry, but also function mimicry for the application of B-cell activation and antigen-specific antibody production. Significantly, since both the IVLN and the traditional viral mimicking nanoparticle control have equivalent hydrodynamic size, zeta potential, shape and peptide capacity, the unique functional differences by these two materials should be credited to a more sophisticated and unconventional viral mimicry by design. Thus, these results provide substantial evidence to support our hypothesis that a more holistic approach to viral-mimicking nanoparticle design is required to provide optimal functionality.

5.2 Iron-Oxide Nanoplatforms for B-cell Activation Future Directions

Moving forward, IVLNs have could be utilized in numerous therapeutic applications including as B-cell epitope-based cancer vaccines, autoimmune disease treatment and anti-viral vaccinations. For example, IVLNs could be employed for HER2+ breast cancer therapy through the production of endogenous antibodies with equivalent functionality of the established treatments with pertuzumab and trastuzumab[32-34]. In this way, IVLN treatment could facilitate sustained titer of these anti-HER2 antibodies in the blood, thereby dramatically limiting the re-dosing requirement and providing a memory response. Before this potential could be realized, a significant hurdle to overcome would be to determine the IVLNs inductive capacity for antigen-specific antibody against self-antigens. While the ability to produce auto-antibodies is a hallmark of viral-like particles, this ability has not yet been explored for the IVLN platform[35,36]. Beyond the ability to produce these antibodies, a completely separate issue is whether or not you should produce them. More specifically, the chronic exposure of auto-antibodies for therapeutic purposes could have unintended non-specific immunity and inflammatory responses[37].

One therapeutic application of the IVLN platform that would not require the production of auto-antibodies is anti-viral vaccinations. In this context, the IVLN platform would be utilized as previously VLPs have for anti-viral immunity (e.g. Gardasil®)[12,38]. Notably, given the formulation ease and potential diversity of antigenic cargo, the IVLN platform could serve as a universal delivery platform for anti-viral immunity for those diseases that currently do not have FDA-approved vaccines in production such as West Nile Virus, Crimean-Congo Hemorrhagic Fever Virus, Chikungunya Virus amongst others[39-41]. Unfortunately, due to established regulatory standards and uncertainty around nanoparticle toxicity analysis, the clinical translation of the IVLN platform for therapeutic applications would be extremely challenging based on nanoparticle composition (i.e. inorganic materials and synthetic polymers)[42-45].

The most realistic application of the IVLN platform would be as a universal vehicle for antigen-specific antibody production in commercial applications. Established commercial techniques for antibody production in animal models most commonly rely on the use of the carrier protein keyhole limpet hemocyanin (KLH) in addition to high antigen and toxic adjuvant requirement[46-48]. Based on preliminary data and as compared to KLH controls, the IVLN platform could dramatically improve the titer and specificity of antibody production while necessitating lower antigen doses and eliminating the toxic adjuvant requirement in a mouse

model. As result of this functional improvement and given the ease and reproducibility of formulation, functionalization and purification of the IVLN platform, we believe the commercialization of these materials is truly feasible. Preliminary data sets demonstrate this potential and justify further investigation in this area.

5.3 Iron-Oxide Nanoplatforms for T-cell Activation Conclusions

Theranostic nanoparticles have a myriad of exciting potential diagnostic and therapeutic applications[49-52]. However, to realize these applications, nanomaterials must facilitate high capacity for cargo loading, while maintaining appropriate size and stability for effective *in-vivo* administration[53-57]. Only lipidoid stabilized, lipid-coated iron-oxide nanoparticles (IONP-ML) can fulfil these requirements. Based on the phenomenon of lipid-stitching[58], the methodology used to formulate the IONP-ML platform yields highly stable and uniform materials that are capable of high-density antigen display and unprecedentedly efficient MRI-monitored lymph node targeting[59-61].

The demonstrated success of the IONP-ML platform is largely due to effective particle size control after biomolecule surface conjugation[53]. Control of particle size is among the most significant determinants of nanoparticle's *in-vivo* performance[53,62]. Specifically, in the context of immunomodulation and lymph node targeting, the size limiting nature of lymphatic vessels leads to inefficient delivery for those nanoparticles incapable of maintaining sub-100 nm particle size *in-vivo*[56,57]. Notably, as compared to alternative methodologies for the production of lipid-coated iron-oxide nanoparticles, the IONP-ML platform is highly stable after biomolecule conjugation both in terms of biomolecule surface adherence and colloidal stability. Thus, the IONP-ML platform promotes highly efficient lymphatic trafficking with high-density antigen display that is critical for immune activation.

5.4 Iron-Oxide Nanoplatforms for T-cell Activation Future Directions

The IONP-ML platform offers promising potential as a lymph node delivery vehicle for subunit vaccines with intended applications in cancer immunotherapy and infectious disease treatment. To date, the delivery of cargo-loaded nanoparticles to lymph nodes remains highly inefficient. Commonly, less than 1% of the initial dose reaches the intended site. This limited efficiency is due to difficulties in controlling particle size and preventing colloidal destabilization after antigen loading[59-61]. Moreover, of the 1% that reaches the lymph nodes, the majority of delivered nanoparticles access the lymph nodes via “active” cell-mediated mechanisms that can reduce the functional efficacy of the vaccine[53,56,57]. As a result, cargo-loaded nanoparticles are typically unable to induce sufficient priming and activation of relevant immune cell populations, namely dendritic cells and CD8+ T-cells, required for induction of robust cellular immunity against cancer and intracellular pathogens.

To address this challenge, we are currently developing the IONP-ML platform as a highly efficient delivery vehicle for subunit vaccines. More specifically, DNA-based covalent conjugate subunit vaccines. As introduced in Chapter 4, subunit vaccines often suffer from poor inherent immunogenicity and thus require co-delivery of adjuvant for improved efficacy. This efficacy can be further improved by physical or chemical association of said adjuvant to the subunit vaccine. One shining example of such a material in the literature is the model DNA-based covalent conjugate vaccine based on the antigen ovalbumin and TLR9 agonist CpG oligonucleotide (OVA-CpG)[63-68]. While soluble OVA-CpG has been applied consistently in the literature as a model, very limited research has been shown for nanoparticle delivered OVA-CpG as an intact covalent conjugate loaded onto nanoparticle surfaces[60,61,63-65,67]. The failures in this area are most likely are result of unsuitable nanoparticle technologies for this application.

Moving forward, we have proposed to loaded OVA-CpG as a model of a DNA-based covalent conjugate vaccine onto IONP-ML surfaces via DNA-directed immobilization, in a process coined “DNA-tethering”[69-74]. Our initial experimental evidence suggests that DNA-tethering is a highly directed and non-damaging mechanism for nanoparticle loading that allows for maintenance of particle size for highly efficient lymph node delivery. With this technology, we believe that we can harness the full potential benefit of applying iron-oxide nanoplatforms in the context of cellular immunity. Although extensive experimental validations are still required, the potential of these nanomaterials for the treatment of a debilitating disease is seeming limitless.

5.5 Bibliography

1 Bachmann, M. F. & Jennings, G. T. Vaccine delivery: a matter of size, geometry, kinetics and molecular patterns. *Nat Rev Immunol* 10, 787-796, doi:10.1038/nri2868 (2010).

2 Chattopadhyay, S., Chen, J. Y., Chen, H. W. & Hu, C. J. Nanoparticle Vaccines Adopting Virus-like Features for Enhanced Immune Potentiation. *Nanotheranostics* 1, 244-260, doi:10.7150/ntno.19796 (2017).

3 Cheng, W. The Density Code for the Development of a Vaccine? *J Pharm Sci* 105, 3223-3232, doi:10.1016/j.xphs.2016.07.020 (2016).

4 Somiya, M., Liu, Q. & Kuroda, S. Current Progress of Virus-mimicking Nanocarriers for Drug Delivery. *Nanotheranostics* 1, 415-429, doi:10.7150/ntno.21723 (2017).

5 Spohn, G. & Bachmann, M. F. Exploiting viral properties for the rational design of modern vaccines. *Expert Rev Vaccines* 7, 43-54, doi:10.1586/14760584.7.1.43 (2008).

6 Fuenmayor, J., Godia, F. & Cervera, L. Production of virus-like particles for vaccines. *New Biotechnol* 39, 174-180, doi:10.1016/j.nbt.2017.07.010 (2017).

7 Cubas, R. *et al.* Virus-like particle (VLP) lymphatic trafficking and immune response generation after immunization by different routes. *J Immunother* 32, 118-128, doi:10.1097/CJI.0b013e31818f13c4 (2009).

8 Plummer, E. M. & Manchester, M. Viral nanoparticles and virus-like particles: platforms for contemporary vaccine design. *Wiley Interdiscip Rev Nanomed Nanobiotechnol* 3, 174-196, doi:10.1002/wnan.119 (2011).

9 Roldao, A., Mellado, M. C., Castilho, L. R., Carrondo, M. J. & Alves, P. M. Virus-like particles in vaccine development. *Expert Rev Vaccines* 9, 1149-1176, doi:10.1586/erv.10.115 (2010).

10 Roy, P. & Noad, R. Virus-like particles as a vaccine delivery system: myths and facts. *Hum Vaccin* 4, 5-12 (2008).

11 Mohsen, M. O., Zha, L., Cabral-Miranda, G. & Bachmann, M. F. Major findings and recent advances in virus-like particle (VLP)-based vaccines. *Semin Immunol* 34, 123-132, doi:10.1016/j.smim.2017.08.014 (2017).

12 Chackerian, B., Lowy, D. R. & Schiller, J. T. Conjugation of a self-antigen to papillomavirus-like particles allows for efficient induction of protective autoantibodies. *J. Clin. Invest.* 108, 415-423, doi:10.1172/jci11849 (2001).

13 Palomares, L. A. & Ramirez, O. T. Challenges for the production of virus-like particles in insect cells: The case of rotavirus-like particles. *Biochem Eng J* 45, 158-167, doi:10.1016/j.bej.2009.02.006 (2009).

14 McCluskie, M. J. *et al.* The effect of preexisting anti-carrier immunity on subsequent responses to CRM197 or Qb-VLP conjugate vaccines. *Immunopharmacol Immunotoxicol* 38, 184-196, doi:10.3109/08923973.2016.1165246 (2016).

15 Jegerlehner, A. *et al.* Carrier induced epitopic suppression of antibody responses induced by virus-like particles is a dynamic phenomenon caused by carrier-specific antibodies. *Vaccine* 28, 5503-5512, doi:10.1016/j.vaccine.2010.02.103 (2010).

16 Lee, C. *et al.* Rabies Virus-Inspired Silica-Coated Gold Nanorods as a Photothermal Therapeutic Platform for Treating Brain Tumors. *Adv Mater* 29, doi:10.1002/adma.201605563 (2017).

17 Lee, C. *et al.* Virus-mimetic polymer nanoparticles displaying hemagglutinin as an adjuvant-free influenza vaccine. *Biomaterials* 183, 234-242, doi:10.1016/j.biomaterials.2018.08.036 (2018).

18 Ingale, J. *et al.* High-Density Array of Well-Ordered HIV-1 Spikes on Synthetic Liposomal Nanoparticles Efficiently Activate B Cells. *Cell Rep* 15, 1986-1999, doi:10.1016/j.celrep.2016.04.078 (2016).

19 Riitho, V. *et al.* Design and evaluation of the immunogenicity and efficacy of a biomimetic particulate formulation of viral antigens. *Sci Rep* 7, 13743, doi:10.1038/s41598-017-13915-x (2017).

20 Bachmann, M. F. *et al.* The influence of antigen organization on B cell responsiveness. *Science* 262, 1448-1451 (1993).

21 Hinton, H. J., Jegerlehner, A. & Bachmann, M. F. Pattern recognition by B cells: the role of antigen repetitiveness versus Toll-like receptors. *Curr Top Microbiol Immunol* 319, 1-15 (2008).

22 Balmelli, C. *et al.* Nasal immunization of mice with human papillomavirus type 16 virus-like particles elicits neutralizing antibodies in mucosal secretions. *J Virol* 72, 8220-8229 (1998).

23 Elsayed, H. *et al.* Intrastructural Help: Harnessing T Helper Cells Induced by Licensed Vaccines for Improvement of HIV Env Antibody Responses to Virus-Like Particle Vaccines. *J Virol* 92, doi:10.1128/JVI.00141-18 (2018).

24 Lee, Y. T. *et al.* Intranasal vaccination with M2e5x virus-like particles induces humoral and cellular immune responses conferring cross-protection against heterosubtypic influenza viruses. *PLoS One* 13, e0190868, doi:10.1371/journal.pone.0190868 (2018).

25 Masavuli, M. G., Wijesundara, D. K., Torresi, J., Gowans, E. J. & Grubor-Bauk, B. Preclinical Development and Production of Virus-Like Particles As Vaccine Candidates for Hepatitis C. *Front Microbiol* 8, doi:ARTN 241310.3389/fmicb.2017.02413 (2017).

26 Schiller, J. T. & Lowy, D. R. Understanding and learning from the success of prophylactic human papillomavirus vaccines. *Nat Rev Microbiol* 10, 681-692, doi:10.1038/nrmicro2872 (2012).

27 Shukla, S., Wen, A. M., Commandeur, U. & Steinmetz, N. F. Presentation of HER2 epitopes using a filamentous plant virus-based vaccination platform. *J Mater Chem B* 2, 6249-6258, doi:10.1039/c4tb00749b (2014).

28 Carrasco, Y. R. & Batista, F. D. B cells acquire particulate antigen in a macrophage-rich area at the boundary between the follicle and the subcapsular sinus of the lymph node. *Immunity* 27, 160-171, doi:10.1016/j.immuni.2007.06.007 (2007).

29 Gray, E. E. & Cyster, J. G. Lymph node macrophages. *J Innate Immun* 4, 424-436, doi:10.1159/000337007 (2012).

30 Junt, T. *et al.* Subcapsular sinus macrophages in lymph nodes clear lymph-borne viruses and present them to antiviral B cells. *Nature* 450, 110-114, doi:10.1038/nature06287 (2007).

31 Kuka, M. & Iannacone, M. The role of lymph node sinus macrophages in host defense. *Ann N Y Acad Sci* 1319, 38-46, doi:10.1111/nyas.12387 (2014).

32 Palladini, A. *et al.* Virus-like particle display of HER2 induces potent anti-cancer responses. *Oncoimmunology* 7, e1408749, doi:10.1080/2162402X.2017.1408749 (2018).

33 Ocana, A., Amir, E. & Pandiella, A. Dual targeting of HER2-positive breast cancer with trastuzumab emtansine and pertuzumab: understanding clinical trial results. *Oncotarget* 9, 31915-31919, doi:10.18632/oncotarget.25739 (2018).

34 Swain, S. M. *et al.* Pertuzumab, trastuzumab, and docetaxel in HER2-positive metastatic breast cancer. *N Engl J Med* 372, 724-734, doi:10.1056/NEJMoa1413513 (2015).

35 Chackerian, B., Lenz, P., Lowy, D. R. & Schiller, J. T. Determinants of autoantibody induction by conjugated papillomavirus virus-like particles. *J Immunol* 169, 6120-6126 (2002).

36 Chackerian, B., Lowy, D. R. & Schiller, J. T. Conjugation of a self-antigen to papillomavirus-like particles allows for efficient induction of protective autoantibodies. *J Clin Invest* 108, 415-423, doi:10.1172/JCI11849 (2001).

37 Suurmond, J. & Diamond, B. Autoantibodies in systemic autoimmune diseases: specificity and pathogenicity. *J Clin Invest* 125, 2194-2202, doi:10.1172/JCI78084 (2015).

38 Wang, J. W. & Roden, R. B. S. Virus-like particles for the prevention of human papillomavirus-associated malignancies. *Expert Review of Vaccines* 12, 129-141, doi:10.1586/Erv.12.151 (2013).

39 Burki, T. Increase of West Nile virus cases in Europe for 2018. *Lancet* 392, 1000, doi:10.1016/S0140-6736(18)32286-4 (2018).

40 Tanabe, I. S. B. *et al.* Cellular and Molecular Immune Response to Chikungunya Virus Infection. *Front Cell Infect Microbiol* 8, 345, doi:10.3389/fcimb.2018.00345 (2018).

41 Manjunathachar, H. V. *et al.* Identification and characterization of vaccine candidates against Hyalomma anatolicum-Vector of Crimean-Congo haemorrhagic fever virus. *Transbound Emerg Dis*, doi:10.1111/tbed.13038 (2018).

42 Dobrovolskaia, M. A. & McNeil, S. E. Immunological properties of engineered nanomaterials. *Nat Nanotechnol* 2, 469-478, doi:10.1038/nnano.2007.223 (2007).

43 Dobrovolskaia, M. A., Germolec, D. R. & Weaver, J. L. Evaluation of nanoparticle immunotoxicity. *Nat Nanotechnol* 4, 411-414, doi:10.1038/nnano.2009.175 (2009).

44 Bawa, R. Regulating nanomedicine - can the FDA handle it? *Curr Drug Deliv* 8, 227-234 (2011).

45 Fischer, S. Regulating nanomedicine: new nano tools offer great promise for the future--if regulators can solve the difficulties that hold development back. *IEEE Pulse* 5, 21-24, doi:10.1109/MPUL.2013.2296797 (2014).

46 Lateef, S. S. *et al.* An improved protocol for coupling synthetic peptides to carrier proteins for antibody production using DMF to solubilize peptides. *J Biomol Tech* 18, 173-176 (2007).

47 Leenaars, M. & Hendriksen, C. F. Critical steps in the production of polyclonal and monoclonal antibodies: evaluation and recommendations. *ILAR J* 46, 269-279 (2005).

48 Stills, H. F., Jr. Adjuvants and antibody production: dispelling the myths associated with Freund's complete and other adjuvants. *ILAR J* 46, 280-293 (2005).

49 Ren, X. Q., Chen, H. W., Yang, V. & Sun, D. X. Iron oxide nanoparticle-based theranostics for cancer imaging and therapy. *Front. Chem. Sci. Eng.* 8, 253-264, doi:10.1007/s11705-014-1425-y (2014).

50 Pusic, K. *et al.* Iron oxide nanoparticles as a clinically acceptable delivery platform for a recombinant blood-stage human malaria vaccine. *Faseb J* 27, 1153-1166, doi:10.1096/fj.12-218362 (2013).

51 Chen, F., Ehlerding, E. B. & Cai, W. Theranostic nanoparticles. *J Nucl Med* 55, 1919-1922, doi:10.2967/jnumed.114.146019 (2014).

52 Lim, E. K. *et al.* Nanomaterials for theranostics: recent advances and future challenges. *Chem Rev* 115, 327-394, doi:10.1021/cr300213b (2015).

53 Bachmann, M. F. & Jennings, G. T. Vaccine delivery: a matter of size, geometry, kinetics and molecular patterns. *Nat. Rev. Immunol.* 10, 787-796, doi:10.1038/nri2868 (2010).

54 Thomas, S. N. & Schudel, A. Overcoming transport barriers for interstitial-, lymphatic-, and lymph node-targeted drug delivery. *Curr Opin Chem Eng* 7, 65-74, doi:10.1016/j.coche.2014.11.003 (2015).

55 Zhao, L. *et al.* Nanoparticle vaccines. *Vaccine* 32, 327-337, doi:10.1016/j.vaccine.2013.11.069 (2014).

56 Manolova, V. *et al.* Nanoparticles target distinct dendritic cell populations according to their size. *Eur. J. Immunol.* 38, 1404-1413, doi:10.1002/eji.200737984 (2008).

57 Reddy, S. T., Rehor, A., Schmoekel, H. G., Hubbell, J. A. & Swartz, M. A. In vivo targeting of dendritic cells in lymph nodes with poly(propylene sulfide) nanoparticles. *J. Control Release* 112, 26-34, doi:10.1016/j.jconrel.2006.01.006 (2006).

58 Zhang, L., Spurlin, T. A., Gewirth, A. A. & Granick, S. Electrostatic stitching in gel-phase supported phospholipid bilayers. *J. Phys. Chem. B* 110, 33-35, doi:10.1021/jp055995s (2006).

59 Thomas, S. N., Vokali, E., Lund, A. W., Hubbell, J. A. & Swartz, M. A. Targeting the tumor-draining lymph node with adjuvanted nanoparticles reshapes the anti-tumor immune response. *Biomaterials* 35, 814-824, doi:10.1016/j.biomaterials.2013.10.003 (2014).

60 Ruiz-de-Angulo, A., Zabaleta, A., Gomez-Vallejo, V., Llop, J. & Mareque-Rivas, J. C. Microdosed Lipid-Coated Ga-67-Magnetite Enhances Antigen-Specific Immunity by Image Tracked Delivery of Antigen and CpG to Lymph Nodes. *ACS Nano* 10, 1602-1618, doi:10.1021/acsnano.5b07253 (2016).

61 Kang, S. *et al.* Effects of gold nanoparticle-based vaccine size on lymph node delivery and cytotoxic T-lymphocyte responses. *Journal of Controlled Release* 256, 56-67, doi:10.1016/j.jconrel.2017.04.024 (2017).

62 Mora-Solano, C. & Collier, J. H. Engaging adaptive immunity with biomaterials. *J. Mater. Chem. B* 2, 2409-2421, doi:10.1039/c3tb21549k (2014).

63 Maurer, T. *et al.* CpG-DNA aided cross-presentation of soluble antigens by dendritic cells. *Eur J Immunol* 32, 2356-2364, doi:Doi 10.1002/1521-4141(200208)32:8<2356::Aid-Immu2356>3.0.Co;2-Z (2002).

64 Heit, A. *et al.* Protective CD8 T cell immunity triggered by CpG-protein conjugates competes with the efficacy of live vaccines. *J Immunol* 174, 4373-4380 (2005).

65 Cho, H. J. *et al.* Immunostimulatory DNA-based vaccines induce cytotoxic lymphocyte activity by a T-helper cell-independent mechanism. *Nature Biotechnology* 18, 509-514 (2000).

66 Tighe, H. *et al.* Conjugation of protein to immunostimulatory DNA results in a rapid, long-lasting and potent induction of cell-mediated and humoral immunity. *Eur J Immunol* 30, 1939-1947, doi:Doi 10.1002/1521-4141(200007)30:7<1939::Aid-Immu1939>3.0.Co;2-# (2000).

67 Hassan, H. A. F. M. *et al.* Dual stimulation of antigen presenting cells using carbon nanotube-based vaccine delivery system for cancer immunotherapy. *Biomaterials* 104, 310-322, doi:10.1016/j.biomaterials.2016.07.005 (2016).

68 Ignacio, B. J., Albin, T. J., Esser-Kahn, A. P. & Verdoes, M. Toll-like Receptor Agonist Conjugation: A Chemical Perspective. *Bioconjugate Chem* 29, 587-603, doi:10.1021/acs.bioconjchem.7b00808 (2018).

69 Meyer, R., Giselbrecht, S., Rapp, B. E., Hirtz, M. & Niemeyer, C. M. Advances in DNA-directed immobilization. *Curr Opin Chem Biol* 18, 8-15, doi:10.1016/j.cbpa.2013.10.023 (2014).

70 Niemeyer, C. M., Boldt, L., Ceyhan, B. & Blohm, D. DNA-Directed immobilization: efficient, reversible, and site-selective surface binding of proteins by means of covalent DNA-streptavidin conjugates. *Anal Biochem* 268, 54-63, doi:10.1006/abio.1998.3017 (1999).

71 Boozer, C. *et al.* DNA directed protein immobilization on mixed ssDNA/oligo(ethylene glycol) self-assembled monolayers for sensitive biosensors. *Anal Chem* 76, 6967-6972, doi:10.1021/ac048908l (2004).

72 Niemeyer, C. M. & Ceyhan, B. DNA-Directed Functionalization of Colloidal Gold with Proteins This work was supported by Deutsche Forschungsgemeinschaft and Fonds der Chemischen Industrie. We thank Prof. D. Blohm for helpful discussions and generous support. *Angew Chem Int Ed Engl* 40, 3685-3688 (2001).

73 Yang, Y. *et al.* High Activity and Convenient Ratio Control: DNA-Directed Coimmobilization of Multiple Enzymes on Multifunctionalized Magnetic Nanoparticles. *ACS Appl Mater Interfaces* 9, 37254-37263, doi:10.1021/acsami.7b08553 (2017).

74 Li, H., Labean, T. H. & Leong, K. W. Nucleic acid-based nanoengineering: novel structures for biomedical applications. *Interface Focus* 1, 702-724, doi:10.1098/rsfs.2011.0040 (2011).

Appendix A

Supporting Information in Chapter 2

Supplementary Figures

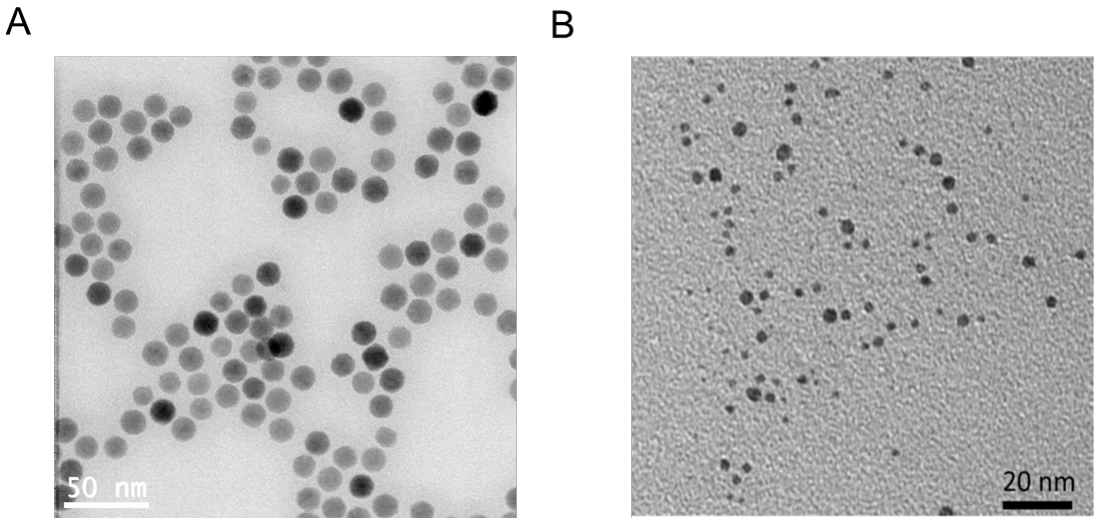

Figure S1. Transmission Electron Microscopy of Individual IVLN Components. (A) Representative transmission electron microscopy (TEM) image of polymer-coated iron-oxide nanoparticle (IONP-Polymer); scale-bar: 50 nm. (B) Representative transmission electron microscopy (TEM) image of gold nanoparticles (AuNP); scale-bar: 20 nm.

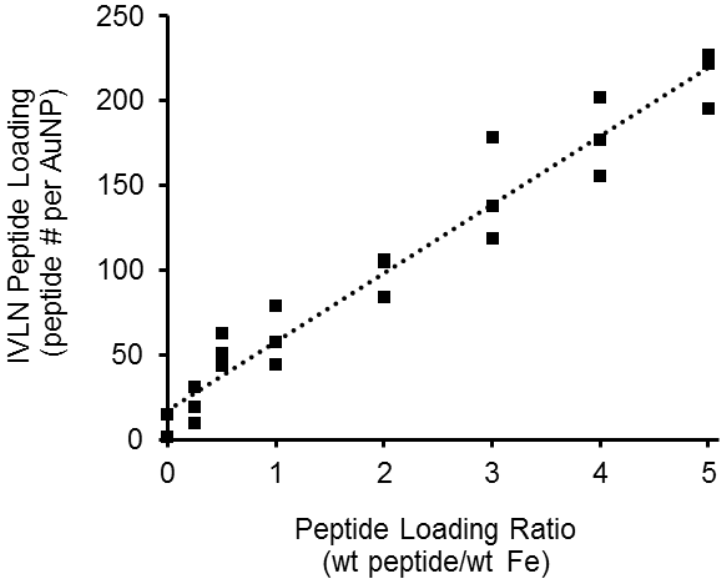

Figure S2. Peptide loading of IVLNs standardized on a per gold nanoparticle basis (R = 0.95).

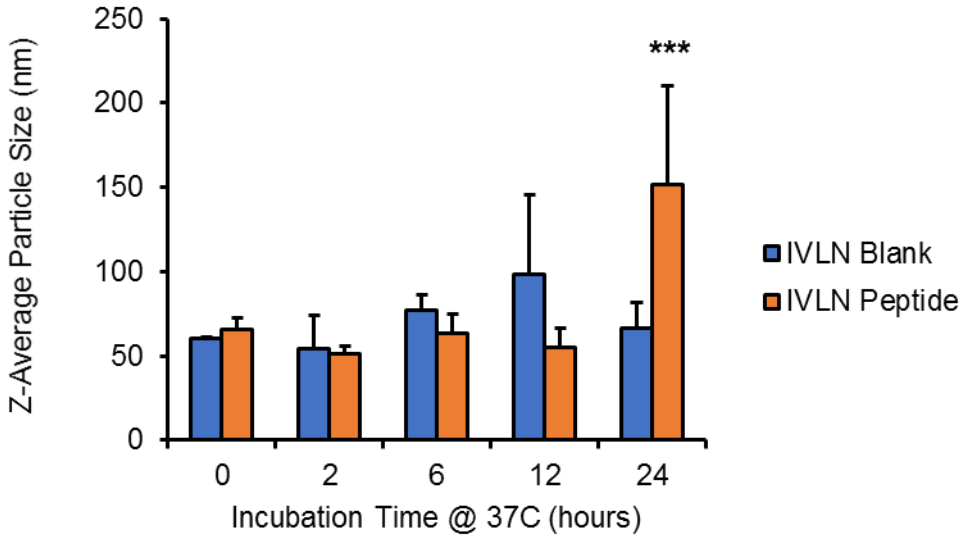

Figure S3. Serum stability study of IVLNs. Studies performed in 50% FBS/PBS at 37C. Stability changes were determined by Z-average particle size (nm) as determined by dynamic light scattering; data represent mean ± SD, n = 3. Statistical comparisons are based on one-way ANOVA, followed by post hoc Tukey's pairwise comparisons. The asterisks denote statistical significance at the level of *** $p < 0.001$. ANOVA, analysis of variance; SD, standard deviation.

	IVLN Blank	IVLN Peptide
Particle Size (nm)	52 ± 3	60 ± 2
Polydispersity Index (PDI)	0.19 ± 0.04	0.20 ± 0.03
Zeta-Potential (mV)	-16 ± 4	-17 ± 1

Table S1. IVLN material properties. Analysis performed before and after peptide conjugation under saturating conditions.

	Lipid IONP	IONP-HER2
Particle Size (nm)	52 ± 4	68 ± 5
Polydispersity Index (PDI)	0.16 ± 0.05	0.22 ± 0.02

Table S2. Lipid-coated IONP material properties. Analysis performed before and after peptide conjugation under saturating conditions.

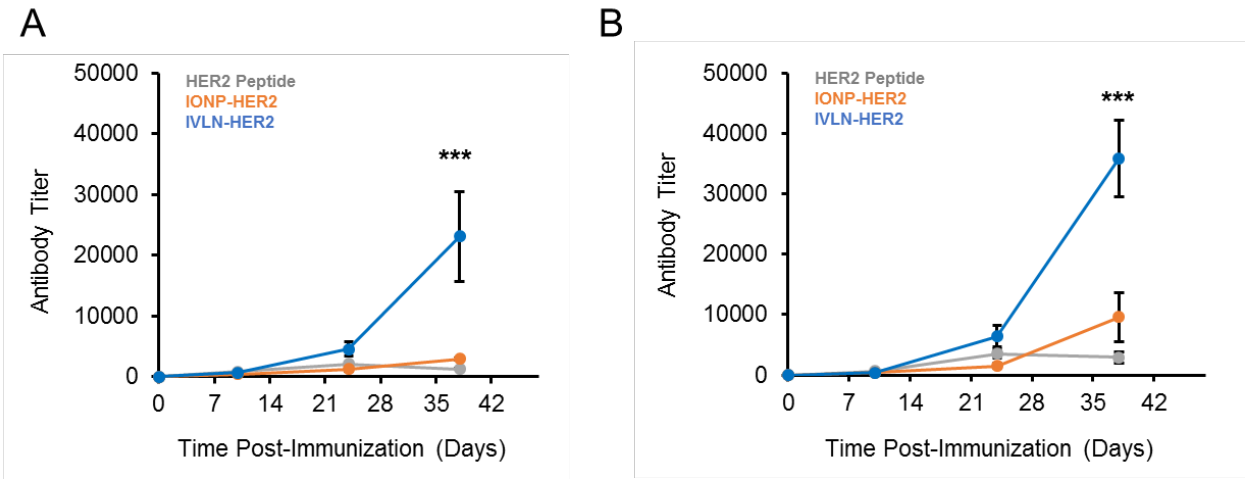

Figure S4. Antigen-Specific IgG Antibody Production Kinetics. Quantification of antigen-specific IgG antibodies by indirect ELISA represented as antibody titer from serum collected 10 days after every immunization (day 10, day 24 and day 38) with either (A) 5 μg HER2 peptide dose + 10 μg cGAMP or (B) 50 μg HER2 peptide dose + 10 μg cGAMP; data represent mean ± SE, n = 5. Statistical comparisons are based on one-way ANOVA, followed by post hoc Tukey's pairwise comparisons. The asterisks denote statistical significance at the level of *** $p < 0.001$. ANOVA, analysis of variance; SE, standard error.

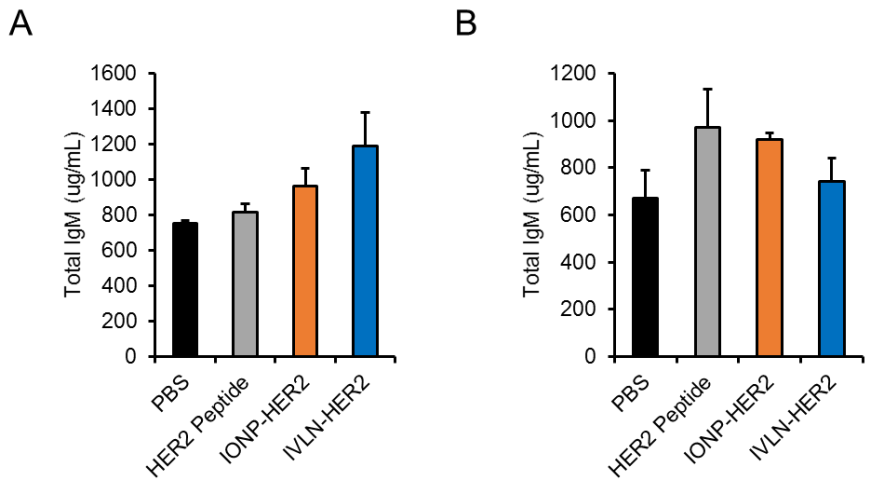

Figure S5. Total non-specific IgM antibody production. Quantification at 10 days post-boost 2 (day 38) for either (A) 5 μg HER2 peptide dose + 10 μg cGAMP or (B) 50 μg HER2 peptide dose + 10 μg cGAMP; data represent mean ± SD, n = 5. SD, standard deviation.

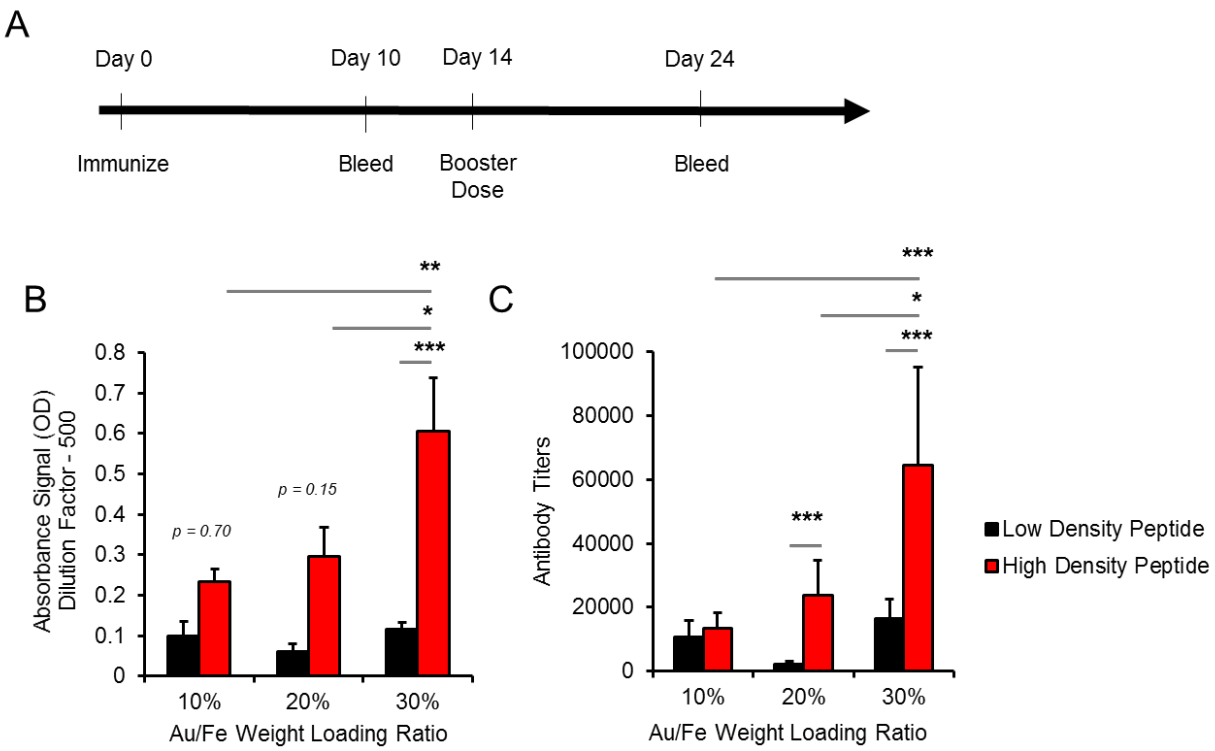

Figure S6. IVLN Antigen-Specific IgG Antibody Production at Different Au/Fe Ratios and Peptide Density. (A) Quantification of antigen-specific IgG antibodies by indirect ELISA represented as the background subtracted absorbance signal (OD) at 450 nm and 500-fold dilution; data represent mean ± SD, n = 5. (B) Quantification of antigen-specific IgG antibodies by indirect ELISA represented as antibody titer; data represent mean ± SE, n = 5. Statistical comparisons are based on one-way ANOVA, followed by post hoc Tukey's pairwise comparisons. The asterisks denote statistical significance at the level of * $p < 0.05$, ** $p < 0.01$, *** $p < 0.001$. ANOVA, analysis of variance; SE, standard error.

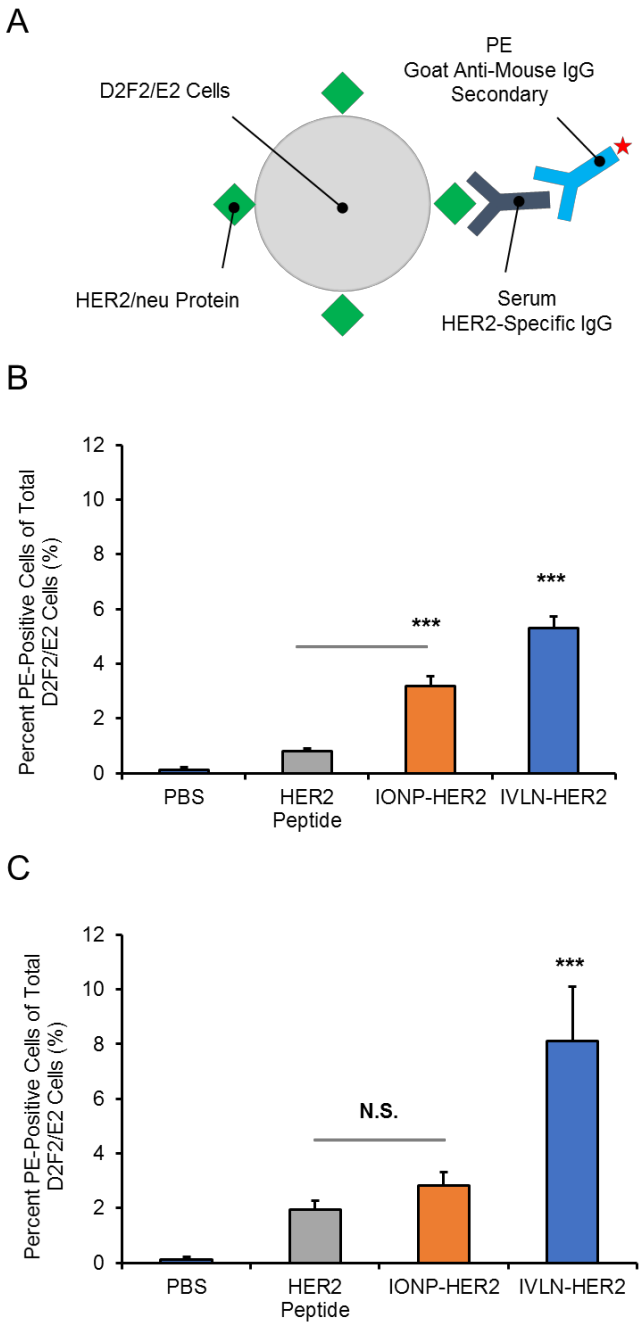

Figure S7. Antigen-Specificity Antibody D2F2/E2 Cell Specificity. (A) Schematic representation of the flow cytometry detection method of anti-HER2 antibody binding specificity to D2F2/E2 cells using PE-labeled IgG secondary antibody detection. (B/C) Anti-HER2 antibody binding specificity to D2F2/E2 cells of serum obtained from mice immunized with (B) 5 μg HER2 peptide dose + 10 μg cGAMP or (C) 50 μg HER2 peptide dose + 10 μg cGAMP; data represent mean ± SD, n = 3. Statistical comparisons are based on one-way ANOVA, followed by post hoc Tukey's pairwise comparisons. The asterisks denote statistical significance at the level of *** $p < 0.001$. ANOVA, analysis of variance; SD, standard deviation. N.S, no statistical significance.

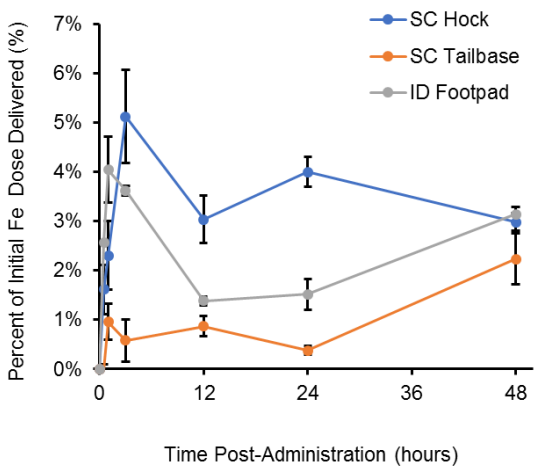

Figure S8. IVLN Lymph Node Delivery by Different Administration Routes. Quantification of nanoparticle delivery to lymph nodes (popliteal + inguinal) ipsilateral to the administration site at designated time intervals represented as the percentage of initial iron-oxide delivered using ICP-MS; data represent mean ± SE, n = 3.

A

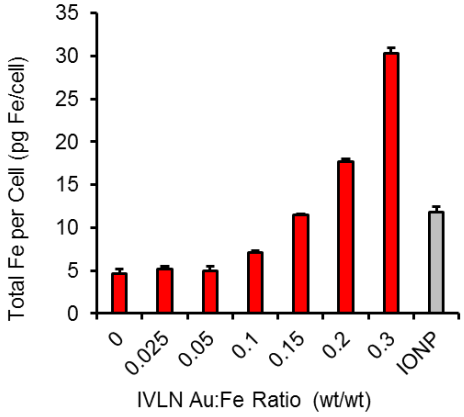

B

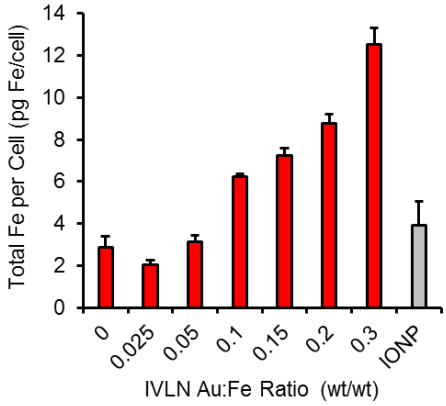

C

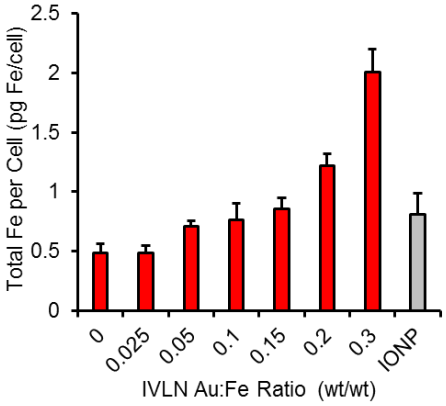

Figure S9. In-vitro Nanoparticle Cell Uptake Study – Surface Topography Effects. Quantification of in-vitro cell uptake of nanoparticles in (A) RAW264.7 macrophages, (B) DC2.4 dendritic cells and (C) murine primary B-cells by ICP-MS quantification of total Fe standardized by cell count (pg Fe per cell); data represent mean ± SD, n = 3. SD, standard deviation.

Mathematical Modeling:

Gold Nanoparticle (AuNP) Loading per Inorganic-Virus Like Nanoparticle (IVLN)

The extent of gold nanoparticle (AuNP) loading to inorganic virus-like nanoparticle (IVLN) surfaces was determined by ICP-MS determination of total elemental gold (Au) and iron (Fe) weights. These weights were then utilized to quantify total number spheres of a given element and particle size based on previously reported methods[1,2]. The ratio of these experimental values was then interpreted as AuNPs per IVLN, or the number of AuNPs per single IONP core.

Due to the crystalline structure of iron-oxide nanoparticles, it is possible to quantify the number of nanoparticles per unit Fe based on known particle size accordingly to previously establish methodologies (Table S3)[1]. Using transmission electron microscopy (TEM), the exact particle size of iron-oxide nanoparticles was quantified using the ImageJ software. The particle size of the polymer-coated iron-oxide nanoparticle core of the IVLN was 15 nm, while the particle size of the lipid-coated iron-oxide nanoparticle control was 30 nm. Based on the known unit cell volume of iron-oxide (Fe_3O_4) and quantified particle size, the number of nanoparticles per gram Fe was determined to be $1.5x10^{17}$ and $1.9x10^{16}$ for 15 nm and 30 nm cores, respectively (Table S3).

The number of gold nanoparticles per unit Au was quantified by two considerations. First, based on literature values reported by Lu et al[2], AuNPs with 3 nm diameters have 479 gold atoms per nanoparticle, which is 56% of the number of gold atoms per solid gold metallic colloids of the same diameter (835 gold atoms per nanoparticle). Therefore, by conversion from weight of Au to atoms of Au through Avogadro's Number it is possible to quantify the number of gold nanoparticle per unit Au. Quantification by this methodology revealed that number gold nanoparticle per gram Au was $6.38x10^{18}$ (Table S4). Second, based on literature values reported for the mass of a single AuNP for 2 nm, 5 nm and 10 nm particle size, the mass of a single 2 nm AuNP was interpolated based on curve fitting. Through curve fitting, the mass of a single 3 nm AuNP was determined to be $2.67x10^{-19}$ grams or $3.67x10^{18}$ AuNPs per gram Au (Table S4). Notably, this quantified value matches those values reported for solid gold colloids based on 835 gold atoms per nanoparticle and is therefore was not considered truly representative of our materials.

Description	Value
Unit cell volume of Fe_3O_4	0.5905 nm^3
Fe atoms per unit Fe_3O_4 cell	24
Molecular weight of Fe	55.85 g/mole
Avogadro's Number	6.022×10^{23}
Volume of 15 nm IONP core – single sphere	1766 nm^3
Volume of 30 nm IONP core – single sphere	14130 nm^3
Surface Area per Sphere - 15 nm IONP core	707 nm^2
Surface Area per Sphere - 30 nm IONP core	2826 nm^2
Number of Fe atoms per g Fe	1.08×10^{22}
Number of Fe_3O_4 unit cells per g Fe	4.5×10^{20}
Number of Fe_3O_4 unit cells per Single Sphere – 15 nm IONP core	2944
Number of Fe_3O_4 unit cells per Single Sphere – 30 nm IONP core	23550
Total Number of Spheres per g Fe – 15 nm IONP core	1.5×10^{17}
Total Number of Spheres per g Fe – 30 nm IONP core	1.9×10^{16}
Total Surface Area per g Fe – 15 nm IONP core	1.1×10^{20} nm^2
Total Surface Area per g Fe – 30 nm IONP core	2.7×10^{20} nm^2

Table S3. Iron-oxide nanoparticle calculations. Quantification of total number of spheres per unit Fe and total surface area per unit Fe for 15-nm and 30-nm iron-oxide nanocrystal cores. Calculations were performed based on equations outlined previously by Kokate et al[1].

Description	Value
Method 1	
Density of Gold	19.32 g/cm^3
Atomic Number	197
Average # of Gold Atoms per AuNP (3 nm)	479
Number of AuNPs per g Fe (3 nm)	6.38E+18
Method 2	
Mass of Single AuNP (g)	2.67E-19
Number of AuNPs per g Au (3 nm)	3.67E+18

Table S4. Gold nanoparticle calculations. Quantification of total number of spheres per unit Au for 3 nm AuNPs

Gold Nanoparticle Spatial Distribution – Inter-Nanoparticle Distance

The distance between AuNPs on IVLN surfaces was modeled based on two methodologies. The first technique was based on the arc length equation for a circle. If homogeneous distribution of AuNPs on a sphere is assumed, the loading of 2, 6 and 14 AuNPs on IVLN surface will yield AuNPs in a single plane (circle) oriented at central angles equivalent to 180º, 90º and 45º, respectively. Using the arc length equation for a circle with radius 7.5 nm, 2, 6 and 14 AuNPs will be located 23.6, 11.8 and 5.9 nm apart, respectively. Plotting these three points and using a power function curve fitting model (R^2 = 0.99) allows for interpolations of inter-nanoparticle distances between 2-14 AuNPs per IVLN surface (Figure S10A, Table S5). The benefit of this technique is that it accounts for arc length and is not a straight-line distance calculation. However, this model represent AuNPs are single points and only has three points for the curve fitting model thereby limiting potential power and accuracy.

The second technique used to quantify inter-nanoparticle distance on IVLN surfaces was based on a triangulation methodology. With the number of AuNPs per IVLN surface known and assuming homogeneous distribution of AuNPs on a sphere around a single central focal point, AuNPs can be triangulated. For AuNP per IVLN equal to or greater than 4, the number of triangles formed around a central focal point is 2n, where n is the number of AuNPs per IVLN.

$$AuNP\ Triangles\ per\ IONP\ core\ = AuNP\ per\ IONP\ core \times 2$$

With the number of triangles determined, the surface occupied by a single triangle was quantified given the surface area of spherical IVLN with 7.5 nm radius.

$$Surface\ Area\ per\ Triangle = \frac{Surface\ Area\ of\ IVLN}{Number\ of\ Triangles}$$

Assuming an equilateral triangle, the surface area of a single triangle can be used to determine the length of a side of the triangle, and therefore the distance between AuNPs represented as single points. By subtracting 2x the radius of the AuNPs, a better surface to surface contact distance can be interpreted (Figure S10B, Table S6).

$$Distance\ between\ AuNPs = \sqrt{\frac{4\ \times Triangle\ Surface\ Area}{\sqrt{3}}} - (\ 2 \times AuNP\ radius)$$

The benefit of this technique is that does not rely on interpolation. However, this model is limited due to the reliance of straight-line distances between AuNPs.

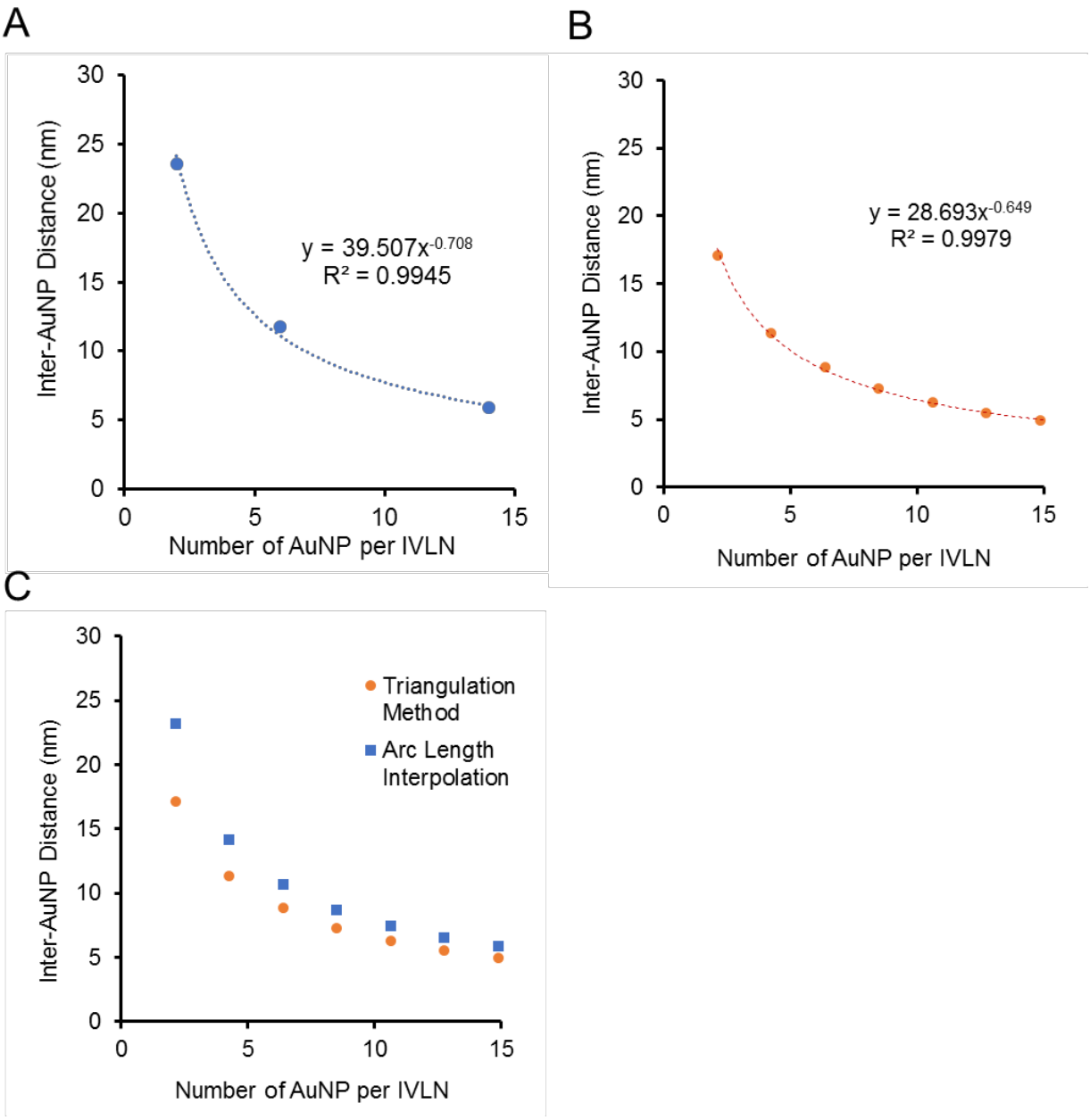

Figure S10. Modeling of inter-nanoparticle distance on IVLN surfaces. (A) Power function curve fit model based on the arc length between 2 (central angle: 180º), 6 (central angle: 90º) and 14 AuNPs (central angle: 45º) homogeneously distributed in 3D space around an IONP core with 15 nm diameter. (B) Power function curve fit model based on the triangulation methodology described above. (C) Overlay comparison of both modeling strategies for inter-AuNP distance (nm).

Au/Fe Ratio (wt/wt)	AuNP per IVLN	Inter-Nanoparticle Distance Arc Length (nm)
0.05	2.1	23.18
0.1	4.2	14.19
0.15	6.4	10.65
0.2	8.5	8.69
0.25	10.6	7.42
0.3	12.7	6.52
0.35	14.9	5.84
0.4	17.0	5.32

Table S5. Inter-nanoparticle distance: Arc Length Interpolation Model. Interpolation data set for inter-AuNP distances based on AuNP per IVLN determined by ICP-MS (Figure 2.2A) and the curve fitting model presented in Figure S10A ($y = 39.51x^{-.708}$, $R^2 = 0.99$).

Au/Fe Ratio (wt/wt)	AuNP per IVLN	Inter-Nanoparticle Distance Arc Length (nm)
0.05	2.1	17.10
0.1	4.2	11.36
0.15	6.4	8.82
0.2	8.5	7.30
0.25	10.6	6.27
0.3	12.7	5.50
0.35	14.9	4.91
0.4	17.0	4.43

Table S6. Inter-nanoparticle distance: Triangulation Model. Data set for inter-AuNP distances based on AuNP per IVLN determined by ICP-MS (Figure 2.2A) and mathematic modeling presented above, and curve fitting model presented in Figure S10B ($y = 28.69x^{-.649}$, $R^2 = 0.99$).

Bibliography:

1 Kokate, M., Garadkar, K. & Gole, A. One pot synthesis of magnetite-silica nanocomposites: applications as tags, entrapment matrix and in water purification. *J Mater Chem A* 1, 2022-2029, doi:10.1039/c2ta00951j (2013).

2 Lu, Y., Wang, L., Chen, D. & Wang, G. Determination of the concentration and the average number of gold atoms in a gold nanoparticle by osmotic pressure. *Langmuir* 28, 9282-9287, doi:10.1021/la300893e (2012).

Appendix B

Supporting Information in Chapter 3

Section 1: Comparison of the stabilization efficiency by the standard and the modified thin film hydration methods

To compare the standard and the modified thin film hydration methods, we tested the ability of both methods to stabilize 20 nm iron oxide nanocrystals with DSPE-mPEG(2000)/C12-98(5) lipidoid (75:25 %w/w) formulations. The thin films of identical composition were hydrated with either phosphate-buffered saline (PBS) or ethanol, heated at 65°C for 2 hours and dialyzed into PBS. The hydration with ethanol resulted in more than 30-fold higher aqueous recovery of stabilized nanoparticles compared to the hydration with PBS (27.0 ± 6.0% vs 0.7 ± 0.8%, $p<0.001$, Figure S11).

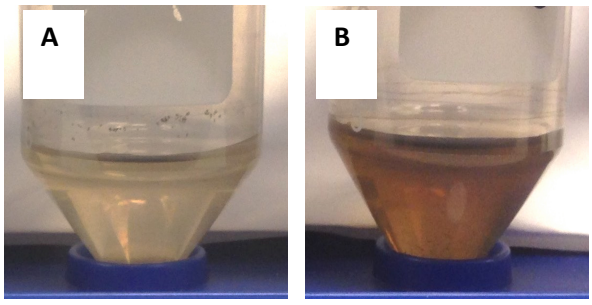

Figure S11. IONP Formulation Method Comparison Images. Representative formulations of 20 nm iron oxide nanocrystals stabilized with DSPE-mPEG(2000)/C12-98(5) lipidoid (75:25 %w/w) using the standard (A, hydration with PBS) or the modified (B, hydration with ethanol) thin film hydration methods.

Section 2: Lipidoid synthesis

Lipidoids were synthesized by conjugate addition of alkyl-acrylamide (N-dodecylacrylamide) to amines using neat synthesis as described by Akinc, et al[1] (Figure S2,A). Briefly, the reactants were mixed in a glass vial and the mixture was stirred at 90C for 7 days. A series of amine monomers (63, 96,98,113) with different structures were used to synthesize lipidoids with different numbers of alkyl chains ("tails") (Figure S2,B). The molar ratios of N-dodecylacrylamide to amine were altered to obtain the desired number of tails per lipidoid . For example, C12-98 was synthesized with a 5:1 molar ratio of N-dodecrylacrylamide (C12) to triethylenetetraamine (98) to yield a 5-tailed lipidoid C12-98(5). The products were purified by gravity silica column chromatography using Silicycle SiliaFlash P60 (230-400 mesh) and dichloromethane/methanol/ammonium hydroxyde (75:22:3 %v/v) as the stationary and the mobile phases, respectively. Lipidoid formation was confirmed by electrospray ionization (ESI) mass spectrometry (Waters Micromass LCT Mass Spectrometer). For example, the lipidoid C12-98(5) [$C_{81}H_{164}N_9O_5$] yielded the m/z ratio of 1343.2 $[M+H]^+$, consistent with the previously reported m/z ratio of 1343.3.[1]

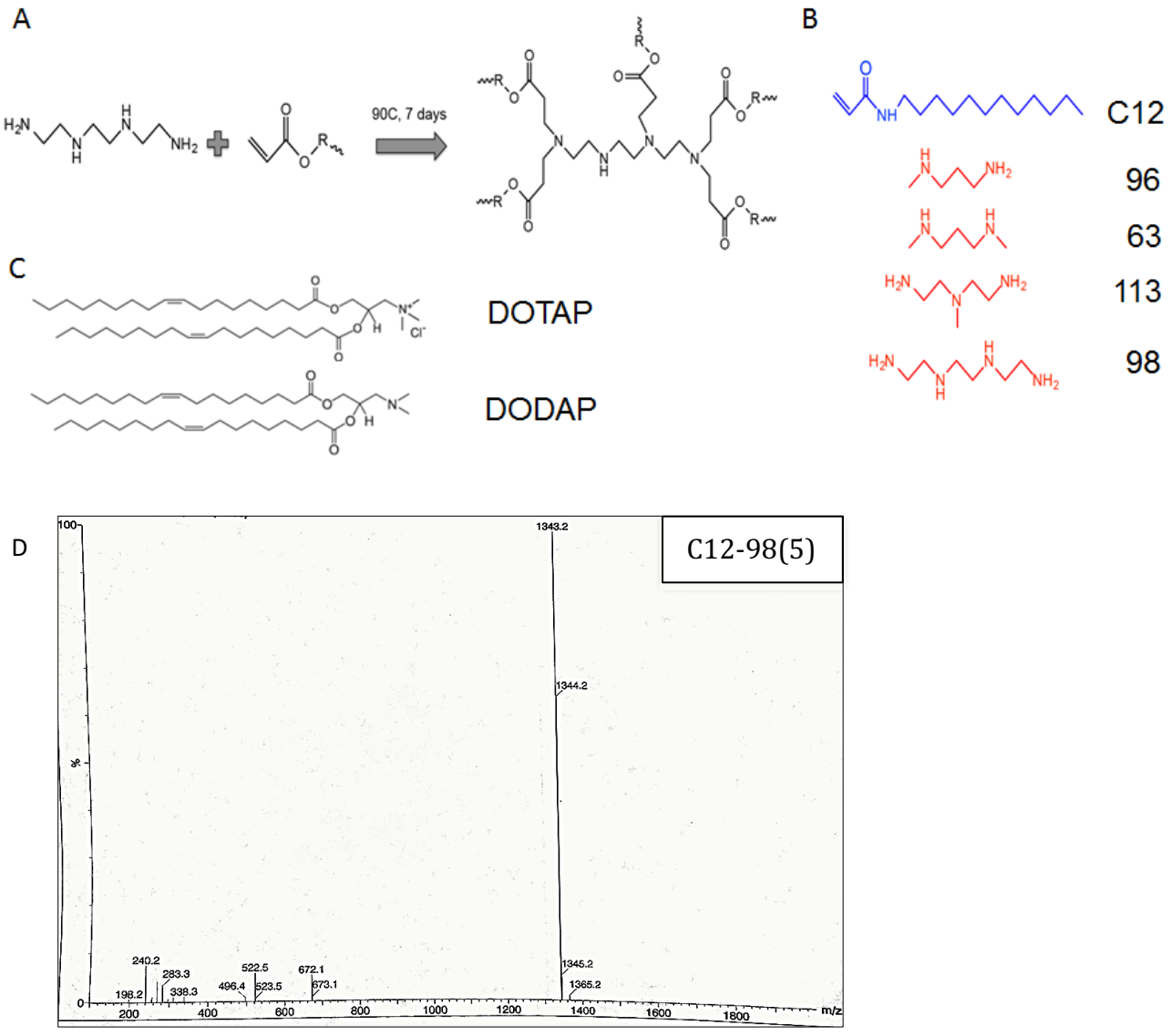

Figure S12. Synthesis of lipidoids. (A) Schematic depiction of the lipidoid synthesis reaction; (B) The chemical structures of the N-dodecylacrylamide (C12) and the amine reactants (96,63,113,98) used for the lipidoid synthesis; (C) Chemical structures of the cationic phospholipids 1,2-dioleoyl-3-trimethylammonium-propane (DOTAP), and 1,2-dioleoyl-3-dimethylammonium-propane (DODAP); (D) Mass spectrograph of the lipidoid C12-98(5)

Section 3: Initial Screening of Lipidoids and Cationic Phospholipids for Iron Oxide Stabilization

Using the thin film ethanol hydration method (S1), we tested a series of lipidoids and cationic phospholipids (Figure S2A, B and C) for their ability to stabilize iron oxide nanocrystals (20 nm). Formulations containing a lipidoid or a cationic phospholipid (25% w/w) were dispersed in a thin film, hydrated with ethanol and dyalized into the aqueous PBS (as described in the Methods section). The cationic phospholipids displayed negligible stabilization efficiency (DODAP: 2± 1%, DOTAP: 3±1%), which could not be significantly improved by either the 2-tailed (C12-62(2), p=0.99) or the 3-tailed (C12-96(3), p=0.55) lipidoids. In contrast, the lipidoids with 5 (C12-98(5), p<0.001) and 4 tails (C12-113(4), p=0.026) were significantly more efficient than cationic lipids in mediating iron oxide stabilization. The 5-tail lipidoid C12-98(5) displayed the highest stabilization efficiency (27 ± 6%) among the tested compounds, and therefore, was selected for further studies.

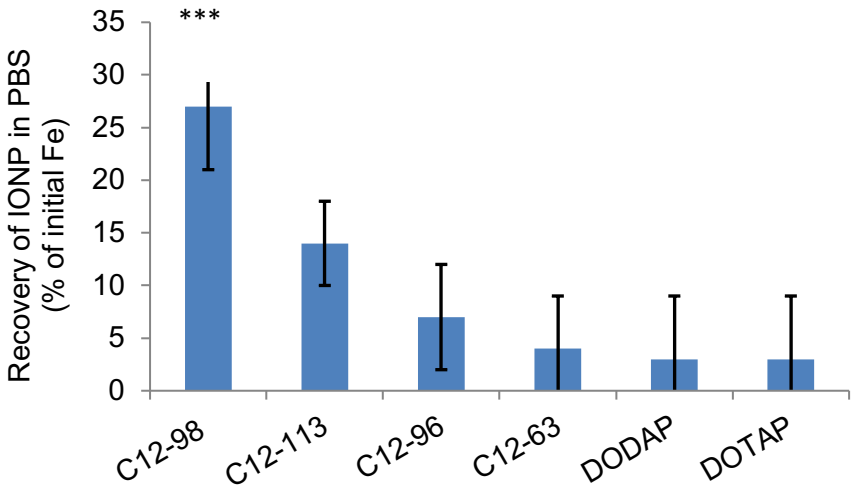

Figure S13. Formulation Stability Lipidoid Comparision. Aqueous stabilization of the iron oxide nanocrystals (20 nm) by lipid formulations containing lipidoids or cationic phospholipids (25% w/w). Stabilization was measured as percent of nanocrystals added to the formulations that could be recovered in aqueous phosphate-buffered-saline (PBS) solution. Data represents mean ± S.D.; asterisks denote statistical significance at the level of *** p < 0.001.

Section 4: Analysis of Lipid Coating Composition of stabilized iron oxide nanoparticles (IONP-ML) by Thin Layer Chromatography

To assess the composition of the lipid coatings extracted from the IONP-ML surface, we carried out the thin layer chromatography (TLC) analysis. TLC was performed as described in the methods section. Coatings extracted from the surfaces of both the 10-nm core (lane 3) and 30-nm core (lane 4) IONP-ML displayed 3 spots on the TLC chromatograms. Two spots with the Rf values of 0.59 ± 0.03 and 0.40 ± 0.02 corresponded to the spots of the DSPE-mPEG(2000) standard (lane1: 0.59 ± 0.07, p=0.99; and 0.41 ± 0.02, p=0.99). The third spot with the Rf value of 0.51 ± 0.06 corresponded to the spot of the C12-98(5) lipidoid standard (lane 2: 0.49 ± 0.02, p=0.99). These results confirmed the presence of the DSPE-mPEG and the C12-98(5) lipidoid on the surface of the stabilized IOMP-ML nanoparticles.

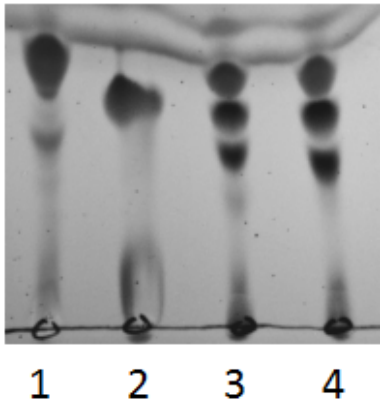

Figure S14: TLC analysis of the IONP-ML coating composition. Representative TLC chromatogram, lane 1: DSPE-mPEG(2000) standard, lane 2: C12-98 (5) standard, lane 3: coating extracted from the 10 nm IONP-ML, lane 4: coating extracted from the 30 nm IONP-ML.

Section 5: Experimental Determination of DSPE-mPEG(2000) Packing Density in the IONP-ML Coatings

To estimate the packing density of the DSPE-mPEG(2000) in the IONP-ML coatings, we replaced the DSPE-mPEG(2000) with the DSPE-PEG(2000)-PDP in the coating formulations. The content of the DSPE-PEG(2000)-PDP that contains the 2-pirydyldithio (PDP) group can be determined by the pyridine-2-thione spectrophotometric assay[2]. Based on the 1:1 molar ratio of DSPE-PEG:PDP in each DSPE-PEG(2000)-PDP molecule, the content of PDP per known quantity of nanoparticles represents the DSPE-PEG(2000)-PDP (or PEG) packing density in the nanoparticle formulations.

Coated nanoparticles (IONP-ML-PDP) were prepared as described in the Methods section using the following lipid composition: C12-98(5):DSPE-PEG(2000)-PDP (77:23 mol %). The resulting formulations were purified by magnetic column chromatography (Miltenyi Biotec) to remove any free lipid micelles and analyzed for Fe content by ICP-EOS. The content of the DSPE-PEG(2000)-PDP in the purified IONP-ML-PDP was quantified by a pyridine-2-thione assay. Briefly, IONP-ML-PDP nanoparticles (at known Fe concentrations) were reduced to release the pyridine-2-thione chromophore (λ=343 nm) by incubation with the reducing agent TCEP-HCl (100 mM aqueous) for 2 hours at 65°C. To prevent absorbance interference, the nanoparticles were removed from the reaction mixture by magnetic separation. The concentration of pyridine-2-thione in nanoparticle-free solutions was determined spectrophotometrically (343 nm, Tecan M1000 PRO) using pyridine-2-thione standard solutions for calibration. The content of PDP per unit Fe (nmole PDP per mg Fe) was calculated as a ratio of the pyridine-2-thione to nanoparticle (IONP-ML-PDP, Fe equivalent) concentrations.

To calculate the content of PDP per single iron oxide sphere, we estimated the Fe content of a single iron oxide nanoparticle as previously described[3]. Assuming that iron oxide nanocrystals comprise of magnetite (Fe_3O_4), iron content of a single nanocrystal can be estimated based on the dimensions and the iron content of the magnetite's crystalline unit cell (Table S7) as following:

(S1) $$N_{Fe,IO} = \frac{V_{IO} \times N_{Fe,UC}}{V_{UC}} = \frac{\frac{4}{3}\pi (R_{IO})^3 \times N_{Fe,UC}}{(l_{UC})^3}$$

(S2) $$m_{Fe,IO} = N_{Fe,IO} \times MW_{Fe}/N_A$$

Where V_{uc} – volume of the unit cell, l_{uc} – cubic edge of the unit cell, R_{IO} – radius of the nanocrystal, V_{IO} – volume of the nanocrystal, $N_{Fe,UC}$ – number of iron atoms per unit cell, $N_{Fe,\ IO}$ – number of iron atoms per iron oxide nanocrystal, $m_{Fe,IO}$ – mass of Fe per iron oxide nanocrystal, MW_{Fe} – molar mass of Fe, N_A – Avogadro's number

The number of DSPE-PEG(2000)-PDP molecules per iron oxide nanoparticle ($N_{PEG\ per\ IO}$) and the number of DSPE-PEG(2000)-PDP molecules per unit nanoparticle surface area ($N_{PEG\ per\ SA}$) were calculated using equations (S3) and (S4), respectively:

(S3) $$N_{PEG\ per\ IO} = C_{PEG\ per\ Fe} \times m_{Fe,IO} \times N_A$$

(S4) $$N_{PEG\ per\ SA} = \frac{N_{PEG\ per\ IO}}{4\pi(R_c)^2}$$

Where $C_{PEG\ per\ Fe}$ is the molar content of PEG (PDP) per unit mass of Fe, and R_c is the radius of the "hard sphere" of the coated iron oxide nanoparticles (section S5).

Table S7 summarizes the parameters and the representative estimates of the PEG packing density for the 30 nm core IONP-ML-PDP nanoparticles calculated using equations (S1)-(S4).

Parameters	Symbol	Value	Units	Ref.
Cubic edge of the magnetite's unit cell	l_{UC}	0.84	nm	4
Number of iron atoms per unit cell	$N_{Fe,UC}$	24		4
Molar mass of Fe	MW_{Fe}	55.85	g/mol	
Avogadro's Number	N_A	6.022×10^{23}	atoms/mole	
Radius of the nanocrystal (measured by TEM)	R_{IO}	14.5	nm	
Radius of the "hard sphere"	R_c	19.5	nm	
Estimated values				
Molar content of PEG per unit Fe	$C_{PEG\ per\ Fe}$	405± 20	nmol/mg Fe	
The number of PEG molecules per iron oxide nanoparticle	$N_{PEG\ per\ IO}$	11740	molecules/particle	
The number of PEG molecules per unit surface area ("hard sphere")	$N_{PEG\ per\ SA}$	2.5	molecules/nm^2	

Table S7. Estimation of the PEG packing Density for the 30 nm core IONP-ML-PDP nanoparticles.

Section 6: Theoretical Estimation of Hydrodynamic Diameter Using a Scaling Model

The hydrodynamic size of the PEGylated core-shell iron oxide nanoparticles in aqueous solution can be theoretically predicted using a starlike scaling model[5]. PEG chains grafted to the surface of spherical particles extend out from the particle surface forming a hydrodynamic layer of thickness L. The combined size of the particle's "hard sphere", a sphere to which the PEG chains are attached, and the thickness of the surface PEG layer provide an estimate of the particle hydrodynamic size. The scaling model relates the PEG layer thickness, L, to the radius, R_c, of the nanoparticle's 'hard sphere', while accounting for polymer characteristics and the number of surface-grafted polymer chains as following:

(S5) $$L = \left[N_{\mathrm{EO}} \times l^{1/v} \times \frac{8f^{(1-v)/2v}}{3v4^{1/v}} + R_c^{1/v}\right]^{v} - R_c$$

Where L is the thickness of the PEG layer, N_{EO} is the number of monomeric ethylene oxide (EO= OCH_2CH_2) units per PEG chain, *l* is the statistical length of the EO monomer, *f* is the number of PEG chains on the nanoparticle surface, *v* is the Flory exponent, R_c is the radius of the "hard sphere".

To estimate the PEG thickness layer, L, for the IONP-ML nanoparticles we used the parameters summarized in Table S8. Similar to previous studies[6], we assumed that the radius of the "hard sphere", R_c, includes the contributions from both the iron oxide core (R_{IO}) and the lipid bilayer formed by DSPE, oleic acid and lipidoid (R_s). The radii of both the iron oxide core and the lipid bilayer for the IONP-ML were measured by TEM. We assumed that the IONP-ML shell observed by TEM represents the tightly packed hydrophobic portion of the coating (DSPE/oleic acid/lipidoid), and hence can be used to approximate R_s. The number of PEG chains per particle, f, was calculated based on the surface area of the "hard sphere" and the PEG grafting density (δ_{PEG}):

(S6) $$f = \delta_{PEG} \times 4\pi(R_{IO} + R_s)^2$$

Using the size estimates for the hard sphere Rc and the PEG thickness layer L, we calculated the hydrodynamic diameter (D_h) of IONP-ML as following:

(S7) $$D_h = (R_{IO} + R_s + L) \times 2$$

Parameter	Symbol	Value	Units	Ref.
Number of monomeric units in PEG2000	N_{EO}	45		5, 6
Length of a PEG monomer (OCH_2CH_2)	l	0.39	nm	5, 6
Flory exponent	v	0.583		5, 6
Radius of the lipid bilayer	R_s	5	nm	Measured by TEM
PEG grafting density	δ_{PEG}	2.5	molecules/nm^2	Table S7

Table S8. Parameters used to estimate the hydrodynamic diameter of IONP-ML

Section 7: Characterization of IONP-ML-PDP

Functionalized nanoparticles IONP-ML-PDP with 10 nm and 30 nm core size were prepared as described in the Methods using lipid composition of C12-98(5):DSPE-mPEG(2000):DSPE-PEG(2000)-PDP (77:11.5:11.5 mol %). Replacement of 50% DSPE-mPEG(2000) with the functionalized lipid DSPE-PEG(2000)-PDP had no significant effect on either the stabilization efficiency (10 nm: p = 0.99; 30 nm: p = 0.98) or the hydrodynamic diameter (10 nm: p = 0.84; 30 nm: p = 0.99) of the resulting nanoparticles (Figure S4, A and B).

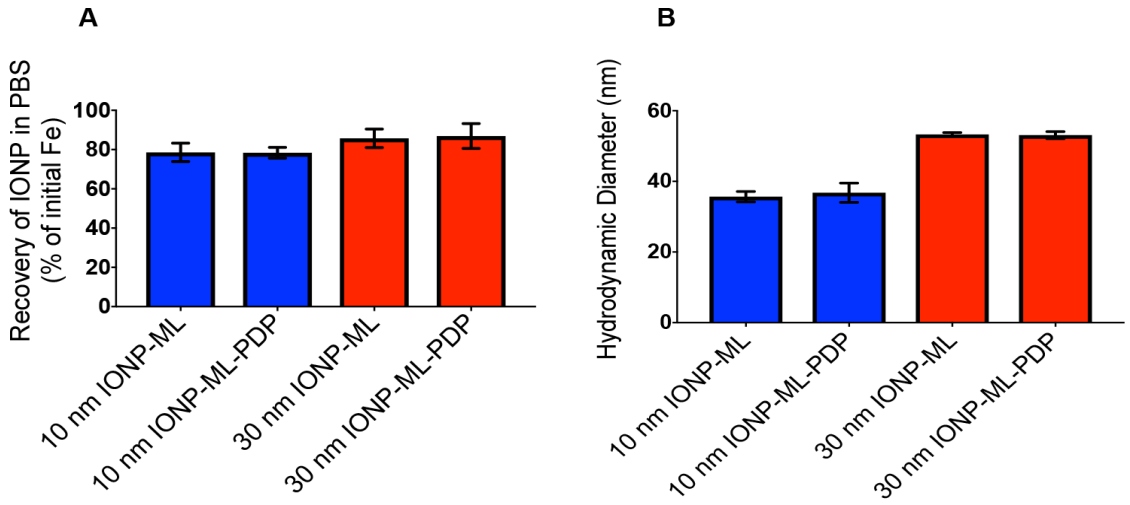

Figure S15. Effect of nanoparticle functionalization on the aqueous stabilization efficiency and hydrodynamic size. (A) Stabilization efficiency for the original IONP-ML and functionalized IONP-ML-PDP nanoparticles with 10 nm and 30nm core size; Data represents mean ± S.D. (n = 3). (B) Hydrodynamic diameter of the original IONP-ML and functionalized IONP-ML-PDP nanoparticles with 10 nm and 30 nm core size; Data represents mean ± S.D. (n = 3)

Section 8: Estimation of Biomolecule Loading per Particle: Loading Multivalency and Density

Molar biomolecule loading ($C_{BM\ per\ Fe}$) per unit nanoparticle mass (Fe equivalent) was determined as described in the Methods. To calculate biomolecule loading per single nanoparticle, we estimated the mass of Fe per iron oxide nanocrystal ($m_{Fe,IO}$) as described in section S4. The unit conversions to calculate the number of biomolecules per single iron oxide nanoparticle ($N_{BM\ per\ IO}$, loading multivalency) and the number of biomolecules per unit nanoparticle surface area ($N_{BM\ per\ SA}$, loading density) were performed using the equations S8 and S9, respectively:

(S8) $$N_{BM\ per\ IO} = C_{BM\ per\ Fe} \times m_{Fe,IO} \times N_A$$

(S9) $$N_{BM\ per\ SA} = \frac{N_{BM\ per\ IO}}{4\pi(D_h/2)^2}$$

Where D_h is the hydrodynamic diameter of the IONP-ML nanoparticle

IONP-ML Core Diameter (nm)	Biomolecule	IONP-ML Hydrodynamic Diameter (nm)	Biomolecule loading (μmol/g Fe)	Mass of Fe per single core (g)	Multivalency (Biomolecules per Sphere)	Surface Area per Sphere ($nm^{2)}$	Biomolecule Surface Density (molecule/nm^2)
10	CpG	~35	87±8	2×10^{-18}	104	~3630	0.03
10	Peptide	~35	201±30	2×10^{-18}	239	~3630	0.06
30	CpG	~54	88±8	5×10^{-17}	2824	~9160	0.3
30	Peptide	~54	170±52	5×10^{-17}	5455	~9160	0.6

Table S9. Biomolecule Loading per Single Nanoparticle: Multivalency and Density

Section 9: Retention of Nanoparticle-Conjugated Biomolecules in Serum

To evaluate the stability of the disulfide linkages selected for conjugation of biomolecules to the nanoparticle surface, we analyzed retention of the biomolecules on nanoparticles following incubation with serum. CpG-functionalized nanoparticles IONP-ML-CpG with 10 nm and 30 nm core size were prepared as described in the Methods. The nanoparticles (0.5 mgFe/mL) were incubated in serum (50% fetal bovine serum (FBS) in PBS) at 37°C for 1 hour under gentle agitation. Subsequently, the nanoparticles were recovered by magnetic chromatography and analyzed for the contents of iron oxide and CpG as described in the Methods. The CpG loading per particle was calculated as described in Section S7 above. Comparison of the CpG loading per particle before and after incubation with serum is presented in Figure S5. The CpG contents of the nanoparticles before and after incubation with serum did not differ significantly (10 nm: before – 120 ± 37 vs after – 115 ± 41, p=0.89; 30 nm: before – 3180 ± 430 vs after – 3150 ± 450, p=0.96) confirming stability of the disulfide linkages in serum.

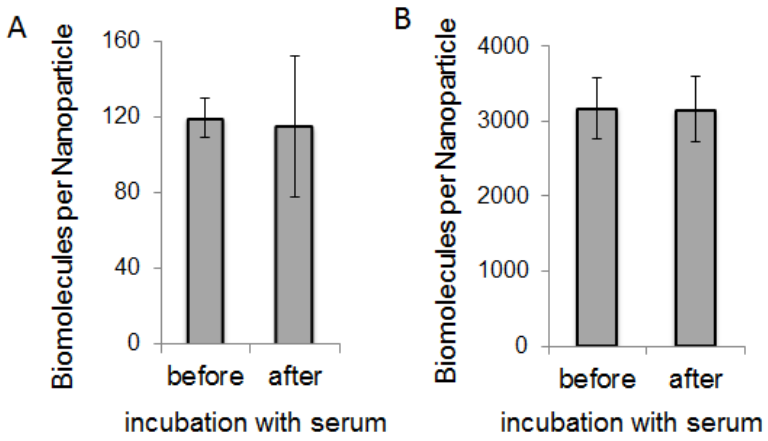

Figure S16. Retention of nanoparticle-conjugated biomolecules in serum. (A) CpG content of IONP-ML-CpG nanoparticles with 10 nm core size before and after incubation with serum (50% FBS in PBS, 37C for 1 hour); Data represents mean ± S.D. (n = 3). (B) CpG content of IONP-ML-CpG nanoparticles with 30 nm core size before and after incubation with serum (50% FBS in PBS, 37C for 1 hour); Data represents mean ± S.D. (n = 3).

Bibliography:

1 Akinc, A. & al., e. A combinatorial library of lipid-like materials for delivery of RNAi therapeutics. *Nat. Biotechnol.* 26, 561-569, doi:10.1038/nbt1402 (2008).

2 Carlsson, J., Drevin, H. & Axen, R. Protein thiolation and reversible protein-protein conjugation. N-Succinimidyl 3-(2-pyridyldithio)propionate, a new heterobifunctional reagent. *Biochem. J.* 173, 723-737 (1978).

3 Kokate, M., Garadkar, K. & Gole, A. One pot synthesis of magnetite-silica nanocomposites: applications as tags, entrapment matrix and in water purification. *J. Mater. Chem. A* 1, 2022-2029, doi:10.1039/c2ta00951j (2013).

4 Verwey, E. J. W. & Heimann, E. L. Physical properties and cation arrangement of oxides with spinel structures. *J. Chem. Phys.* 15, 174 (1947).

5 Johnsson, M., Hansson, P. & Edwards, K. Spherical micelles and other self-assembled structures in dilute aqueous mixtures of poly(ethylene glycol) lipids. *J. Phys. Chem. B* 105, 8420-8430, doi:10.1021/jp0110881 (2001).

6 Tong, S., Hou, S., Zheng, Z., Zhou, J. & Bao, G. Coating optimization of superparamagnetic iron oxide nanoparticles for high T2 relaxivity. *Nano Lett.* 10, 4607-4613, doi:10.1021/nl102623x (2010).

Appendix C

Supporting Information in Chapter 4

Experimental Section

Materials. All reagents were used as obtained from commercial sources without further purification. Ovalbumin (OVA) was purchased from MP Biomedical. Succinimidyl 3-(2-pydridylthio) propionate) (SPDP) was obtained from CovaChem. CpG oligonucleotides with a 3' terminal disulfide bridge modification (3' Thiol Modifier C3 S-S; 1-propanol-disulfide, 1'-succinyl-lcaa-CPG) were purchased from IDT DNA Technologies (CpG 1826 (5') TCCATGACGTTCCTGACGTT-$(CH_2)_3$-S-S-CH_3 (3')). 2-Nitrophenyl β-D-galactopyranoside (ONPG), tris(2-carboxyethyl) phosphine hydrochloride (TCEP-HCl), ammonium persulfate and N,N,N',N'-tetramethylethylenediamine (TEMED) were acquired from Sigma-Aldrich. SYBR Gold Nucleic Acid Gel Stain (10,000X) and the microBCA protein assay kit were obtained from Thermo Fisher. Macrophage Colony Stimulating Factor (M-CSF) and Anti-CD45.2 APC were purchased from eBiosciences. B3Z T-cell hybridoma cells were generously donated by Dr. Stephen Schoenberger (La Jolla Institute for Allergy and Immunology).

Synthesis and purification of Ovalbumin-CpG conjugate (OVA-CpG). OVA-CpG covalent conjugates were synthesized using a three-step disulfide coupling chemistry. In the first step, OVA was reacted with SPDP to produce functionalized OVA-PDP. The reaction was carried out as previously described[1] with minor modifications. Briefly, OVA (1 mg/mL in 100 mM PBS buffer, pH 7.4) was reacted with a molar excess of SPDP (20 mM SPDP, dimethylsulfoxide DMSO) for 12 hours at room temperature. The molar ratios of SPDP to OVA were varied to produce conjugates with different degrees of functionalization (5-fold to 15-fold molar excess). OVA-PDP was purified sequentially by anion exchange chromatography (HiTrap Q FF, 5 mL) and ultrafiltration (10,000 MWCO) to remove unreacted species. Purified OVA-PDP was analyzed by microBCA and pyridine-2-thione spectrophotometric assays[2] to determine the PDP content of the functionalized protein. In the second step, CpG oligonucleotides modified with a terminal protected disulfide were reacted with a reducing agent (TCEP-HCL, 100 mM,

overnight) to produce oligonucleotides with a free terminal sulfhydryl group (CpG-SH). CpG-SH was purified by anion exchange chromatography (HiTrap Q FF, 1 mL), followed by desalting with ultrafiltration (1,000 MWCO). The purified oligonucleotides were quantified by spectrophotometric analysis (NanoQuant Plate, Tecan M1000 PRO)[3]. In the third step, OVA-CpG covalent conjugates were produced by reacting OVA-PDP (1 mg/mL in 100 mM PBS, pH 7.4) with CpG-SH (at 1:1 molar ratio of PDP:CpG) at room temperature for 48 hours. To isolate OVA-CpG conjugates with defined CpG content, the reaction mixture was fractionated using anion exchange chromatography with a stair-step sodium chloride (NaCl) elution gradient (0-2 M, NaCl). Fractions were desalted and purified of unreacted oligonucleotide species using centrifugal filtration (30,000 MWCO, 15 mL).

Characterization of Ova-CpG conjugates. To confirm isolation of major conjugate species from heterogeneous product mixtures, purified species were characterized by anion exchange chromatography. Anion exchange chromatography was carried out using quaternary ammonium solid phase (HiTrap Q FF, 5 mL) with a stair-step sodium chloride (NaCl) elution gradient (0-2 M, NaCl). Molecular weights were estimated by SDS polyacrylamide gel electrophoresis (SDS-PAGE, 10% crosslinking, 75V, 2 hours) visualized with silver staining[4]. Migration distances on SDS-PAGE electrograms were quantified by Image J and used as a relative measure of the molecular weight. Calibration was performed using protein standards of known molecular weights (Bio-Rad). The calibration curve was linear (R^2 = 0.98) in the range of 28-78 kDa. The propensity of proteins to aggregation was determined by gel densitometry image analysis[5]. Image analysis was carried out using Matlab R2016b software. For qualitative analysis, pixel densities of individual lanes were averaged axially and the means plotted as a function of migration distance. For quantitative analysis, lane densities above the defined threshold for aggregation intermediates (77 kDa) were integrated and normalized by total lane density. To determine the oligonucleotide content per unit protein in conjugate species, conjugates were analyzed using SYBR Gold[6, 7] and microBCA assays (Thermo Scientific) to quantify single-stranded DNA and protein, respectively.

***In vitro* cross-presentation assay using B3Z CD8 T cell hybridoma.** The ability of OVA-CpG conjugates to facilitate antigen cross-presentation was evaluated by an *in vitro* cross-presentation assay using the $CD8^+$ T-cell hybridoma B3Z cell line and bone marrow derived macrophages (BMDMs). The B3Z T-cell hybridoma is a genetically modified T-cell line that can be triggered to produce beta-galactosidase via activation by antigen-presenting cells that display the OVA epitope SIINFEKL in the context of a murine K^b MHC Class I molecule[8]. In this

way, the B3Z T-cell hybridoma assay provides a measure of the extent of antigen cross-presentation and T-cell activation[9]. Prior to beginning experiments, BMDMs[10] were cultured in 12-well plates seeded at 500,000 cells/well (IMDM, 10% FBS, 10 ng/mL M-CSF). B3Z T-cell hybridoma cells were cultured in suspension at a concentration of 5 x 10^6 cells/100mL (RPMI, 10% FBS, 1% penicillin/streptomycin, 1mM pyruvate, 2 mM glutamine, 50 μM β-mercaptoethanol). All cells were maintained at 37°C, 5% CO_2/95% air atmosphere and approximately 85% relative humidity. The cross-presentation assay was conducted essentially according to the protocol of Karttunen et al[8] with minor modifications. Briefly, BMDMs (5 x10^5 cells/well) were co-cultured with B3Z T-cell hybridoma cells (1 x 10^6 cells/well) in 12-well plates in RPMI complete media (10% FBS). To this co-culture, OVA-CpG conjugates and controls were added to a final concentration of 9μM (OVA-equivalent) and incubated for 24 hours (37°C, 5% CO_2 incubator) with gentle agitation. Subsequently, the B3Z cells were recovered and processed to extract β-Gal as previously described[11]. The activity of β-Gal in extracted samples was quantified by the ONPG spectrophotometric method (at 420 nm)[11], using purified β-Gal enzyme with known enzymatic activity for calibration.

Statistical analysis. Data are expressed as mean ± S.D. Means of multiple groups were compared with the one-way ANOVA, followed by *post hoc* Tukey's pairwise comparisons. All probability values are two-sided, and values of $p < 0.05$ were considered statistically significant. Statistical analyses were carried out using the GraphPad Prism 7 software package.

Supplementary Figures

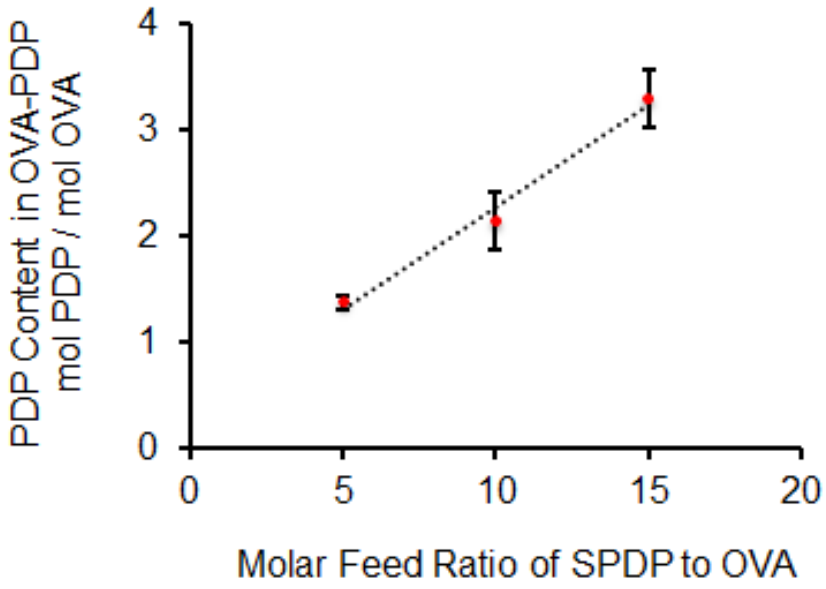

Figure S17. Generation of OVA-PDP species with controlled extent of PDP functionalization. The content of PDP functional groups per unit OVA was quantified using the BCA and the pyridine-2-thione spectrophotometric assays to determine the contents of protein and the PDP functional group, respectively. Data represent mean ± S.D., n = 3

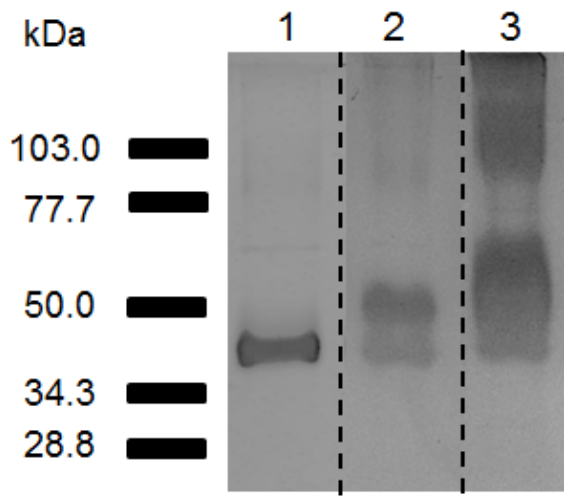

Figure S18. SDS polyacrylamide gel electrophoresis (SDS-PAGE) of crude OVA-CpG conjugates. Representative image of SDS-PAGE analysis (10%, 75V, 90 minutes) for OVA (lane 1), crude OVA-1-CpG (lane 2) and crude OVA-2-CpG (lane 3) conjugates prior to purification by anion exchange chromatography. Molecular weights were analyzed using the ladder of protein standards.

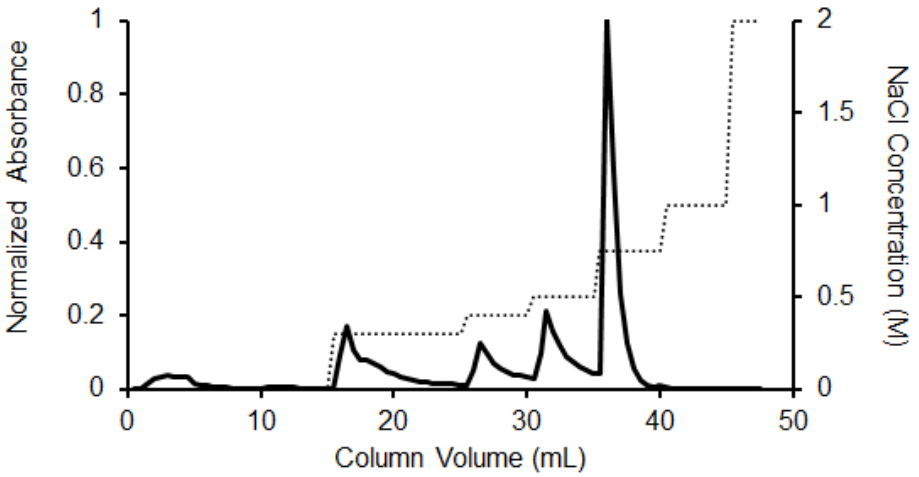

Figure S19. Representative anion exchange chromatogram for crude OVA-3-CpG species. Anion exchange chromatography was carried out using quaternary ammonium solid phase with a stair-step sodium chloride (NaCl) elution gradient (dashed line).

Bibliography:

1 Carlsson, J., Drevin, H. & Axen, R. Protein thiolation and reversible protein-protein conjugation. N-Succinimidyl 3-(2-pyridyldithio)propionate, a new heterobifunctional reagent. *The Biochemical journal* 173, 723-737 (1978).

2 Slutter, B. *et al.* Conjugation of ovalbumin to trimethyl chitosan improves immunogenicity of the antigen. *J Control Release* 143, 207-214, doi:10.1016/j.jconrel.2010.01.007 (2010).

3 Lucena-Aguilar, G. *et al.* DNA Source Selection for Downstream Applications Based on DNA Quality Indicators Analysis. *Biopreservation and Biobanking* 14, 264-270, doi:10.1089/bio.2015.0064 (2016).

4 Wray, W., Boulikas, T., Wray, V. P. & Hancock, R. Silver staining of proteins in polyacrylamide gels. *Anal Biochem* 118, 197-203 (1981).

5 Pathak, M., Dutta, D. & Rathore, A. Analytical QbD: Development of a native gel electrophoresis method for measurement of monoclonal antibody aggregates. *Electrophoresis* 35, 2163-2171, doi:10.1002/elps.201400055 (2014).

6 Tuma, R. S. *et al.* Characterization of SYBR Gold nucleic acid gel stain: a dye optimized for use with 300-nm ultraviolet transilluminators. *Anal Biochem* 268, 278-288, doi:10.1006/abio.1998.3067 (1999).

7 Goldshtein, H., Hausmann, M. J. & Douvdevani, A. A rapid direct fluorescent assay for cell-free DNA quantification in biological fluids. *Ann Clin Biochem* 46, 488-494, doi:10.1258/acb.2009.009002 (2009).

8 Karttunen, J., Sanderson, S. & Shastri, N. Detection of rare antigen-presenting cells by the lacZ T-cell activation assay suggests an expression cloning strategy for T-cell antigens. *Proc Natl Acad Sci U S A* 89, 6020-6024 (1992).

9 Mant, A., Chinnery, F., Elliott, T. & Williams, A. P. The pathway of cross-presentation is influenced by the particle size of phagocytosed antigen. *Immunology* 136, 163-175, doi:10.1111/j.1365-2567.2012.03558.x (2012).

10 Ying, W., Cheruku, P. S., Bazer, F. W., Safe, S. H. & Zhou, B. Investigation of macrophage polarization using bone marrow derived macrophages. *J Vis Exp*, doi:10.3791/50323 (2013).

11 Smale, S. T. Beta-galactosidase assay. *Cold Spring Harb Protoc* 2010, doi:10.1101/pdb.prot5423 (2010).